Institut für Chemie – Supramolekulare Chemie

Ionic liquid precursors for multicomponent inorganic nanomaterials

Kumulative Dissertation

Zur Erlangung des akademischen Grades

"doctor rerum naturalium"

(Dr. rer. nat.)

in der Wissenschaftsdisziplin Materialchemie

eingereicht an der Mathematisch-Naturwissenschaftlichen Fakultät

der Universität Potsdam

von

Ahed Abouserie

geboren am 29.03.1987 in Giza, Egypt

Potsdam, den 28. März 2018

1. Prof. Dr. Andreas Taubert, University of Potsdam

2. Prof. Dr. Stefanie Dehnen, University of Marburg

3. Prof. Dr. Peer Schmidt, Brandenburg University of Technology

*Prof. Peter Strauch, of blessed memory, acted as my second supervisor.

Dedicated to

My parents

My brother, Mohanad

My brother, Kaream

Derya Yildirim

Abstract

A series of relatively low-cost ionic liquids (ILs), based on the *N*-alkylpyridinium cations, and tetrachloridometallate $[MCl_4]^{2-}$ (M = Cu, Co, Zn, or Cu/Co) and hexachloridodicuprate(II) $[Cu_2Cl_6]^{2-}$ anions were synthesized for non-enzymatic amperometric detection and organic photovoltaic cells. The packing diagram of these ILs and the interaction between the cations and the anions have been investigated by single-crystal X-ray diffraction.

The single crystal analysis shows that all crystal structures are stabilized by several non-classical hydrogen bonding, and all ILs based on the same chain pyridinium cation are isostructural. The ILs based on short chain cation are monoclinic and crystallize in the space group $P2_1/n$, while the crystals of the ILs based on long chain cation are triclinic and form in the space group $P\bar{1}$. Powder X-ray diffraction (XRD) confirms the single-crystal X-ray analysis and shows that the alkyl chain length is the critical factor in controlling the crystal structure of these ILs.

The thermal stability and the phase behavior of all ionic liquids were investigated by thermogravimetric analysis (TGA) and differential scanning calorimetry (DSC). Liquid crystalline phases were only observed, in this study, in the case of ILs based on the *N*-dodecylpyridinium cations, while ILs based on short chain cation exhibit just glass and/or melting transitions. Polarized optical microscopy (POM) confirms the formation of the liquid crystalline phases.

Binary and ternary metal chalcogenides such as copper sulfide and copper-cobalt sulfide were synthesized using a simple hot-injection method from bis(trimethylsilyl)sulfide and the ionic liquid precursor (ILP). The ILP acts not only as a metal source but also as a morphology directing template and as a stabilizer for the micro/nanoparticles. The CuS particle morphology, size, and the chemical composition are controlled by different parameters such as the ILP, reaction temperature, and the growth time.

Hexagonal p-type semiconductor CuS nanoplates were synthesized by using the long alkyl chain ILP bis(*N*-dodecylpyridinium) tetrachloridocuprate (II). The nanoplates were successfully incorporated as hole conduction materials into organic photovoltaic (OPV) resulting in increasing the power conversion efficiency about 16% higher than without using the nanoplates.

On the other hand, CuS with hierarchical flower-like microstructures (CuS_{flower}) were synthesized by using the short alkyl chain ILP bis(*N*-butylpyridinium) tetrachloridocuprate (II). The flower-like morphologies can be adjusted with reaction time and temperature. CuS_{flower} microstructures show high performance non-enzymatic H_2O_2 amperometric detection with superior electrocatalytic activity and sensitivity (3.82 mM^{-1} cm^{-2}), very low detection limit (0.1 μM) along with exceptional selectivity and long-term stability compared to CuS sensor materials obtained with conventional processes and structures.

With regards to the successful and efficient transformation of the ILP to inorganic NPs, the concept of the ILP has been expanded by increasing the fraction of the metal in the ILP, such as $[C_4Py]_2[Cu_2Cl_6]$.

Furthermore, $CuCo_2S_4$ nanoparticles were synthesized by using *N*-butylpyridinium tetrachloridocuprate(II)cobaltate(II) as a single source precursor. Copper cobalt sulfides are promising materials with excellent electrochemical performance with high capacity and excellent cyclic stability in comparison to the single metal sulfide owing to the multiple oxidation states.

Table of Contents

Nomenclature

List of Abbreviations

Abbreviation	Full name
2ME	2-methoxyethanol
AILS	Aprotic ionic liquids
a.u.	Arbitrary unit
AA	Ascorbic acid
Atm	Atmosphere
AFM	Atomic force microscope
ATR	Attenuated total reflection
BSE	Back-scattered electrons
TMS, $(TMS)_2S$	Bis (trimethylsilyl) sulfide
BET	Brunauer Emmett Teller
BHJ	Bulk hetero-junction
CCDC	Cambridge crystallographic data centre
CHB	Chlorobenzene
Cifs	Crystallographic information files
CBM	Conduction band minimum
(C)	Conventional
J-V	Current density-voltage
CNPs	CuS nanoplates
CVs	Cyclic voltammograms
T_d	Decomposition point
DFT	Density functional theory calculations
DSC	Differential scanning calorimetry
DMSO-d_6	Dimethyl-d_6 sulfoxide
CHN analysis	Elemental analysis
EIS	Electrochemical impedance spectroscopy
EPR	Electron paramagnetic resonance spectroscopy
ESI	Electrospray ionization
ETL	Electron transport layer
EDX	Energy dispersive X-ray spectroscopy
FHJ	Flat heterojunction

FTIR	Fourier transform infrared
GCE	Glassy carbon electrode
GLU	Glucose
GNs	Graphene sheets
HOMO	Highest occupied molecular orbital
HCL	Hole collection layer
HRP	Horseradish peroxidase
ITO	Indinium tin oxide
IR	Infrared
ICSD	Inorganic crystal structure database
ICDD	International centre for diffraction data
ILCs	Ionic liquid crystals
ILS	Ionic liquids
ILPs	Ionic liquid precursors
IE	Ionization energy
ICP	Inductively coupled plasma
(I)	Inverted
I	Isotropic phase
JCPDS	Joint committee on powder diffraction standards
LIBs	Lithium-ion batteries
LUMO	Lowest unoccupied molecular orbital
MS	Mass spectroscopy
MILs	Metal-containing ionic liquids
mM	Millimolar
$[C_nPy]_2[MCl_4]$	N-alkylpyridinium tetrachloridometallate salts
$[C_4Py]_2[MCl_4]$	N-butylpyridinium tetrachloridometallate salts
$[C_{12}Py]_2[MCl_4]$	N-dodecylpyridinium tetrachloridometallate salts
$[C_4Py]Cl$	N-butylpyridinium chloride
$[C_{12}Py]Cl$	N-dodecylpyridinium chloride
NDs	Nanodendrites
nm	Nanometer
NPs	Nanoparticles
NTs	Nanotubes
NW	Nanowire
NIR	Near-infrared

NMR	Nuclear magnetic resonance spectroscopy
OAm	Oleylamine
1 D	One dimensional
V_{oc}	Open-circuit voltage
E_g	Optical band gap
OPV	Organic photovoltaic
OPVs	Organic photovoltaic solar cells
R_{pv}	Peak-to-valley roughness
PBS	Phosphate buffered saline
PCBM	Phenyl-C61-butyric acid methyl ester
PILs	Protic ionic liquids
POM	Polarized optical microscopy
P3HT	Poly(3-hexylthiophene)
PEDOT	Poly(3,4-ethylenedioxythiophene)
PSS	Poly(styrenesulfonate)
PTFE	Polytetrafluoroethylene
XPS	X-ray photoelectron spectroscopy
XRD	Powder X-ray diffraction
PCEs	Power conversion efficiencies
RGO	Reduced graphene oxide
RILS	Room-temperature ionic liquids
R_q	Root-mean-square roughness
SCE	Saturated calomel electrode
SE	Secondary Electrons
SEM	Scanning electron microscopy
J_{sc}	Short-circuit current density
R_{sh}	Shunt resistance
SmA	Smectic A phase.
TCE	Tetrachloroethylene
TMAH	Tetramethylammonium hydroxide pentahydrate
TGA	Thermogravimetric analysis
TEM	Transmission electron microscopy
3 D	Three dimensional
2 D	Two dimensional
UA	Uric acid

UV	Ultraviolet
VBM	Valence band maximum
Vis	Visible
0 D	Zero-dimensional

List of Chemical Symbols

Chemical symbol	Chemical name
$C_3H_8O_2$	2-methoxyethanol
C_2H_3N	Acetonitrile
$C_6H_8O_6$	Ascorbic acid
$AlCl_3$	Aluminium Chloride
Co_9S_8	Cobaltpentlandite
$Cu_{1.75}S$	Anilite
$[[CH_3]_3Si]_2S$	Bis (trimethylsilyl) sulfide
$CuCo_2S_4$	Copper Cobalt Sulfide, Carrollite
CuS	Copper Sulfide, Covellite
C_6H_5Cl	Chlorobenzene
CdS	Cadmium sulfide
Ca	Calcium
CuO	Cupric Oxide
Cu_2O	Cuprous Oxide
$CoCl_2 \cdot 6H_2O$	Cobalt(II) Chloride Hexahydrate
$CuCl_2 \cdot 2H_2O$	Copper(II) Chloride Dihydrate
$CuSo_4.5H_2O$	Copper Sulfate Hydrate
Cu_9S_5, Cu_2S	chalcocite
$Cu_{1.8}S$	digenite
$[CD_3]_2OS$	Dimethyl-d_6 sulfoxide
$Cu_{1.96}S$	djurleite
$C_6H_{12}O_6$	Glucose
Au	Gold
PF_6	Hexafluorophosphate
H_2O_2	Hydrogen Peroxide
In_2O_5Sn	Indium tin oxide
Fe_3O_4	Iron(II, III) oxide
FeS	Iron(II) sulfide
C_3H_8O	Isopropanol
MnO_2	Manganese dioxide
MoO_3	Molybdenum trioxide
$C_9H_{14}NCl$	N-butylpyridinium chloride

$C_{18}H_{28}Cl_4N_2M$	N-butylpyridinium tetrachloridometallate salts
$C_{18}H_{28}N_2Cu_2Cl_6$	N-butylpyridinium hexachloridodicuprate(II)
$C_{17}H_{30}NCl$	N-dodecylpyridinium chloride
$C_{34}H_{60}Cl_4N_2M$	N-dodecylpyridinium tetrachloridometallate salts
$C_{18}H_{37}N$	Oleylamine
$C_{72}H_{14}O_2$	Phenyl-C61-butyric acid methyl ester
Pd	Palladium
Pt	Platinum
$[C_{10}H_{14}S]_n$	Poly(3-hexylthiophene)
$[C_6H_4O_2S]_n$	Poly(3,4-ethylenedioxythiophene)
$[C_8H_7SO_3^-]_n$	Poly(styrenesulfonate)
$[C_2F_4]_n$	Polytetrafluoroethylene
Ag	Silver
NaH_2PO_4	Sodium phosphate monobasic
$Na_2HPO_4.7H_2O$	Sodium dihydrogen phosphate Heptahydrate
$[CuCl_4]^{2-}$	Tetrachloridocuprate (II)
$[CoCl_4]^{2-}$	Tetrachloridocobaltate (II)
$[ZnCl_4]^{2-}$	TetrachloridoZincate (II)
C_2Cl_4	Tetrachloroethylene
$[CH_3]_4N[OH].5H_2O$	Tetramethylammonium hydroxide pentahydrate
$C_5H_4N_4O_3$	Uric acid
CH_4N_2O	Urea
$ZnCl_2$	Zinc chloride
ZnO	Zinc oxide

List of Symbols

Symbol	Name	Unit
A	Absorbance	
E_a	Activation energy	J
A_r	Atomic weight	-
N_A	Avogadro constant	$6.023 \cdot 10^{23}$ mol^{-1}
E_g	Band gap	eV
K_B	Boltzmann constant	$1.3806 \cdot 10^{-23}$ J / K
δ	Chemical shift	ppm
c	Concentration of substance	mol / m^3 , mol / l (M)
e	Charge of electrons	C
T_c	Clearing Point	°C
T_{cry}	Crystallization temperature	°C
T_d	Decomposition Point	°C
2θ	Detection angle in XRD	Degree
D, ρ	Density	Kg / m^3
C	Electric capacity	C / V
I	Electric current	A
E	Electric field strength	V / m
χ	Electronegativity	-
E	Energy	J
ΔH	Enthalpy	J
F	Faraday constant	96485.3 C / mol
FF	Fill Factor	-
F	Force	N
T_f	Freezing Point	°C
ΔG	Free Gibbs energy	J
f	Frequency	Hz
T_g	Glass Transition Point	°C
I_o	Incident intensity	A

T_{iso}	Isotropic phase transition	°C
d	Lattice spacing	Å
L	Length of the light pass	cm
B	Magnetic field	T
m	Mass	mg, g, kg
T_m	Melting Point	°C
M_w	Molecular weight	$g \cdot mol^{-1}$
$\hbar$	Plank constant	$6.626 \cdot 10^{-34}$ J·s
Q	Quantity of heat	J
[hkl]	Represents a direction	-
<hkl>	Represents a family of directions	-
(hkl)	Represents a plane	-
{hkl}	Represents a family of planes	-
C_P	Specific heat of sample	$J \cdot Kg^{-1} \cdot K^{-1}$
C_R	Specific heat of reference material	$J \cdot Kg^{-1} \cdot K^{-1}$
J	The J-coupling	Hz
T	Temperature	K or °C
t	Time	h or s
I	Transmittance intensity	A
λ	X-ray wavelength	Å

Chapter 1. Introduction

1.1.   Ionic Liquids (ILs)

Ionic liquids (ILs) have become one of the essential branches of chemistry, because of they are highly diverse of chemical composition and unusual properties. ILs have been used in a wide range of applications, including organic synthesis, catalysis, separation and extraction, electrochemistry, biotechnology, and synthesis of inorganic materials and nanoparticles.[1-8]

The field of IL-based inorganic nanomaterials synthesis has been early studies using an IL, or a mixture of IL with an organic solvent as reaction media. This concept has been expanded to use the ILs as a reactant, stabilizer, and morphology directing template, which provides a better understanding of the nucleation and the growth processes of the resulting inorganic materials.[1]

Consistent with Francis Crick who stated that "if you want to understand function, study structure.",[9] the structure of ILs should be discussed before understanding the role of ILs on the formation of inorganic nanomaterials. ILs are low-temperature molten salts consisting of ions only. They are composed of organic cations and organic or inorganic anions. ILs have attracted considerable interest over the last decades; this is mostly due to their unusual physical and chemical properties like high thermal stability, very low vapor pressure, low melting points (below or around 100 $°C$), broad liquid range, and ionic conductivity.[5, 10-12]

ILs are often considered as designer solvents, a new generation of solvents, for synthesis and catalysis.[2, 13-16] They can be tuned by an appropriate choice of the cation and the anion. It means that the physical, chemical and biological properties can be tailored by changing the anions or the cations, by mixing two or more ILs, or by designing specific function group into the cation and/or the anion. Some of ILs are called room-temperature ionic liquids (RILs). They are fluid-like (exist as liquids) at temperatures close to room temperature because of their chemical structure. ILs have been extensively used for a multitude of applications such as extraction and separation,[17-19] batteries,[20] electrochemistry,[4] fuel cells,[21] solar cells,[22] nanotechnology,[23] drug delivery,[24] and many other usages. The most popular cations and anions employed in ILs are shown in Figure 1.1.

The physicochemical properties of ILs can be characterized by understanding their molecular structure and their intermolecular forces. ILs display coulombic interactions

between the centers of gravity of the charges, cation – cation repulsion, the van der Waals hydrophobic interaction between long alkyl chains, and hydrogen bonding between cations and anions.[25] The molecular structure can explain the low melting points and high viscosity of ILs compared to molten salts. The ionic bonds in molten salts, mostly made of monoatomic ions such as $NaCl$ (m.p > 801 °C), are powerful due to the short distance between their small ions resulting in high melting points.[26] On the other hand, ILs have low melting points due to their low lattice energy, which in turn is a consequence of increasing the distance between two ions resulting in low melting points.[27] The molecular structure affects the properties of ILs such as melting point, viscosity, thermal stability, surface tension, heat capacity, and conductivity.[28]
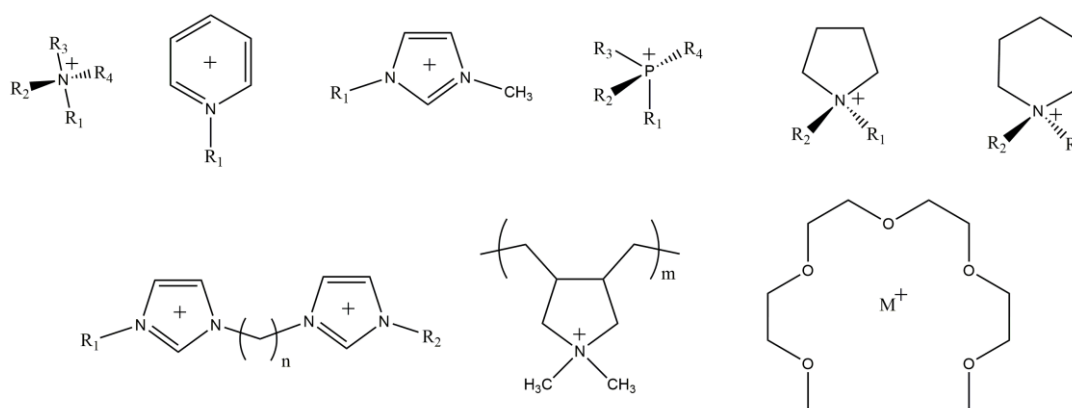
Commonly some used cations in ILs
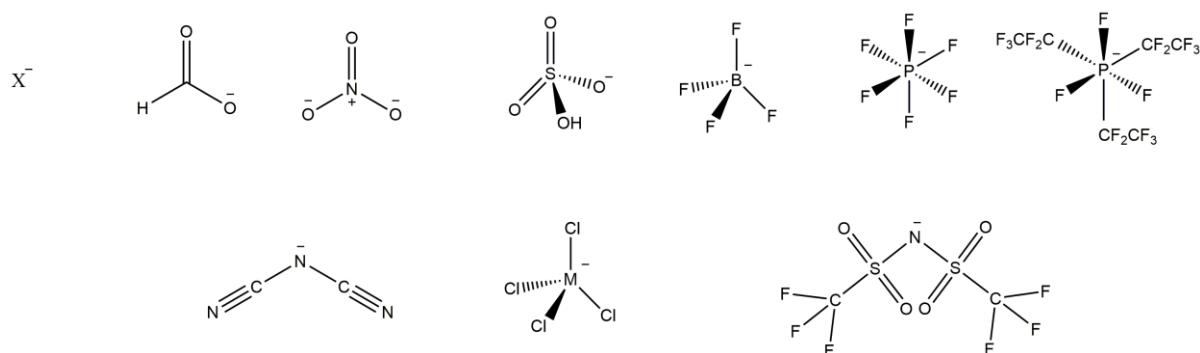
Commonly some used anions in ILs

Figure 1.1. The commonly used cations and anions used in the chemical structures of ILs. From left to right, the cations (first row) ammonium, pyridinium, 1-methyl-3-alkylimidazolium, phosphonium, pyrrolidinium, piperidinium; (second row) 1,3-bis [3-methylimidazolium-1-yl]alkane, poly(diallyldim- ethylammonium), metal tetraglyme. The anions (third row) halides, formate, nitrate, hydrogen sulfate, tetrafluoroborate, hexafluorophosphate, tris (pentafluoroethyl)trifluorophosphate; (Last row) dicyanamide, tetrachloridometallate, bis(perfluoroethylsulfonyl)imide.

1.2. History of ionic liquids

The development and investigation of ILs dates back to **1914**, when the first room-temperature molten salt (ethylammonium nitrate – melting point 12.5 °C) was reported by Walden.[29] This salt was formed by the reaction of ethylamine with concentrated nitric acid.

In 1934, Graenacher[30] used 1-ethylpyridinium chloride in the presence of nitrogen-containing bases to dissolve cellulose. **In 1938**, the first ionic liquid crystals (ILCs) were reported by Knight and Shaw.[31] The authors observed the thermotropic mesomorphism of pyridinium salts.

In 1943, Barrer[32] used the term "ionic liquid" in the general sense for the first time. **In 1948,** Hurley and Wier[33] developed the first ILs with chloridoaluminate anions when they mixed ethylpyridinium halides with aluminum to produce colorless liquids at room temperature. **In 1951**, Hurley and Wier[34] were able to use these salts for the electroplating of aluminum.

In 1961, Bloom[35] used the term (ionic liquid) to refer to pure molten salts. **In 1963**, Yoke and co-workers[36] reported RTIL (triethylammonium dichloridocuprate $[(C_2H_5)_3NH][CuCl_2]$ – melting point 25 °C) by reaction of copper (I) chloride with triethylammonium hydrochloride.

In 1968, King and co-workers[37] reported an IL, 1-ethylpyridinium bromide with aluminum chloride, as electrolytes for batteries based on patents from 1948.

In 1972, Parshall[38] reported the use of the low-melting tetraalkylammonium salts of the $SnCl_3^-$ and $GeCl_3^-$ anions for homogeneous catalytic reactions of olefins.

In 1975, Osteryoung and co-workers[39] reported the use of a room temperature, high Lewis acid molten salt on the electrochemistry of organometallics and an alkylaromatic compound. **In 1976**, Osteryoung and co-workers[40] elaborated the physiochemical properties of room-temperature molten salt and used them as media for organic electrochemistry. **In 1978**, Osteryoung and co-workers[41] rediscovered chloridoaluminate salts and succeeded in preparing room temperature chloridoaluminate melts. This salt, $[C_4Py]Cl\text{-}AlCl_3$, is a liquid at room temperature.

In 1981, Knifton[42] used phosphonium ILs to synthesis ethylene glycol from synthesis gas (CO + H_2). **In 1982**, Wilkes and co-workers[43] reported a new class of RTILs, dialkylimidazolium chloridoaluminates. Pool and co-workers[44] used ethylammonium nitrate for gas-liquid chromatography. **In 1984**, Magnuson and co-workers[45] reported the first study of the IL-enzyme system.

In 1990, Chauvin and co-workers[46] used ILs for the first time as solvents for homogenous transition metal catalysts. **In 1992**, Wilkes and co-workers[47] prepared the first water-stable ILs with 1-ethyl-3-methylimidazolium as cation and tetrafluoroborate as an anion. In contrast to chloridoaluminate ILs, these salts could be prepared and safely stored without an inert atmosphere. These salts can be regarded as the second generation of ILs.

In 2004, Taubert and co-workers[1, 48-50] reported the formation of $CuCl$ nanoplatelets from an ionic liquid crystal precursor (ILCP), have been termed as "all-in-one" solvent-reactant-template.

Nowadays, the field of ILs is one of the most popular areas of research both in academia and industry. Figure 1.2. shows the growing academic and industrial interest in IL technology as represented by the yearly increase in the number of publications (according to Sci-Finder) starting from less than 10 articles in 1990 to more than 7000 articles in 2014.

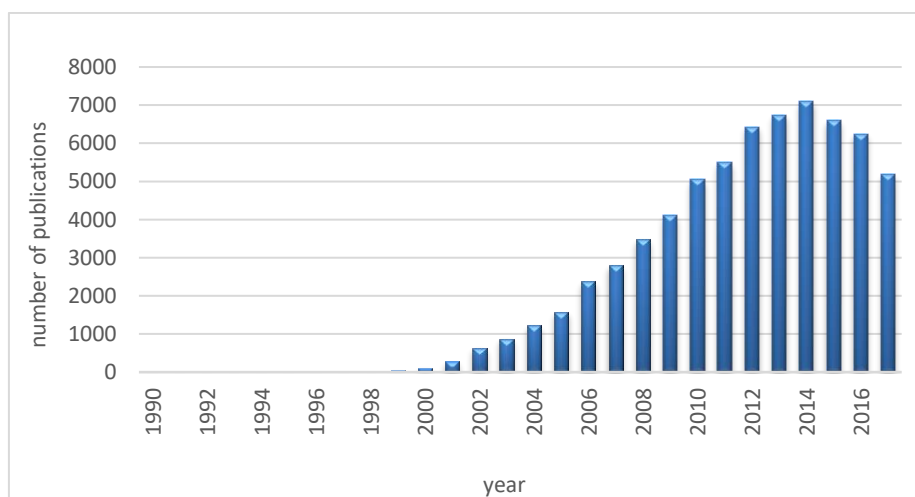**Figure 1.2**. Annual growth of ILs publications determined by SciFinder.

1.3.   Classification of Ionic liquids (ILs)

Based on their composition, ILs can be classified into four classes such as protic Ionic liquids (PILs), aprotic ionic liquids (AILs), zwitterionic liquids (ZILs), and metal-containing ionic liquids (M-ILs).[4, 51-55] However, this classification is not so rigid as there are some other

several ILs which can be considered as subclasses of ILs such as amino acids ILs, polymeric ILs, divalent ILs, and chiral ILs.[11] This makes classifying ILs a big challenge depending on the cation, the anion, and the functional group.

1.3.1. Protic ionic liquids (PILs) (Proton-donating)

Protic ILs (a pure mixture of ions) are formed by a proton transfer from a combination of a Bronsted acid and a Bronsted base. Due to the proton transfer, Proton-donor and acceptor sites are created on the ions.[11] They have been widely used as electrolytes in fuel cells.[54, 56]

1.3.2. Aprotic ionic liquids (AILs) (Nonproton-donating)

Ions in aprotic ILs are formed by the covalent bond between two functional groups. This leads to making a good ionic behavior (more thermally and electrochemically stable than PILs).[11] AILs are suitable for lithium batteries, supercapacitors, electrochemistry, synthesis of nanostructured materials, and catalysis.[57-65]

1.3.3. Zwitterionic liquids (ZILs)

Zwitterionic liquids composed of a cation and an anion tethered covalently (two hydrocarbon chains, a bridge, and two polar groups). They are electrically neutral, and they can behave as acids or bases (donor or acceptor).[66] They are suitable for ionic-liquid-based membranes.[4]

1.3.4. Metal-containing ionic liquids (M-ILs)

Metal-ILs have received much attention due to the additional properties, including magnetic, optical, or catalytic depends on the metal ion, which as a part of the cation or the anion. They are suitable for organic synthesis and mercury removal from natural gas. They are used as the precursor for the inorganic nanomaterial beside their solvent role.[12, 67-70]
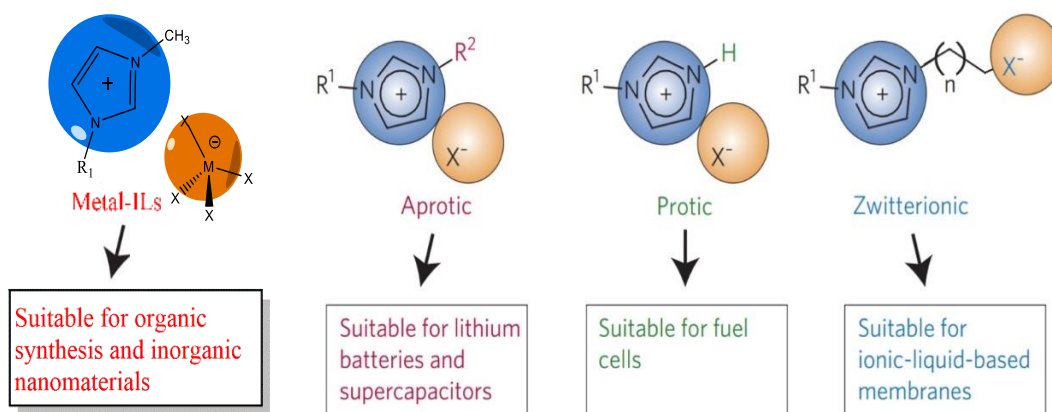
Figure 1.3. Basic types of ionic liquids: Metal-ILs, aprotic, protic and zwitterionic liquids. Adapted from Ref.[4]

1.4.   *Liquid Crystals (LCs)*

"Liquid crystals are considered as the fourth state of matter."

Saeva, F. D. Liquid Crystals: The Fourth State of Matter; Marcel Dekker: New York, 1979.[71]

As some of ILs can form liquid crystals (LCs), which exhibit different degrees of order,[1] it is necessary to briefly discuss the structure of the LCs. The states of the matter, solid, liquid, and gas, differ depends on the type and the degree of order present in their phase. Most substances go from solid to liquid by heating. However, some materials exhibit intermediate states, called liquid crystal states, of matter, as shown in Figure 1.4.[72]
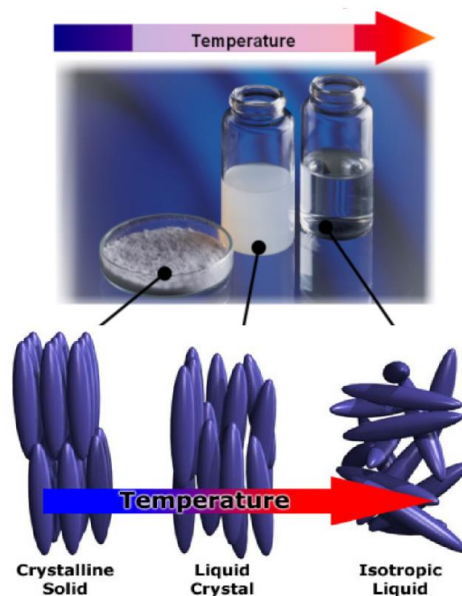
Figure 1.4. Schematic illustration of the occurrence of LC phase as an intermediate state between the solid crystal and the isotropic liquid. Adapted from refs.[73, 74]

The liquid crystal state is an exciting intermediate phase between solid state (perfectly ordered crystalline) and liquid state (totally disordered),[75-76] which combines the properties of crystals and liquids. Figure 1.5 shows the arrangement of molecules in the liquid crystal phases - nematic, smectic, and cholesteric. The molecules are parallel, and the ends are interdigitated at random intervals in the nematic phase, while in the smectic phase, the molecules are parallel and arranged in planes. For cholesteric phase, the molecules are arranged in layers, and these layers are rotated with respect to each other to give a spiral structure. The molecular order increases from the nematic phase to the smectic phase to the cholesteric phase as shown in Figure.1.5.[77]
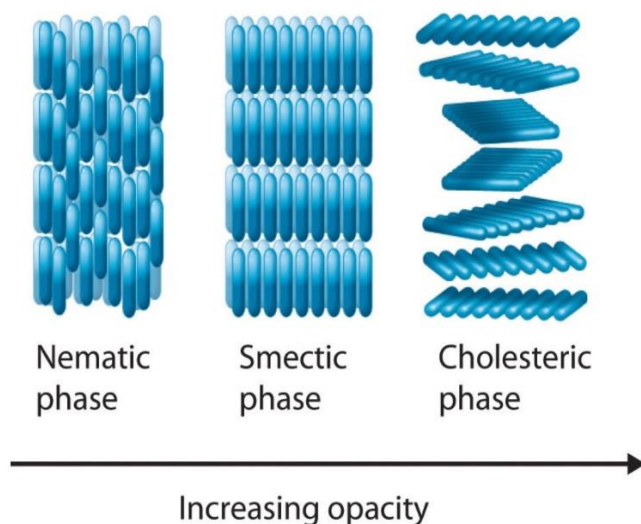
Figure 1.5. The Arrangement of Molecules in the Nematic, Smectic, and Cholesteric Liquid Crystal Phases.[77]

There are three types of LCs - lyotropic LC, thermotropic LC, and amphitropic LC. Lyotropic LCs can be generated by adding a suitable solvent into the system, and thermotropic LCs are produced by varying the temperature. Amphitropic LCs would be capable of forming both lyotropic as well as thermotropic LC phases.[78] Figure 1.6 shows a schematic representation of the different types of mesophases exhibited by *N*-alkyl β-D-glucopyranoside (this figure only represents different types of LCs, not ILCs). This compound can be accurately described as being amphitropic, *i.e.*, being a thermotropic as well as a lyotropic liquid crystal.[79]
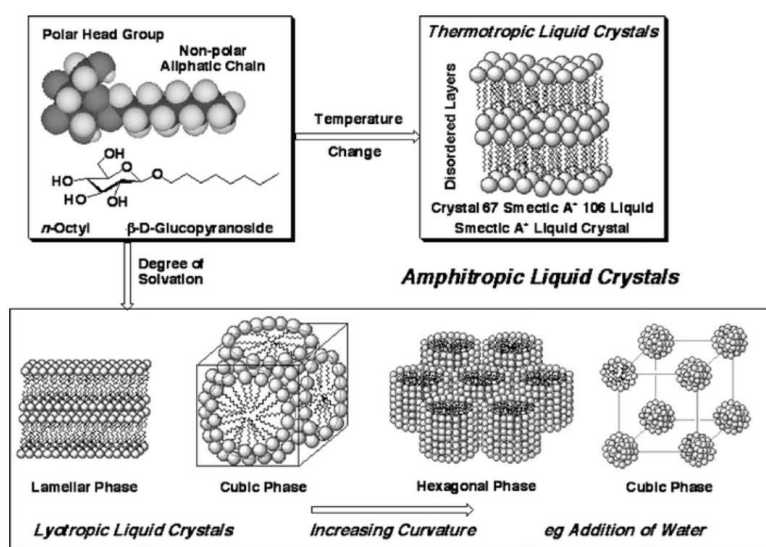
Figure 1.6. Schematic structures of the different types of liquid crystal.[79]

1.5. A Brief history of Liquid Crystals (LCs)

Ionic liquid crystals (ILCs) are fascinating liquid-crystalline materials. However the first ILC was reported in **1938**,[31] the history of liquid crystal (LC) dates back to **1888** when Reinitzer[80] noticed a reversible color change during heating and cooling cycles of cholesterol derivates. The cholesteryl benzoate melted at 145.5 °C into a milky fluid which existed until 175.5 °C where the cloudiness suddenly disappeared, giving way to a bright and transparent liquid. **In 1889,** Lehmann[81] confirmed Reinitzer's observation and called these materials "flowing crystals or slimy liquid crystals". **In 1890**, Gettermann[82] synthesized the first liquid crystalline compounds (the derivatives of azoxybenzene).

In 1900, Vorländer and co-workers[83] synthesized the first smectic thermotropic compound (diethyl 4,4'-azoxybenzene). **In 1908**, Vorländer[84] obtained up to 170 liquid crystalline compounds as he was able to drive rules of liquid crystallinity as relating to chemical structure.

In 1922, Friedel[85] proposed a classification of LCs based upon the different molecular orderings of each substance (nematic, smectic, and cholesteric). **In 1923**, De Broglie and Friedel[86] confirmed the existence of equidistant parallel layers in smectic materials. **In 1942**, Tsvetkon[87] established the present equation for the degree of the orientation of liquid crystal.

In 1968, Heilmeier et al.,[88] demonstrated the first liquid crystal display (LCD) based on the dynamic scattering effect. **In the 1970s**, Schadt and Helfrich,[89] and Fergason[90] got a patent on an electro-optical field effect which has become known as the twisted nematic (TN) cell.

In the 1980s-1990s, LCDs replace conventional display devices in many applications. Liquid crystal technology is an evidence for the importance of research and development - from the first observation in a laboratory to a billion dollar market.

1.6. Pyridinium based ionic liquids

The field of ionic liquid crystals (ILCs) have attracted considerable interest due to their unique properties, which resulting from the combination of ionic liquid (IL) and liquid crystal (LC) properties. The govering and stablization of the liquid crystalline phase depends on the molecular shape and the size of the ionic groups, microphase seperated structured – where polar and nopolar regions are seperated, and intermolecular interactions, which includes the hydrophobic interactions between the long alkyl chains, hydrogen bonding, dipole-dipole interactions, anion-cation interactions, and the π-π stacking of the aromatic rings.[1, 91]

The search for ILs, which includes ILCs, with optimal properties for a given application requires an understanding of the link between the structure and the chemical composition of these salts and their resulting dynamic and thermophysical properties. The ILs can comprise an organic cation selected from the group consisting of ammonium, guanidinium, imidazolium, phosphonium, pyrrolidinium, and pyridinium.[25, 92-97]

Pyridinium based ILs are of particular interest to us,[98] given their excellent thermal stability,[99-103] lower cost,[104-105] lower solubility in water[106-107] and have higher biodegradability[108-109] in comparison to imidazolium ILs – However, some others researchers reported that Imidazolium ILs are more stable than pyridinium, tetraalkylammonium, and piperidinium ILs.[110] Pyridinium salts are water-stable, non-volatile, non-corrosive, immiscible with many organic solvents, and behave as short chain cationic surfactants when they are dissolved in water.[111-113]

The thermal behavior as well as the mesophase type of the pyridinium-based ILs depends on the alkyl chain length, the anion size, the position and the nature of the mesogenic group, which attached to the pyridinium ring.

In 1938, Knight and Show[114] observed mesophases for *N*-alkylpyridinium halides **(1)** with alkyl chains (n= 12, 14, 16, 18). The clearing point decreased with changing the halide in the order of chloride > bromide > iodide because of the smaller ionic radius with respect to iodide and it leads to less shielding of the positive charges of the pyridinium rings and therefore increased the electrostatic repulsion between the headgroups.[115-116]
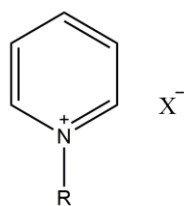
(1)

Knight and Show concluded that the clearing point was affected a lot by the choice of the anions and that the stability of the mesophase is increased with increasing the alkyl chain length.[114]

In 1982, Sudhölter et al.,[116] reported several compounds with an *N*-alkyl pyridinium core. They concluded that the head group plays an essential role in determining the mesomorphic behavior. When the nitrogen in the pyridine ring is protonated, a simple phase transition from the solid state to an isotropic liquid is observed (no LC phase behavior was found).

The compounds with protonated 4-alkylpyridinium core **(2)** did not show liquid crystal phase behavior,[116] while Knight and Show reported that the compounds with protonated 2-alkylpyridinium core **(3)** exhibit LC phase behavior in the case of chloride salt **(4)** but not in the fact of picrate **(5)** or picolinate salts **(6)**.[114, 117]
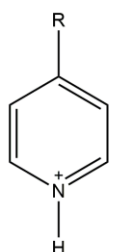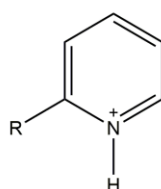
(2)   **(3)**
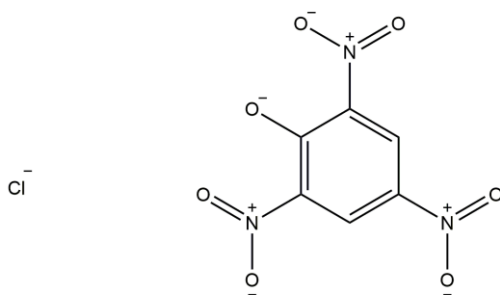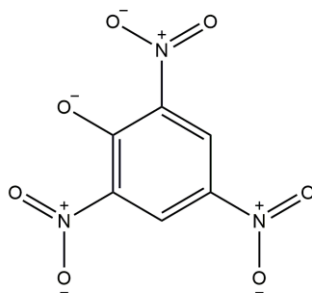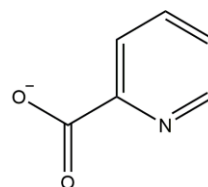
(4)   **(5)**   **(6)**

The structure of the cation head group plays an important role in determining the mesomorphic behavior. As it is mentioned before, when the nitrogen in the pyridine ring is protonated, 4-alkyl pyridinium halide compounds **(7),** no liquid crystal behavior was observed, On the other hand, methylation of the N-atom on 4-alkyl pyridinium iodide **(8)** induces mesomorphism.[116, 118] In 1956, Fürtz and Dietz[118] reported that these compounds (N-methyl-3-alkylpyridinium **(9)**, N-methyl-3-thioalkylpyridinium **(10)**, and N-methyl-3-alkoxypyridinium **(11)** as cations and tosylate **(12)** and methosulfate **(13)** as anions) show LC phase behavior.

| (7) | (8) | (9) | (10) | (11) |

| (12) | (13) |
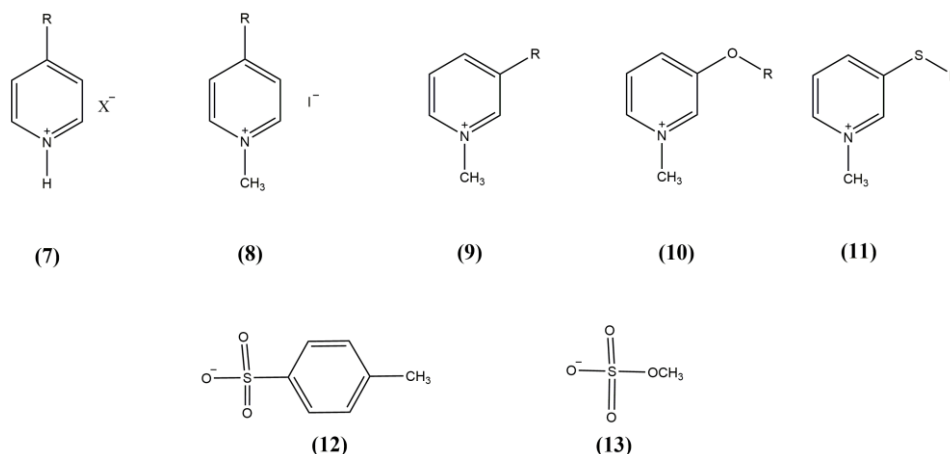
In 1993, Nusselder et al.,[119] concluded that the occurrence and the range of the mesophase depend on several variations of the structure. They rely on the length of the unbranched alkyl chain, the presence of an ester group between the alkyl group and the pyridinium ring, and the counterion. The branched alkyl chain influences the width of the temperature range over which a mesophase is observed.

There are several subtle variations and parameters that can effect on the forming, stabilizing, and increasing the width of the temperature range of the liquid crystal phase behavior.

1.7. Applications of pyridinium based ionic liquids

Pyridinium IL salts have been used in many applications such as solvents, organic synthesis, electrochemical applications, catalysts, surface active agents, biocatalysis, polymerization, metal-ion extraction, light-modulating materials in liquid crystal displays (LCDs), anisotropic ion conductor in molecular electronics, fuel cells, capacitors separation of the products from a reaction mixture, dye-sensitized solar cells, lithium-ion batteries, and extraction of heavy metal cations.[107, 120-126]

Pyridinium IL salts have a successful effect in organic reactions such as Friedel-Crafts and Grignard, and their catalytic role in the synthesis of some pharmaceutical agents such as 1,4-dihydropyridine, 3,5-bis(dodecyloxycarbonyl)1,4-dihydropyridine, and dihydropyrimidinones derivatives.[127-131] They are also used as catalysts in different reactions such as the synthesis of 1,4-dibromonaphthalene, Fischer esterifications and tert-butylation of phenol and esterifications of cyclic olefins with acetic acid.[132-134]

Li et al.[135] reported the use of ILs containing pyridine rings as catalysts for esterification and transesterification of Jatropha oil. This IL, 1-(4-sulfonic acid) butylpyridinium trifluoromethanesulfonate, showed high catalytic activity and biphasic behavior. The product was easily separated from the catalytic system, and the IL keeps its catalytic activity unchanged even after seven reuses.

The ultimate goal is to show the brilliant role of pyridinium ILs and ILCs to achieve functionalized materials that can be used in different applications. ILCs have great potential as oriented materials, ordered solvents or organized reaction media emitting polarized light. There are several reviews that show various applications of ILCs.[136-137]

1.8. Inorganic materials from ionic liquids

Research on ionic liquids (ILs) has also received attention from the inorganic materials community. The unique physicochemical properties of ILs promises synthesis new materials with unusual features. ILs can serve as electrostatic and steric stabilizers. The other influence of the ILs on the formation of inorganic materials is that ILs, which exhibit liquid crystal (LC) phase behavior, enable the morphology tuning of the resulting particles. The use of ILs can act as a nucleating aid for a growing particle due to the presence of internal interfaces and phase-separated domains. They have been used as a stabilizer, structure directing template, and precursor.[1, 138]

ILs have proven to be suitable for the generation and stabilization of different inorganic nanoparticles, including metal nanoparticles (M-NPs).[138] Indeed, Dupont et al.,[139] reported **in 2002**, the preparation and stabilization of M-NPs (Ir nanoparticles) in IL media, and it was used as catalysts for the hydrogenation of olefins. **In 2003**, Nakashima and Kimizuka[140] fabricated hollow titania microspheres in ILs. The IL acts not only as a solvent but also as a stabilizer for the hollow microspheres. Zhou et al.,[141] synthesized excellent crystalline anatase particles in a RTIL.

Hamill et al.,[142] reported that the IL on palladium clusters allow complete recyclability and simple product separation. **In 2004**, Taubert[50] brought a new concept "All-in-one" by the synthesis of $CuCl$ nanoplatelets from an IL precursor. On the other hand, Morris et al.,[143] brought another concept "ionothermal synthesis" by the synthesis of porous materials "a new class of zeolites – such as aluminophosphate zeolite analogues" in the presence of ILs and eutectic mixtures as solvents.

In 2007, Migowski and co-workers[144] reported that the IL provides a favorable environment for the formation of metal nanoparticles with a small diameter and size distribution. They suggest that the use of task-specific ILs may offer stronger stabilizing fluids for the metal nanoparticles without losing their catalytic properties.

In addition, many subsequent studies have been reported on the synthesis and stabilization of transition metal nanoparticles in the presence of IL media. **In 2004**, Itoh et al.,[145] reported the synthesis and functions of water-soluble gold nanoparticles modified with ILs. They demonstrated the phase transfer of the capped gold nanoparticles from aqueous media to IL resulting hydrophilic and hydrophobic properties will be tuned via anion exchange.

The synthesis of the diversity of metal oxides, metal salts (halides, carbonates, oxalates, and phosphates), and metal chalcogenides with different sizes and morphologies in the presence of ionic liquids has gained significant interest.

Taubert and co-workers[48-50, 69, 146-149] reported the synthesis of nanomaterials in the presence of ILs, $CuCl$ nanoplatelets (Figure 1.7a), metal carbonates, gold nanoplatelets, zinc silicates (Figure 1.7b), titanium oxide nanoparticles, and CaF_2 cubes.
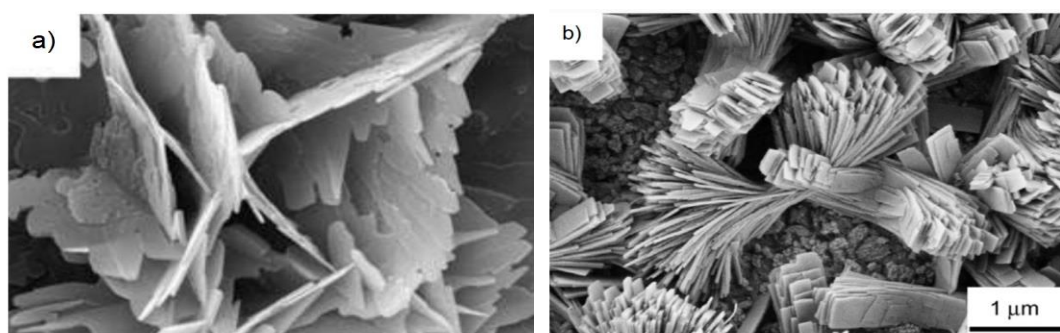
Figure 1.7. SEM images of the a) $CuCl$ nanoplatelets from an IL precursor,[50] and b) zinc silicate by using IL precursor.[148]

To synthesize the desired NPs, the stability of the NPs dispersion should be carefully controlled. The stabilization of the NPs occurs through steric, or electrostatic, or a combination of both steric and electrostatic stabilization. The NPs have to be kinetically stabilized to avoid the coagulation and agglomeration. The morphology and size distribution can be controlled by temperature, time, pH, and concentration.[27-28, 150]

The Derjaguin-Landau-Verwey-Overbeek (DLVO) theory is classically used to describe the overall interaction potential in colloidal systems. The DLVO approach is the combination of the repulsive Coulomb and the attraction van der Waals forces of the colloidal system. This theory assumes that the surfaces of the particles are flat, the charge density is homogenous and remain homogenous – even upon approach of the particles, and the concentration of the counterions is constant.[27, 150]

The stability of the colloidal, which is the balance between the repulsive coulomb and the attraction van der Waals forces, depends on the thickness of the Debye layer. The Debye layer is the sum of the counterions layers surrounding the NP. The NP with thicker Debye layer is more stable as the distance to the other NPs is greater resulting in reducing the van der Waals attraction forces.[27, 150]

The DLVO theory has been extended to other effects such as hydrogen bonding, the hydrophobicity and steric interactions.[150]

In ILs, there are many factors affecting the stability of the NPs such as the influence of the IL-cation and the IL-anion, alkyl chain length, IL-viscosity, hydrogen-bonding capability, the relative ratio of polar and non-polar domains of ILs, and the functional groups. For example, the small IL anions exhibiting strong cation-anion coulomb attraction resulting in a conglomeration of unstable prime NPs which form large size NPs or varied morphologies. Another example, the high temperature can cause decreasing the IL viscosity resulting in increasing the diffusion velocities of the sputtered NPs.[28]

The ILs play an essential role in the stabilization of the NPs and keep it from aggregation. The ions or ion clusters are attracted on the NPs surface by electrostatic forces. The ion clusters with negative net charge are drawn to the surface of a positive charge NPs to form a negative ion layer, and then the ion clusters with positive net charge form the second layer by electrostatic attraction,[28] as shown in Figure 1.8. ILs form a double layer structure (cationic-anionic ions) around the synthesized nanoparticles to provide electrostatic repulsion which keeps the nanoparticles from aggregation through balancing with van der Waals

interactions. Ionic liquids can stabilize the nanoparticles through the H-bonding within the ionic liquid structure and between the Ionic liquid and the nanoparticles surface. It was also reported that the alkyl side chains of ionic liquids play an essential role through stretching away from the surface of the nanoparticles and prevent the aggregation.[28, 151-153]
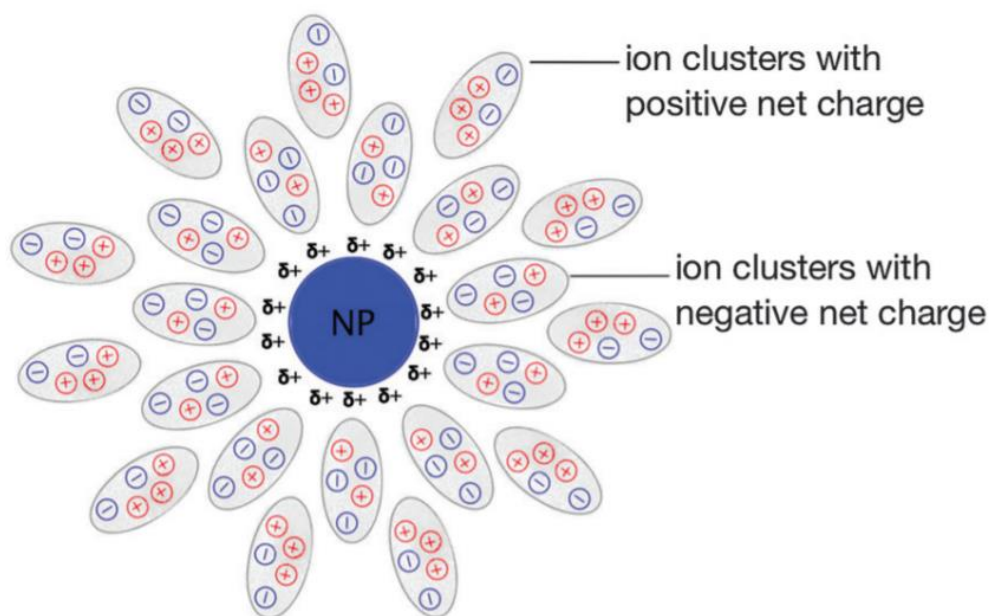
Figure 1.8. The ion clusters form double layer offers electrostatic interaction which keeps nanoparticles from aggregation.[28]

1.8.1. Metal Chalcogenides (MCs)

Metal chalcogenide (MC) semiconductor nanostructures consider as the most important class of nanomaterials.[154] MCs are a family of semiconductors. There are many kinds of MCs can be formed due to the non-metallic properties of the chalcogens such as binary $CuSe$, $CaTe$, Na_2S; ternary $CuInS$, $CsBi_4Te_6$, $Cd_{0.6}Zn_{0.4}Se$; quaternary Cu_2ZnSnS_4. Transition metal chalcogenides (TMCs) are an exciting class of MCs displaying interesting electronics and optical properties depend on the transition metal and the chalcogenide. These materials have different structures and compositions due to the unfilled d-orbital of the transition metal. However, the synthesis of MCs by using ILs still needs so much effort in comparison to synthesis of metal oxides.[155-156]

In 2004, Jiang and Zhu,[157] reported the synthesis of ZnS and CdS nanoparticles by using ILs. And in 2005, They synthesized single-crystalline Bi_2S_3 and Sb_2S_3 nanorods by the microwave-assisted IL method.[158]

In 2007, Rao et al.,[159] reported the synthesis of nanocrystals and nanorods of different semiconducting metal chalcogenides such as CdS, $CdSe$, PbS, $ZnSe$, and ZnS. They synthesized three different particle size of CdS by changing the anion of the IL. In 2009, Wang et al.,[160] synthesized 3D (three-dimensional) flowerlike MoS_2 with IL assisted hydrothermal route highlighting the crucial role of IL on the morphology of MoS_2, as shown in Figure 1.9.
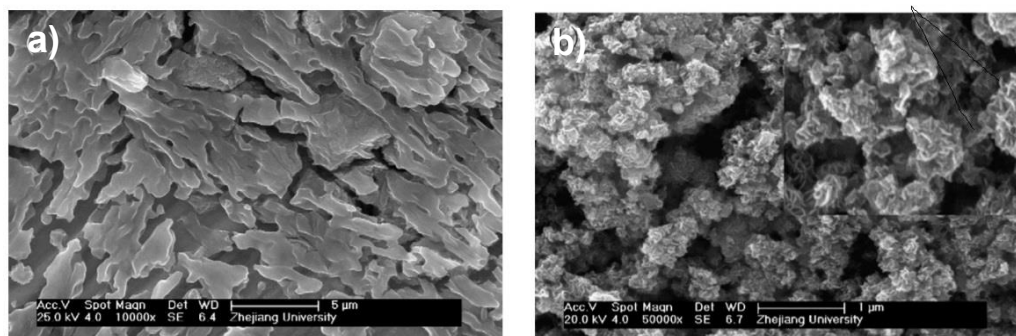
Figure 1.9. SEM images of prepared MoS_2 samples a) without adding IL and b) with adding IL assisted hydrothermal route.[160]

In fact, a lot of MCs were synthesized by using ILs such as Bi_2S_3 nanostructures (Figure 1.10),[161] ZnS,[159, 162] hierarchical copper sulfide (CuS) nanoparticles,[163] and MoS_2 microspheres[2].

As discussed before, there are many factors affecting on the morphology, the particle size, template, and the stability of IL-based NP dispersion e.g., the intermolecular interactions between ILs and NPs (van der Waals, electrostatic repulsion, steric interaction, and hydrogen bonding), and the exogenous variables (the interfacial structure and the physicochemical properties of ILs and NPs, temperature, pressure, and water concentration).[28]
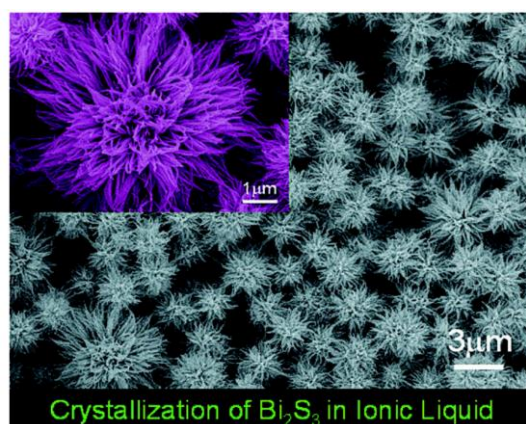
Figure 1.10. SEM images of prepared Bi_2S_3 nanoflowers at low temperature and ambient atmosphere using IL solution as the solvent and template.[161]

1.8.2. Copper Sulfide (CuS)

Copper sulfide (CuS), one of the most crucial semiconductor transition metal chalcogenides,[164] has been extensively studied for its application potential in solar cells,[165] lithium-ion batteries,[166] photocatalysis,[167] optical limiters,[168] biological markers,[169] and biosensors.[170] This is attributed to its unique electrical, mechanical, optical, physical, and chemical properties.[171-172]

Figure 1.11[173-174] shows the phase diagram of the Copper-sulfur system. Copper sulfides compounds, $Cu_{2-x}S$ ($0 \leq x \geq 1$), exist in a wide variety of compositions ranging from "copper (metal) rich phase" at chalcocite (Cu_2S)[175] to "sulfide (chalcogen) rich phase" at CuS_2, covellite (CuS), anilite ($Cu_{1.75}S$)[176], digenite ($Cu_{1.8}S$)[177], and djurleite ($Cu_{1.96}S$)[178]. Each of these compounds, except CuS, exists in several phases depending on temperature and some of them are stable at room temperature. The structure of $Cu_{2-x}S$ consists of a close-packed lattice of S atoms with mobile Cu atoms occupying various types of interstitial sites with a statistical distribution depending on temperature. By pure definition, Cu_xS compounds can be considered as Cu liquid inside the S structure lattice resulting in high ionic conductivity and low thermal conductivity.[179-180] $Cu_{2-x}S$ possess Cu vacancies in the lattice leading to a p-type semiconducting nature.[181]
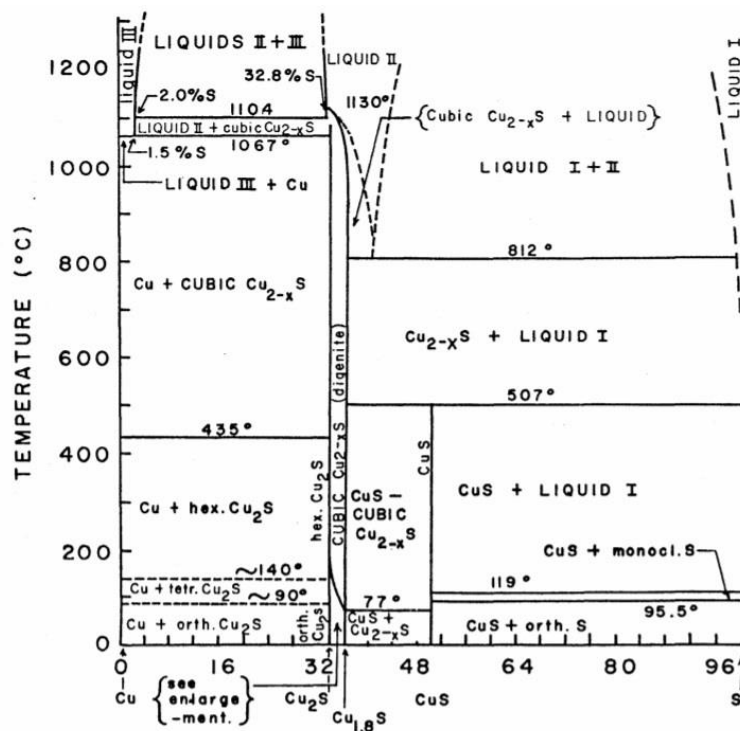
Figure 1.11. The Cu-S phase diagram.[182]

17

$Cu_{2-x}S$ can be divided into monoclinic (low-chalcocite), cubic close packing (anilite, digenite, and cubic-chalcocite), hexagonal close packing (djurleite and high-chalcocite), and an integration of hexagonal close packing and covalent bonding of sulfur atoms (covellite), as shown in Figure 1.12.

(a) Low-chalcocite Cu_2S (b) High-chalcocite Cu_2S (c) Cubic-chalcocite Cu_2S

(d) Djurleite $Cu_{1.94}S$ (e) Digenite $Cu_{1.8}S$ (f) Anilite $Cu_{1.75}S$ (g) Covellite hexagonal CuS
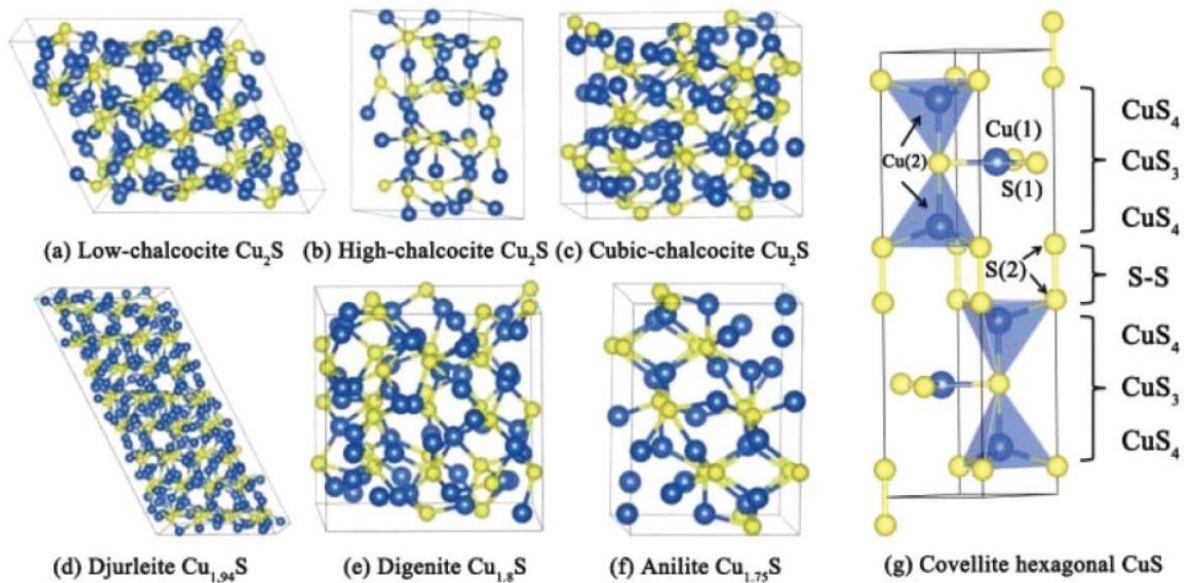
Figure 1.12. Crystal structures of $Cu_{2-x}S$. Blue and yellow spheres are copper and sulfide atoms, respectively.[181, 183-184]

Covellite (CuS) is a p-type semiconductor with a direct band gap 1.2 – 2.0 eV which has been applied in many applications, including optical materials, organic solar cell, gas sensors, and lithium-ion batteries.[169, 185-187] Copper Sulfide – Covellite (CuS) has a simple formula but a complex structure consisting of alternating layers of planar CuS_3 triangles and CuS_4 tetrahedrons with S–S bonds [Figure 1.12(g)].[184] No other metal ions with sulfur or selenium are known to crystallize in the same or resemble the crystal structure of covellite. The S ions in the covellite structure have an average oxidation state -1, due to the presence of the S–S covalent bonds. The S–S covalent bonds are essential for the nanoscale transformations in the presence of divalent metal cations.[181, 188] The diversified $Cu_{2-x}S$ micro-/nano-structures has been synthesized by different methods, e.g., hydrothermal method, solvothermal method, hot-injection, electrodeposition, thermolysis, and microwave irradiation.[189] The different crystal structures, morphologies, and compositions of the $Cu_{2-x}S$ micro-/nanostructures have been demonstrated to generate unique optical, electrical, and thermoelectric properties making them extremely suitable in different applications[189] such as photocatalysis,[190] biomedical,[191] solar cells,[192] and energy storage devices.[193]

In Chapter 6, the as-prepared CuS flower-like microstructures exhibited outstanding performance as non-enzymatic H_2O_2 sensors. In Chapter 7, the CuS nanoplates were successfully incorporated into organic photovoltaic (OPV) cells as hole conduction materials.[184]

1.9. Applications

1.9.1. Electrochemical biosensors[194-199]

Sensors are consisting of an active sensing material with a signal transducer, which can be classified, depends on the output signals, into electrical, thermal or optical. The electrodes can sense the materials which are present within the host without doing any damage to the host system.

Electrochemical phenomena are measured using a cell consists of three electrodes - working electrode (WE), a counter electrode (CE), and a reference electrode (RE) as shown in Figure.1.13a. The working electrode (WE) is considered as the most important electrode, which the redox reactions occur on its surface. The counter electrode (CE), usually platinum or carbon, is controlled by the potentiostat, and it is used to close the current circuit by applying a voltage difference respectively to the WE. The reference electrode (RE) is used to provide stable and well-known electrode potential. The transfer of electrons across the solution/solid interface depends on the electrode size, material, geometry, and the surface structure.

An electric double layer of ions is formed at the surface when the ions in the solution comes in contact with the electrode, which has excess charge on its surface. The closest layer is called the inner layer, which is balanced with an equal number of oppositely charged of ions in the solution. The second layer, which composed of oppositely charged ions, is called the diffusion layer. An electric potential energy exists as a result from the amount of the charges and the distance between them. The electric potential, E, of an electrochemical reaction of the chemical species undergoing the redox reactions, which is measured between the WE and RE, vary according to the Nernst equation:

$$E = E^0 + RT/zF \ln C_o/C_R$$

- E^0 is the standard potential of the reaction
- R is the universal gas constant
- T is the temperature in kelvins
- F is the Faraday constant
- z is the number of electrons transferred involved in the reaction
- C_o/C_R is the concentration of chemical species being oxidized or reduced

There are a lot of electrochemistry techniques, which can be classified into three classes - voltammetric, impedimetric, and amperometric. Voltammetric sensors measure the charge/potential at a sensor surface when no current flows. Impedimetric sensors measure the impedance change (the change of resistance or the change of capacitance) at the sensor surface. While amperometric sensors measure the current, which generated at the sensor surface, is recorded as a function of time.

Cyclic voltammetry (CV) is a powerful and popular technique, used to study the reduction and oxidation process of molecular species, and the electron transfer-initiated chemical reactions. The current is measured between the working electrode (WE) and the counter electrode (CE), while the potential is measured between the working electrode (WE) and the reference electrode (RE). Figure.1.13b. shows the results of CV, which the current is plotted versus the applied voltage.
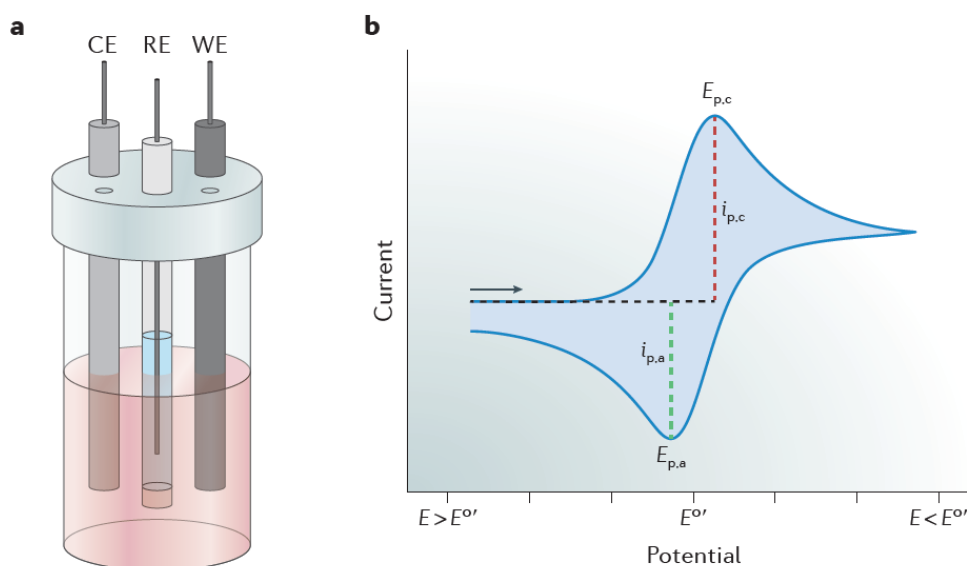
Figure.1.13. illustration of a) three-electrode electrochemistry cell and b) an ideal example of a cyclic voltammogram. Adapted from Lee, Katherine J., et al., *Nature Reviews Chemistry* 1 (2017).[196]

The principle parameter is the scan rate v. The scan rate v is the change of the potential per time. The shape of the voltammogram depends on the electrode dimensions and the diffusion length of the analyte (dependent on the scan rate). When the analyte is oxidized, the electric potential E become positive, and when the analyte is reduced, the E become negative, associated with a peak current i_p.

Randles–Sevcik equation describes the relationship between v and i_p:

$$i_p = (2.69 \cdot 10^5)\, ACD^{1/2}n^{3/2}v^{1/2}$$

Where the analyte concentration can be determined by the magnitude of the i_p, A is the electrode area, C is the concentration of the analyte, D is the diffusion of the analyte, and n is the number of the electrons, which involved in the reaction.

1.9.2. Organic Photovoltaic solar Cells[200-202]

Solar cells are semiconductor devices which absorb the sunlight photons and convert the incident light to electrical energy. The carriers are then generated from excition dissociation and they are collected by the electrodes, generate the current, and enter the external circuit. The typical solar cell consists of a metallic back contact, a semiconductor pn-junction, and a transparent top contact. All photovoltaic devices work based on a pn-junction. Some of the electrons from the n-type semiconductor, which have reached the conduction band, can diffuse across the junction, leaving behind static positive charges on atoms in the solid, and combine with the holes to form negative ions. Near the pn-junction is called the depletion zone where there are no charges carriers anymore. The separated static positive and negative charges mean there is an electric field across the depletion zone, as shown in Figure 1.14 .
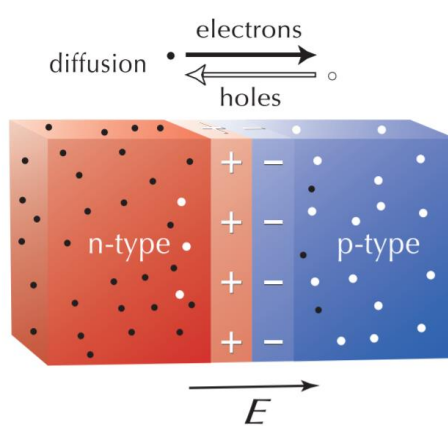
Figure.1.14. Diffusion of electrons and holes establishes an electric field.[203]

When the sunlight energy is absorbed by the semiconductor resulted in dislodging an electron, which creating an extra mobile electron and an extra mobile hole. The electric field

makes the electron flow to the n-type semiconductor and the hole flow to the p-type semiconductor. The resulting separation of positive and negative charges across the junction is called a potential difference or voltage. The net current is zero since the drift current and the diffusion charges are equal, and the Fermi level is constant.

When an external bias is applied (forward bias or reverse bias), the width of the depletion zone (the junction potential barrier) can be altered. The width of the depletion zone becomes wider in the case of reverse bias and narrower in the case of the forward bias. In the case of equilibrium, when no external force is applied like voltage or heat or incident light, the closest electrons in the n-type semiconductor from the boundary tend to diffuse into the p-type semiconductor resulting the creation of minority negative charged ions in the p-type semiconductor and minority of positive charge ions in the n-type semiconductor.

In the case of reverse bias, the external force is applied and the positive terminal connected to the n-type semiconductor and the negative terminal connected to the p-type semiconductor. The depletion zone becomes wider resulting increasing the resistance of the material to flow the current as the diffused electrons and holes pulled further away from the boundary, as shown in Figure 1.15. In this case, the electrons must jump to the LUMO of the donor component to move from the anode to the cathode.
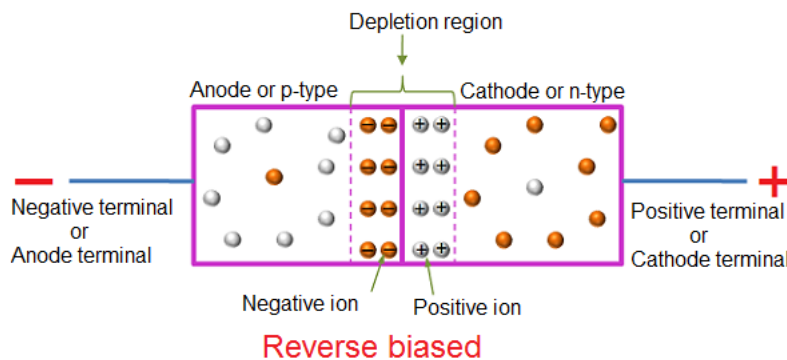
Figure.1.15. Reverse-biased pn junction.[204]

While in the case of forward bias, the external force is applied and the positive terminal connected to the p-type semiconductor and the negative terminal connected to the n-type semiconductor. The depletion zone becomes narrower resulting in the movements of the electrons from the cathode to the anode and flowing the current, as shown in Figure 1.16.
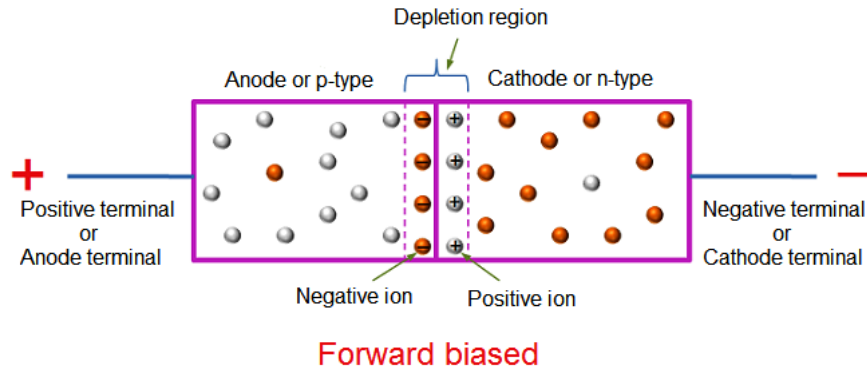
Figure.1.16. Forward-biased pn junction.[205]

Determination of the performance of solar cell depends on some parameters such as open-circuit voltage (V_{oc}), short-circuit current (I_{sc}), fill factor (FF) and power conversion efficiency (PCE). The current-voltage characteristics of a solar cell under dark and illumination conditions as shown in Figure.1.17. I_{sc} is the current produced by the solar cell under illumination without any external potential. V_{oc} is the potential difference between the terminals of the solar cell under illumination when there is no current flowing through the terminals. FF is the maximum power (P_m) generated by the product of open-circuit voltage and short-circuit current ($P_m = I_m * V_m$). PCE is the ratio of the maximum power generated by the solar cell to the incident radiant energy.[206]
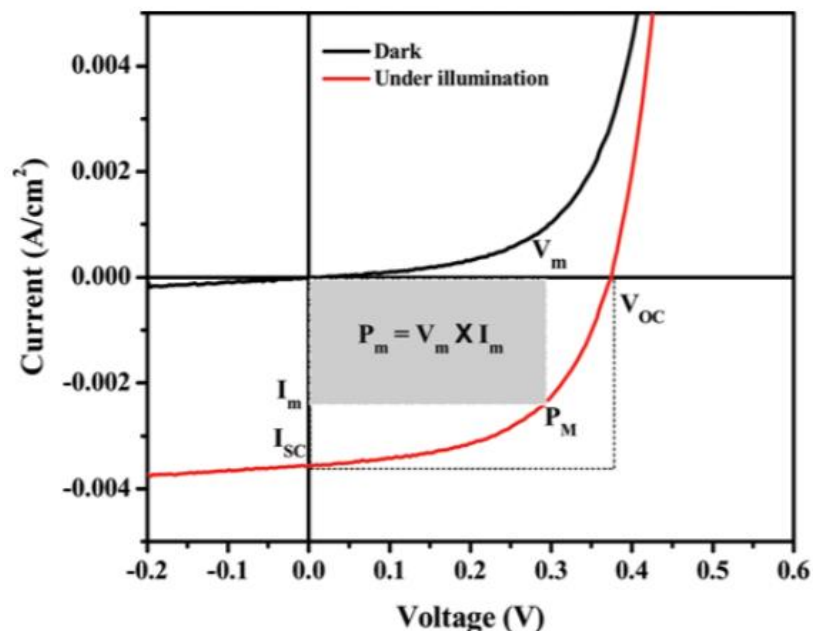
Figure.1.17. J-V characteristics of solar cell. Adapted from Abdulrazzaq, Omar A., et al. Particulate science and technology 31.5 (2013).[206]

23

Chapter 2. Methods

2.1. **General Background**

Crystals are highly ordered structures which are composed of a regular arrangement of units (atoms, molecules, or ions) that is repeated infinitely in the three dimensions. Crystals display a high degree of symmetry. The crystallographic unit cell is the smallest unit by which the periodic order in the crystal is repeated to produce the bulk crystal. It means that crystals are defined by their unit cells. The crystallographic unit cell is characteristic by three vectors a, b, and c, which lie along the three directions x, y, and z, respectively, and by the angles between these vectors α, β, and γ, as shown in Figure 2.1. Crystals are divided into 7 crystal systems (Figure 2.1) that contain 14 Bravais lattices (Figure 2.2), 32 Point groups, and 230 space groups.[207]
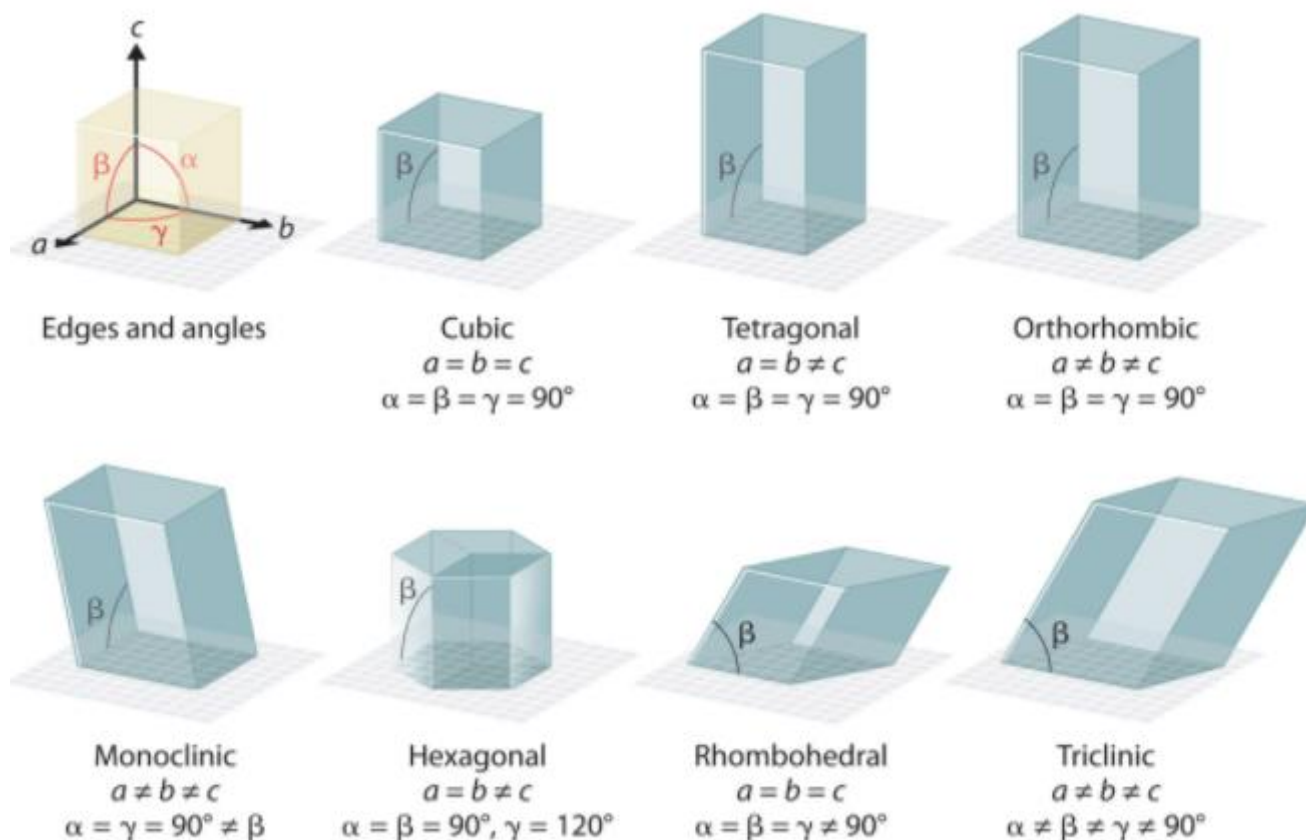
Figure 2.1. The reference axes used to characterize the seven crystal systems.[208]
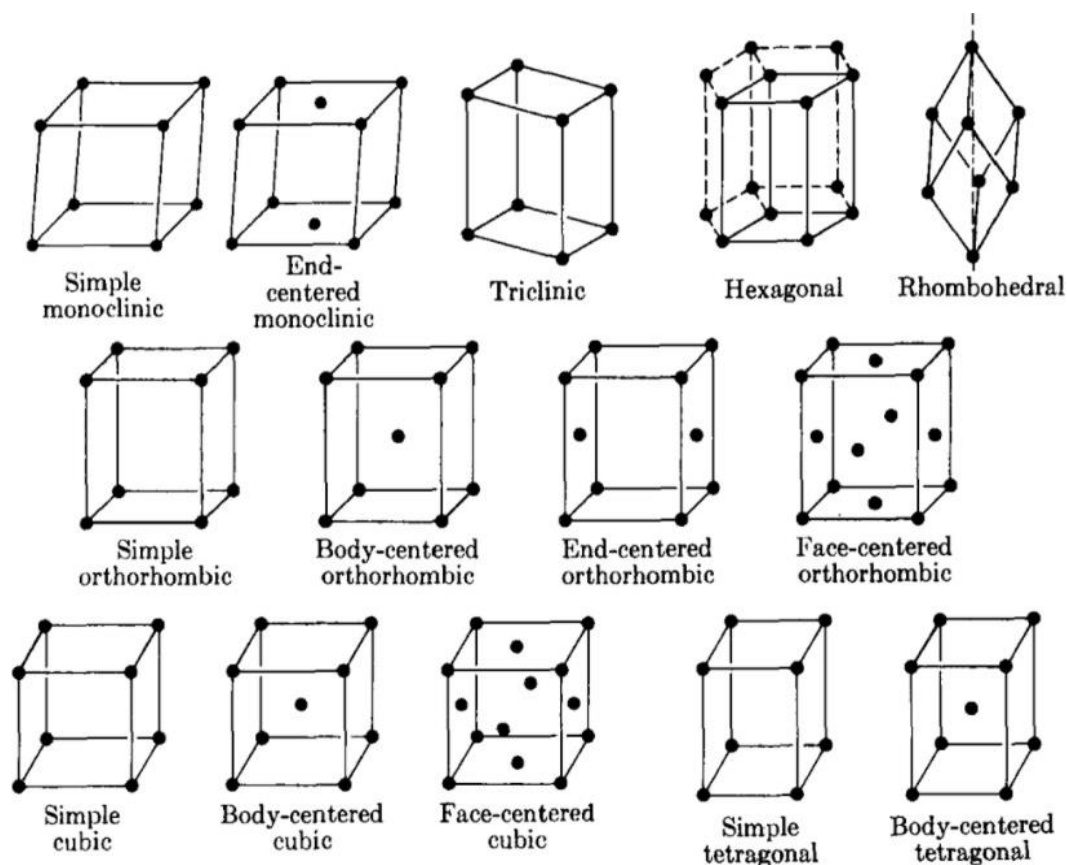
Figure 2.2. The unit cells of the 14 Bravais lattices.[209]

2.2. **Powder X-ray diffraction (XRD)**[133, 210-214]

Powder X-ray diffraction (XRD) is a powerful technique to determine the crystal structure (phase identification of a crystalline material), provide information on unit cell dimensions and estimate sample purity. It is worth to mention that high-temperature X-ray diffraction is used to identify the type of mesophase and investigate the molecular organization within the mesophase.

X-rays are high energy electromagnetic radiation $(0.1 - 100 \text{ keV})$ with short wavelength between $0.01 - 1 \text{ nm}$. They can pass through many materials that absorb visible light including body tissues. These rays are suitable for a structural determination as they are photons having wavelength λ of the same order of the interatomic distance in the condensed matter.

In 1901, Wilhelm Röntgen was awarded the Nobel prize in Physics for his discovery of X-rays in **1895**. X-rays are generated in a high vacuum tube by accelerating electrons from a tungsten filament towards a target (anode metal such as Cu or Mo) by applying a high voltage. **In 1912**, Max von Laue suggested that a crystal lattice composed of atoms might have a spacing small enough to produce diffraction pattern using X-rays.

Foils or crystal monochrometers are used for filtering in order to obtain an almost monochromatic X-rays needed for diffraction. After the collimated X-rays are diffracted at the sample and collected at the detector, the intensity of the reflected X-rays is recorded. Crystalline materials obtain sharp peak of the reflections. On the other hand, a high and broad background indicates the presence of amorphous constituents in the sample. The obtained reflections are used for the phase identification of a crystalline material and it can provide information on the crystallite sizes or material defects.

Crystals consist of a three-dimensional arrangement of atoms, which is repeated in all three spatial directions. Atoms are arranged in a crystal lattice as shown in Figure 2.3. The separation distance is on the order of the wavelength of the X-rays. X-rays can interact with the electron clouds of the periodically arranged atoms by elastic scattering, leading to constructive and destructive scattering. Two parallel incident X-ray beams must be in phase (when they travel a total distance that differs by a whole number multiple of their wavelength), and the angle of the incidence must be equal to the angle of the reflection to produce constructive interface and provide a signal. The constructive scattering is described by the Bragg's law:

$$2d_{hkl} \sin \theta = n \lambda$$

Where hkl are the Miller indices, n is the order of scattering, λ is the wavelength, d is the spacing between atomic or diffracting layers, and θ is the incident angle.
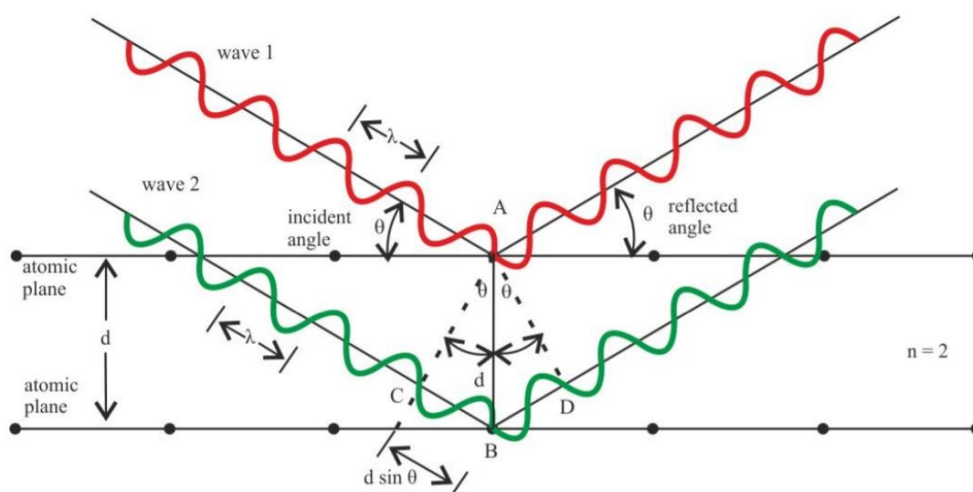
Figure 2.3. Schematic illustration of the Bragg's law which can be derived from the triangle ABC.[215]

2.3. **Single crystal X-ray diffraction**[212, 216-217]

Single crystal X-ray diffraction is used to get the information about the unit cell dimensions, bond angles, bond lengths and location of the atoms. The crystal structure is obtained after collection and refinement of the X-ray data. Growing a high-quality single crystal is very important to get a good quality diffraction data and to get precise of the atomic geometry parameters. Crystals should be transparent - generally sparkly and large enough without any cracks. They should have excellent regular shape, faces, and edges. Large crystals can be cut. Figure 2.4. shows some of the single crystals that obtained in this study.
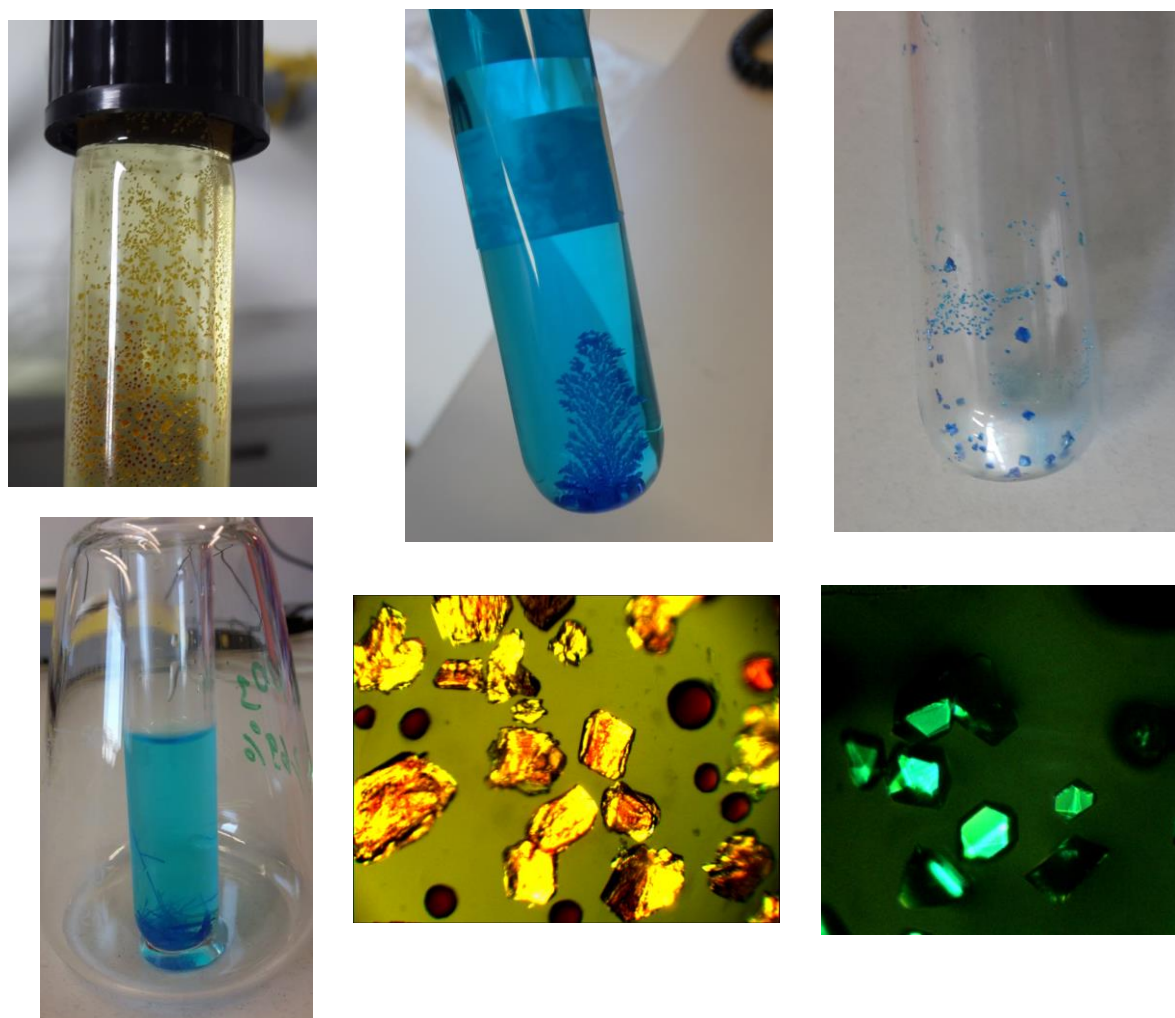
Figure 2.4. Single crystals of ILs that obtained in this study.

First, All information should be collected about the crystals if they are sensitive to air or they are unstable at room-temperature. Then a suitable crystal is mounted on a thin glass fiber for data collection on an Imaging Plate. Crystals will rotate through various angles to produce diffraction patterns. This process takes several hours depending on the sample and

the diffractometer. The diffraction patterns are converted to the 3D structure by Fourier transforms combined with the known chemical information of the sample. Crystallographic information file (CIF) file of the structure is created when the Lorentz-polarization corrections are carried out, the phase problem is solved, and the structure is refined.

2.4. Polarized optical microscopy (POM)[218-219]

Polarized optical microscopy (POM) is one of the most influential techniques that used to detect the existence of LC phases and to determine the phase transition temperatures. It is used for optical anisotropic materials, which almost all types of LCs – Cubic LCs are known as a viscous isotropic phase.[220] These materials, considered as birefringent materials (double-refraction materials), have optical properties and they act as beam splitters. Their refractive index n depends on the propagation of the light direction. It means that anisotropic materials such as LCs and crystalline solids are dependent on direction, while isotropic materials are independent of direction.

POM composed of two polarizers (polarizer and analyzer), which they are oriented at right angle to each other as shown in Figure 2.5. This concept is commonly termed as crossed polarized. When the incident beam passes through the first polarizer, which is oriented vertically to the incident beam, only the waves with vertical direction can pass through it. Then, when the light passes through the birefringent material, it will be split into two waves with different delays and become out of phase. At the end, these waves are recombined by constructive and destructive interference when they pass through the analyzer and give a bright domain on the sample.
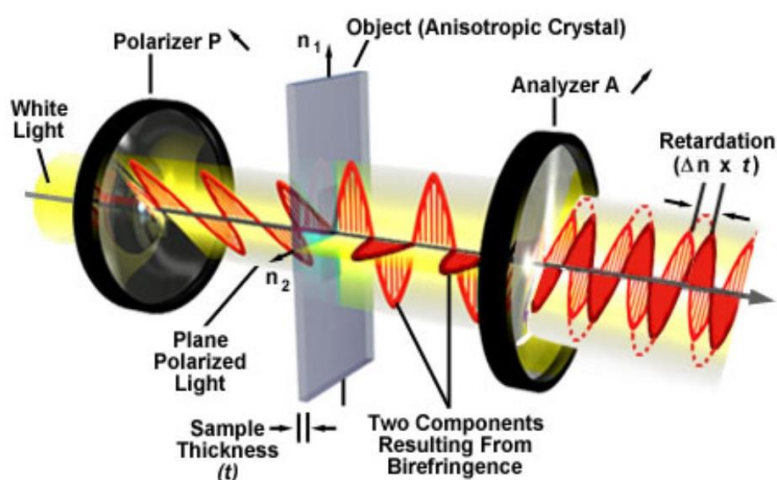
Figure 2.4. Birefringent material between crossed polarizers.[221]

2.5. **Differential scanning calorimetry (DSC)[219]**

Differential scanning calorimetry (DSC) is used to determine the heat capacity, the enthalpy of crystallization, the enthalpy of melting (fusion), and the phase transition. And it is a useful tool to determine the LC phases. A loss of order will take place during the phase transition from crystalline phase (3D) to anisotropic-LC phase (2D or 1D) and to isotropic-liquid phase (0D), corresponding to an entropy change. The entropy of a system undergoing a phase transition increases if the phase transition is towards higher internal energy (e.g., melting) and decreases if the phase transition is towards lower internal energy (e.g., freezing). There are two techniques of DSC: power-compensated DSC, which the power supply is constant, and heat-flux DSC, which the heat flux is constant.

The experiments were done by the heat-flux DSC, which the empty reference crucible and the sample crucible are placed in one single furnace and heated at the same rate. The temperature is measured at the heat-flux plate. An exothermic effect takes place in the sample when the temperature of the sample will be higher than the temperature of the reference. On the other hand, the endothermic impact takes place in the sample when the temperature of the sample will be lower than the reference. The enthalpy change (the energy of the transition) can be calculated from the known sample mass and the temperature lag. For exothermic transitions, which the heat is released by the sample, the heat flow has a negative value. In the case of endothermic transitions, which the heat is absorbed by the sample, the heat flow has a positive value.

The enthalpy changes between the two liquid-crystalline phases (if detectable) or between the liquid crystal phase and the isotropic phase are quite small ($0.5 - 10$ kJ·mol^{-1}). While the enthalpy changes are quite significant ($10 - 80$ kJ·mol^{-1}) between the crystalline phase and the isotropic phase, corresponding to the large variation in the molecular organization of the sample. Examples of DSC traces is given in Chapter 4 (Figure 4.9).

2.6. **Electron microscopy[222-224]**

An electron microscope is an instrument that uses electrons instead of light (in case of POM) or X-rays (in case of XRD) as radiation for the imaging of objects. Electrons interact more strongly than X-rays with the matter. That is why electron microscopy (EM) can be applied to smaller crystals. One more advantage, the electrons can be bent by the electromagnetic lens, so the diffracted electrons can be focused to produce atomic resolution image.

The development of the electron microscope was based on theoretical work done by Louis de Broglie, who found that wavelength is inversely proportional to momentum. In 1926, Hans Busch discovered that magnetic fields could act as lenses by causing electron beams to converge to a focus. A few years later, Max Knoll and Ernst Ruska made the first modern prototype of an electron microscope.

There are several types of electron microscopes. The idea of electron microscopy is that the sample is bombarded with a stream of electrons. Electrons are emitted by thermionic emission source (tungsten hairpin cathodes or lanthanum hexaboride (LaB_6) crystals) or by field emission gun from tungsten needles. The wavelength of electrons can be calculated according to the de Broglie wavelength equation

$$\lambda = h / p = h / m_e v_e$$

where λ is the wavelength, h is the Plank constant ($h = 6.626 \cdot 10^{-34}$ J·s), p is the momentum of the electron, m_e is the electron mass, and v_e is the velocity of the electron.

The electrons which are scattered through large angles, including back-scattered electrons (BSE) and secondary electrons (SE), are of the most significant interest for scanning electron microscopy (SEM) to give surface-sensitive information, such as topography. On ther hand, the electrons which are transmitted are of greatest interest for transmission electron microscopy (TEM). Scanning electron microscopy (SEM) and transmission electron microscopy (TEM) are the standard methods for imaging and dimensional measurements of micro- and nanostructures due to their high resolution and high imaging speed.

2.6.1. Scanning electron microscopy (SEM)[223]

SEM is used to provide information on the surface and topography of the samples. SEM consists of two major parts: the microscope column and the electronics console. The microscope column includes of the electron gun (cathode, wehnelt cylinder, and an anode), one or two condenser lenses, the objective lens, two pairs of beam deflection coils, and some aperatures. At the lower end of the microscope column, there is a specimen chamber. In the specimen chamber, there are specimen stage and the detectors. The microscope column and the specimen chamber are evacuated to prevent the interaction of the gas molecules and the beam electrons.

On the other hand, the electronics console consists of the electric power supplier for the acceleration voltage, the condenser and the objective lenses, the scan generator, and electronic amplifier for the different signals.

The beam electrons are emitted from the electron gun (which typically has an energy ranging from 0.2 - 40 keV) and accelerated between the cathode and the anode to form a smallest beam cross section. But the crossover near the anode is too large (diameter about 10-50 μm) to create a sharp image. One or two condenser lenses and objective lenses are needed to demagnify the crossover and focus on the specimen surface.

The two pairs of beam deflection coils scan the electron probe line (direct and position the focused beam onto the sample surface) and are located in front of the objective lenses. The beam electron induces the emission of the secondary electrons from the sample, and these electrons are detected by the secondary electron detector.

The interaction between the electron beam and the specimen can be divided into elastic interactions (negligible energy loss during the collision) and inelastic interactions. When the incident electron is deflected by the specimen atomic nucleus or by the outer shell electrons, the elastic scattering is obtained. The backscattering electrons (BSE) is achieved when the incident electrons are elastically scattered by an angle of more than 90°. These Backscattered electrons are used to detect the contrast between areas with different chemical compositions. While the inelastic scattering is obtained during the interaction between the incident electron and the electrons and atoms of the sample. That leads to the excitation of the electrons in the sample and generates the secondary electrons (SE). These reflected secondary electrons are used to record the images. The advantage of the SEM is its high spatial resolution and high depth of field images.

2.6.2. Transmission electron microscopy (TEM)[225]

TEM is well suited to observe nanoscale materials such as single layers, nanotubes, nanowires, quantum dots, and nanoparticles. These materials can be seen by TEM without modification as these materials are thin enough for direct observation. In contrast to SEM, TEM samples must be thin enough, that is comparable to the mean free path of the electrons, to be electron-transparent.

TEM is a powerful technique which is used for structural characterization of the sample (morphological, information-size, and shape). It is possible to obtain crystallographic information (e.g., lattice spacing (d-spacing)) by using electron diffraction (ED).

The electron beam is produced by the electron gun (20 - 1000 keV). Electrons transfer into the vacuum in the column of a microscope which accelerates between the cathode and the anode. TEM consists of three stages of lenses: the condenser lenses, the objective lenses, and the projector lenses. The condenser lenses are responsible for primary beam formation, the objective lenses which focus the electron beam to the desired size and location, and the projector lenses are used to expand the beam. The electrons will move as the interaction of electrons with a magnetic field passing through the specimen to form a highly magnified image. To ensure that the electrons will not be scattered by air molecules or particles, the high vacuum will be applied. TEM can provide topographical, morphological, compositional and crystalline information.

Chapter 3. Publications

This doctoral thesis is based on the following scientific publications

3.1. Publications

1. **"Alkylpyridinium tetrahalidometallate ionic liquids and ionic liquid crystals: insights into the origin of their phase behavior."**

   Ahed Abouserie, Kerstin Zehbe, Philipp Metzner, Alexandra Kelling, Christina Günter, Uwe Schiele, Peter Strauch, Thomas Körzdörfer, and Andreas Taubert

   European Journal of Inorganic Chemistry **2017**, *5640 (2017)*
   DOI: 10.1002/ejic.201700826

   The synthesis, characterization (except EPR), as well as analysis, writing, and revision of the manuscript, were done by me with the consultation of Prof. Dr. Andreas Taubert. The differential scanning calorimetry (DSC) and polarized optical microscopy (POM) were done by me.

2. **"Crystal structure of *N*-butylpyridinium bis(μ2-dichlorido)-tetrachlorido-di-copper(II), $C_{18}H_{28}N_2Cu_2Cl_6$."**

   Ahed Abouserie, Uwe Schilde, and Andreas Taubert

   *Zeitschrift für Kristallographie - New Crystal Structures (**submitted**)*

   The synthesis, characterization, writing, and revision of the manuscript were done by me with the consultation of Prof. Dr. Andreas Taubert and Prof. Dr. Uwe Schilde.

3. **"Hierarchically structured copper sulfide microflowers with excellent amperometric hydrogen peroxide detection performance."**

   Ahed Abouserie, Gumaa A. El-Nagar, Benjamin Heyne, Radwan M. Sarhan, Yohan Kim, Christopher Pries, Enrico Ribacki, Christina Günter, Christina Roth, Armin Wedel, and Andreas Taubert

   Journal of Materials Chemistry A (**submitted**)

The synthesis and characterization of CuS were done by me. I prepared the figures and wrote the manuscript (except the electrocatalytic performance of the as-prepared CuS microstructure in nonenzymatic H_2O_2 detection) with the consultation of Prof. Dr. Andreas Taubert. The scanning electron microscopy (SEM) was done by me.

4. **"CuS nanoplates from ionic liquid precursors – application in organic photovoltaic cells."**

Yohan Kim, Benjamin Heyne, **Ahed Abouserie**, Christopher Pries, Christian Ippen, Christina Günter, Andreas Taubert and Armin Wedel

The Journal of Chemical Physics **148**, 193818 (2018)
DOI: 10.1063/1.4991622

The synthesis and characterization of ILP and CNPs using XRD, FTIR, and UV measurements were done by me. I took an active role in the preparation and revision of the manuscript.

3.2. **Unpublished material**

- **"The ionic liquid $[C_4Py]_2[Cu_{0.39}Co_{0.61}Cl_4]$ is a single source ionic liquid precursor (ILP) for carrolite $CuCo_2S_4$ nanomaterials and its exploitation for water splitting."**

Ahed Abouserie, Gumaa A. El-Nagar, Benjamin Heyne, Alexandra Kelling, Christina Günter, Uwe Schiele, Armin Wedel, Christina Roth and Andreas Taubert

In preparation (**planned submission in May 2018**)

The synthesis and characterization of new ILP $[C_4Py]_2[Cu_{0.39}Co_{0.61}Cl_4]$ and $CuCo_2S_4$ were done by me. I prepared the figures and wrote the manuscript with the consultation of Prof. Dr. Andreas Taubert. The differential scanning calorimetry (DSC) was done by me. The $CuCo_2S_4$ nanoparticles will be applied to the electrocatalytic driven-water splitting, a process established in the Roth group.

Chapter 4

Alkylpyridinium tetrahalidometallate ionic liquids and ionic liquid crystals: insights into the origin of their phase behavior

4.1. Abstract

Six *N*-alkylpyridinium salts $[C_nP_y]_2[MCl_4]$ (n = 4 or 12 and M = Co, Cu, Zn) were synthesized, and their structure and thermal properties were studied. The $[C_4Py]_2[MCl_4]$ compounds are monoclinic and crystallize in the space group $P2_1/n$. The crystals of the longer chain analogues $[C_{12}Py]_2[MCl_4]$ are triclinic and crystallize in the space group $P\bar{1}$. Above the melting temperature, all compounds are ionic liquids (ILs). The derivatives with the longer C_{12} chain exhibit liquid crystallinity and the shorter chain compounds only show a melting transition. Consistent with single-crystal analysis, electron paramagnetic resonance spectroscopy suggests that the $[CuCl_4]^{2-}$ ions in the Cu-based ILs have a distorted tetrahedral geometry.

4.2. Introduction

Ionic liquids (ILs) have attracted considerable interest over the last decades;[12, 14, 56, 226-231] this is largely due to their unusual properties, chemical variability, and their high (projected) application potential. ILs are salts with rather low melting points compared to traditional salts. Moreover, ILs often have a broad liquid range. Among others, this makes them interesting for applications covering larger temperature windows such as batteries or chemical reactions.[14, 43, 57, 232-239] ILs have therefore been explored for virtually any application, from chemical synthesis and electrochemistry to batteries, catalysts, fuel cells, and many more.[57-65] Ionic liquid crystals (ILCs) are an interesting IL sub-class; ILCs combine ionic moieties and strong intermolecular forces with supramolecular order. This combination enables the construction of stable ion conductive materials for a wide variety of applications.[240-244]

Another interesting and potentially very useful subclass of ILs, metal-containing ionic liquids (MILs),[242] has attracted less attention. This is somewhat surprising because the presence of a metal ion furnishes the IL with additional magnetic, optical, catalytic, or electrochemical properties that are not accessible otherwise.[12, 231, 245-259] AlCl₃-based ILs are arguably the first examples of MILs,[43, 260] but especially transition metal-based ILs have been studied in the last 20 years for their structure and for their optical, magnetic and catalytic properties.[261]

Of particular relevance to the current study is a set of reports by Neve and co-workers.[262-264] These authors described alkylpyridinium ILs based on the tetrachloridocuprate(II) moiety, $[CuCl_4]^{2-}$. Among others, they showed that all compounds with alkyl chains longer than twelve carbon atoms exhibit thermotropic liquid crystalline phases. The same compounds have also been studied as precursors for inorganic nanoparticles.[50, 139-141, 158, 265-267] These ILs and ILCs are thus interesting both for their physical properties and as precursors for nanomaterials – possibly for a very broad range of different nanomaterials with high application potential.

The current article describes several new ILs based on alkylpyridinium cations and $[CoCl_4]^{2-}$, $[ZnCl_4]^{2-}$, or $[CuCl_4]^{2-}$ anions and correlates their phase behavior with their crystal structure. The study expands the pool of transition metal-based pyridinium ILCs to Co and Zn-based derivatives, which have been unknown so far. Scheme. 4.1 shows the chemical structures of the ILs.

a) b)

$$\left[\text{pyridinium}-C_4H_9 \right]_2 \left[MCl_4 \right]^{2-} \qquad \left[\text{pyridinium}-C_{12}H_{25} \right]_2 \left[MCl_4 \right]^{2-}$$

M = (Cu, Co, or Zn)
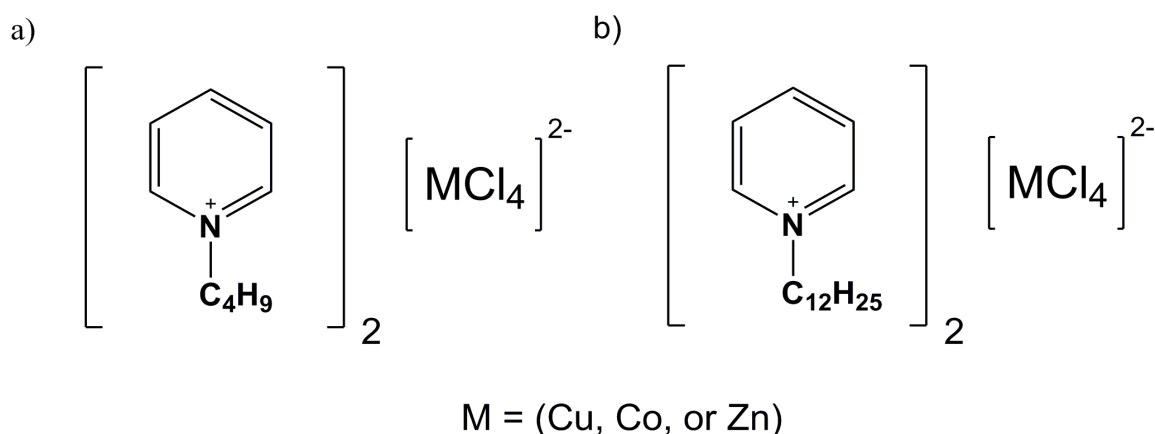
Scheme 4.1. Chemical structures of *N*-butylpyridinium ILs $[C_4Py]_2[MCl_4]$ (a), and *N*-dodecylpyridinium ILs $[C_{12}Py]_2[MCl_4]$ (b).

4.3. Experimental Section

Chemicals: *N*-butylpyridinium chloride (Iolitec, 99 %), *N*-dodecylpyridinium chloride (Aldrich, ≥ 98 %), $CuCl_2 \cdot 2H_2O$ (Fluka, ≥ 99 %), $ZnCl_2$ (Fluka, 98 %), $CoCl_2 \cdot 6H_2O$ (Ucb, 98 %), $[D_6]$dimethyl sulfoxide ($[D_6]$DMSO, 99.8 atom-% D, Armar Chemicals), and acetonitrile (Aldrich, 99.8 %) were used without further treatment.

General IL Synthesis: IL synthesis was done according to literature procedures.[263, 268]

[C4Py]2[CuCl4] (1): To a solution of *N*-butylpyridinium chloride (1.71 g, 10 mmol) in dry acetonitrile (6 mL) was added copper(II) chloride (0.86 g, 5 mmol), and the mixture was stirred to reflux for 3 h. The solvent was evaporated with a rotary evaporator at 60 °C under reduced pressure. The product was dried in vacuo. The other butylpyridinium-based ILs were synthesized accordingly. Yield: 2.37 g (ca. 98 %). $C_{18}H_{28}Cl_4CuN_2$ calculated (found): C, 45.25 % (45.12 %); H, 5.91 % (5.69 %); N, 5.86 % (5.86 %). ^{1}H NMR: (500 MHz, [D_6]DMSO): δ = 0.93 (t, J = 5.99 Hz, 3 H) 1.26–1.39 (b, 2 H) 1.94 (b, 2 H) 4.65 (b, 2 H) 8.19 (b, 2 H) 8.63 (b, 1 H) 9.16 (b, 2 H) ppm. ^{13}C NMR: (126 MHz, [D_6]DMSO): δ = 14.45, 19.88, 33.83, 61.70, 129.23, 145.63, 146.53 ppm.

[C4Py]2[CoCl4] (2): Yield 2.31 g (ca. 97 %). $C_{18}H_{28}Cl_4CoN_2$ calculated (found): C, 45.69 % (45.50 %); H, 5.96 % (6.07 %); N, 5.92 % (5.88 %). ^{1}H NMR: (500 MHz, [D_6]DMSO): δ = 0.92 (b, 3 H) 1.29 (b, 2 H) 1.90 (b, 2 H) 4.57 (b, 2 H) 8.11 (b, 2 H) 8.56 (b, 1 H) 9.09 (b, 2 H) ppm. ^{13}C NMR: (126 MHz, [D_6]DMSO): δ = 14.64, 20.10, 34.11, 62.19, 129.55, 145.90, 146.80 ppm.

[C4Py]2[ZnCl4] (3): Yield 2.25 g (ca. 94 %). $C_{18}H_{28}Cl_4ZnN_2$ calculated (found): C, 45.07 % (45.69 %); H, 5.88 % (5.73 %); N, 5.84 % (5.86 %). ^{1}H NMR: (500 MHz, [D_6]DMSO): δ = 0.89–0.94 (t, J = 7.25 Hz, 3 H), 1.25–1.34 (sxt, J = 7.30 Hz, 2 H), 1.87–1.94 (quin, J = 7.60 Hz, 2 H), 4.60–4.65 (t, J = 7.57 Hz, 2 H), 8.14–8.20 (t, J = 7.09 Hz, 2 H), 8.59–8.64 (t, J = 7.88 Hz, 1 H), 99.11–9.15 (d, J = 5.67 Hz, 2 H) ppm. ^{13}C NMR: (126 MHz, [D_6]DMSO): δ = 14.18, 19.62, 33.53, 61.41, 128.96, 145.65, 146.34 ppm.

[C12Py]2[CuCl4] (4): To a solution of *N*-dodecylpyridinium chloride (8.5 g, 30 mmol) in acetonitrile (10 mL) was added copper(II) chloride (2.58 g, 15 mmol), and the mixture was stirred to reflux for 3 h. The solvent was evaporated on a rotary evaporator at 60 °C under reduced pressure. The product was dried in vacuo. The other dodecylpyridinium ILs were made accordingly. Yield 10 g (ca. 94 %). $C_{34}H_{60}Cl_4CuN_2$ calculated (found): C, 58.15 % (57.67 %); H, 8.61 % (8.29 %); N, 3.99 % (3.91 %). ^{1}H NMR: (500 MHz, [D_6]DMSO): δ = 0.84 (b, 3 H), 1.11–1.47 (b, 18 H), 1.92 (b, 2 H), 4.60 (b, 2 H), 8.16 (b, 2 H), 8.47–8.74 (b, 1 H), 8.94–9.33 (b, 2 H) ppm. ^{13}C NMR: (126 MHz, [D_6]DMSO): δ = 14.84, 22.94, 26.35, 29.28, 29.55, 29.65, 29.77, 29.84, 31.69, 32.14, 61.83, 129.07, 145.58, 146.44 ppm.

[C₁₂Py]₂[CoCl₄] **(5):** Yield 9.79 g (ca. 93 %). $C_{34}H_{60}Cl_4CoN_2$ calculated (found): C, 58.54 % (57.7 %); H, 8.67 % (8.71 %); N, 4.02 % (3.96 %). ^{1}H NMR: (500 MHz, [D₆]DMSO): δ = 0.86 (t, J = 6.62 Hz, 3 H) 1.25 (b, 18 H) 1.91 (b, 2 H) 4.56 (b, 2 H) 8.11 (b, 2 H) 8.37–8.74 (b, 1 H) 9.08 (b, 2 H) ppm. ^{13}C NMR: (126 MHz, [D₆]DMSO): δ = 14.96, 23.04, 26.65, 29.48, 29.64, 29.89, 29.94, 29.95, 32.08, 32.23, 62.27, 129.39, 145.79, 146.67 ppm.

[C₁₂Py]₂[ZnCl₄] **(6):** Yield 9.89 g (ca. 93 %). $C_{34}H_{60}Cl_4ZnN_2$ calculated (found): C, 58 % (57.65 %); H, 8.59 % (8.29 %); N, 3.98 % (3.97 %). ^{1}H NMR: (500 MHz, [D₆]DMSO): δ = 0.86 (t, J = 6.94 Hz, 3 H) 1.18–1.35 (m, 18 H) 1.92 (quin, J = 7.17 Hz, 2 H) 4.62 (t, J = 6.94 Hz, 2 H) 8.17 (t, J = 6.94 Hz, 2 H) 8.62 (t, J = 7.57 Hz, 1 H) 9.13 (d, J = 5.67 Hz, 2 H) ppm. ^{13}C NMR (126 MHz, [D₆]DMSO): δ = 14.81, 22.94, 26.26, 29.24, 29.55, 29.63, 29.76, 29.85, 31.59, 32.15, 61.63, 128.96, 145.63, 146.33 ppm.

Elemental Analysis: CHN analysis was carried out with an Elementar vario EL III analyzer. LOD is 0.3 %.

Nuclear Magnetic Resonance Spectroscopy: ^{1}H and ^{13}C NMR spectra were recorded with a Bruker Avance 500 MHz Spectrometer at room temperature.

Electron Paramagnetic Resonance Spectroscopy: EPR spectra were recorded at ca. 9.4 GHz (X-band) with a Bruker CW Elexsys E 500 spectrometer at 150 K from pure powder samples. The experimental errors for all g values are ±0.005.

Thermogravimetric Analysis: TGA experiments were done with a Netzsch TG 209 F1 Iris thermo-microbalance at a heating rate of 10 K min^{-1} under nitrogen in aluminum oxide crucibles.

Differential Scanning Calorimetry: DSC measurements were done with a Netzsch DSC 214 Polyma at 5 or 10 °C min^{-1} under nitrogen. In each experiment, three heating-cooling cycles were measured.

Powder X-ray Diffraction: PXRD data were collected with a PANalytical Empyrean powder X-ray diffractometer in transmission geometry operating at 40 kV and 40 mA. The instrument was configured with a focusing X-ray mirror for Cu radiation (λ = 1.5419 Å) and a PIXcel1D detector. Theta-theta scans were run for 72 min over a 2θ range of 2–70° with step size of 0.0131° and a sample rotation time of 1 s.

Polarized Optical Microscopy: POM experiments were done with a Hengtech NP-400 microscope with crossed polarizer/analyzer at 10 × magnification. The samples were placed between two cover slips and heated using a Linkam TMS94 hot stage with a temperature control accuracy of ±0.1 °C. POM images were acquired during the cooling cycles after the sample had been heated above its clearing point and was then allowed to slowly cool.

Single-Crystal X-ray Diffraction: Crystals of **1**–**3** and **5** were grown by diffusion of methyl *tert*-butyl ether vapor into ethanol solutions of the respective compounds. Crystals of **6** were grown by diffusion of methyl *tert*-butyl ether vapor into methanol solution of the compound. The crystals were mounted on a glass fiber for data collection on an Imaging Plate Diffraction System IPDS-2 (STOE) with graphite-monochromated Mo-K_α radiation (λ = 0.71073 Å) at 150 K (**1**, **5**) or 210 K (**2**, **3**, **6**). All data were corrected for Lorentz and polarization effects. Numerical absorption corrections were applied using optimized shape.[269] For **1** and **3** extinction corrections were performed.

The structures were solved by direct methods using the program SHELXS-2013/1[270] and refined against F^2 by means of full-matrix least-squares procedures using the program SHELXL-2014/7.[271] Non-hydrogen atoms were refined with anisotropic temperature factors. In **1** the carbon atoms C7 to C9 were disordered over two sites with occupation factors of 0.8/0.2. The hydrogen atoms were located from the difference Fourier map and refined with U_{iso}(H) = 1.2U_{eq}(C) with the following exceptions. In **1** the hydrogen atoms of the disordered carbon atoms were calculated in their expected positions and refined as riding with HFIX 23 and HFIX 33, respectively. Some hydrogen atoms were calculated and refined with HFIX 137 (**2**: C9A and C9B, **3**: C9, **6**: C17 and C17A). In **5** and **6** the hydrogen atoms of the pyridinium rings were calculated with HFIX 43, and these of the dodecyl substituents with HFIX 23 or HFIX 33 (excluding those at C17 and C17A in **6**, see above). In **6** some restraints for the C–C bonds are used. For the visualization, the programs DIAMOND[272] and ORTEP[273] were used.

CCDC 1494949 (for **1**), 1494950 (for **2**), 1494951 (for **3**), 1494952 (for **5**), and 1494953 (for **6**) contain the supplementary crystallographic data for this article. These data can be obtained free of charge from The Cambridge Crystallographic Data Centre.

Density Functional Theory Calculations: Geometry optimizations were carried out using periodic boundary conditions, the PBEsol functional,[274] a tight grid and a tier 2 basis set as implemented in the FHIaims program package.[275]

4.4. Results

Initially, the compounds were characterized by single-crystal X-ray diffraction. Determination of the single-crystal structures of $[C_4Py]_2[MCl_4]$ (M = Cu (1), Co (2), and Zn (3)) and $[C_{12}Py]_2[MCl_4]$ (M = Co (5) and Zn (6)) was performed, and DIAMOND[272] drawings of the asymmetric units of 2 and 5 are depicted in Figure 4.1 and Figure 4.4, respectively. Table 4.1 summarizes the experimental details and crystallographic data; selected bond lengths of the complex anions and their bond angles are summarized in Table 4.2 and Table 4.3, respectively. To further validate the experimental results, the crystal structure of $[C_{12}Py]_2[CoCl_4]$ (5) was studied using density functional theory (DFT) calculations. Overall, we found an excellent agreement between the experimental and the theoretical structures, as shown in Tables 4.S21, 4.S22, and 4.S23 of appendix A, suggesting that DFT calculation could provide at least qualitative insights into the crystal structures that can be expected for these compounds.

All crystal structures are stabilized by several non-classical hydrogen bonds. Compounds **1**-**3** are isostructural and crystallize in the monoclinic space group $P2_1/n$. As an example, we shall discuss the structure of $[C_4Py]_2[CoCl_4]$ (**2**), the asymmetric unit of which contains four cations and two anions (Figure 4.1). The $[CoCl_4]^{2-}$ anion is connected to cations through C–H⋯Cl hydrogen bonds. The geometry of the $[CoCl_4]^{2-}$ anion is close to perfectly tetrahedral.

Table 4.2 shows that the averaged Co−Cl bond length of **2** is equal to the Co−Cl bond length of **5** (2.28 Å), and the averaged Zn–Cl bond length of **3** is 2.28 Å, which is comparable to the Zn−Cl bond length of **6** (2.27 Å). The Cu−Cl distance is slightly longer; this is consistent with distances found in other compounds with tetrahedral $[CuCl_4]^{2-}$ units, for example in $[C_{15}Py]_2[CuCl_4]$ (2.053 Å).[263]

The Cl−M−Cl angles are close to tetrahedral and range from 100.15(2) − 133.86(3)° in **1**, 106.6(2) − 114.96(2)° in **2**, and 106.39(3) − 114.85(3)° in **3**. The shortest cation⋯anion contact in **2** is found between Cl4 and one of the hydrogen atoms at C5B [2.76(2) Å]. An extensive literature search has provided no other examples of *N*-butylpyridinium tetrahalidometallate crystal structures for comparison.

Figure 4.1. The asymmetric unit of $[C_4Py]_2[CoCl_4]$ (**2**), with the numbering scheme. Hydrogen bonds are shown as dashed lines.

Figures 4.2 and 4.3 show a packing diagram of the ions of **2**. The cations and anions are arranged in alternating layers. In every cation layer, all the planar pyridinium rings are parallel to each other. Two π-π stacking interactions between pyridinium cations are observed. The first stacking interaction is characterized by an interplanar distance ranging from 5.3 to 7.2 Å with a displacement angle of 18.7(8)°, while the second stacking interaction is characterized by an interplanar distance of 5.9 Å and a displacement angle of 10.98(8)°.
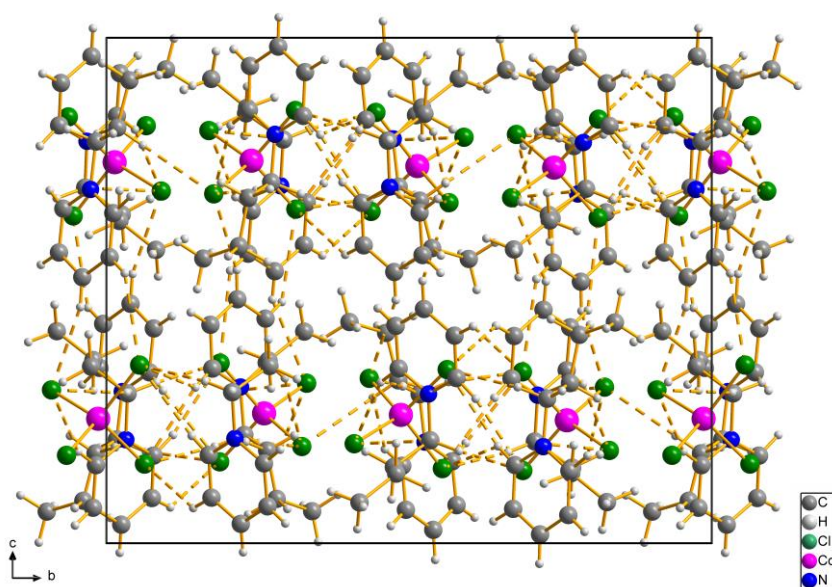
Figure 4.2. Packing diagram of $[C_4Py]_2[CoCl_4]$ (2). View along the crystallographic *a* axis. Hydrogen bonds are indicated by dashed lines.
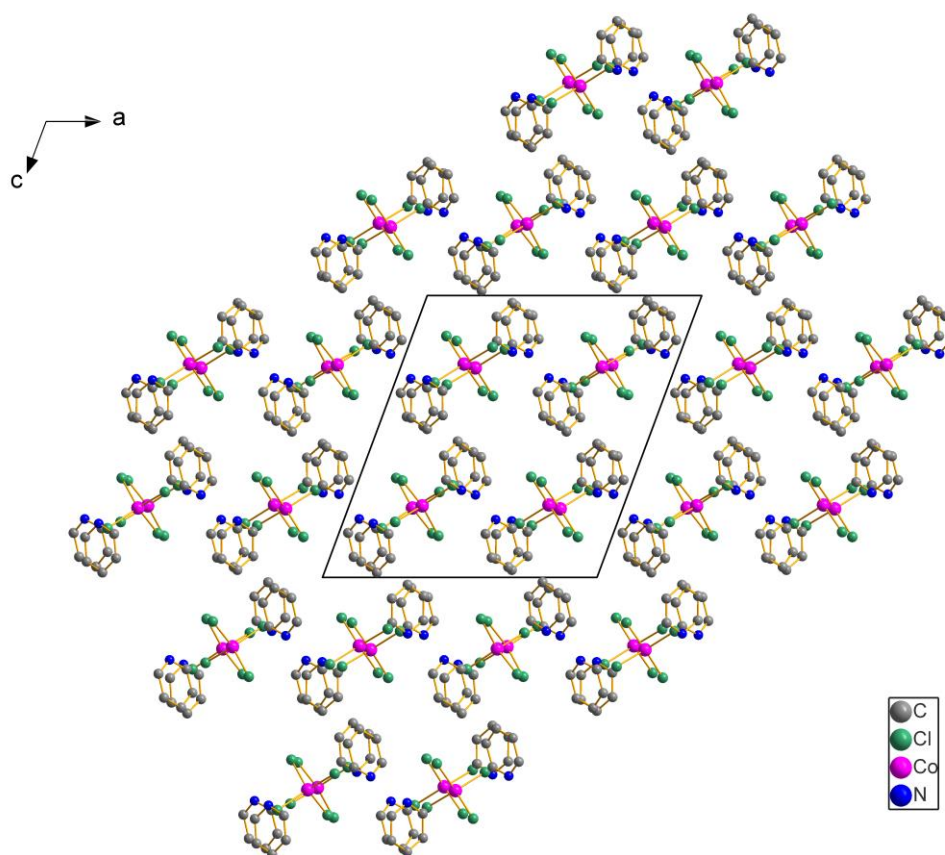
Figure 4.3. Packing diagram of $[C_4Py]_2[CoCl_4]$ (2). View along the crystallographic *b* axis. All *N*-alkyl chains are omitted for clarity.

Compounds 5 and 6 are isostructural and crystallize in the triclinic space group $P\bar{1}$. The organic cations in the unit cell are arranged centrosymmetrically around the $[MCl_4]^{2-}$ anion. For example, the asymmetric unit of $[C_{12}Py]_2[CoCl_4]$ (5) contains two cations and one anion (Figure 4.4). The geometry of the $[CoCl_4]^{2-}$ anion is close to tetrahedral as shown in Figure 4.4. The two pyridinium rings are parallel, and the M atom is located in the inversion center. As a result, the two dodecyl chains are arranged in opposite directions. The dashed lines show hydrogen bonds between H atoms and chloride ions. The anions are situated in an approximately tetrahedral symmetry, and the angles range from 107.2(3) - 111.6(3)°. Figure 4.5 shows a packing diagram of 5.

The results of the DFT calculations for $[C_{12}Py]_2[CoCl_4]$ (5) can directly be compared with the X-ray data. The calculated lattice parameters obtained at 0 K are a = 8.764 Å, b = 15.159 Å, c = 15.413 Å, α = 68.652°, β = 79.298° and γ = 83.394°, which is very close to the experimental values. Experimental and theoretical crystal structures show a very good agreement with cell vectors varying up to 6.5 % and a maximum difference in the cell angles

of 6.2 %, leading to a difference in cell volume of 2 %. Experimental and calculated values of selected bond lengths [Å], bond angles [°], and torsion angles [°] obtained for compound 5 are given in Tables 4.S21, 4.S22, and 4.S23 of appendix A, respectively.

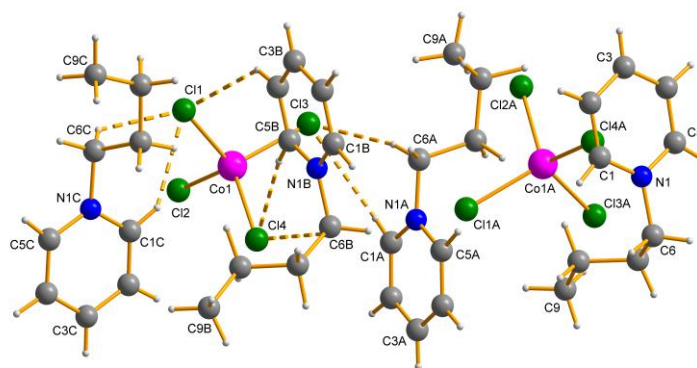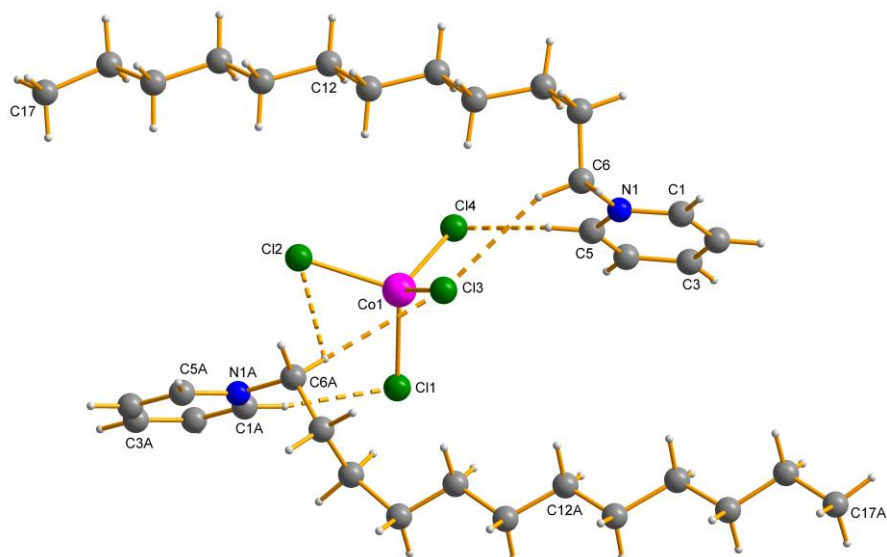**Figure 4.4.** The asymmetric unit of $[C_{12}Py]_2[CoCl_4]$ (5), with the numbering scheme. Hydrogen bonds are shown as dashed lines.
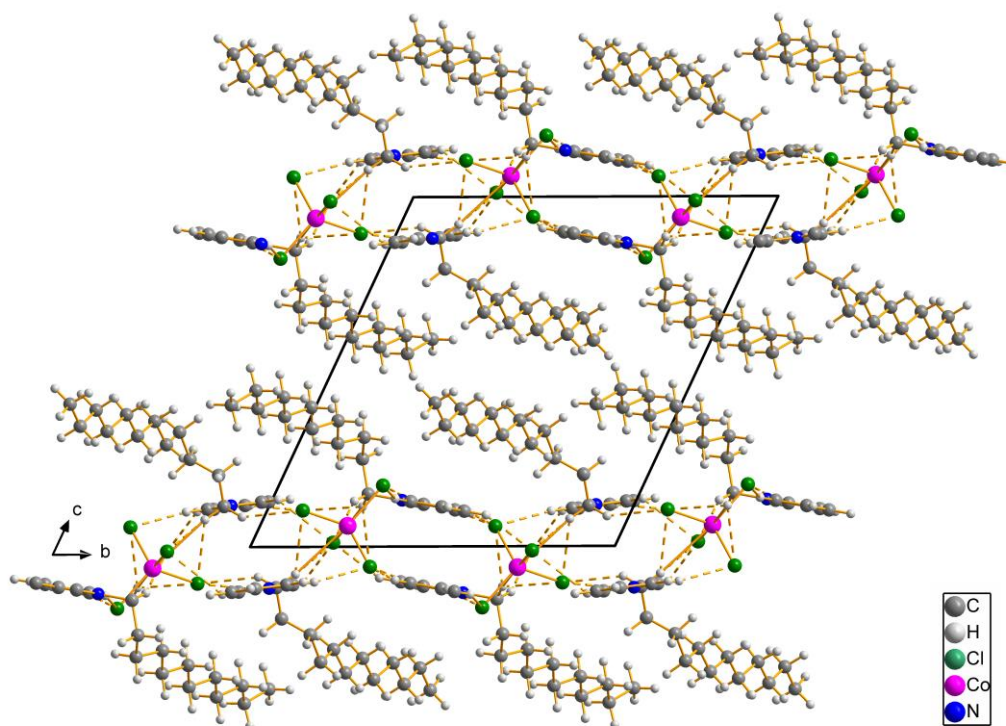
Figure 4.5. Packing diagram of $[C_{12}Py]_2[CoCl_4]$ (5). View along the crystallographic a axis. Hydrogen bonds are shown as dashed lines.

The cations and anions in the $[C_{12}Py]_2[MCl_4]$ compounds are arranged in alternating layers along the a axis. In every cation layer, the planar pyridinium rings are oriented parallel to each other. The molecular structures exhibit a normal geometry with fully extended alkyl chains. The bond lengths and bond angles of the organic cation are in good agreement with those found in the literature for other *N*-alkylpyridinium salts.[276] A full list of bond lengths, bond angles, torsion angles and hydrogen bond geometry for all structures is given in Tables 4.S1-4.S20 of the appendix A.

The ionic layer is stacked along b and individual $[CoCl_4]^{2-}$ layers are separated by alkylpyridinium moieties. This is similar to previous examples.[262-263] Besides electrostatic interactions, the cations and anions are held together through non-classical H-bonding interactions (Figures 4.4 and 4.5).

The pyridinium cations show a significant π–π stacking along c, as shown in Figure 4.5. The π-π interaction is realized through perfect face-to-face alignment with a zero displacement angle and an interplanar distance of 3.4 Å. Moreover, all chlorine atoms of the $[CoCl_4]^{2-}$ anion participate in H···Cl contacts with the hydrogen atoms of the pyridinium ring cations and some of the hydrogen atoms of the alkyl chains. These contacts are significantly shorter than the sum of the van der Waals radii for hydrogen and chlorine (2.95 Å).[277] The crystal structure and the number of H-bonding observed in $[C_{12}Py]_2[CoCl_4]$ (5) is comparable to those found in $[C_{12}Py]_2[ZnCl_4]$ (6).

Table.4.1. Crystallographic data and details of the refinement for 1-3, 5 and 6.

Compounds	[C4Py]2[CuCl4] (1)	[C4Py]2[CoCl4] (2)	[C4Py]2[ZnCl4] (3)	[C12Py]2[CoCl4] (5)	[C12Py]2[ZnCl4] (6)
Molecular Formula	$C_{18}H_{28}Cl_4N_2Cu$	$C_{18}H_{28}Cl_4N_2Co$	$C_{18}H_{28}Cl_4N_2Zn$	$C_{34}H_{60}Cl_4N_2Co$	$C_{34}H_{60}Cl_4N_2Zn$
Formula weight / $g \cdot mol^{-1}$	477.76	473.15	479.59	697.57	704.01
Crystal system	monoclinic	monoclinic	monoclinic	triclinic	triclinic
Space group	$P\,2_1/n$ (No. 14)	$P\,2_1/n$ (No. 14)	$P\,2_1/n$ (No. 14)	$P\bar{1}$ (No. 2)	$P\bar{1}$ (No. 2)
T / K	150(2)	210(2)	210(2)	150(2)	210(2)
a / Å	15.7318(5)	15.3539(4)	15.3418(5)	8.4847(4)	8.5090(5)
b / Å	17.7033(5)	18.7109(4)	18.7196(8)	15.3738(8)	15.3133(9)
c / Å	16.9471(5)	16.7085(4)	16.7117(5)	16.4863(8)	16.6595(11)
α / °	90	90	90	64.411(4)	65.362(5)
β / °	110.233(2)	110.526(2)	110.420(2)	79.801(4)	80.512(5)
γ / °	90	90	90	85.366(4)	85.287(5)
V / Å³	4428.6(2)	4495.36(19)	4497.9(3)	1908.91(17)	1945.9(2)
Z	8	8	8	2	2
D_{calc} / $g \cdot cm^{-3}$	1.433	1.398	1.416	1.214	1.202
μ / mm^{-1}	1.473	1.243	1.572	0.753	0.929
Crystal size / mm	0.20 x 0.26 x 0.30	0.35 x 0.40 x 0.45	0.21 x 0.22 x 0.26	0.08 x 0.25 x 0.48	0.07 x 0.10 x 0.9
Reflections collected	48166	28884	34169	24904	12032
Independent reflections	10162	7782	9469	6717	6122
R_{int}	0.0408	0.0334	0.0560	0.0431	0.0359
No. reflns with $I>2\sigma(I)$	6857	6211	5684	5360	4138
No. refined parameters	627	603	590	370	373
$R_1{}^a$, $wR_2{}^b$ [$I>2\sigma(I)$]	0.0326, 0.0728	0.0260, 0.0587	0.0339, 0.0541	0.0353, 0.0872	0.0424, 0.1054
$R_1{}^a$, $wR_2{}^b$ (all data)	0.0599, 0.0813	0.0376, 0.0624	0.0802, 0.0637	0.0501, 0.0930	0.0707, 0.1163
Goodness-of-fit on F^2	0.961	1.005	0.929	1.018	0.988

[a] $R_1 = \Sigma||F_o| - |F_c||/\Sigma|F_o|$. [b] $wR_2 = [\Sigma w(F_o^2 - F_c^2)/\Sigma[w(F_o^2)^2]]^{1/2}$.

Table.4.2. Selected bond lengths (Å) for the complex anions

1		2		3		5		6	
Cl1–Cu1	2.2843(6)	Cl1–Co1	2.2880(5)	Cl1–Zn1	2.2577(8)	Cl1–Co1	2.2763(7)	Cl1–Zn1	2.2744(11)
Cl2–Cu1	2.2319(6)	Cl2–Co1	2.2657(5)	Cl2–Zn1	2.29028(8)	Cl3–Co1	2.2848(6)	Cl2–Zn1	2.2881(10)
Cl3–Cu1	2.2715(6)	Cl3–Co1	2.2682(5)	Cl3–Zn1	2.2628(7)	Cl2–Co1	2.2945(6)	Cl3–Zn1	2.2785(9)
Cl4–Cu1	2.2325(6)	Cl4–Co1	2.2891(5)	Cl4–Zn1	2.2894(9)	Cl4–Co1	2.2570(7)	Cl4–Zn1	2.2493(11)
Cl1A–Cu1A	2.2759(6)	Cl1A–Co1A	2.2622(5)	Cl1A–Zn1A	2.2558(7)	–	–	–	–
Cl2A–Cu1A	2.2284(6)	Cl2A–Co1A	2.2856(5)	Cl2A–Zn1A	2.2872(8)	–	–	–	–
Cl3A–Cu1A	2.2782(6)	Cl3A–Co1A	2.2915(5)	Cl3A–Zn1A	2.2950(9)	–	–	–	–
Cl4A–Cu1A	2.2369(6)	Cl4A–Co1A	2.2721(5)	Cl4A–Zn1A	2.2629(8)	–	–	–	–
Cu–Cl (Aver.)	**2.26**	**Co–Cl (Aver.)**	**2.28**	**Zn–Cl (Aver.)**	**2.28**	**Co–Cl (Aver.)**	**2.28**	**Zn–Cl (Aver.)**	**2.27**

48

Table.4.3. Selected bond angles (°) for the complex anions

1		2		3		5		6	
Cl2–Cu1–Cl4	133.86(3)	Cl2–Co1–Cl3	113.62(2)	Cl1–Zn1–Cl3	113.62(3)	Cl4–Co1–Cl1	109.71(3)	Cl4–Zn1–Cl1	110.03(4)
Cl2–Cu1–Cl3	102.58(2)	Cl2–Co1–Cl1	107.25(2)	Cl1–Zn1–Cl4	111.34(3)	Cl4–Co1–Cl3	109.70(3)	Cl4–Zn1–Cl3	109.39(4)
Cl4–Cu1–Cl3	100.49(2)	Cl3–Co1–Cl1	110.185(19)	Cl3–Zn1–Cl4	107.61(3)	Cl1–Co1–Cl3	109.90(3)	Cl1–Zn1–Cl3	109.93(4)
Cl2–Cu1–Cl1	101.58(2)	Cl2–Co1–Cl4	111.56(2)	Cl1–Zn1–Cl2	107.53(3)	Cl4–Co1–Cl2	111.59(3)	Cl4–Zn1–Cl2	111.70(4)
Cl4–Cu1–Cl1	101.48(3)	Cl3–Co1–Cl4	107.38(2)	Cl3–Zn1–Cl2	110.02(3)	Cl1–Co1–Cl2	107.20(3)	Cl1–Zn1–Cl2	107.45(4)
Cl3–Cu1–Cl1	118.64(2)	Cl1–Co1–Cl4	106.640(19)	Cl4–Zn1–Cl2	106.51(3)	Cl3–Co1–Cl2	108.70(2)	Cl3–Zn1–Cl2	108.30(4)
Cl2A–Cu1A–Cl4A	132.81(3)	Cl1A–Co1A–Cl4A	114.96(2)	Cl1A–Zn1A–Cl4A	114.85(3)	–	–	–	–
Cl2A–Cu1A–Cl1A	101.19(2)	Cl1A–Co1A–Cl2A	108.02(2)	Cl1A–Zn1A–Cl2A	108.20(3)	–	–	–	–
Cl4A–Cu1A–Cl1A	101.85(2)	Cl4A–Co1A–Cl2A	109.487(19)	Cl4A–Zn1A–Cl2A	109.58(3)	–	–	–	–
Cl2A–Cu1A–Cl3A	103.44(3)	Cl1A–Co1A–Cl3A	109.08(2)	Cl1A–Zn1A–Cl3A	109.12(3)	–	–	–	–
Cl4A–Cu1A–Cl3A	100.15(2)	Cl4A–Co1A–Cl3A	108.32(2)	Cl4A–Zn1A–Cl3A	108.37(3)	–	–	–	–
Cl1A–Cu1A–Cl3A	119.36(2)	Cl2A–Co1A–Cl3A	106.653(19)	Cl2A–Zn1A–Cl3A	106.39(3)	–	–	–	–
Cl–Cu–Cl (Aver.)	109.79	Cl–Co–Cl (Aver.)	109.43	Cl–Zn–Cl (Aver.)	109.43	Cl–Co–Cl (Aver.)	109.47	Cl–Zn–Cl (Aver.)	109.47

To gain further structural information complementary room temperature powder X-ray diffraction (XRD) studies were performed. The XRD patterns for all salts (except $[C_{12}Py]_2[CuCl_4]$ where single-crystal data is not available) show the same unit cell and confirm that the single-crystal structure is identical to the powder samples obtained directly from the synthesis, Figure 4.6. The reflection with the lowest 2θ value displays the highest intensity for all salts. The calculated d-spacing from this peak increases with increasing alkyl chain length, Table 4.4.
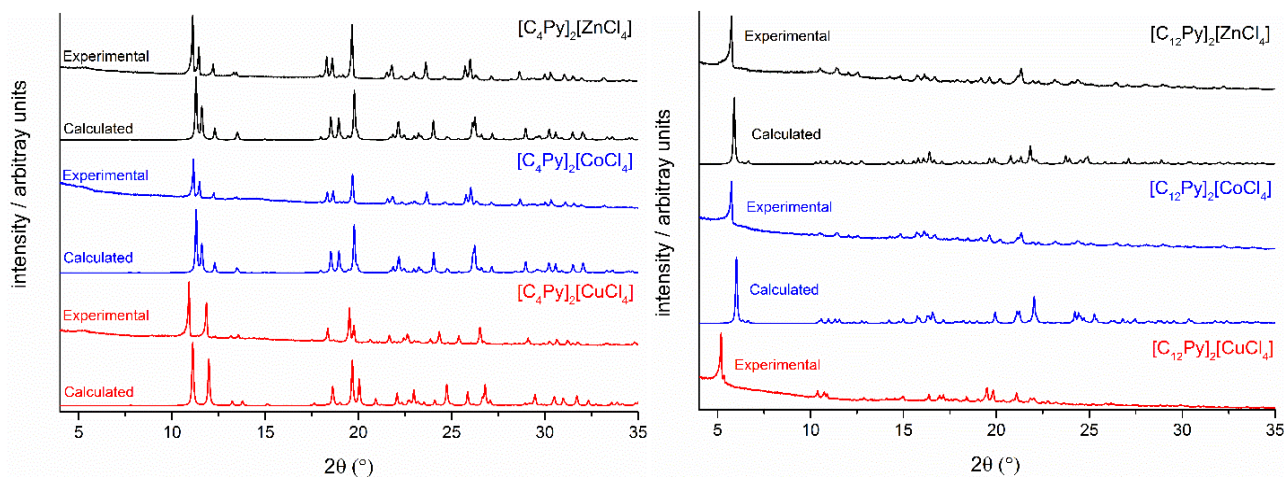
Figure 4.6. Experimental and calculated XRD patterns of $[C_4Py]_2[MCl_4]$ (left) and $[C_{12}Py]_2[MCl_4]$ (right). Calculated patterns were obtained from the single-crystal data, except for $[C_{12}Py]_2[CuCl_4]$, for which no single-crystal data is available.

Table 4.4. Layer spacings obtained from powder and single crystal X-ray diffraction.

| | Layer separation/ Å | | | | |
Compound	Powder XRD	Single crystal XRD	h	k	l
(1)	8.12	7.95	0	0	2
(2)	7.94	7.82	0	0	2
(3)	7.95	7.83	0	0	2
(4)	17.12	_a	-	-	-
(5)	15.47	14.68	0	0	1
(6)	15.48	14.98	0	0	1

[a] The single-crystal structure of $[C_{12}Py]_2[CuCl_4]$ (**4**) is not available, as no crystals suitable for single-crystal X-ray crystallographic analysis could be obtained.

XRD confirms single-crystal analysis and proves that the powder samples are identical to the single-crystal samples. Moreover, these data show that all salts with the same pyridinium cation are isostructural. This is consistent with single-crystal data: compounds

1-**3** crystallize in the monoclinic space group $P2_1/n$, while compounds **5** and **6** crystallize in the triclinic space group $P\bar{1}$. The layer separation calculated from XRD for all salts is similar to that obtained from the single-crystal data (Table 4.4).

Besides X-ray diffraction, the paramagnetic compounds $[C_4Py]_2[CuCl_4]$ (**1**) and $[C_{12}Py]_2[CuCl_4]$ (**4**) were investigated by electron paramagnetic resonance (EPR) spectroscopy to obtain further information on the structural flexibility of the $[CuCl_4]^{2-}$ moieties. Due to the incomplete separation of the paramagnetic centers in the pure samples no hyperfine structure of the copper was observed (^{63}Cu, ^{65}Cu; nuclear spin I = 3/2 for each isotope). In addition, the four chloride ligands should lead to a further splitting of the signals (^{35}Cl, ^{37}Cl; nuclear spin I = 3/2 each); this is also not resolved but contributes to the line broadening in the EPR spectra. In spite of this, the g-tensor parameters for the axial symmetry ($g_\parallel$ and $g_\perp$, compound **1**) and for the rhombic symmetry (g_1, g_2, g_3, compound **4**) could be determined.

Figure 4.7 shows the spectra of both compounds, $[C_4Py]_2[CuCl_4]$ (**1**) and $[C_{12}Py]_2[CuCl_4]$ (**4**). The spectrum of compound **1** indicates an axial symmetry of the crystalline compound, and $g_\parallel(g_{parallel}/g_{par.})$, as well as $g_\perp(g_{perpendicular}/g_{perp.})$, can be determined. The averaged g value, g_{av}, for the axial symmetric spectrum was calculated by the following expression:

$$g_{av} = \frac{g_{\parallel} + 2 \cdot g_{\perp}}{3} \qquad (1)$$

The g_{av} value corresponds to the isotropic g_{iso} value of liquid systems (e.g., solutions or ILs). The variation of the parameters reflects well-known structural flexibility of the tetrachloridocuprate(II) moiety.[278]

For compound **1**, the g_{av} value is 2.155, which reflects a significant distortion from the expected tetrahedral coordination geometry of the $[CuCl_4]^{2-}$ dianion. This is consistent with the crystal structure of $[C_4Py]_2[CuCl_4]$ (**1**; Table 4.3).
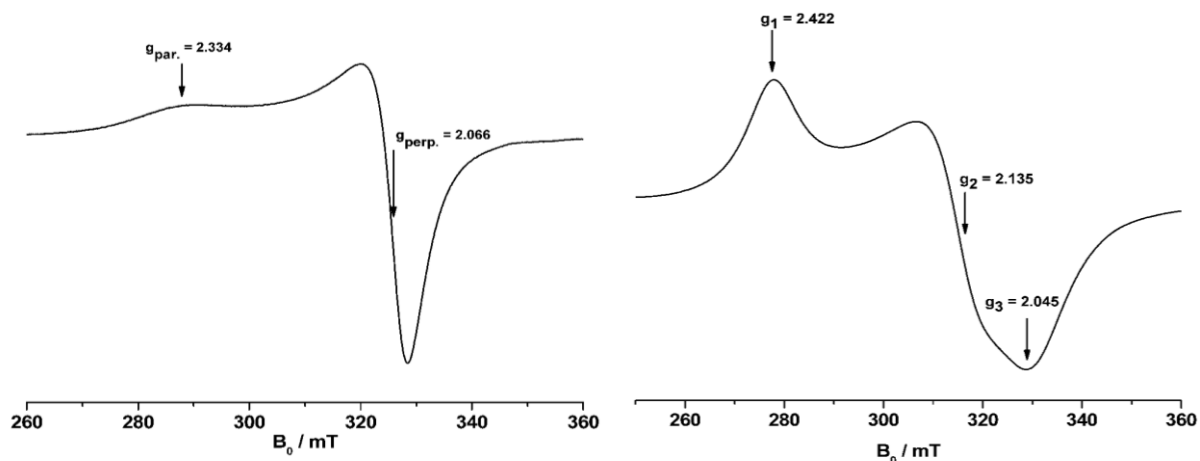
Figure 4.7. EPR spectrum of a pure powdered sample of $[C_4Py]_2[CuCl_4]$ (**1**) (left) and $[C_{12}Py]_2[CuCl_4]$ (**4**) (right), measured at 150 K.

The average g value, g_{av}, for the spectrum of compound **4** was calculated by using the expression:

$$g_{av} = \frac{g_1 + g_2 + g_3}{3} \qquad (2)$$

For compound **4** a g_{av} value of 2.201 was determined, which reflects a slight distortion of the expected tetrahedral coordination geometry of the $[CuCl_4]^{2-}$ dianion closer to a tetrahedron.[278]

The thermal behavior of all ILs was investigated by differential scanning calorimetry (DSC), hot-stage polarizing optical microscopy (POM), and thermogravimetricanalysis (TGA). Figure 4.8 shows the TGA curves obtained for compounds **1**-**6**. Decomposition temperatures are summarized in Table 4.5.

All TGA data are similar but differ slightly from sample to sample. The TGA data of all salts show that the solids do not contain significant amounts of water or other solvent and consequently only a very minor weight loss is observed until around 175 °C. In the case of $[C_4Py]_2[MCl_4]$, the TGA data shows that $[C_4Py]_2[CuCl_4]$ is stable up to ca. 185 °C and only a minor weight loss of below 1% is observed. This is in good agreement with data by Thiel et al.[268] $[C_4Py]_2[CuCl_4]$ then decomposes in two broad steps between ca. 185 and 434 °C with a weight loss of 79 % and another weight loss of 20 % between ca. 434 °C and 639 °C.

Similarly, $[C_4Py]_2[CoCl_4]$ is stable up to ca. 233 °C and only loses below 1% of its original mass. It then decomposes in two broad steps between ca. 233 - 409 °C and 409 - 583 °C with weight losses of 71% and 12%, respectively. The residual mass is 15%. Finally, $[C_4Py]_2[ZnCl_4]$ is stable up to ca. 210 °C and only loses below 1%. It then also decomposes in two broad steps between ca. 210 - 432 °C and 432 - 508 °C with weight losses of 74% and 24%, respectively.

The longer chain derivatives $[C_{12}Py]_2[MCl_4]$ exhibit an analogous behavior. $[C_{12}Py]_2[CuCl_4]$ is stable up to ca. 177 °C with a weight loss of below 1%. It then decomposes in two broad steps between ca. 177 - 412 °C and 412 - 510 °C with weight losses of 85 and 9%, respectively. $[C_{12}Py]_2[CoCl_4]$ is stable up to ca. 227 °C with a weight loss of below 1%. It then decomposes in two broad steps between ca. 227 - 400 °C and 400 – 578 °C with weight losses of 80% and 8%, respectively. The residual mass is 10%. $[C_{12}Py]_2[ZnCl_4]$ is stable up to ca. 202 °C with a weight loss of below 1%. It also decomposes in two broad steps between ca. 202 - 427 °C and 427 – 520 °C with weight losses of 83 and 15%, respectively.

The first decomposition step is likely due to de-alkylation and related fragmentation reactions. The combustion step is the complete destruction of the residual organic and inorganic materials. Except in the case of $[C_4Py]_2[CoCl_4]$ and $[C_{12}Py]_2[CoCl_4]$, some inorganic remains behind as a residue.
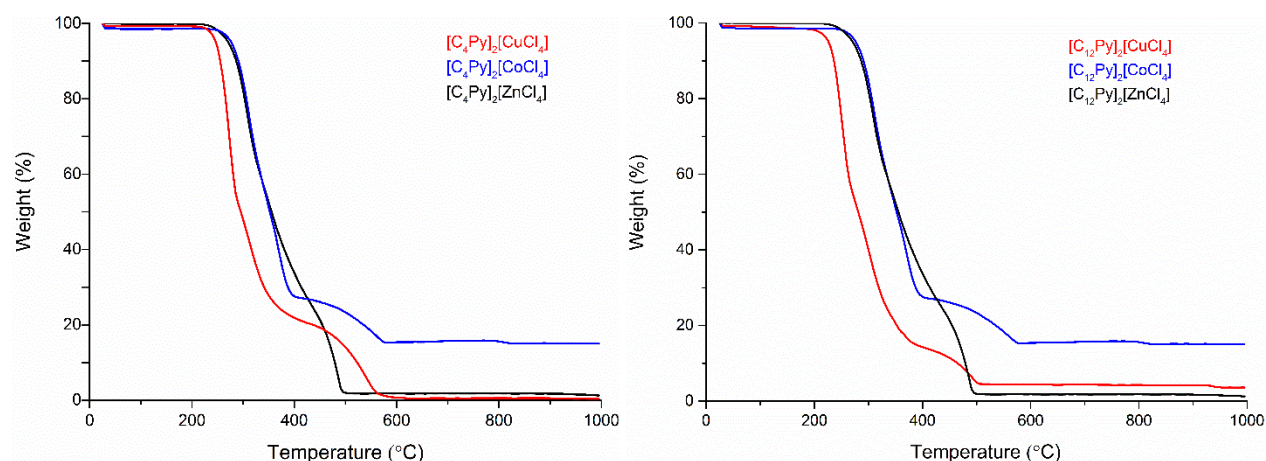
Figure 4.8. TGA curves of $[C_4Py]_2[MCl_4]$ (left) and $[C_{12}Py]_2[MCl_4]$ (right) (M= Cu, Co, Zn).

The phase behavior of compounds **1**-**6** was investigated by DSC and POM. All compounds are ILs with melting points below 100 °C. In the case of **1**, **2**, and **3**, DSC and POM find no liquid crystalline phases, consistent with data of similar compounds.[262-263] $[C_4Py]_2[CuCl_4]$ shows, with an onset temperature, a glass transition at -40.4 °C, a cold

crystallization at -3.7 °C, and a melting point at 67.9 °C in the first heating cycle. In the second heating cycle, it reproducibly only shows, with an onset temperature, a cold crystallization at -9.3 °C and a melting point at 67 °C. $[C_4Py]_2[CoCl_4]$ shows a melting point in the first and second heating cycle with an onset temperature of 89.8 and 91.3 °C respectively. $[C_4Py]_2[ZnCl_4]$ shows a melting point in the first and second heating cycle with an onset temperature of 90.9 and 88.4 °C, respectively.

Figure 4.9 shows that in the case of the dodecylpyridinium derivatives, the DSC heating curve of $[C_{12}Py]_2[CuCl_4]$ reveals a second phase transition with an onset temperature of 71.4 °C. This signal is assigned to a liquid crystal-isotropic phase transition, which has previously been assigned to a crystalline–smectic A (SmA) transition.[263] Moreover, a glass transition is observed in the first and second heating cycle with an onset temperature of -41.8 and -43.9 °C, respectively.

In contrast to $[C_{12}Py]_2[CuCl_4]$, the heating curves of the new compounds $[C_{12}Py]_2[CoCl_4]$ and $[C_{12}Py]_2[ZnCl_4]$ only show a melting transition with an onset temperature of 72.7 and 78.2 °C in $[C_{12}Py]_2[CoCl_4]$ and $[C_{12}Py]_2[ZnCl_4]$, respectively. This melting transition is reproducible, and the corresponding crystallization step is also visible in the respective cooling traces with an onset temperature of 46.6 °C ($[C_{12}Py]_2[CoCl_4]$) and 53.8 °C ($[C_{12}Py]_2[ZnCl_4]$). The heating traces do, however, not show additional signals indicating any further phase transitions.

In spite of this, all cooling curves exhibit weak signals analogous to those observed for $[C_{12}Py]_2[CuCl_4]$ above the melting transition. This suggests that $[C_{12}Py]_2[CoCl_4]$ and $[C_{12}Py]_2[ZnCl_4]$ also exhibit liquid crystalline phases. As the samples are isostructural, these signals are likely also caused by isotropic-SmA phase transition, similar to $[C_{12}Py]_2[CuCl_4]$.

The existence of mesophases for **4**, **5**, and **6** is indeed confirmed by POM, Figure 4.9. A focal conic fan texture characteristic of a lamellar phase, most likely a SmA phase, is observed in all dodecylpyridinium compounds upon cooling from the isotropic state at around 70 °C. These observations are consistent with data on $[C_{12}Py]_2[CuCl_4]$ by Neve and co-workers,[263] and $[C_{12}Py]_2[CoCl_4]$ by Bowlas and co-workers.[279] Table 4.5 summarizes the DSC and TGA data for all compounds.
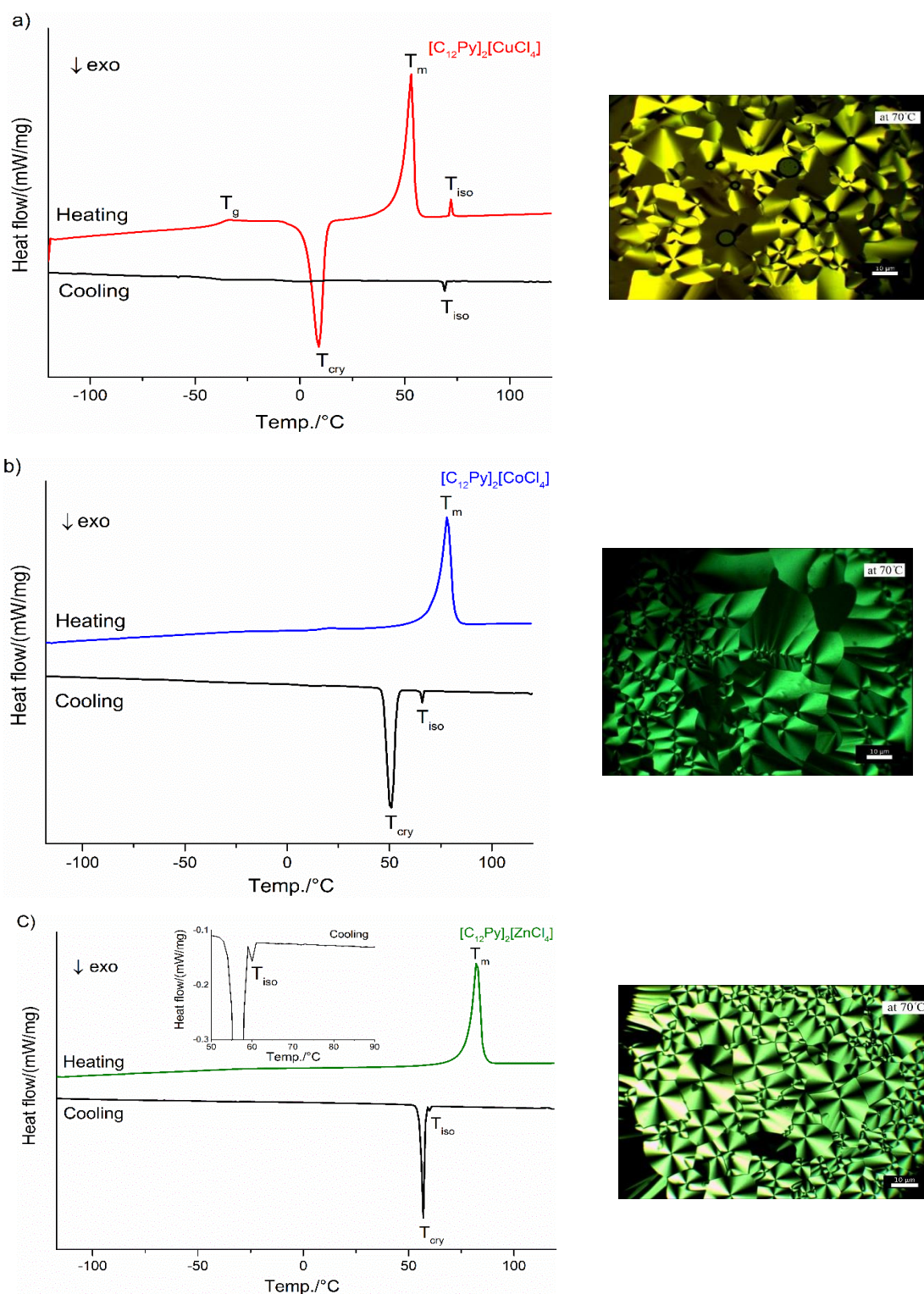
Figure 4.9. (a) DSC traces (first heating/cooling cycle) and POM image of $[C_{12}Py]_2[CuCl_4]$. (b) DSC traces (second heating/cooling cycle) and POM image of $[C_{12}Py]_2[CoCl_4]$. (c) DSC traces (second heating/cooling cycle) and POM image of $[C_{12}Py]_2[ZnCl_4]$. All POM images were taken at 70 °C. T_{cry}: crystallization temperature; T_m: melting temperature; T_{iso}: isotropic phase transition temperature; T_g: glass transition temperature.

55

Table 4.5. DSC and TGA data of (1)-(6)[a].

Cpd.		Transition	T/ °C	ΔH / kJ.mol^{-1}	Decomposition
(1)	**1st Cooling**	I - Cr	-11.6	-9.83	185 °C
	1st Heating	Cr - I	67.9	29.59	
	2nd Cooling	I - Cr	-1.1	-21.72	
	2nd Heating	Cr - I	67.0	28.97	
(2)	**1st Cooling**	I - Cr	43.9	-32.54	233 °C
	1st Heating	Cr - I	89.8	29.16	
	2nd Cooling	I - Cr	38.4	-32.23	
	2nd Heating	Cr - I	91.3	28.95	
(3)	**1st Cooling**	I - Cr	27.0	-30.28	210 °C
	1st Heating	Cr - I	90.9	31.82	
	2nd Cooling	I - Cr	30.6	-31.18	
	2nd Heating	Cr - I	88.4	32.38	
(4)	**1st Cooling**	I - SmA	68.3	-0.66	177 °C
	1st Heating	Cr - SmA	48.2	32.02	
		SmA - I	71.4	0.65	
	2nd Cooling	I - SmA	68.0	-0.41	
	2nd Heating	Cr - SmA	46.7	31.27	
		SmA - I	71.1	0.34	
(5)	**1st Cooling**	I - SmA	65.4	-0.6	227 °C
		SmA - Cr	46.6	-26.79	
	1st Heating	Cr - I	72.7	28.52	
	2nd Cooling	I - SmA	65.2	-0.57	
		SmA - Cr	46.7	-26.7	
	2nd Heating	Cr - I	72.8	28.4	
(6)	**1st Cooling**	I - SmA	60.0	-0.35	202 °C
		SmA - Cr	53.8	-28.39	
	1st Heating	Cr - I	78.2	30.11	
	2nd Cooling	I - SmA	59.9	-0.42	
		SmA - Cr	57.0	-28.57	
	2nd Heating	Cr - I	78.5	29.77	

[a] Phase-transition temperature (± 0.5 °C) and enthalpies (± 5 %) of $[C_nPy]_2[MCl_4]$ salts, determined from DSC experiments after an initial heating to 120 or 150 °C to ensure that the samples are water-free; Cr: crystalline phase; I: isotropic phase; SmA: smectic A phase.

Chapter 5

Crystal structure of N-butylpyridinium bis(μ₂-dichlorido)-tetrachlorido-di-copper(II), $C_{18}H_{28}N_2Cu_2Cl_6$
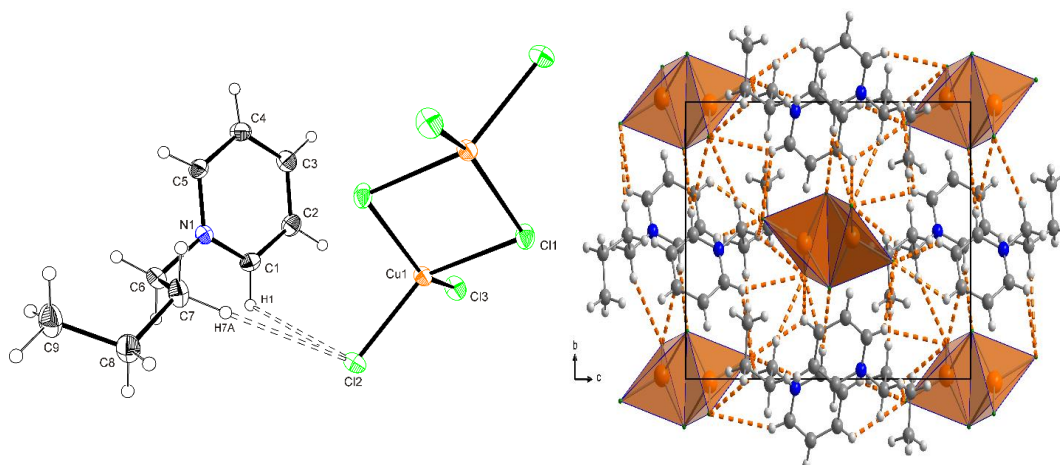
5.1. Abstract

$C_{18}H_{28}N_2Cu_2Cl_6$, monoclinic, $P2_1/n$ (no. 14), a = 9.6625(6) Å, b = 9.3486(3) Å, c = 14.1168(8) Å, β = 102.288(5)°, V = 1245.97(11) Å^3, Z = 4, R_{gt} (F) = 0.0182, wR_{ref} (F^2) = 0.0499, T = 210(2) K.

The molecular structure and the packing diagram of the title compound are shown in the figures. Atoms labelled A are centrosymmetrically related to the others. The hydrogen bonds are illustrated by dashed lines. Tables 5.1 contains a list of the atoms including atomic coordinates and displacement parameters.

5.2. Source of material

The title compound has been prepared according to refs.[50, 263, 280-281] To a solution of N-butylpyridinium chloride (0.342 g, 2 mmol) in dry acetonitrile (6 mL) copper(II) chloride (0.34 g, 2 mmol) was added. This mixture was stirred to reflux for 3 h. The solvent was evaporated with a rotary evaporator at 60 °C under reduced pressure, and the product was dried in vacuo. Yield: 0.59 g (98.3 %). MS positive mode: m/z = 136.1126 $[C_9H_{14}N]^+$, and MS negative mode: m/z = 169.8 $[CuCl_3]^-$. Elemental analysis for $C_{18}H_{28}Cl_6Cu_2N_2$ calculated (found) C, 35.31% (35.34%); H, 4.61% (4.43%); N, 4.58% (4.59%). Red crystals (Mp. 94-96 °C) suitable for single crystal X-ray diffraction were grown by diffusion of methyl tert-butyl ether vapor into ethanolic solution of the compound.

5.3. Experimental details

Coordinates of hydrogen atoms were refined without any constraints or restraints. Elemental Analysis (CHN) was carried out on an Elementar vario EL III analyser with a limit of detection of 0.3 %. Mass spectroscopy (MS) was performed on a Micromass QTOF (Quadrupol – Time of flight) with an electrospray ionization (ESI) source operating in positive and negative ionization modes, with a range of m/z 50-800. Samples were injected as dilute solutions in methanol. Melting points were measured with a Melting Point Meter KSP1N.

Table 5.1: Fractional atomic coordinates and isotropic or equivalent isotropic displacement parameters(Å^2).

Atom	x	y	z	U_{iso}*/U_{eq}
C1	0.21892(16)	1.34958(18)	0.13482(12)	0.0297(3)
H1	0.2378(19)	1.322(2)	0.1974(15)	0.039(5)*
C2	0.12862(17)	1.27846(19)	0.06119(12)	0.0343(4)
H2	0.089(2)	1.191(2)	0.0757(15)	0.051(6)*
C3	0.10826(16)	1.33051(19)	-0.03214(12)	0.0331(4)
H3	0.0436(19)	1.288(2)	-0.0842(13)	0.035(5)*
C4	0.17871(17)	1.45291(19)	-0.04981(12)	0.0329(4)
H4	0.163(2)	1.4933(19)	-0.1093(16)	0.038(6)*
C5	0.26794(18)	1.51946(18)	0.02547(12)	0.0297(3)
H5	0.311(2)	1.601(2)	0.0194(14)	0.037(5)*
C6	0.38816(16)	1.53919(19)	0.19600(11)	0.0289(3)
H6A	0.384(2)	1.635(2)	0.1834(14)	0.038(5)*
H6B	0.352(2)	1.5181(19)	0.2543(15)	0.035(5)*
C7	0.53618(18)	1.48169(19)	0.20422(15)	0.0350(4)
H7A	0.533(2)	1.378(2)	0.2114(14)	0.045(5)*
H7B	0.562(2)	1.501(2)	0.1446(17)	0.042(6)*
C8	0.64016(19)	1.5454(2)	0.29048(14)	0.0395(4)
H8A	0.725(3)	1.495(2)	0.2967(16)	0.043(6)*
H8B	0.607(2)	1.525(2)	0.3482(17)	0.044(6)*
C9	0.6639(2)	1.7040(2)	0.28281(17)	0.0471(5)
H9A	0.584(2)	1.757(2)	0.2827(14)	0.042(5)*
H9B	0.739(2)	1.741(2)	0.3342(16)	0.059(6)*
H9C	0.695(3)	1.726(3)	0.2235(19)	0.071(7)*
Cl1	0.50633(4)	0.82761(4)	-0.00540(3)	0.03410(12)
Cl2	0.44379(4)	1.07973(4)	0.22997(2)	0.03259(12)
Cl3	0.20539(4)	0.87418(4)	0.08240(3)	0.03547(12)
Cu1	0.40485(2)	0.98814(2)	0.08398(2)	0.02442(10)
N1	0.28674(13)	1.46735(14)	0.11596(9)	0.0242(3)

5.4. Comment

Copper (II) complexes exhibit a very rich and diverse coordination geometries due to the presence of the Jahn-Teller distortions in the d^9 electronic system.[282] Among those, chloridocuprate (II) salts have attracted considerable interest dut to their magnetic,[283-284] thermochromic,[282] phase transition,[285] and non-linear optical behavior.[161] For example, Willett and co-workers[286-287] demonstrated that the hydrogen bonding plays an important role in the thermochromism that these compounds are known for; these authors also associated the color change with a change in ligand geometry.

Quite some of the tetrachloridocuprates are ionic liquids (ILs). ILs, low-temperature molten salts of a highly diverse chemical composition, have received tremendous attention for their (projected) high potential in many fields.[57] A number of these applications are driven by the specific physical and chemical properties of ILs, such as very low vapor pressure or low melting points but high ionicity.[2, 10, 12, 226, 229] As ILs are composed entirely of ions, their properties can be tuned by an judiciuous choice of the cation and the anion.[288]

Of particular interest to the current study, metal-containing ILs (MILs) have been studied for a variety of properties such as their structural flexibility,[278, 289] electrochemical behavior,[67] and the exploitation of their unique redox behavior, for example in applications for mercury removal from natural gas, etc.[231, 241, 290-291]

Besides their intrinsic properties and application, MILs have also been used as ionic liquid precursors (ILPs) for inorganic nanomaterials, where the ILP acts as the solvent, the template, and the precursor for the inorganic material at the same time.[12, 69-70] For example, ILPs have been used to synthesize $CuCl$, Au, Ag, metal oxide, Fe_3C, and CuS nanomaterials. [48, 50, 69, 146, 266, 292-294]

One of the key challenges in the ILP approach is the fact that for successful and efficient inorganic nanomaterials synthesis the fraction of the metal (which will be transformed to, e.g., a metal sulfide in the course of the reaction) needs to be fairly high. Strategies to increase the metal content in the ILPs are thus of a very direct interest for improved yields from the synthetic procedure. In the quest for higher metal contents in the ILPs, we have therefore expanded the ILP platform to multinuclear ILs that can also serve as ILPs. The title compound is the first example of such a binuclear ILP. The article current focuses on the structure of the title compound. The transformation of the ILP to a series of inorganic materials will be described elsewhere.

The asymmetric unit of the title compound contains one cation and a half anion. The second half is generated by symmetry because the $[Cu_2Cl_6]^{2-}$ unit is centrosymmtric. The $CuCl_3$ subunits are bibridged over the inversion centre. The average Cu–Cl bond lengths are 2.1936(4) Å (terminal) and 2.3100(4) Å (bridging) with a bridging Cu–Cl–Cu angle of 91.27(2)°, giving a distance between both copper atoms of 3.3027(4) Å. The coordination environment of the Cu^{2+} ions can be better described by a flattened tetrahedron rather than square-planar. The corresponding angles are 88.73(2)° [Cl(bridging) - Cu - Cl(bridging)], 100.01(2)° [Cl(terminal) – Cu – Cl(terminal)] and 98.79(2)° to 140.43(2)° [Cl(terminal) – Cu – Cl(bridging)]. The plane formed by the Cu atom and both terminal Cl atoms is twisted by an angle of 55.12° with respect to the plane defined by both Cu atoms and the bridging Cl atoms. The Cambridge Database contains 64 structures with isolated bibridged $[Cu_2Cl_6]^{2-}$ dimers, for example in $[P(C_6H_5)_4]_2[Cu_2Cl_6]$. [295]

In contrast to the synthesis described here where a 1:1 ratio of copper(II) chloride and N-butylpyridinium chloride was used yielding the dinuclear species, mononuclear isolated tetrachloridocopper(II) $[CuCl_4]^{2-}$ was formed when N-butylpyridinium and copper(II) chloride in a ratio of 2:1 are used.[5] In contrast, infinite zig-zag chains where the $[Cu_2Cl_6]^{2-}$ moieties are linked by weak interactions are observed when piperazinium rather than N-butylpyridinium cation is employed.[296]

The packing of the title compound is stabilized by non-classical C–H⋯Cl hydrogen bonds between the $[Cu_2Cl_6]^{2-}$ anions and the pyridinium cations - for details, see Table 3. There are no interactions between neighboring $[Cu_2Cl_6]^{2-}$ groups.

Chapter 6

Hierarchically structured Copper Sulfide Microflowers with Excellent Amperometric Hydrogen Peroxide Detection Performance

6.1. Abstract

This study introduces an efficient non-enzymatic hydrogen peroxide sensor based on copper sulfide with a hierarchical flower-like microstructure (CuS_{flower}) assembled from nanoflakes. CuS_{flower} microstructures were made via a novel, facile, and highly controllable hot-injection synthesis method using the ionic liquid bis butylpyridinium tetrachloridocuprate (II) as copper source, nanoparticle stabilizer, and structural template. The flower-like morphologies can be adjusted with reaction temperature and time. The resulting CuS_{flower} materials exhibit outstanding performance for amperometric H_2O_2 detection with superior electrocatalytic activity and sensitivity ($3.82 \ mM^{-1} \ cm^{-2}$), very low detection limit ($0.1 \ \mu M$) along with exceptional selectivity and long-term stability compared to CuS sensor materials obtained with conventional processes and structures. This substantial efficiency enhancement is attributed to the unique flower-like morphology providing a higher number of active surface sites and their lower H_2O_2 reduction charge transfer resistance along with a faster dislodge rate of the *in-situ* generated oxygen bubbles from the roughened CuS surface.

6.2. Introduction

Hydrogen peroxide (H_2O_2) plays a vital role in several fields including food, clinical, pharmaceutical, paper, and chemical industries, as well as in biological systems and environmental protection.[169, 297-298] Additionally, high H_2O_2 concentration levels in blood are associated with diseases like Alzheimer's, cancer, atherosclerosis, and progressive neurodegenerative diseases (e.g., Parkinson's).[299] Moreover, H_2O_2 is essential in cell signaling pathways and for the function of the immune system.[169, 300-301] Thus, the construction of a cost-effective and efficient (i.e., accurate, sensitive, stable, selective, etc.) H_2O_2 sensor is of high technical, medical, and societal relevance.

Enzyme-based electrochemical biosensors are very popular for H_2O_2 detection thanks to their high sensitivity and excellent selectivity. However, disadvantages of these enzyme-based biosensors include high cost, environmental instability, limited lifetime, tedious preparation, and denaturation, all of which limits their practical application.[169, 302-303]

As a result, noble metal-based nanomaterials have been explored as alternative, non-enzymatic H_2O_2 electrochemical sensors.[304-310] Unfortunately, however, the limited availability and correspondingly high prices clearly limit their application on a larger scale and other materials are thus necessary for the development of reliable H_2O_2 sensors.[311]

Nanostructured transition metals including iron, nickel, or copper and their oxides and sulfides have attracted increasing attention as alternative H_2O_2 sensors.[312-315] This is due to their low cost, intrinsic peroxidase-like catalytic activity, high performance, and potentially large active surface. Moreover, they can be prepared in a wide variety of different morphologies and crystal phases. Among them, copper sulfide (CuS), one of the most important metal chalcogenide p-type semiconductors,[164] has been extensively studied for its application potential in solar cells,[165] lithium-ion batteries,[166] photocatalysis,[167] optical limiters,[168] biological markers,[169] and biosensors.[170] This interest is attributed to the unique electrical, mechanical, optical, physical, and chemical properties of CuS.[171-172]

Lately, CuS nanostructures have been employed for biosensor fabrication; advantages of these materials include easy preparation, simple storage, low toxicity, low price, and high performance.[195, 316] Besides, recent studies demonstrate that three-dimensional CuS materials with hierarchical architectures have an intrinsic peroxidase-like catalytic activity similar to Fe_3O_4 nanomaterials[317-318]. As a result, nano- and microstructured CuS with hierarchical architectures are excellent candidates for enzyme-mimetic materials for sensor development.

In particular, the properties of CuS can be tuned by adjusting the stoichiometry, morphology, structure, and Cu valence state. Consequently, $Cu_{2-x}S$ ($0 \leq x \geq 1$) with various morphologies and compositions such as covellite (CuS), anilite ($Cu_{1.75}S$)[176], digenite ($Cu_{1.8}S$)[177], djurleite ($Cu_{1.96}S$)[178], and chalcocite (Cu_2S)[175] have been prepared; synthetic approaches include arc discharge, electron beam irradiation, laser ablation, spray pyrolysis, solvothermal synthesis, chemical vapor deposition, vapor-liquid-solid growth, hot-injection solution synthesis, and sonochemical synthesis.[319-322] However, the construction of CuS microstructures with a defined shape, size, size distribution, hierarchical organization, controlled stoichiometry, and defined crystal structure via a simple, low cost, and the scalable process is still highly sought after. Additionally, van der Waals interactions between the CuS nanoparticles result in a strong aggregation; these prevent an effective catalytic utilization of

many of the existing solid materials.[323-324] Therefore, the creation of robust CuS nanostructures with the high active surface area is an unresolved issue as of now.

The current article, therefore, describes the synthesis of CuS 3D-microstructures with hierarchical geometries via a facile and efficient synthesis method for high performance non-enzymatic H_2O_2 amperometric detection. CuS microstructures were prepared via a hot-injection process using the ionic liquid precursor (ILP) bis butylpyridinium tetrachloridocuprate(II), $[C_4Py]_2[CuCl_4]$, and bis (trimethylsilyl) sulfide (TMS) as the sulfur source. The CuS particle morphology, size, and the chemical composition are controlled by reaction time and temperature. The as-prepared CuS hierarchical flower-like powders show better catalytic performance and stability than natural enzymes[325] and existing CuS sensors.[326]

6.3. Experimental

6.3.1. Chemicals and Apparatus:

Chemicals: N-butylpyridinium chloride (Iolitec, 99%), bis (trimethylsilyl) sulfide (Sigma-Aldrich, 99%), $CuCl_2.2H_2O$ (Fluka, ≥ 99%), H_2O_2 (Sigma-Aldrich, 30%), NaH_2PO_4 (Sigma-Aldrich, ≥99%), $Na_2HPO_4.7H_2O$ (Sigma-Aldrich, ≥99.99%), and acetonitrile (Sigma-Aldrich, 99.8%) were used as received. All solutions were freshly prepared using deionized water (18.2 M MΩ cm^{-1}, Milli-Q, Millipore).

Apparatus: Sample morphology was investigated via scanning electron microscopy using a JEOL JSM-6510 operated at 15 kV. Samples were mounted on an aluminum stub with adhesive carbon tape and coated with 40 - 60 nm of Pd/Au in an SC7620 Mini Sputter Coater. Powder X-ray diffraction (XRD) was done on a PANalytical Empyrean with Bragg-Brentano geometry equipped with a PIXcel1D detector using Cu K_α radiation (λ = 1.5419 Å). The average crystallite sizes D were estimated using the Scherrer equation[327-328]

$$D = K \lambda / (\beta \cos \theta)$$

where K is the Scherrer constant (0.9), λ is the wavelength of X-ray radiation, β is the full-width-at-half-maximum of the (012) reflection, and θ is the position (peak maximum) of the reflection ($2\theta_{012}$ = 29.30°). The reflection at 29.30° was chosen for calculation of the crystallite size because it is well separated from other reflections.

Electrochemical analysis was done with a Gamry Potentiostat/Galvanostat using a conventional three-electrode glass cell at room temperature. A glassy carbon electrode

(GCE, 3 mm diameter), coiled Pt wire, and a saturated calomel electrode (SCE) served as working, counter, and reference electrode, respectively. Electrochemical impedance spectroscopy (EIS) measurements were carried out at -0.2 V (Nyquist plots were first determined at different potentials and -0.2 V was selected because the kinetic control region is best observed at -0.2 V) with a disturbance potential of 5 mV and a frequency range from 1 MHz to 0.1 Hz. The electrocatalytic performance of the as-prepared materials was investigated in 0.1 M phosphate buffer solutions purged with high-purity nitrogen for at least 40 minutes prior to the measurements to remove oxygen.

6.3.2. CuS Microstructures Synthesis and Electrode Fabrication

Preparation of CuS: The ILP $[C_4Py]_2[CuCl_4]$ was synthesized as reported previously.[289] In short, CuS nanoparticles were synthesized via hot-injection under argon as follows: 1 mmol (0.478 g) of $[C_4Py]_2[CuCl_4]$ was heated to 160 °C, then 1 mmol (0.211 mL) of $(TMS)_2S$ was rapidly added via a syringe. Upon injection, the color of the liquid immediately turned from orange to dark black; this color change was accompanied by the precipitation of CuS powder. The reaction mixture was vigorously stirred for 1 h at 160 °C and then allowed to cool to room temperature. After cooling, the CuS particles were isolated and purified by repeated washing/centrifugation cycles with deionized water and absolute ethanol. Finally, the CuS powders were dried under vacuum for 12 h at room temperature. CuS particles with different geometries and crystal structures were obtained by varying the reaction times (from 1 to 8 h) and reaction temperatures (from 120 to 200 °C).

Electrode Preparation: First, a GCE was mechanically cleaned using 0.05 μm alumina slurry with the help of a microcloth, then sonicated in nitric acid, absolute alcohol, and deionized water for 10 minutes each and then dried under a nitrogen stream. CuS-modified GCE electrodes were prepared by casting 10 μl of a CuS suspension (5 mg of CuS in 2 mL of isopropanol/ water mixture, 2:1) on the cleaned GCE surface. This surface was left in air to dry for 30 minutes before use.

6.4. Results

6.4.1. Morphology and Crystal Phase

The crystal structure and morphology of the as-prepared CuS particles were investigated by X-ray diffraction (XRD) and scanning electron microscopy (SEM) to correlate the synthesis parameters (reaction temperature and time) to the crystallography and morphology of the resulting CuS particles.

Effect of reaction temperature: CuS particles were synthesized at different reaction temperatures (120-200℃) using the same reaction time (1 h). Figures 6.1 and 6.2 show the corresponding SEM images and XRD patterns of the CuS particles, respectively. SEM images clearly show that the reaction temperature has a significant effect on the created morphology of the CuS particles: at 120 ℃, highly aggregated particles with irregular morphologies form. At 140 ℃, highly aggregated flake-like particles are observed. They form dense mats of interlaced elongated features resulting in rather large particles. As a result, it is difficult to determine the real average particle sizes, but the size of the primary rod- or flake like features is around 2 μm. At 160 ℃, hierarchically structured flower-like microstructures composed of intersecting nanoflakes are obtained. The primary building blocks (the flakes) are on the order of 1.5 μm and the aggregated microflowers have a diameter on the order of 2 μm. The shape of the spherical aggregates resembles desert roses with highly intertwined individual flake-like plates, although of course on a much smaller length scale.

Higher reaction temperatures of 170 ℃ yield particles with a rather diverse set of morphologies: some of the features are quite similar to the morphologies observed in the obtained materials synthesized at 140 or 160 ℃, while others resemble ZnO particles with a "stack of pancakes" morphology.[329] Moreover, SEM data of these samples suggest that the larger, roughly spherical particles are indeed aggregates of plate-like rather than rod-like particles. Finally, the sizes of the aggregates appear larger (on the order of 4 μm) and also appear to have a larger size distribution. Again, this is difficult to determine because of the high degree of aggregation in these materials.

Even higher reaction temperatures of 180 °C produce particles with different morphologies, mainly flower-like microstructures, similar to the ones produced at 160 °C. Moreover, ball-like microstructures with a diameter around 3 μm are also observed. At 200 °C, the "stack of pancakes" morphology is observed again with the objects having a similar dimension as before. However, the material shows much lower degree of morphological order and uniformity than the materials made at lower temperature.
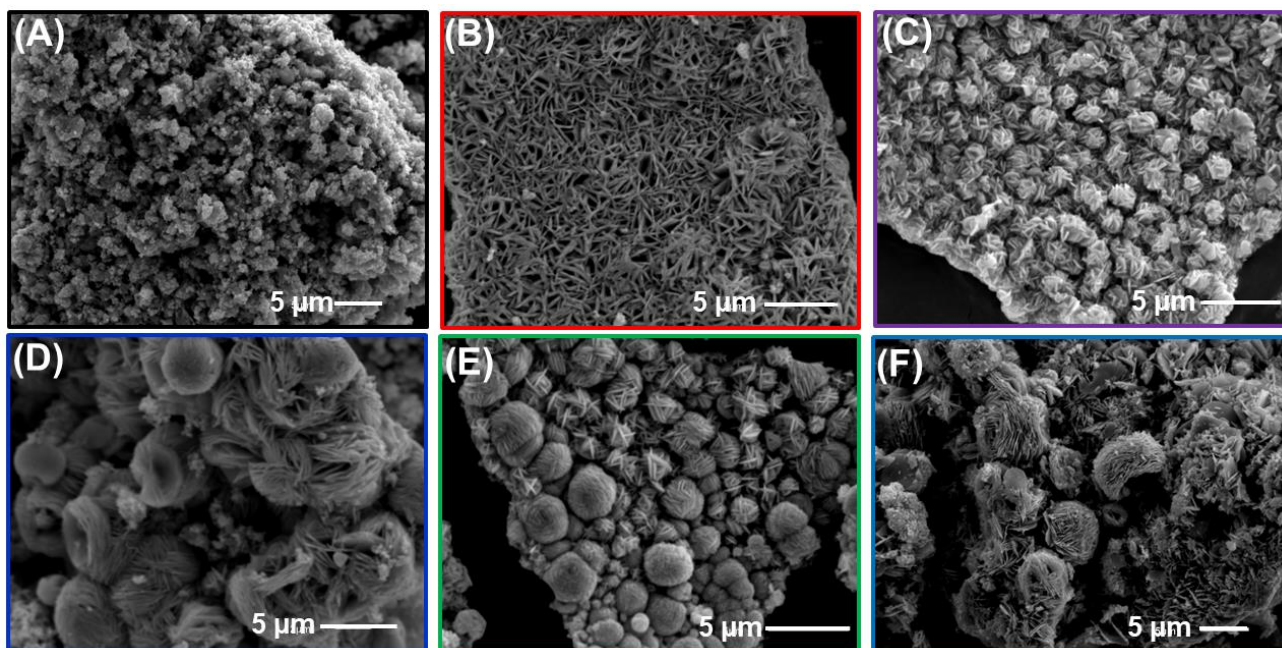
Figure 6.1. SEM images of CuS particles synthesized at different reaction temperatures. (A) 120 ℃, (B) 140 ℃, (C) 160 ℃, (D) 170 ℃, (E) 180 ℃, and (F) 200 ℃ using a constant reaction time of 1 h.

Covellite (CuS) structure has a rich atomic environment consisting of Cu-S layers linked together by S-S covalent bonds. Every Cu-S layer consisting of a triangular CuS_3 layer which is sandwiched between two layers of tetrahedral CuS_4, as shown in Figure 6.2(A). Figure 6.2(B) shows the corresponding XRD patterns of the CuS particles. All samples exhibit reflections that can be indexed to the hexagonal phase of the covellite (CuS) structure ($P6_3/mmc$, primitive hexagonal unit cell with a = b = 3.7900 and c = 16.3400 Å, JCPDS 98-002-6968). However, the products obtained at 120 and 140 °C show additional reflections at 2θ = 15 – 25 °, which are assigned to impurities (copper sulfate hydrate, $CuSo_4.5H_2O$, JCPDS 00-011-0646). At 160 °C, the XRD pattern can be indexed as pure hexagonal CuS. The presence of a strong and sharp (110) reflection suggests the presence of a preferred orientation of the CuS powders. Particles prepared at 170 and 180 ℃ display additional reflections assigned to $Cu_{2-x}S$ besides the CuS hexagonal phase reflections. The XRD results are in good agreement with literature[330-331], where many studies report the reversible transformation between covellite CuS and $Cu_{2-x}S$ at 160 ℃ ≤ T ≤ 180 ℃, while only CuS is present at lower (T ≤ 160 ℃) and higher (T ≥ 180 ℃) temperatures.

With a further increase to 200 ℃, the XRD patterns of the corresponding products can be indexed as pure hexagonal CuS (JCPDS 98-002-6968) again, consistent with literature.[330-331] Concluding from the XRD data, especially the samples grown at 160 ℃ are pure CuS with

a high crystallinity suggesting that these materials would be good candidates for further investigation because they are uniform both on a crystallographic and morphological level. The crystallite size obtained from Scherrer´s equation of these materials is 25 nm (see experimental part for details).
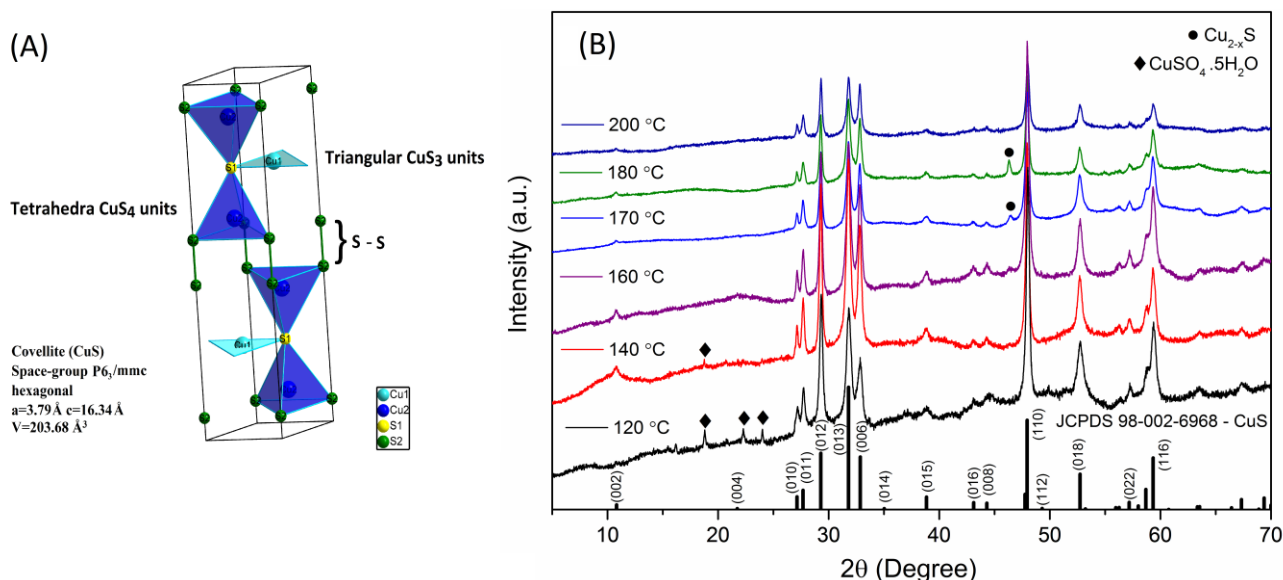
Figure 6.2. (A) Structure of covellite CuS. Adapted from Evans et al. "Crystal structure refinement of covellite." Am. Mineral 61.9-10 (1976): 996-1000.[332] (B) XRD patterns of CuS particles prepared at different temperatures (same color code as in Figure 6.1).

Effect of reaction time: Figure 6.3 shows SEM images of CuS microstructures prepared using various reaction times at constant synthesis temperature of 160 ℃. A reaction temperature of 160 ℃ was selected because the experiments shown above demonstrate that at 160 ℃ produces the most clearly defined particle morphologies. Overall, the particles resemble desert roses composed of intersected micrometer-sized flakes (Figure 6.3(A)), although they are on a different size scale than true desert roses. SEM clearly shows that the reaction time has a significant effect on particle morphologies as well as the individual flake sizes. The size distribution of the flakes and the aggregates appears rather narrow, but as the individual particles are highly aggregated, an exact determination of the size distribution is difficult.

Longer reaction times change the morphologies of the precipitates. Reaction times of 4 h result in larger, quite densely aggregated and strongly intertwined flake-based ball-like objects with diameters of 2 - 2.5 μm and flakes size of around 1 μm (Figure 6.3(B)). Increasing the reaction time to 6 h results in the formation of chrysanthemum-like structures with particle sizes between 4 – 5 μm and flake sizes of around 1 μm (Figure 6.3(C)). Finally, the

hierarchical flower-like structures obtained after 8 h of reaction seem to be composed of well-assembled and closely packed CuS flakes. The particle diameter is around 5 - 5.5 μm with sizes of the individual flakes around 1 μm (Figure 6.3(D)). Overall, SEM thus suggests that the individual building blocks (i.e., the flakes) remain roughly the same, but the aggregation of these individual flakes is strongly affected by the reaction temperature.
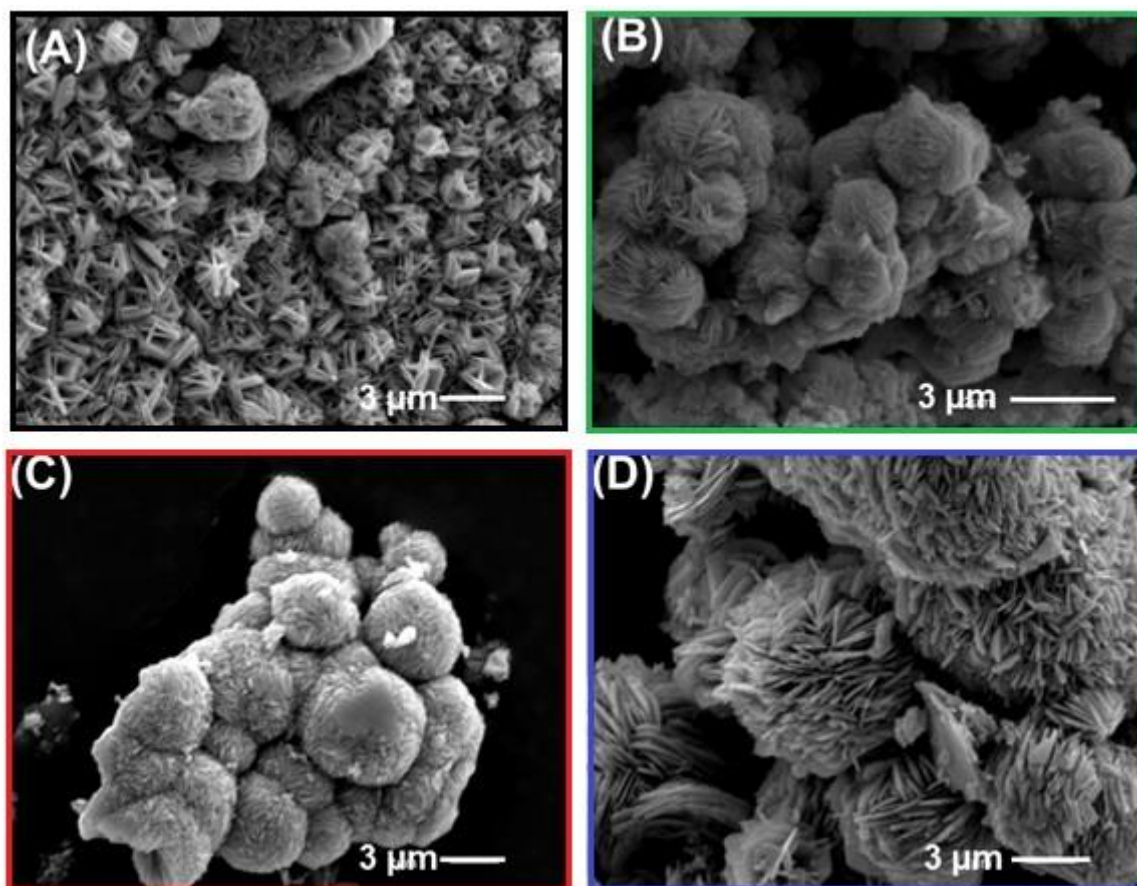
Figure 6.3. SEM images of CuS particles obtained at 160 ℃ after various reaction times; (A) 1 h, (B) 4 h, (C) 6 h, and (D) 8 h.

It is worth to mention that all the CuS structures obtained at different reaction times exhibit the same XRD patterns indicating the formation of hexagonal covellite (Figure 6.4). This confirms the main role of the reaction temperature and time in the assembly of the CuS nanoflakes into different morphologies and less on the crystal structure.
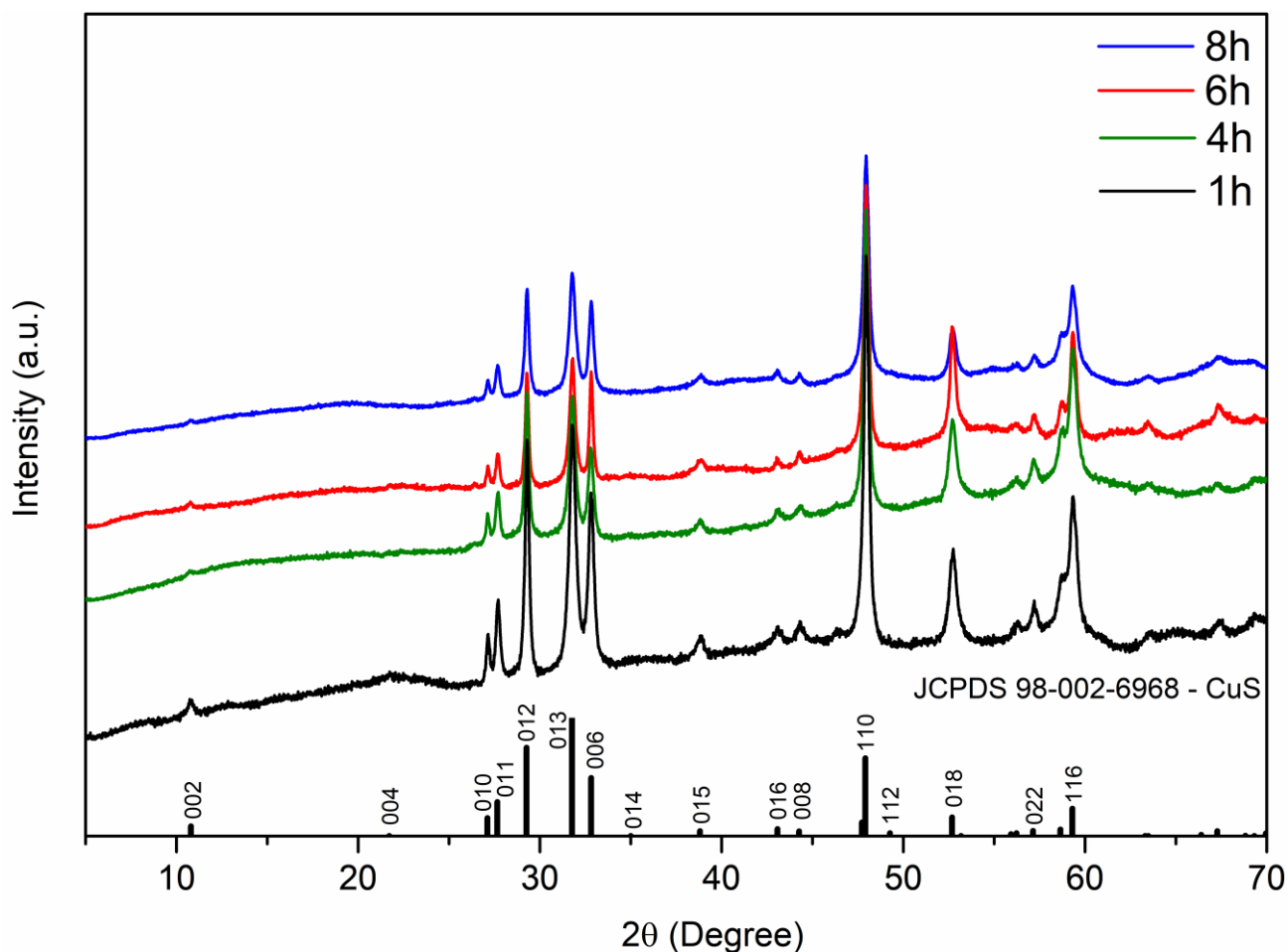
Figure 6.4. XRD patterns of CuS particles prepared at different reaction time (same color code as in Figure 6.3).

6.4.2. Sensor Performance in Nonenzymatic H_2O_2 Detection

The electrocatalytic performance of the as-prepared CuS microstructures towards electrochemical sensing of H_2O_2 was investigated and compared to some of the best H_2O_2 electrochemical sensors currently available (Table 6.1). Figure 6.5 shows cyclic voltammograms (CVs) obtained from glassy carbon (GC) electrodes modified with CuS with irregular (CuS$_{irregular}$, created at 120 ℃ for 1 h, Figure 6.1(A)), intersected nanoflakes (denoted as CuS$_{nanoflakes}$, obtained at 160 ℃ for 1 h, Figure 6.1(C)), and hierarchical flower-like (CuS$_{flower}$, obtained at 160 ℃ for 8 h, Figure 6.3(D)) morphologies. Data obtained in the absence (dashed lines) and presence (solid lines) of 2 mM H_2O_2 in 0.1 M PBS are shown. In neat PBS (no H_2O_2), all electrodes exhibit a redox peak couple around -0.25 V and 0.0 V attributed to the Cu_2S/CuS redox couple transformation (analogous to the Cu_2O/CuO transformation), see Inset I of Figure 6.5.[169]

To understand the charge transport features, CVs of all CuS-modified GC electrodes were recorded in PBS at various scan rates (data not shown)[1]. The anodic and cathodic peak currents increase linearly with the scan rate up to 0.3 $V\ s^{-1}$, while the peak potential remains essentially constant with increasing scan rates. This indicates that the Cu_2S/CuS redox transformation is a surface-confined process. It also suggests that the CuS microstructures have a favorable electrochemical reactivity and exhibit fast electron transfer kinetics[169].

The addition of 2 mM of H_2O_2 results in a significant increase of the reduction current attributed to H_2O_2 electroreduction (Figure 6.5). The CuS_{flower}-modified GC electrodes show outstanding activity compared to that of the $CuS_{irregular}$ and $CuS_{nanoflakes}$-modified GC electrodes. This is demonstrated by the substantial positive shift of the onset potential along with the much higher current density of the H_2O_2 reduction. That is, the CuS_{flower}/GC electrode exhibits a 10 and 5 times, respectively, higher electrocatalytic activity for H_2O_2 reduction compared to $CuS_{irregular}$/GC and $CuS_{nanoflakes}$ electrodes. This substantial enhancement of the CuS_{flower}/GC electrode towards H_2O_2 reduction is attributed to its unique flower-like morphology providing a higher number of active surface sites and a facilitating charge transfer during H_2O_2 reduction. Moreover, the CuS_{flower}/GC electrode shows 6 and 3 times higher electrochemically active surface area compared to that of the $CuS_{irregular}$/GC and $CuS_{nanoflakes}$ electrodes as estimated from chronocoulometry via the Anson equation.[333]

Figure 6.5. CVs measured at $CuS_{irregular}$ (black-lines), $CuS_{nanoflakes}$ (red-lines) and CuS_{flower} (green-lines) modified GC electrodes in 0.1 M PBS (pH~7.4) in the absence (dashed lines) and presence of 2 mM H_2O_2 with scan rate of 20 mV s^{-1}. Insets show (I) Zoom of the CuS_{flower} in the blank PBS (in the absence of H_2O_2) and (II) current transients (i-t, stability test) obtained at CuS_{flower} (green-line) and $CuS_{irregular}$ (black-line) modified GC electrodes in 0.1 M PBS containing 2 mM H_2O_2 at -0.3 V vs. SCE.

The inset II of Figure 6.5 shows the current transient curves (*i-t*, stability test) of the CuS_{flower}/GC and $CuS_{irregular}$/GC electrodes measured in 0.1 M PBS (*pH*~7.4) containing 2 mM H_2O_2 at -0.3 V vs. SCE. The $CuS_{irregular}$/GC electrode catalytic stability rapidly decreases with time and is reduced by about 57% after 5 h of continuous H_2O_2 electroreduction. The catalytic activity of the CuS_{flower}/GC electrode is only reduced by 2.5% confirming a higher electrochemical stability of the CuS flower-like structures. The rather noisy signal in these curves is attributed to the accumulation and detachment of in-situ generated oxygen bubbles from H_2O_2 reduction, similar to an existing example, where a higher bubble accumulation rate and larger bubble size in combination with a lower bubble dislodge rate result in a faster degradation/deactivation of silver-based nanostructured catalysts performance in H_2O_2 electrosensing.[280]

In this regard, the rate of in-situ formed oxygen bubbles accumulation and dislodge as well as their size on the various CuS microstructures were examined. Interestingly, the CuS_{flower}/GC electrode shows an about 8 times smaller bubble size and 17 times higher bubble detachment rate compared to the $CuS_{irregular}$/GC electrode. This quite strong influence on both the bubble size and detachment rate could be a reason for the higher stability of the CuS_{flower}/GC electrode compared to the $CuS_{irregular}$/GC electrode.

It is worth to mention here that the electrochemically active surface area of the CuS_{flower} and $CuS_{nanoflakes}$ electrodes increases by factor of ca. 6 and 2, while their electrocatalytic activities improve by factors of ca. 10 and 4.5 compared to that of $CuS_{irregular}$, respectively. This suggests that the observed efficiency improvement of the CuS flower- and nanoflake-like structures cannot only be attributed to their higher electroactive surface area, but also to other factors. For example, the morphology may play an important role in the observed enhancement. This is indeed confirmed by the respective Nyquist plots obtained from measurements in 0.1 PBS containing 2 mM H_2O_2 at -0.2 V vs. SCE in order to examine their charge transfer resistances toward H_2O_2 electroreduction (Figure 6.6). As shown in this figure, the CuS_{flower}-based electrode exhibits a lower charge transfer resistance (~0.28 kΩ) compared to that of the $CuS_{nanoflakes}$ (~0.59 kΩ) and $CuS_{irregular}$ (~1.2 kΩ). This indicates that the CuS flower-structures have a 4 and 2 times lower charge transfer resistance for H_2O_2 electroreduction compared to CuS with irregular- and nanoflakes-like structures. These data demonstrate that indeed the morphology is a decisive factor favoring the outstanding activity of the CuS flower-like structures for H_2O_2 reduction.
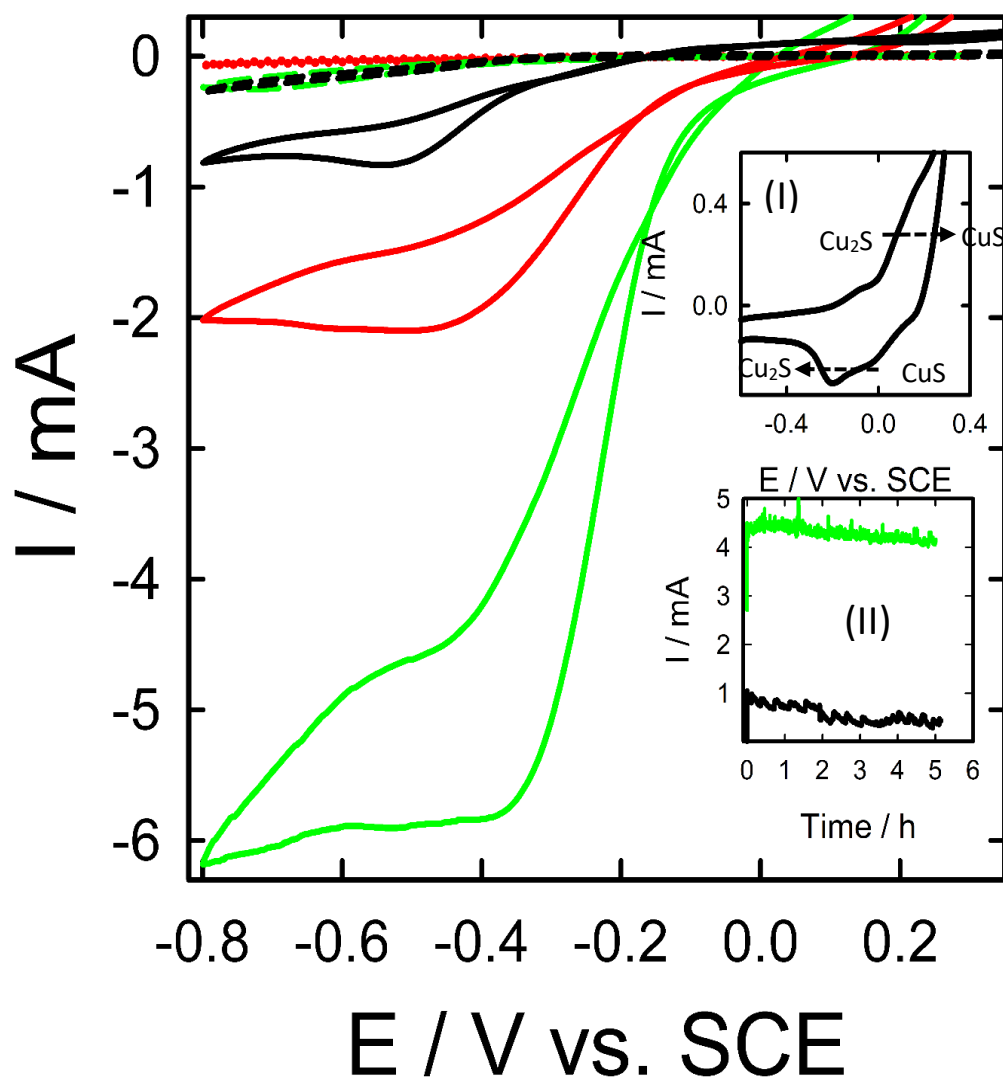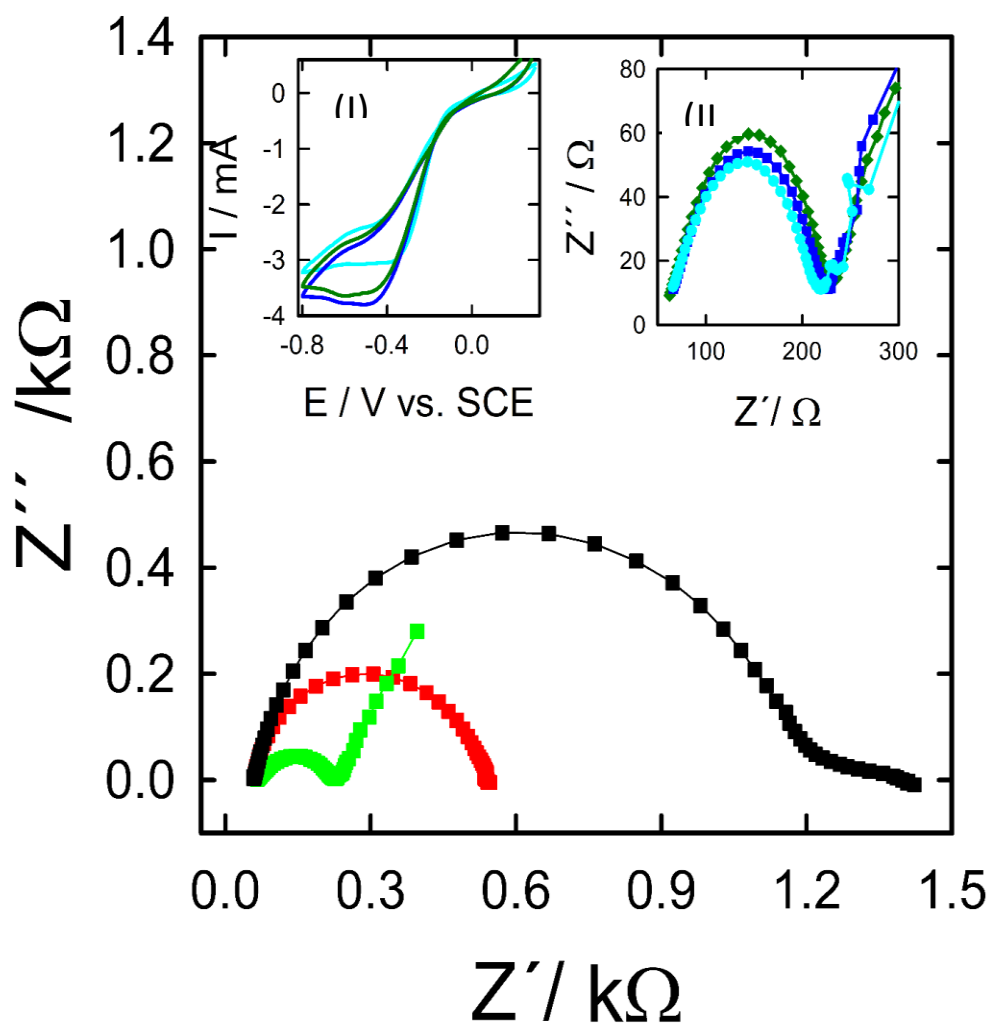
Figure 6.6. Nyquist plots obtained at CuS$_{irregular}$ (black-lines), CuS$_{nanoflakes}$ (red-lines) and CuS$_{flower}$ (green-lines) modified GC electrodes in 0.1 M PBS (*pH*~7.4) containing of 2 mM H_2O_2 at -0.2 V vs. SCE (same color coding as in Figure 6.5). Insets show (I) CVs and (II) their respective Nyquist plots obtained at CuS$_{flower}$ modified GC electrode in the above-mentioned solution after 1 (cyan-lines), 7 (blue-lines) and 10 (green-lines) days. (Same color coding as in Figure 6.5)

Furthermore, the ageing (long-term performance) effect on the electrocatalytic activity of the CuS$_{flower}$ structures for H_2O_2 electroreduction was investigated from their CVs (Inset I of Figure 6.6) and their respective Nyquist plots (Inset II of Figure 6.6) in 0.1 PBS containing 1 mM H_2O_2 after ageing for 1, 7 and 10 days in the above-mentioned solution. As revealed in these figures, neither the activity (onset potential and current intensity) nor the charge transfer resistance of the CuS$_{flower}$ towards H_2O_2 electroreduction is significantly affected at longer operation times; this proves the high durability of the CuS$_{flower}$ materials.

The electrochemical sensing performance with respect to selectivity, durability, and sensitivity of the as-prepared CuS microstructures for H_2O_2 detection was also examined

by amperometry. Figure 6.7(A) displays the sensitivity test of the CuS with irregular-, nanoflakes-, and flowerlike structures. The data clearly show that the CuS_{flower} structures exhibit the best H_2O_2 electrochemical sensing efficiency as evaluated by their higher sensitivity with a rapid response time (3.82 mM mA^{-1} cm^{-2}, 48 times higher) and lower detection limit (0.1 μM, 18 times lower) than the $CuS_{irregular}$ structures. Additionally, the CuS_{flower}-based sensor exhibited superior or comparable performance as H_2O_2 sensor to that of the commercial enzymatic and non-enzymatic sensors, Table 6.1. At the moment, we assign these enhancements to the unique CuS flower-like morphology with high electrochemical active surface area and a lower H_2O_2 reduction charge transfer resistance as demonstrated from impedance investigation, see Figure 6.6.

The interference-tolerance of the as-prepared CuS structures for the common electroactive interfering species, including ascorbic acid, urea, glucose, and uric acid is illustrated in Figure 6.7(B). All CuS-modified GC electrodes exhibit a clear amperometric response with the addition of 1 mM H_2O_2, while the successive addition of the aforementioned interfering species only exhibits very small amperometric current responses on the CuS microstructures. This indicates a high selectivity of the CuS-modified electrodes for H_2O_2. Interestingly, the CuS_{flower} sensors exhibit nearly the same amperometric response of the first H_2O_2 addition after the second H_2O_2 addition in the presence of the above-mentioned interfering substances. On the other hand, CuS with irregular- and nanoflakes-like structures only show 20% and 15% of their original amperometric response. This demonstrates a much higher durability and interference tolerance of the flower-shaped CuS microstructures compared to the irregular and nanoflake-like structures.
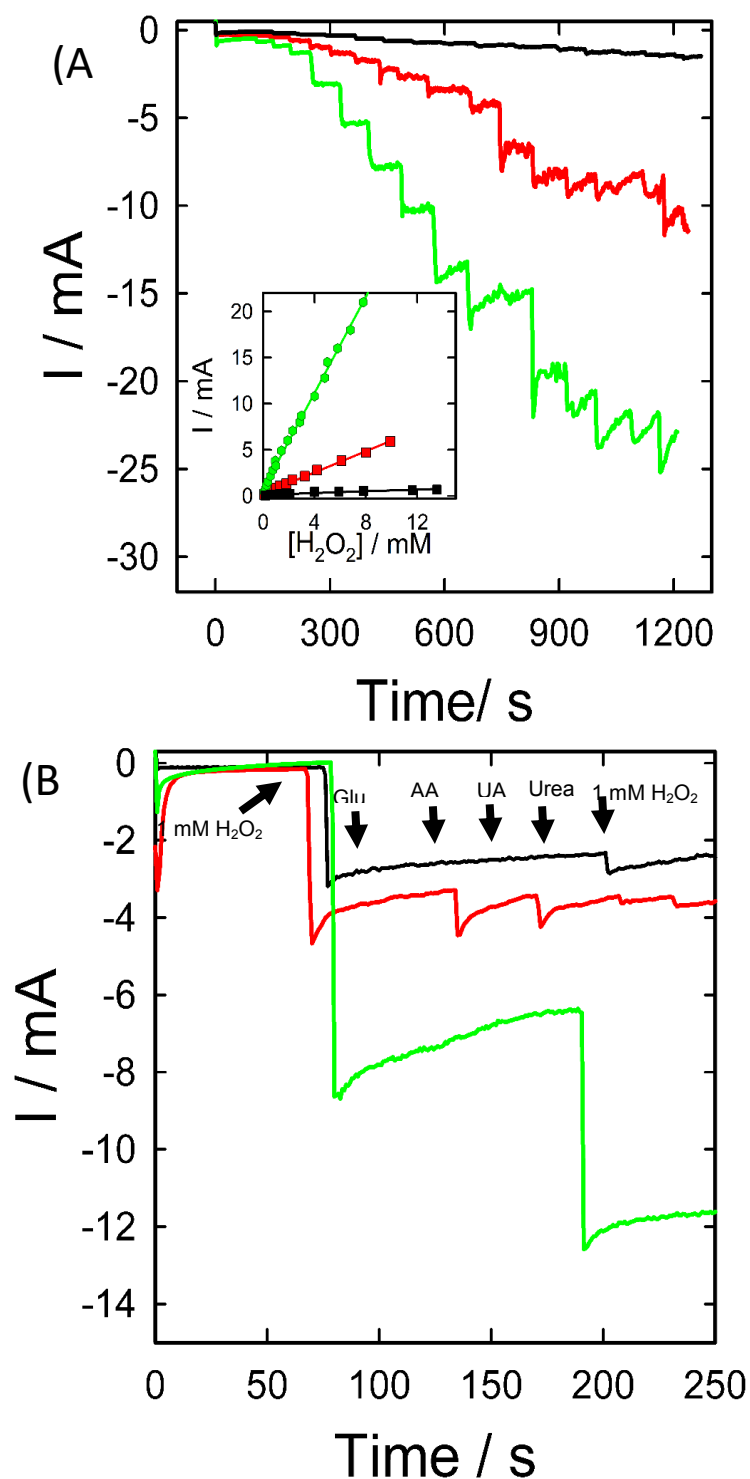
Figure 6.7. (A) Amperometric response (sensitivity test) obtained at CuS microstructures with irregular- (black-lines), nanorod- (red-lines) and flower- (green-lines) like structures with successive addition of H_2O_2 in N_2-saturated 0.1 M PBS measured at -0.4 V. The inset shows the stepwise increase in the concentrations, which results in the stepwise response of the current (mA), same colors code as in Figure 6.5. (B) Amperometric response (selectivity test) of the same electrodes after adding 1 mM H_2O_2, 0.1 mM ascorbic acid (AA), glucose (Glu), uric acid (UA) and Urea, respectively (same colors code as in Figure 6.7(A).

Table 6.1. Comparison of amperometric response parameters of CuS/GC with previously published non-enzymatic H_2O_2 sensors

Sensors	Sensitivity (mA mM^{-1}cm^{-2})	Detection limit (μM)	Linear range (mM)	References
CuS/RGO/GC	-	0.27	0.005-1.5	[169]
CdS/GC	0.00099	0.28	0.001-1.9	[169]
Ag$_{ball}$/GCE	0.022	1.8	Up to 14	[280]
Ag$_{lily-flower}$/GCE	0.480	1.0	Up to 14	[280]
Cu$_2$O/GNs	0.0024	20.8	0.3-7.8	[334]
CuS/GC	0.0629	1.1	0.01-1.9	[335]
FeS/GC	0.0085	4.3	0.005- 0.14	[336]
HRP	0.0128	1.6	0.004-1.0	[337]
CuS$_{irregular}$/GCE	0.068	1.8	Up to 13	This work
CuS$_{nanoflakes}$/GCE	0.856	0.4	Up to 11	This work
CuS$_{flowers}$/GCE	3.82	0.1	Up to 8	This work

Chapter 7

CuS nanoplates from ionic liquid precursors – Application in organic photovoltaic cells

7.1. Abstract

Hexagonal p-type semiconductor CuS nanoplates were synthesized via a hot injection method from bis(trimethylsilyl)sulfide and the ionic liquid precursor bis(*N*-dodecylpyridinium) tetrachloridocuprate(II). The particles have a broad size distribution with diameters between 30 and 680 nm and well-developed crystal habits. The nanoplates were successfully incorporated into organic photovoltaic (OPV) cells as hole conduction materials. The power conversion efficiency of OPV cells fabricated with the nanoplates is 16% higher than that of a control device fabricated without the nanoplates.

7.2. Introduction

Semiconductor nanoparticles (NPs) have attracted tremendous attention for countless applications. This is mainly due to their unique properties arising from size-dependent quantum confinement effects.[338-339] Moreover, their nanometer dimensions generate a much higher surface area-to-volume ratio, which provides enhanced interaction between the NPs and the surrounding material.[326] Among others, metal chalcogenide NPs such as ZnS,[340] CuS,[183] $CuIn(Se,S)_2$,[341-342] $CuInGa(Se,S)_2$,[343-344] and $Cu_2ZnSn(Se,S)_4$[345-346] have been used to improve the optoelectronic properties of solar cells or light emitters.[192, 347-352] For example, CuS, a p-type semiconductor, has been investigated for its application in ultraviolet (UV) photodetectors and organic photovoltaic (OPV) cells.[165, 167, 353-357]

One of the issues in the development of such devices is the design of NPs suitable for these applications. While the precipitation of metal sulfide NPs can be achieved via numerous processes, the detailed control over the NP shapes, sizes, size distributions, crystal phase, crystal phase homogeneity, and possible doping is not straightforward.[154, 358] This particularly applies to the *a priori* design of their electronic and optical properties.[154, 359] New approaches towards a rational and reliable a priori design of metal chalcogenide NPs are therefore highly sought after.

Among others, ionic liquids (ILs) have shown potential for nanomaterials design and NP tuning[4, 69] Of relevance to the current study, we have previously introduced the concept of ionic liquid precursors (ILPs) for nanomaterials synthesis, where the IL acts as solvent-template-reactant and provides access to materials that are difficult to synthesize otherwise.[48-49, 268]

The work reported here is rooted in the ILP concept and describes the synthesis of hexagonal CuS nanoplates (CNPs) synthesized via hot-injection from bis(*N*-dodecylpyridinium) tetrachloridocuprate(II), $[C_{12}Py]_2[CuCl_4]$,[263, 268] and bis(trimethylsilyl)sulfide, (TMS)$_2$S. The resulting particles were evaluated as hole transport materials in bulk hetero-junction (BHJ) OPV cells based on poly(3-hexylthiophene): phenyl-C61-butyric acid methyl ester (P3HT:PCBM) active layer blends. The hole transport (hole collection) properties of CuS in OPV cells have already been demonstrated for single CuS anode buffer layers.[357] In spite of this, relatively few studies on such systems are available, and these studies were performed only with a conventional device structure.[355-356]

Here, the effects of the CNP on OPV cell performance were investigated by embedding the NPs in the P3HT:PCBM active layer blends for both conventional and inverted structures. CNPs in the active layer blends provide a broad optical absorption window and improve the charge transport.[360-361] The hole collection process strongly depends on film preparation and film homogeneity, and the CNPs are viable candidates for the fabrication of new hybrid OPV cells.

7.3. Experimental

7.3.1. Materials

N-dodecylpyridinium chloride (Aldrich, $\geq$ 98%), $CuCl_2 \cdot 2H_2O$ (Fluka, $\geq$ 99%), acetonitrile (Aldrich, 99.8%), (TMS)$_2$S (Aldrich, 99%), oleylamine (OAm) (Aldrich , 98%), zinc acetate dihydrate (Aldrich, 99%), tetramethylammonium hydroxide pentahydrate (TMAH) (Aldrich, 97%), poly(3,4-ethylenedioxythiophene):poly(styrenesulfonate) (PEDOT:PSS) (Heraeus, Clevios P VP AI4083, aqueous dispersion with 1.3–1.7 wt. %), poly(3-hexylthiophene) (P3HT) (Aldrich, 90%), phenyl-C61-butyric acid methyl ester (PCBM) (Solenne BV, 99.0%), Ca (Aldrich, 99.0%), Ag (Umicore, 99.9%), MoO_3 (Aldrich, 99.99%), ethanol (Rotisolv, 99.8%), dimethyl sulfoxide (DMSO) (Merck, 99%), 1-butanol (Chemsolute, 99.5%), chlorobenzene (CHB) (Aldrich, anhydrous, 99.8%), 2-methoxyethanol (2ME) (Aldrich, 99.5%), ethanolamine

(FLUKA 99%), n-hexane (Rotisolv, 96%), toluene (Chemsolute, 99.5%), tetrachloroethylene (TCE) (Aldrich, 99%), hydrophobic filters (Rotilabo, PTFE 5 μm, 1 μm, 0.2 μm, and 0.45 μm), and hydrophilic filters (Rotilabo, nylon 0.2 μm) were used as received.

7.3.2. Synthesis of CNPs

The ILP $[C_{12}Py]_2[CuCl_4]$ was prepared according to Refs.[263, 268] CNPs were synthesized via hot-injection under argon. First 4 mmol of $[C_{12}Py]_2[CuCl_4]$ were heated to 120 °C. Then 4 mmol of (TMS)$_2$S were added in one step with a syringe, and the reaction was allowed to proceed for 4 h at 120 °C. After cooling to room temperature, the dark solid products were collected by centrifugation, washed several times with absolute ethanol, and dried in a vacuum oven at room temperature for 12 h.

7.3.3. Stabilization and redispersion of CNPs

For the fabrication of OPV cells, the CNPs were capped with OAm ligands according to Ref.[165] 10 mg of dry CNPs was dispersed in 2 mL of DMSO, then 2 mL of OAm was added at room temperature. The mixture was gently shaken by hand for 60 s. Upon standing at room temperature, a two-phase system formed and the CNPs transferred to the OAm phase as indicated by the dark color of the upper phase. Finally, the OAm-capped NPs were washed once with 26 mL of ethanol and dried under vacuum for 24 h at room temperature.

7.3.4. Synthesis of ZnO NPs

ZnO NPs were synthesized according to a procedure modified from refs.[362-363] First, 5.5 mmol of zinc acetate dihydrate were dissolved in 80 mL of 2ME. Then 10 mmol of TMAH dissolved in 8 mL of 2ME were added dropwise to the zinc acetate solution over 10 min followed by the addition of 1.6 mL of ethanolamine. The ZnO NPs were precipitated by addition of toluene (176 mL) and hexane (80 mL), and centrifugation. 1/3 of the toluene was added first to the solution followed by adding 1/3 of hexane. This was repeated three times upon which the solution turned turbid. After centrifugation and decantation of the supernatant, the ZnO NPs were redispersed in 1-butanol (22 mL, ca. 1.4 wt. % of ZnO). Synthesis and washing were done at ambient conditions.

7.3.5. Device fabrication

Eight types of OPV cells containing different active layers and device structures were built. Devices A, B, E, F, G, and H were designed with a conventional device structure (i.e., ITO/PEDOT:PSS/P3HT:PCBM:CuS/Ca/Ag). Devices C and D were designed with an

inverted device structure (i.e., ITO/ZnO/P3HT:PCBM:CuS/Ag). All devices were fabricated on indium tin oxide (ITO) glass substrates cleaned in an ultrasonic bath with 2 vol. % Hellmanex III solution.

Hole collection layer (HCL): PEDOT:PSS solution (1.3–1.7 wt. %) was filtered through a hydrophilic membrane filter with 0.2 μm pore size and spin-coated at 3000 rpm for 30 s onto the ITO glass substrate followed by drying at 120 °C for 15 min.

Electron transport layer (ETL): ZnO NPs dispersed in 1-butanol (1.4 wt. %) were filtered with a hydrophobic membrane filter with 0.2 μm pore size and spin-coated at 2000 rpm for 30 s onto the ITO glass substrate followed by drying at 180 °C for 15 min.

Active layer: For active layer deposition, a mixture of P3HT:PCBM:CuS with a different blending weight ratio in CHB and a total concentration of 54 mg/mL was stirred at 75 °C for 12 h. A P3HT:PCBM:CuS ratio of 1:1:0.1 was applied in the cases of the devices A, B, C, and D. In addition, ratios of 1:0.8:0.1, 1:0.8:0.2, and 1:0.8:0.3 were applied for optimizing the conventional OPV cells (i.e., devices E, F, G, and H). The solution was filtered through a hydrophobic membrane filter with different pore sizes (0.45 or 0.2 μm), spin-coated at 1500–1850 rpm for 30 s, and dried at 120 °C for 15 min to form an approximately 200 nm thick active layer. The active pixel area of 4 mm^2 was defined with the passivation layer pre-patterned on top of the ITO glass.

Top electrode: 30 nm/150 nm of Ca/Ag for conventional and 150 nm of Ag for inverted devices were deposited by thermal evaporation in a high vacuum chamber (3 × 10^{-6} torr).

7.3.6. Characterization

Powder X-ray diffraction (XRD) data were collected on a PANalytical Empyrean powder X-ray diffractometer with Bragg-Brentano geometry, equipped with a PIXcel1D detector using Cu Kα radiation (λ = 1.5419 Å) and operating at 40 kV and 40 mA. Theta-theta scans were run during 190 min over a 2θ range of 4–70° with a step size of 0.0131° and a sample rotation time of 1 s. For fluorescence reduction, the PHD Level of the detector was set to 45–80.

Transmission electron microscopy (TEM) images were acquired on a Philips CM 200 instrument with a LaB_6 cathode operated at 200 kV. TEM samples were prepared by drop-casting the CNP dispersion on a carbon-coated Cu grid. The diameter of the CNPs was determined from the TEM images using the ImageJ software.

Ultraviolet (UV)–visible (vis)–near infrared (NIR) absorption spectroscopy data were acquired with a PerkinElmer Lambda 19 spectrometer with a scan step of 1 nm between 300 and 2500 nm. The UV–vis–NIR absorption of CNPs in CHB and TCE (i.e., for NIR measurement) was determined from NP dispersions with a concentration of 0.1 mg/mL. Absorption spectra of P3HT:PBMB:CuS active films were measured with the samples deposited on ITO glass by the same process applied in device preparation. The bandgap of the CNPs was determined from Tauc-plots drawn from the absorption spectrum. According to Tauc, the dependence of the absorption coefficient α on the photon energy $h\nu$ for near-edge optical absorption in semiconductors is

$$(\alpha h\nu)^{1/m}=k(h\nu-E_g) \qquad\qquad (1)$$

where E_g is the optical band gap, k is a constant, m is a number which relates to the mechanism of the transmission process, and m = *1/2 or 3/2* for direct allowed or direct forbidden transitions while m = *2 or 3* for indirect allowed or indirect forbidden transitions, respectively. Since the CNPs have a directly allowed transition, *(αhν)²* was plotted versus $h\nu$. The direct bandgap of the CNPs was obtained by extrapolation of the linear part to the zero of the ordinate.[42,43]

Fourier transform infrared (FTIR) spectroscopy was done on a NEXUS 6700 FT-IR spectrometer (Thermo-Nicolet, Diamond). Attenuated total reflection (ATR) correction was done via Omnic 6.2 (Thermo Fischer Scientific, Germany). Spectra were recorded between 4000–400 cm^{-1} with a resolution of 4 cm^{-1} and 32 scans per spectrum.

UV-photoelectron spectroscopy (PESA, Riken Keiki AC-2) to measure ionization energy (IE), which corresponds to the valence band maximum (VBM), was done with CNP thin films deposited on a glass substrate. UV intensity was 300 nW, and energy step was 0.1 eV. Measurements were done in air.

Atomic force microscopy (AFM) was done on a Nanosurf Easyscan-2 (cantilever ACLA-20, n-type silicon, spring constant 36–90 N/m, scan size of 5 × 5 μm). Roughness values in the article are averages obtained from three randomly selected scan regions per sample.

Contact profilometry to determine the film thicknesses was done with Veeco Dektak 150 with the vertical bit resolution of 1 Å and a stylus radius of 12.5 μm.

Characterization of OPV cells: Current density-voltage (J-V) data were measured under nitrogen using a Keithley 2400 source meter in the dark or with 100 mW/cm^2 of simulated solar irradiation (AM 1.5G, K.H Steuernagel light source). A silicon reference diode with a KG3 filter calibrated at Fraunhofer ISE was used to adjust the light intensity prior to the measurements. Open-circuit voltage (V_{oc}), short-circuit current density (J_{sc}), fill factor (FF), and power conversion efficiency ($PCE = J_{sc} \times V_{oc} \times FF / P_{in}$, where P_{in} is the incident optical power) were calculated from the J-V curve.

7.4. Results

7.4.1. CuS nanoplates (CNPs)

The synthesis produced 260 mg of CNPs in powder form, which corresponds to a yield of 68%. Figure 7.1(a), 7.1(c), and 7.1(d) show powder XRD and TEM data of the hexagonal CNPs obtained by the reaction of $[C_{12}Py]_2[CuCl_4]$ and $(TMS)_2S$. The reflections in the XRD patterns are broad, indicating nanocrystalline products.[364] The XRD pattern can be assigned to hexagonal covellite (ICDD 98-006-3327). TEM confirms the formation of hexagonal NPs. The particles are hexagonal plates with a broad diameter distribution ranging from 30 to 680 nm. TEM shows that the particles are rather thin at only 4-20 nm; this can be seen from TEM images showing particles standing upright on the TEM grid. Finally, the line patterns that are visible in Figure 7.1(d) are Moiré patterns arising from overlapping particles with a slightly different crystal orientation. These patterns prove the high level of crystallinity in the NPs.[365]

Figure.7.1b shows UV–vis–NIR spectroscopy of as-prepared CNPs dispersed in TCE. TCE is a good dispersant for measurements in the NIR because it does not show an absorption in this range. The spectra demonstrate that the CNPs have a very broad absorption spanning the entire UV–vis–NIR range. This is in a good agreement with previous data.[366] The absorption spectrum of as-prepared CNPs shows a strong absorption below

550 nm with a shoulder around 420 nm. This shoulder, the lowest energy exciton transition peak of CuS, is blue-shifted compared to bulk CuS (490 nm) due to the quantum confinement effects of the smaller particle size.[367] Moreover, the spectrum shows a strong and very broad absorption in the near infrared region originating from the localized surface plasmon resonance of CNPs.[368-369]
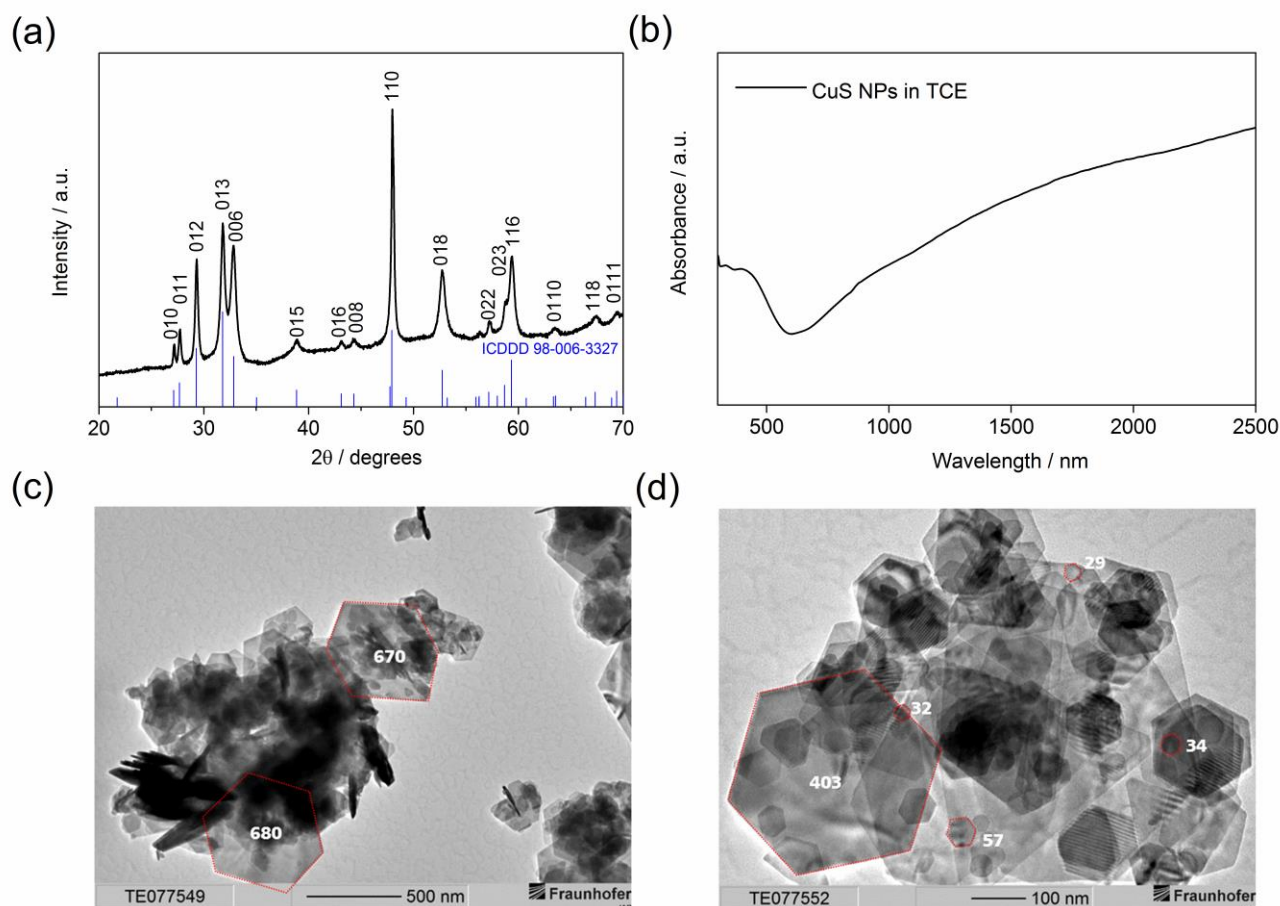
Figure 7.1. (a) XRD pattern of CNPs. The blue bars indicate the positions of the reflections from the hexagonal phase CuS from the International Centre for Diffraction Data (ICDD 98-006-3327) (b) UV–vis–NIR spectrum of CNP dispersion (0.1 mg/mL dispersion in TCE). [(c) and (d)] TEM images of CNPs. The red lines in the TEM images highlight the geometry of individual hexagonal particles. The numbers on individual NPs are the diameters of the respective particles in nm.

7.4.2. P3HT:PCBM:CuS active layers

Prior to building the entire devices, the active layers were characterized. Figure 7.2(a) shows an active layer structure used to evaluate the effect of the CNPs on OPV cell performance. To eventually incorporate the CNPs in the P3HT:PCBM active matrix, the as-prepared CNPs must be compatible with the matrix. To this end, the particles were hydrophobically modified by capping with OAm.

Figure 7.2(b) shows that the NPs have a high affinity to the OAm additive because after only 2–4 $\min$ the transfer from the more polar dispersant DMSO to the unpolar OAm is essentially complete. Figure 7.2(b) also shows that the dispersions of the OAm-modified NPs are more stable than dispersions of the as-synthesized particles in CHB. While the as-prepared particles sediment after ca. 10 $\min$, the dispersions of the OAm-modified particles in CHB are stable for up to 2 h.

Comparison of the FTIR spectra of pure OAm, as-prepared CNPs, and OAm-modified CNPs prove ligand capping of the CNPs, Figure 7.2(c). Spectra obtained from the as-prepared CNPs do not show specific bands indicating that the NPs do not contain organic components such as residues from the ILs or $(TMS)_2S$.[370-372] However, the presence of OAm on the respective CNPs is indicated by the CH_2 and CH_3 symmetric and asymmetric stretching vibrations at 2857 and 2931 cm^{-1}, which are very weakly visible in the spectra of OAm-modified CNPs.[373] The bands do not shift compared to pure OAm; this indicates that the ligands are only weakly bound to the particles.[357]

Figure 7.2(d) shows the UV–vis absorption spectra of CNPs. The CNPs capping with OAm result in minor spectral changes. The absorbance below 420 nm slightly increases, while the absorption in the region above 420 nm is less pronounced than in the as-prepared sample. Moreover, the shoulder at around 420 nm is blue - shifted by ca. 10 nm upon capping with OAm.
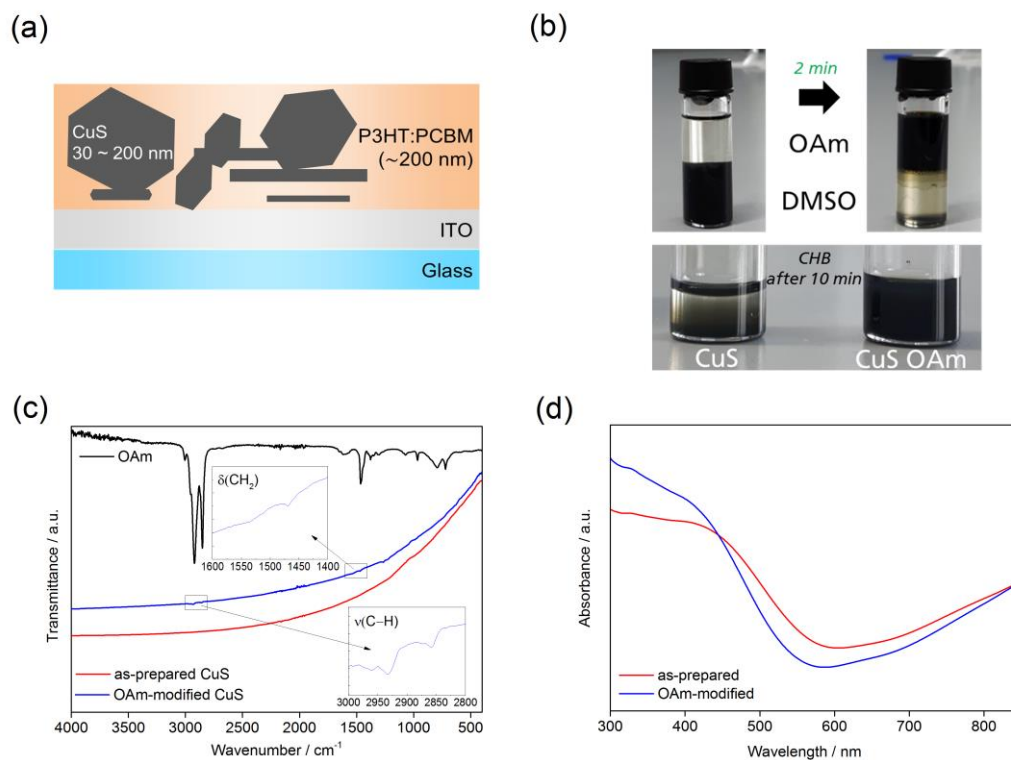
Figure 7.2. (a) Scheme of the active matrix of P3HT:PCBM:CNPs. (b) Photographs of the effect of OAm addition to a CNP dispersion in DMSO and 5 mg/mL CNP dispersion in CHB showing the improved stability of the OAm-stabilized NPs. (c) FTIR spectra; insets highlight the weak bands mentioned in the text. (d) UV-Vis absorption spectra of CNPs before and after OAm capping.

Figure 7.3(a) shows the effect of filtration on the optical properties of the OAm-modified CNP dispersion. The absorption spectrum of pure OAm dissolved in CHB shows an absorption only below 400 nm. This indicates that the absorbance at the lower wavelength originates from both the NPs and OAm. Accordingly, the spectra of the dispersions containing the as-prepared, unfiltered CNPs show a broad absorption essentially over the entire UV-vis-NIR range.

The spectra of dispersions made with the CNP samples filtered with 0.45 and 0.2 μm filters, respectively, are essentially identical. They show a strong absorption below 450 nm, but the signals previously observed above 450 nm are not visible anymore. The only remaining signal is a weak and broad band centered at around 650 nm.

The absorption above 450 nm visible in the spectra of the as-prepared samples has previously been observed in amorphous and bulk CuS.[367, 374-375] It has been assigned to localized surface plasmon resonance of CNPs but also to particle aggregation. As a result, the disappearance of this signal after filtration shows that filtration efficiently removes large

particles and aggregates present in the as-synthesized products. TEM (Figure 7.S1 of the appendix B) indeed confirms a significant reduction of the particle size by filtration.

The remaining fraction of CuS nanoparticles was estimated by the change of absorbance after the filtration, based on Beer's Law. After filtration with a 0.2 μm PTFE filter, the absorbance at 420 nm decreases by ca. 69% indicating that only ca. 31% of the particles remain after filtration.

Bandgap estimations were done via Tauc-plots, Figure 7.3(b). As-prepared CNPs have a bandgap of 2.3 eV, while samples filtered with 0.2 μm pore filters have a bandgap of 3.1 eV. The fact that the bandgap is larger after filtration with the 0.2 μm pore filter indicates that the filtration indeed removes larger particles and thus confirms TEM and absorption spectroscopy.

Figure 7.3(c) shows the photoelectron yield spectra of CNP films upon increasing UV excitation light energy. The valence band maximum (VBM), a measure of ionization energy (IE), is the onset of photoelectron emission, which is 4.8 and 5.3 eV for the OAm-modified unfiltered and filtered CNPs, respectively.

Figure 7.3(d) shows the resulting band diagram of the CNPs and their position relative to P3HT and PCBM. The energy levels of P3HT and PCBM were obtained from the literature.[357] According to the band diagram, the CNPs should be a good hole collection layer (HCL) material; they should also be a good electron blocking layer with a barrier of 0.8 eV between the lowest unoccupied molecular orbital (LUMO) of P3HT and the conduction band minimum (CBM) of the CNPs.
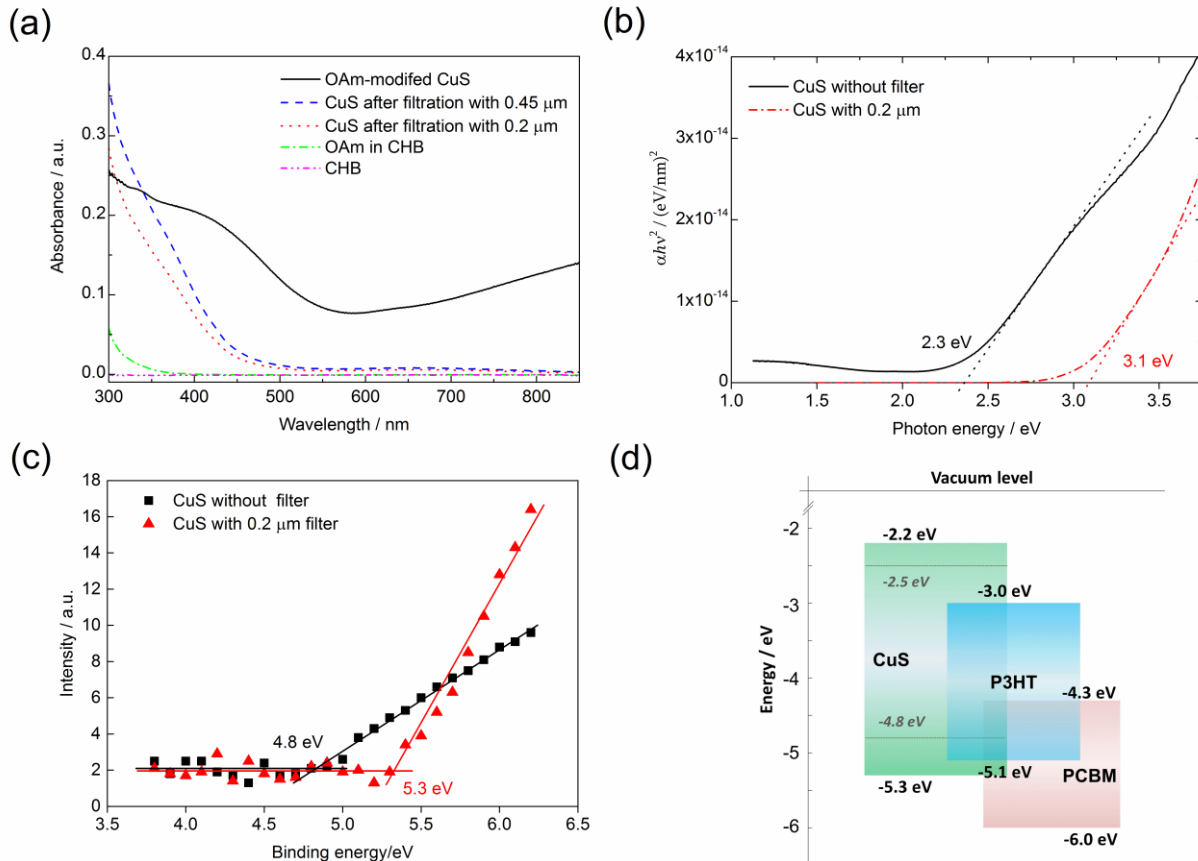
Figure 7.3. (a) UV–Vis–NIR absorption spectra. (b) Tauc-plots obtained from the absorption spectra. (c) VBM determined from photoelectron yield spectra. (d) Band diagram of OAm-modified CNPs after filtration relative to P3HT and PCBM. The gray dashed lines in the band diagram of CuS indicate the values obtained for the CNPs prior to filtration.

Finally, the morphology of the active P3HT:PCBM:CuS blend layer [Figure 7.2(a)] was evaluated via AFM. Different preparation parameters were studied - mainly the ratios of the three components P3HT, PCBM, and CuS along with different filtration steps (no filtration vs. 0.45 μm vs. 0.2 μm PTFE filter).

Figure 7.4 shows the surface morphology of the resulting films. A P3HT:PCBM film without CNPs [Figure 7.4(a)] where the blended solution was filtered with a 0.2 μm filter shows rather homogeneous films but has a root-mean-square roughness (R_q) and peak-to-valley roughness (R_{pv}) of 3.3 nm and 28.8 nm, respectively. The P3HT:PCBM:CuS blend film where the CNPs were filtered with a 0.45 μm filter [Figure 7.4(b)] is very similar to the reference film but has a slightly higher roughness (i.e., R_q = 3.9 nm and R_{pv} = 31.0 nm).

In stark contrast to both films above, the P3HT:PCBM:CuS films produced with a 0.2 μm filter [Figure 7.4(c)] are very homogeneous and show no protrusions, crazes, or other features.

Consequently, the R_q and R_{pv} are only 1.4 nm and 11.1 nm, respectively. In addition, the P3HT:PCBM blend film produced with a 0.2 μm filter [Figure 7.4(d)] has a slightly lower roughness (i.e., R_q = 1.1 nm and R_{pv} = 9.2 nm) than the P3HT:PCBM:CuS films produced with a 0.2 μm filter. Therefore, the surface roughness of the blend film where the CNPs were filtered with a 0.2 μm filter is smoother due to the fact that the larger particles in the P3HT:PCBM blend are removed. Overall, these results clearly show that the embedded CNPs do not significantly affect the film roughness compared to the film prepared without CNPs.
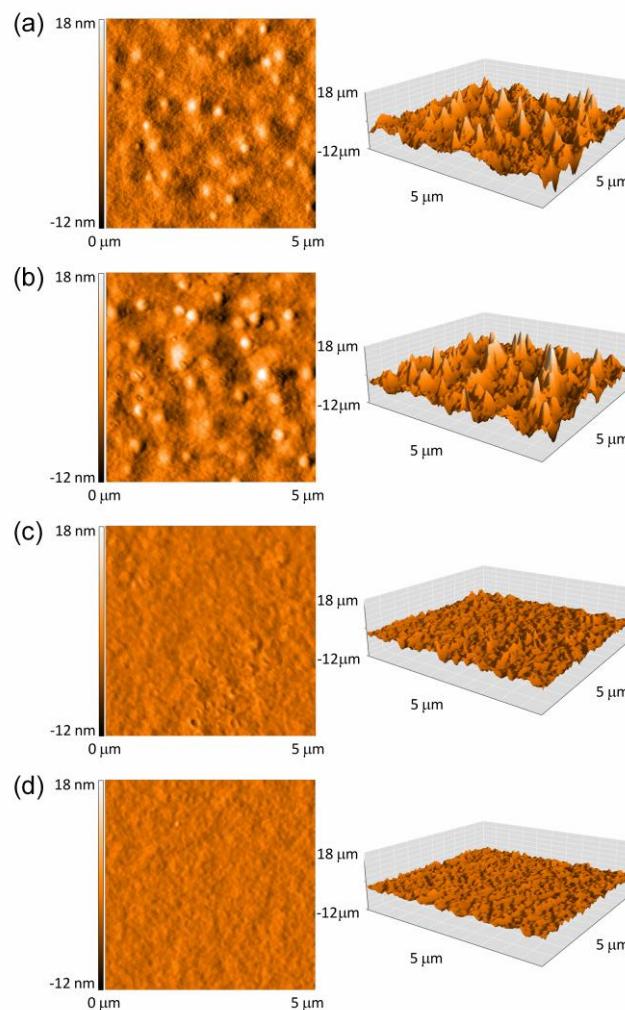
Figure 7.4. AFM height images obtained from different films. (a) P3HT:PCBM (1:1) reference film without CNPs. Prior to spin coating, the samples were filtered with a 0.45 μm PTFE filter. R_q = 3.3 nm and R_{pv} = 28.8 nm. (b) P3HT:PCBM:CuS (1:1:0.1) hybrid film. Prior to spin coating, the samples were filtered with a 0.45 μm PTFE filter. R_q = 3.9 nm and R_{pv} = 31.0 nm. (c) P3HT:PCBM:CuS (1:1:0.1) hybrid film. Prior to spin coating, the samples were filtered with a 0.2 μm PTFE filter. R_q = 1,4 nm and R_{pv} = 11.1 nm. (d) P3HT:PCBM (1:1) film without CNPs. Prior to spin coating, the samples were filtered with a 0.2 μm PTFE filter. R_q = 1.1 nm and R_{pv} = 9.2 nm.

7.4.3. P3HT:PCBM:CuS active layers in conventional and inverted devices

The potential of the CNPs as hole transport materials (i.e., p-type semiconductors) in the P3HT:PCBM:CuS active matrix was evaluated in both conventional and inverted OPV cells. Figure 7.5 shows the architecture of both devices and the corresponding band diagrams. The energy levels of ZnO NPs[362] and MoO_3[376] were obtained from the literature. In the following, the J-V characteristics of the devices shown in Figure 7.5 were investigated. To that end, several devices with different architectures and compositions were made, Table 7.1 and Table 7.S2 of the appendix B.
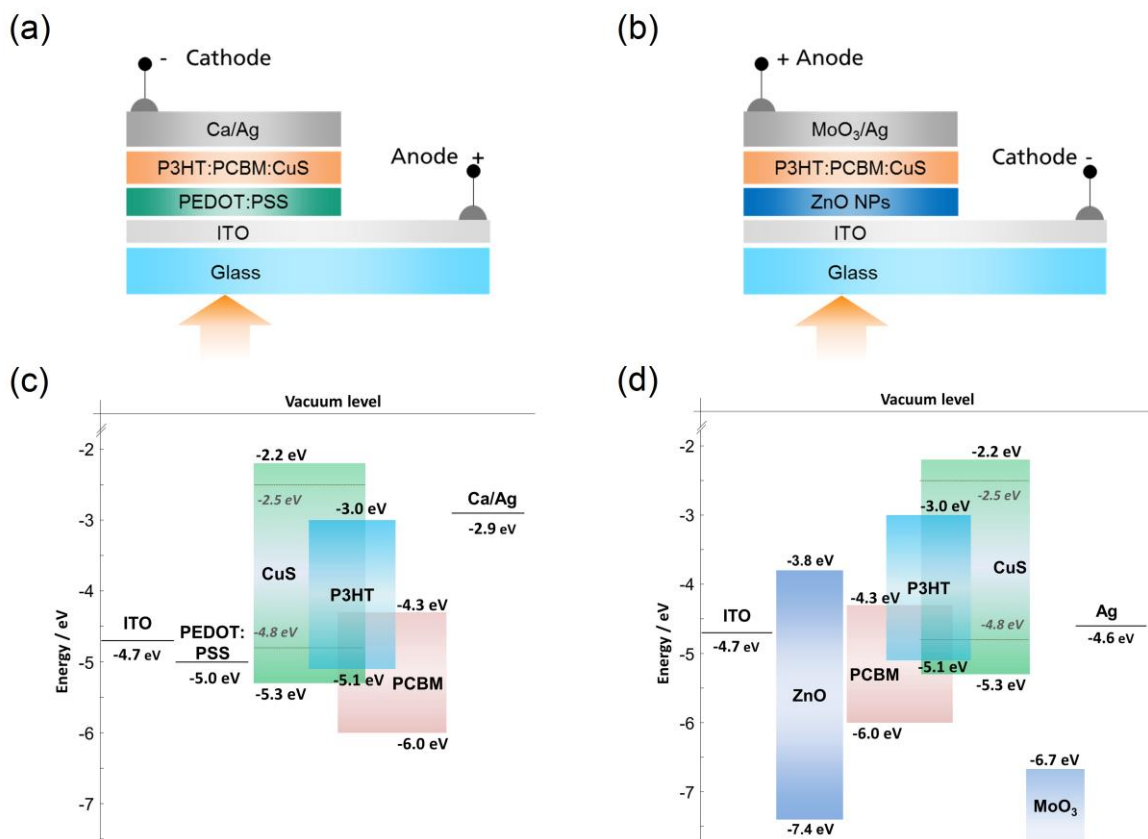
Figure 7.5. Schematic representation of (a) conventional and (b) inverted device structures used in the current study. (c) and (d) show the corresponding band diagrams. MoO_3 was used only for investigating the properties of the reference inverted device.

Table 7.1. Device architectures and compositions studied in this work.

Device	Composition	Active blends (P3HT:PCBM or P3HT:PCBM:CuS)	Conventional (C) / Inverted (I)
A	ITO/PEDOT:PSS/P3HT:PCBM/Ca/Ag	1 : 1	C
B	ITO/PEDOT:PSS/P3HT:PCBM:CuS/Ca/Ag	1 : 1 : 0.1	C
C	ITO/ZnO/P3HT:PCBM/Ag	1 : 1	I
D	ITO/ZnO/P3HT:PCBM:CuS/Ag	1 : 1 : 0.1	I
E	ITO/PEDOT:PSS/P3HT:PCBM/Ca/Ag	1 : 0.8	C
F	ITO/PEDOT:PSS/P3HT:PCBM:CuS/Ca/Ag	1 : 0.8 : 0.1	C
G	ITO/PEDOT:PSS/P3HT:PCBM:CuS/Ca/Ag	1 : 0.8 : 0.2	C
H	ITO/PEDOT:PSS/P3HT:PCBM:CuS/Ca/Ag	1 : 0.8 : 0.3	C

Figure 7.6 shows the J-V characteristics of devices A to D, including the reference devices fabricated without CNPs, which are designed to investigate the role of CNPs in both conventional and inverted device architectures.

Figure 7.6(a) shows the data for the conventional devices. The reference device A (ITO/PEDOT:PSS/P3HT:PCBM/Ca/Ag) shows an S-shape (i.e., S-kink or double diode) J-V curve. S-kink J-V curves are normally observed in BHJ or flat heterojunction (FHJ) OPV cells with various drawbacks such as high energy barriers for carrier extraction and injection or an imbalance of charge carrier mobilities.[377-379]

We assign this behavior to the combination of a 1:1 blending ratio of P3HT:PCBM and the high sheet resistance of ITO (50–70 Ω/sq) in the conventional device structure because the S-shape curve is not observed when the device is fabricated only with low sheet resistance (10–15 Ω/sq) and 1:0.8 blending ratio (Figure 7.S2(a) and Table 7.S3 of the appendix B). This suggests that the hole transport is delayed by the higher concentration of the PCBM acceptor material (i.e., electron transport material) and the high resistance of the anode. In addition, this reference structure provides good contact between the active layer and both the anode and the cathode (i.e., metal-semiconductor contact) by a PEDOT:PSS and Ca buffer layer, respectively. Therefore, control device A is a good reference to evaluate the effect of the CNPs on the hole transport properties.

Upon addition of the CNPs to the active matrix, the S-shape of the J-V curve of the conventional device A changes, Figure 7.6(a). J_{sc} increases from 1.26 mA/cm^2 (device A) to

2.68 mA/cm^2 (device B) and the fill factor (FF) increases from 17.78% to 22.60%, respectively. Overall, this leads to an increase of power conversion efficiency (PCE) from 0.14% to 0.35%, Table 7.S1 of the appendix B.

Figure 7.6(b) shows the corresponding data for the inverted devices. A control device C (ITO/ZnO/P3HT:PCBM/Ag), designed without HCL, was chosen to determine if the CNPs could reduce the V_{oc} by improving the contact property between the Ag cathode and the active layer. Consequently, Figure 7.6(b) shows that a device D containing CNPs increases V_{oc} from 0.39 V to 0.56 V, which leads to an overall increase of the PCE from 0.39% to 0.49%, Table 7.S1 of appendix B.
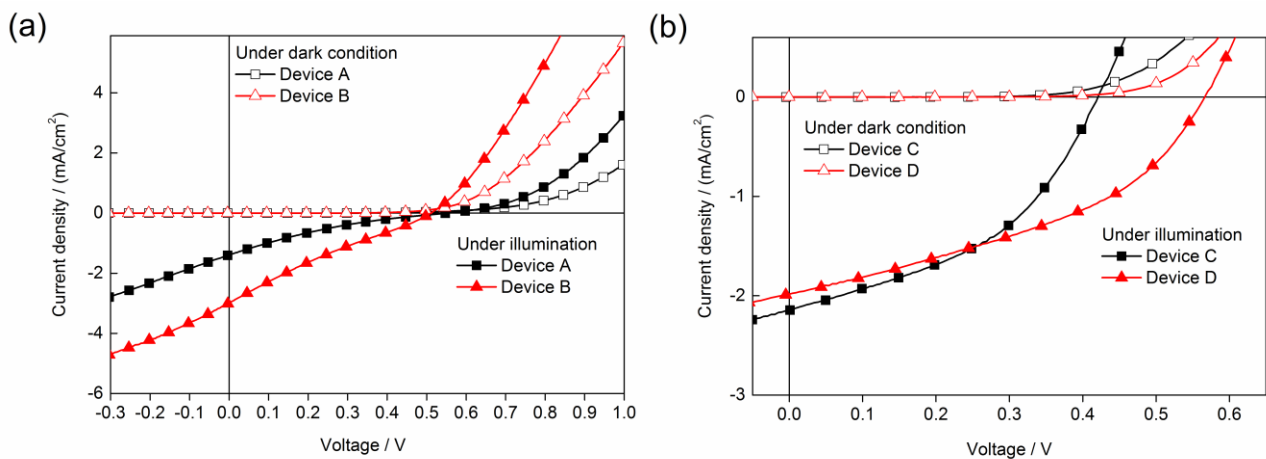
Figure 7.6. (a) J-V characteristics of conventional and (b) inverted OPV cells.

7.4.4. Efficiency enhancement by CNP concentration variation

To increase OPV performance in the conventional structures, different CNP concentrations were investigated, see Table 7.1 above. The different CNP concentrations do not dramatically change the surface roughness of the active layer, but device G shows the lowest R_q and R_{pv} (i.e., 1.13 nm and 8.96 nm, respectively), Table 7.S4 and Figure 7.S3 of the appendix B. Device performance was not enhanced by the roughness, but the slightly different roughness, especially R_{pv}, brought only a minor difference in dark current measurement as shown in Figure 7.7(b). This aspect will be discussed below.

Figure 7.7(a) shows the J-V characteristics of device E to device H under illumination; the corresponding OPV parameters are summarized in Table 7.2. V_{oc} is almost identical at around 0.6 V for all devices. However, the change of J_{sc} strongly depends on the CNP concentration, with device G having the highest current density (J_{sc}) of 8.38 mA/cm^2.

Even though the FF of the devices decreases from 46.64% to 43.72% as the CNP concentration increases from device E to device H, the P3HT:PCBM:CuS ratio of 1:0.8:0.2 (device G) consequently increases the PCE from 2.27% to 2.64% (i.e., by 16%) compared to the control device E. This is due to the highest J_{sc} in this sample. Table 7.S5 of the appendix B shows the complete results obtained from all devices with different pixel areas demonstrating a high reproducibility of these experiments and proving that the device performance shows the same trends.

Figure 7.7(b) shows the dark current (J_{dc}) characteristics of the devices with semi-log plots. The three regions indicated account for where different effects dominate: region I, region II, and region III account for leakage (i.e., shunt) currents, recombination currents, and series resistance, respectively.[380-381] Region II and III are quite similar for all devices. However, region I shows a different current density behavior. The shunt resistance (R_{sh}), correlated with the J-V curve slope of region I (i.e., $R_{sh} \sim$ 1/slope), is reduced when CNPs are embedded in the active layer compared to the control device; this leads to low FFs.

However, the different CNP concentrations do not significantly change the slope. Additionally, the level of current density in region I, which indicates the difference of leakage current in the devices, is lowest in device G. This low leakage current correlates with the higher J_{sc} and the lower surface roughness of the blended layer in device G (Table 7.S4 of the appendix B). Since the control device shows also a lower current density in region I compared to the other devices containing CNPs, the higher leakage current is due to the presence of the CNPs.
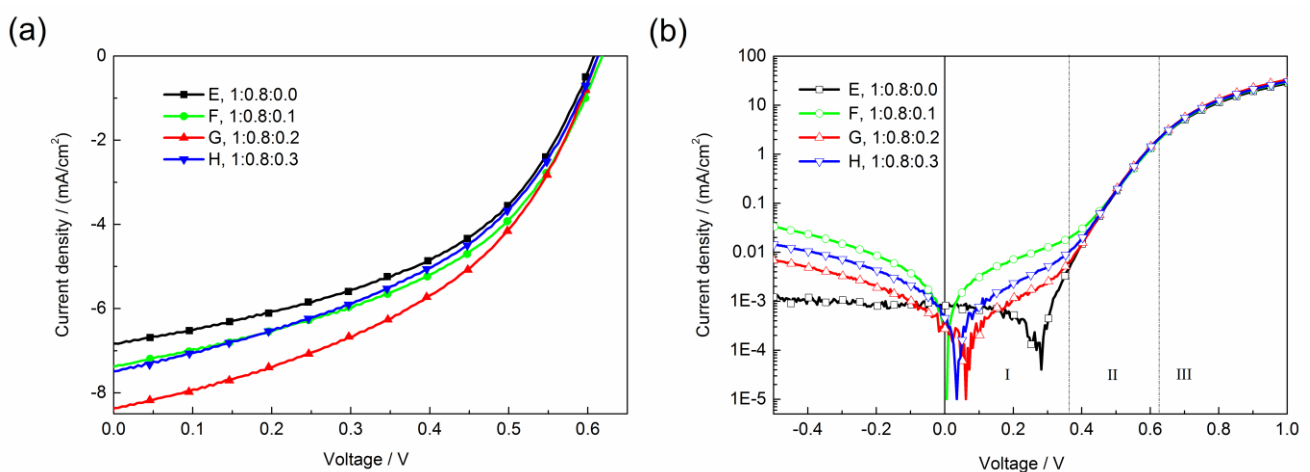
Figure 7.7. J-V characteristics of conventional OPV cells under (a) illumination and (b) dark condition. Numbers are the mixing ratios as specified in the text.

Table 7.2. Device performance vs. CNP concentrations. Average values and standard deviation are calculated from three different pixels. The boldface indicates the performance of the best device.

Device	P3HT:PCBM:CuS(weight ratio)	V_{oc}(V)	J_{sc}(mA/cm^2)	FF(%)	PCE(%)
E	1:0.8:0.0	0.61 ± 0.01	6.91 ± 0.10	46.64 ± 0.24	2.27 ± 0.02
F	1:0.8:0.1	0.62 ± 0.01	7.38 ± 0.10	46.45 ± 0.37	2.45 ± 0.02
G	**1:0.8:0.2**	**0.62 ± 0.01**	**8.38 ± 0.04**	**44.33 ± 0.20**	**2.64 ± 0.02**
H	1:0.8:0.3	0.62 ± 0.01	7.53 ± 0.04	43.72 ± 0.51	2.33 ± 0.03

Chapter 8

The ionic liquid $[C_4Py]_2[Cu_{0.39}Co_{0.61}Cl_4]$ is a single source ionic liquid precursor (ILP) for carrolite $CuCo_2S_4$ nanomaterials

8.1. Abstract

The ionic liquid (IL) $[C_4Py]_2[Cu_{0.39}Co_{0.61}Cl_4]$ is a single source precursor for copper cobalt sulfide nanoparticles. The IL crystallizes in the monoclinic space group $P2_1/n$ with eight molecules in the unit cell. The crystal structure is stabilized by a number of non-classical hydrogen bonds, and the crystalline compound melts at 74.7 °C. The IL is available in good yields, and the transformation to the metal sulfides proceeds with over 80% yield using a simple hot injection method. The resulting materials consist of highly aggregated carrollite $CuCo_2S_4$ nanoparticles where the Cu is present as $Cu(II)$, and Co is present as $Co(III)$ as determined from X-ray photoelectron spectroscopy.

8.2. Introduction

Ionic liquids (ILs) are widely regarded, due to their unusual physical and chemical properties, as promising materials for applications in batteries,[20] fuel cells,[21] extraction and seperation,[17-19] drug delievery,[24] solar cells,[22] and electrochemistry.[4] ILs have the potential for more flexible structural design, through an appropriate choice of the cation and the anion.[288]

A subclass of ILs, Metal-containing ILs (MILs), have been widely studied due to their applicability for a multitude of applications such as organic synthesis,[382-383] electrodeposition,[2, 384] CO_2 capture,[385] biomass refining,[386] mercury sorption,[231, 291] and biomedicine.[387] MILs have also been used as ionic liquid precursors (ILPs) for inorganic nanomaterials, where the ILP acts as the solvent, the template, and the precursor for the inorganic material at the same time.[12, 69-70]

Examples of inorganic materials made using the ILP approach include Ag,[293] or Au^{146} have been made by using ILs as precursors, where the IL provides at least one component of the final material. Accordingly, these ILs have been termed ionic liquid precursors (ILPs)[388] and an analogous synthesis strategy has also been developed for (doped) carbon materials,[389-391] Ni and NiO nanomaterials,[392-394] CuS,[292] Fe_3C,[395] $In_2O_3{}^{396}$, ZnO,[397-398] and CuO.[294] Other studies have focused on the synthesis using fluorine-containing anions as fluoride precursors.[399-402] Alternatively, deep eutectic solvent precursors (DESPs) have also

been introduced for the synthesis of such materials.[383, 403-405] As a result, proper choice of an ILP (or DESP) will lead to materials with interesting and useful properties via synthesis strategies such as carbonization or precipitation, whereby the IL is at the same time the solvent, template, and the precursor for the (inorganic) material.

Transition metal chalcogenides have attracted tremendous attention due to their excellent electrical, optical, and catalytic properties,[171-172, 406-407] and their important applications in different fields such as lithium-ion batteries (LIBs),[166] dye-synsitized solar cells,[408] supercapacitors,[409] and electrochemical sensing.[410] Copper sulfide[411] and cobalt sulfide[412] are among the most important binary chalcogenides, and mixed-metal sulfides provide access to yet other electronic, optical, and magnetic properties. Carrollite ($CuCo_2S_4$) has a spinel structure with the Cu^{2+} ions occupying the tetrahedral sites and the Co^{3+} ions occupying the octahedral sites (Figure 8.1),[413] where the octahedral sites of the spinel structure are catalytically active, while the tetrahedral sites are almost inactive.[414-416]

Classically, mixed metal sulfides are made via electrodeposition,[417] ion-layer gas reaction,[418-419] spray pyrolysis,[133] sputtering,[420] microwave-assisted synthesis,[421] and hot-injection method.[422] The hot-injection method offers a cheap and convenient method for the formation of high quality nanocrystalline that have the desired stoichiometry and phase.

The current study demonstrates that ILPs containing more than one metal are viable precursors for the synthesis of ternary sulfides such as carrollite nanomaterials. The ILP is based on the tetrachloridometallate(II) anion and the N-butypyridinium (C_4Py) cation where the metal cation is $Cu(II)$ and $Co(II)$ and the IL has the composition $[C_4Py]_2[Cu_{0.39}Co_{0.61}Cl_4]$.
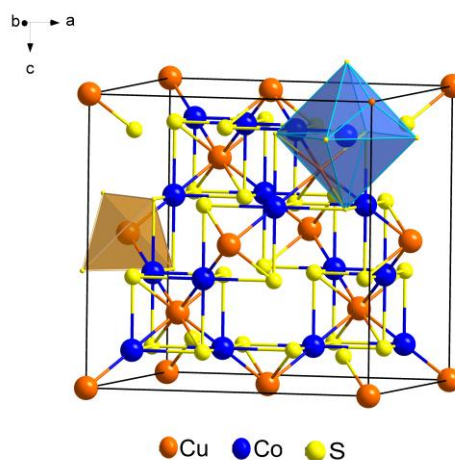
Figure 8.1. Structure of carrollite $CuCo_2S_4$. Adapted from De Jong et al. "Carrollit (Sychnodymit)." *Zeitschrift für Kristallographie* 66 (1928): 168-171.[423]

8.3. Experimental

8.3.1. Chemicals

N-butylpyridinium chloride (Iolitec, 99%), $CuCl_2.2H_2O$ (Fluka, ≥ 99%), $CoCl_2·6H_2O$ (Ucb, 98%), bis (trimethylsilyl) sulfide (Sigma-Aldrich, 99%), and acetonitrile (Sigma-Aldrich, 99.8%) were used without further purification.

8.3.2. Apparatus

Elemental Analysis (CHN) was carried out on an Elementar vario EL III analyzer with a limit of detection of 0.3%. **Inductively coupled plasma** (ICP) analysis was performed by the Mikroanalytisches Labor Kolbe, Mülheim, Germany. The transition metal ions were measured by Perkin Elmer AAnalyst 200 Atomic Absorption. **Mass spectroscopy** (MS) was performed on a Micromass QTOF (Quadrupol – Time of flight) with an electrospray ionization (ESI) source operating in positive and negative ionization modes, with a range of m/z 50-800. Samples were injected as dilute solutions in methanol. **Differential scanning calorimetry** (DSC) measurements were done with a Netzsch DSC 214 Polyma under nitrogen atmosphere. The samples were weighed in aluminum pans with a pierced lid from the same manufacturer. Samples were measured over three heating and cooling cycles from -100 to 150 °C at 10 K min^{-1}. Isothermal time between heating and cooling cycles were 10 min. **Powder X-ray diffraction** (XRD) was done on a PANalytical Empyrean with Bragg-Brentano geometry equipped with a PIXcel1D detector using Cu K_α radiation (λ = 1.5419 Å). Sample morphology and bulk chemical composition were investigated via **scanning electron microscopy** (SEM, JEOL JSM-6510, 15 kV), and **energy dispersive X-ray spectroscopy** (EDX) was done with an Oxford Instruments INCA x-act detector mounted to the SEM. Samples were mounted on an aluminum stub with adhesive carbon tape and coated with carbon using a Polaron CC7650 Carbon Coater. **Transmission electron microscopy** (TEM) images were acquired on a Philips CM 200 with a LaB_6 cathode operated at 200 kV. TEM samples were prepared by drop-casting a $CuCo_2S_4$ solution on a carbon-coated Cu grid.

A suitable single crystal of $[C_4Py]_2[Cu_{0.39}Co_{0.61}Cl_4]$ was selected for single crystal X-ray analysis. The single crystal, which was grown by diffusion of methyl tert-butyl ether vapor into ethanolic solution, was mounted on a thin glass fiber for data collection on an Imaging Plate Diffraction System IPDS-2 (STOE) with graphite-monochromated Mo-Kα radiation (λ = 0.71073 Å) at 210 K. All data were corrected for Lorentz and polarization effects. Numerical absorption corrections were applied using optimized shape.[269] The structure was solved by direct methods using the program SHELXS-2013/1[270] and refined against F^2 by means of full-matrix least-squares procedures using the program SHELXL-2014/7.[271] Non-hydrogen atoms were refined with anisotropic temperature factors. For the visualization, the programs DIAMOND[272] and ORTEP[273] were used.

8.3.3. Synthesis of N-butylpyridinium tetrachloridocuprate(II)cobaltate(II)

IL synthesis was done according to refs.[268, 280] To a solution of *N*-butylpyridinium chloride (1.026 g, 6 mmol) in dry acetonitrile (6 mL), copper(II) chloride (0.258 g, 1.5 mmol) and cobalt(II) chloride (0.357 g, 1.5 mmol) were added. This mixture was stirred at reflux for 3 h. The solvent was evaporated with a rotary evaporator at 60 °C under reduced pressure, and the product was dried in vacuo. Yield: 1.40 g (98.6 %). MS positive mode: *m/z* = 136.1123 $[C_9H_{14}N]^+$. Elemental analysis for $C_{18}H_{28}Cl_4Cu_{0.39}Co_{0.61}N_2$ calculated (found) C 45.52% (45.03%); H 5.94% (6.12%); N 5.9% (5.92%). ICP analysis gives the contents of Cu and Co as 5.04 and Co 7.50 wt % , respectively. The compositional analysis results are in agreement with the empirical formula, $[C_4Py]_2[Cu_{0.39}Co_{0.61}Cl_4]$, given by single crystal structure analysis.

8.3.4. Synthesis of CuCo$_2$S$_4$ nanoparticles

CuCo$_2$S$_4$ nanoparticles were synthesized via hot-injection under argon as follows: 0.5 mmol (0.237 g) of $[C_4Py]_2[Cu_{0.39}Co_{0.61}Cl_4]$ were heated to 180 °C, then 2 mmol (0.422 mL) of bis (trimethylsilyl) sulfide, (TMS)$_2$S, were added with a syringe. Upon injection, the color of the liquid immediately turned from green to dark black; this color change was accompanied by the precipitation of a dark solid. The reaction mixture was vigorously stirred for 6 h at 180 °C and then allowed to cool to room temperature. After cooling, the CuCo$_2$S$_4$ particles were isolated and purified by repeated washing/centrifugation cycles with deionized water and absolute ethanol. The powders were dried under vacuum for 12 h at room temperature. The synthesis produced 127.8 mg of CuCo$_2$S$_4$ in powder form, which corresponds to the yield of (82.7 %).

8.4. Results

8.4.1. Characterization of metal-containing ionic liquid

Single crystal structure analysis reveals that the asymmetric unit of $[C_4Py]_2[Cu_{0.39}Co_{0.61}Cl_4]$ comprises four independent cations and two anions. The crystal structure of the complex is stabilized by extended networks of several non-classical hydrogen bonds, and non-covalent contacts and the compound crystallizes in the monoclinic space group $P2_1/n$.

As illustrated via DIAMOND[272] drawing in Figure 8.2, the M (II) (M = Cu and Co) center displays a tetrahedral geometry and is embraced by four chlorido ligands to afford the anionic entity, in which the Co−Cl bond lengths adopt the values from 2.259(3) to 2.300(3) Å, and the Cu−Cl bond lengths adopt the values from 2.255(4) to 2.305(4) Å. The Cl−Co−Cl angles fall within the interval of 105.90(18)° to 117.24(14)°, and the Cl−Cu−Cl angles fall within the interval of 105.92(16)° to 116.4(3)°.

Table 8.2 shows that the averaged Co−Cl bond length is equal to the Cu−Cl bond length (2.28 Å) and The averaged Cl−Co−Cl angles are equal to the average Cl−Cu−Cl angles (109.43°) close to tetrahedral, which is comparable with those found in the literature for other compounds with tetrahedral $[CoCl_4]^{2-}$ and $[CuCl_4]^{2-}$ units.[280, 424-425]

The complex anion is connected to cation through C−H···Cl hydrogen bonds. The geometry of the anion is close to perfectly tetrahedral. The experimental details and crystallographic data are summarized in Table 8.1, and selected bond lengths of the complex anion, as well as the bond angles, are summarized in Tables 8.2 and 8.3, respectively.
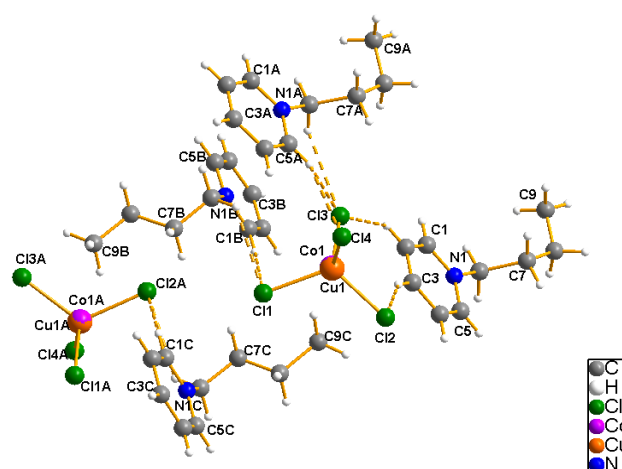
Figure 8.2. The asymmetric unit of $[C_4Py]_2[Cu_{0.39}Co_{0.61}Cl_4]$, with numbering scheme. Hydrogen bonds as dashed lines.

A 3-D extended supramolecular architecture (Figure 8.3) is formed by the cation-anion interactions and the non-classical hydrogen bonds ($C–H…Cl$) between the cations and the anions (Table 8.4). All chlorine atoms of the $[MCl_4]^{2-}$ anion participate in $H…Cl$ contacts with the hydrogen atoms of the pyridinium ring cations and some of the hydrogen atoms of the alkyl chains. These Hydrogen bonding interactions play an important role in the formation of the 3-D supramolecular architecture. Moreover, the cations and anions are arranged in alternating layers. In every cation layer, all the planar pyridinium rings are parallel to each other. The pyridinium cations show a significant stacking along *b* direction. Two π–π stacking interactions between pyridinium cations are observed. The first stacking interaction is characterized by an interplanar distance ranging from 5.9 to 7 Å with a displacement angle of 18.4(2)°, while the second stacking interaction is characterized by an interplanar distance ranging from 5.8 to 7.2 Å with a displacement angle of 10.95(2)°.
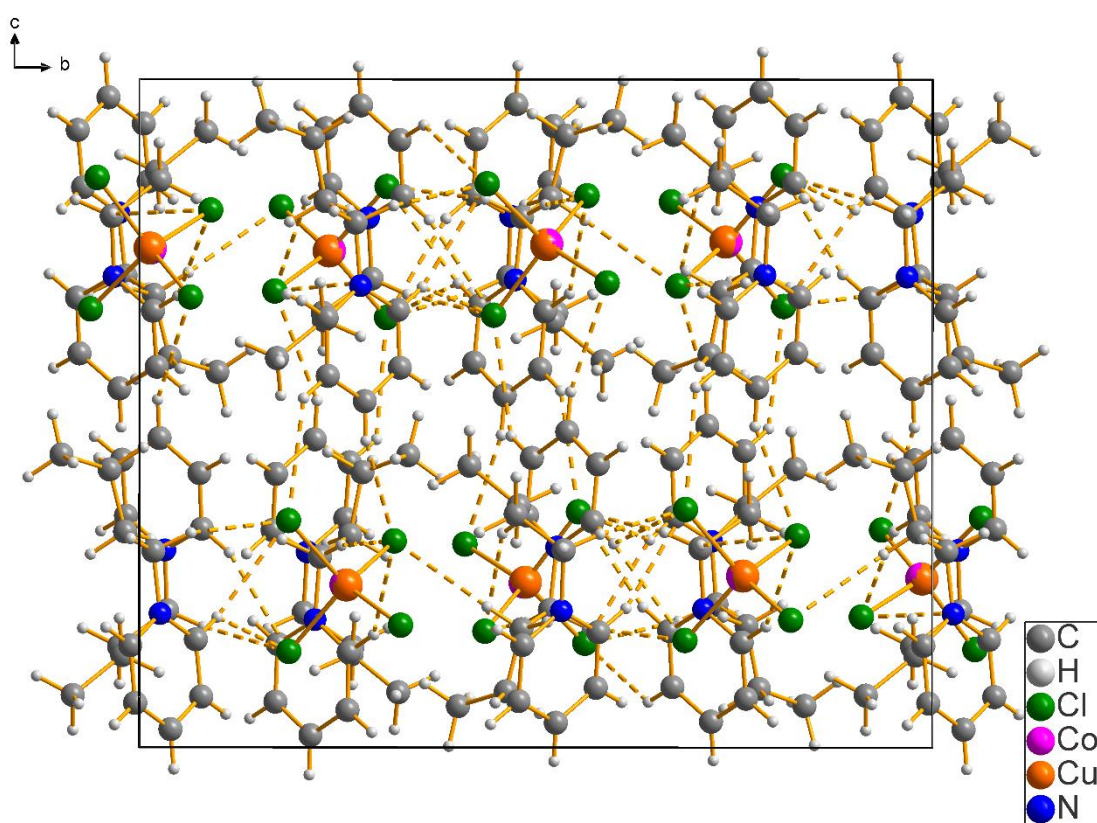
Figure 8.3. Packing diagram of $[C_4Py]_2[Cu_{0.39}Co_{0.61}Cl_4]$. View along the crystallographic *a* axis. Hydrogen bonds are indicated by dashed lines.

Table 8.1. Crystallographic data and details of the refinement for the compound.

Compound	$[C_4Py]_2[Cu_{0.39}Co_{0.61}Cl_4]$
Molecular Formula	$C_{18}H_{28}Cl_4N_2Cu_{0.39}Co_{0.61}$
Formula weight / $g \cdot mol^{-1}$	474.95
Crystal system	monoclinic
Space group	$P\ 2_1/n\ (No.\ 14)$
T / K	210(2)
a / Å	15.4341(8)
b / Å	18.6481(13)
c / Å	16.7651(9)
α / °	90
β / °	110.359(4)
γ / °	90
V / $Å^3$	4523.8(5)
Z	8
D_{calc} / $g \cdot cm^{-3}$	1.395
μ / mm^{-1}	1.316
Reflections collected	60094
Independent reflections	7960
R_{int}	0.1249
No. reflns with $I>2\sigma(I)$	3644
No. refined parameters	469
$R_1{}^a$, $wR_2{}^b$ $[I>2\sigma(I)]$	0.1094, 0.0877
$R_1{}^a$, $wR_2{}^b$ (all data)	0.0403, 0.0738
Goodness-of-fit on F^2	0.742

[a] $R_1 = \Sigma||F_o| - |F_c||/\Sigma|F_o|$. [b] $wR_2 = [\Sigma w(F_o{}^2 - F_c{}^2)/\Sigma[w(F_o{}^2)^2]\ ]^{.1/2}$.

Table 8.2. Selected bond lengths (Å) for the complex anion

Cl1−Co1	2.260(4)	Cl1−Cu1	2.265(4)
Cl2−Co1	2.280(5)	Cl2−Cu1	2.255(4)
Cl3−Co1	2.273(5)	Cl3−Cu1	2.305(4)
Cl4−Co1	2.298(4)	Cl4−Cu1	2.290(4)
Cl5−Co2	2.300(3)	Cl5−Cu2	2.298(6)
Cl6−Co2	2.261(3)	Cl6−Cu2	2.276(6)
Cl7−Co2	2.259(3)	Cl7−Cu2	2.266(5)
Cl8−Co2	2.294(3)	Cl8−Cu2	2.272(5)
Cl−Co (Aver.)	**2.28**	**Cl−Cu (Aver.)**	**2.28**

Table 8.3. Selected bond angles (°) for the complex anion

Cl1−Co1−Cl3	107.12(18)	Cl2−Cu1−Cl1	115.62(15)
Cl1−Co1−Cl2	114.8(2)	Cl2−Cu1−Cl4	107.01(16)
Cl3−Co1−Cl2	109.64(17)	Cl1−Cu1−Cl4	110.92(15)
Cl1−Co1−Cl4	110.77(18)	Cl2−Cu1−Cl3	109.41(14)
Cl3−Co1−Cl4	108.51(19)	Cl1−Cu1−Cl3	105.92(16)
Cl2−Co1−Cl4	105.90(18)	Cl4−Cu1−Cl3	107.72(14)
Cl7−Co2−Cl6	117.24(14)	Cl7−Cu2−Cl8	107.3(2)
Cl7−Co2−Cl8	106.82(12)	Cl7−Cu2−Cl6	116.4(3)
Cl6−Co2−Cl8	108.76(9)	Cl8−Cu2−Cl6	109.0(2)
Cl7−Co2−Cl5	108.23(9)	Cl7−Cu2−Cl5	108.1(2)
Cl6−Co2−Cl5	107.57(12)	Cl8−Cu2−Cl5	108.7(3)
Cl8−Co2−Cl5	107.90(13)	Cl6−Cu2−Cl5	107.1(2)
Cl−Co−Cl (Aver.)	**109.43**	**Cl−Cu−Cl (Aver.)**	**109.43**

Table 8.4. Hydrogen bond geometry (Å, °)

D–H...A	D–H	H...A	D...A	D-H...A
C1–H1...Cl7 [I]	0.94	2.99	3.810(5)	146.4
C2–H2...Cl8 [II]	0.94	2.88	3.575(6)	131.6
C5–H5...Cl3	0.94	2.84	3.629(5)	142.6
C5–H5...Cl4	0.94	2.91	3.584(5)	130.2
C6–H6A...Cl7 [I]	0.98	2.81	3.745(5)	160.7
C6–H6B...Cl3	0.98	2.86	3.628(5)	135.9
C7–H7A...Cl2 [III]	0.98	2.88	3.756(6)	149.9
C10–H10...Cl8 [I]	0.94	2.79	3.693(6)	161.1
C11–H11...Cl5 [I]	0.94	2.97	3.647(6)	129.7
C13–H13...Cl4 [IV]	0.94	2.89	3.581(6)	131.5
C14–H14...Cl1	0.94	2.96	3.813(5)	151.9
C15–H15A...Cl8 [I]	0.98	2.97	3.866(5)	152.4
C15–H15B...Cl1	0.98	2.91	3.611(5)	128.8
C19–H19...Cl2 [IV]	0.94	2.95	3.777(5)	147.4
C20–H20...Cl3	0.94	2.90	3.567(5)	129.0
C23–H23...Cl5 [V]	0.94	2.88	3.716(5)	148.6
C23–H23...Cl8 [V]	0.94	2.92	3.598(5)	130.5
C24–H24A...Cl2 [IV]	0.98	2.73	3.687(5)	165.4
C24–H25B...Cl5 [V]	0.98	2.83	3.626(5)	138.5
C28–H28...Cl6	0.94	2.91	3.769(6)	151.8
C32–H32...Cl4 [VI]	0.94	2.80	3.701(6)	160.3
C33–H33A...Cl6	0.98	2.92	3.613(6)	128.8
C33–H33B...Cl4 [VI]	0.98	2.95	3.845(6)	152.2

Symmetry codes: [I] 1.5-x, 0.5+y, 1.5-z; [II] -0.5+x, 0.5-y, -0.5+z; [III] 0.5-x, 0.5+y, 1.5-z; [IV] 0.5+x, 0.5-y, 0.5+z; [V] 1-x, -y, 2-z; 0.5-x, [VI] -0.5+y, 1.5-z;

The DSC heating curve of the $[C_4Py]_2[Cu_{0.39}Co_{0.61}Cl_4]$ is shown in Figure 8.4. Two endothermic peaks with an onset temperature of -37.6 °C and 74.7 °C, and one exothermic peak with an onset temperature of 8.6 °C were assigned to the glass transition, the melting temperature, and the recrystallization of the IL, respectively. The heat of recrystallization calculated from the exothermic peak (-28.73 $kJ·mol^{-1}$) showed an agreement with the heat of melting (29.2 $kJ·mol^{-1}$).
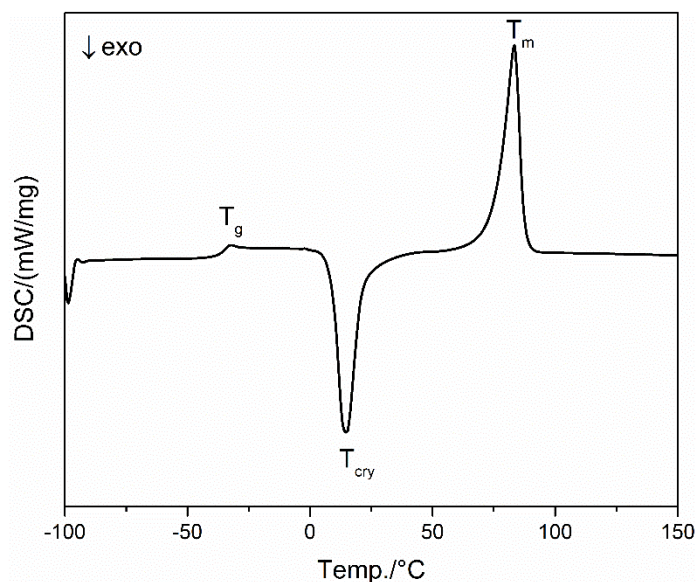
Figure 8.4. DSC thermogram of $[C_4Py]_2[Cu_{0.39}Co_{0.61}Cl_4]$. T_{cry}: crystallization temperature; T_m: melting temperature; T_g: glass transition temperature.

8.4.2. Characterization of $CuCo_2S_4$ nanoparticles

Fig ure 8.5a shows a representative XRD pattern of the precipitates. The reflections of the sample synthesized at 180 °C can be indexed to the cubic phase of the carrollite ($CuCo_2S_4$) structure (Fd-3m, primitive cubic unit cell with a= 9.458 Å, JCPDS 98-003-1107). Additional reflections at 2θ = 29.8° and 52.1° can be assigned to cobaltpentlandite (Co_9S_8, JCPDS 98-003-1753). All reflections are broad, indicating the formation of nanocrystalline products. Energy dispersive X-ray spectroscopy (EDXS, Figure 8.5b) shows the presence of Cu, Co, and S in the powders consistent with the XRD analysis.
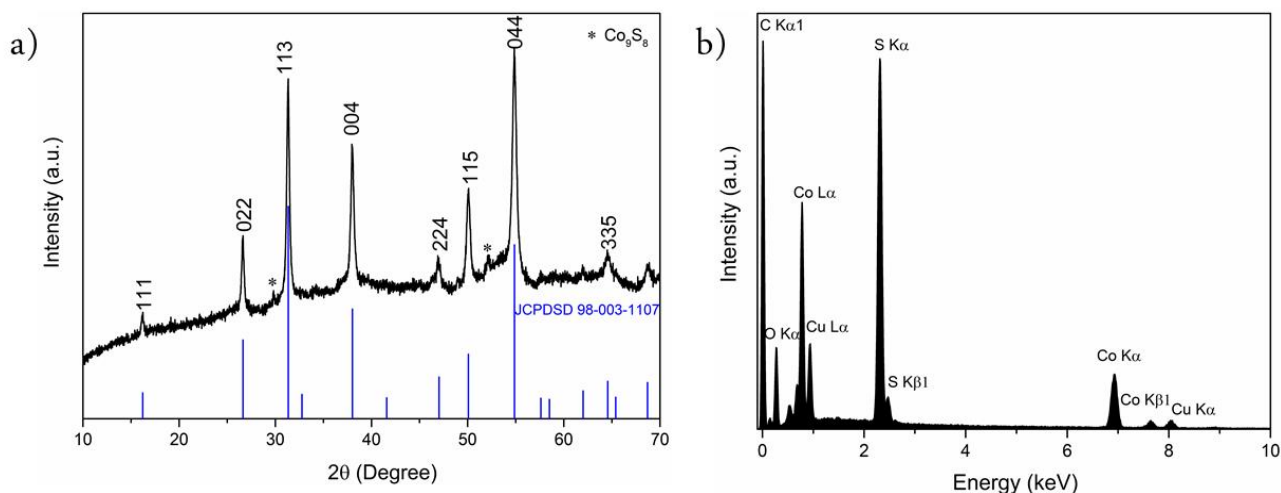
Figure 8.5. (a) XRD patterns of $CuCo_2S_4$ nanoparticles. The blue ticks indicate the positions of the reflections from the cubic phase $CuCo_2S_4$ (ICDD 98-003-1107). (b) EDX spectrum of the $CuCo_2S_4$ nanoparticles.

Figure 8.6a shows a typical survey XPS spectrum showing the presence of Cu, Co, and S in the sample. The peaks of Cl and C may stem from the residual IL precursor $[C_4Py]_2[Cu_{0.39}Co_{0.61}Cl_4]$, and the peaks from O and C might come from O_2, H_2O, or CO_2 adsorbed on the surface of the sample and adventitious hydrocarbon from the XPS instrument itself.[426]

Figure 8.6b shows the XPS spectrum of Cu energy region. The binding energies peaks of $Cu2p_{3/2}$ and $Cu2p_{1/2}$ at around 950.97 and 931.2 eV (E= 19.75 eV), respectively. This confirmed the existence of Cu^{2+}.[427] In addition, a peak corresponding to the satellite peak of Cu^{2+} at 943.95 eV is observed.[428] In the Co 2p region (Figure 8.6c), The binding eneregies peaks of Co $2p_{1/2}$ and Co $2p_{3/2}$ at around 793.09 and 778.09 eV (ΔE= 15 eV), respectively. This confirmed the existence of Co^{3+}.[429] Figure 8.6d showed the XPS spectrum of S energy region. The binding energies peaks at 161.3 and 162.4 can be assigned to $2p_{1/2}$ and $2p_{3/2}$ core level at S^{2-}. The broad peaks detected at 168.97 can be ascribed to the existence of So_4^{2-}, which indicated that the sulfur species on the surface was partially oxidized by air.[430] According to the results of the XPS analysis, the sample's surface contained Cu^{2+}, Co^{3+}, and S^{2-}. This is in a good agreement with literature, which the oxidation state in carrollite are generally shown as $Cu^{2+}Co_2^{3+}S_4^{2-}$ to comply with charge balance.[431]
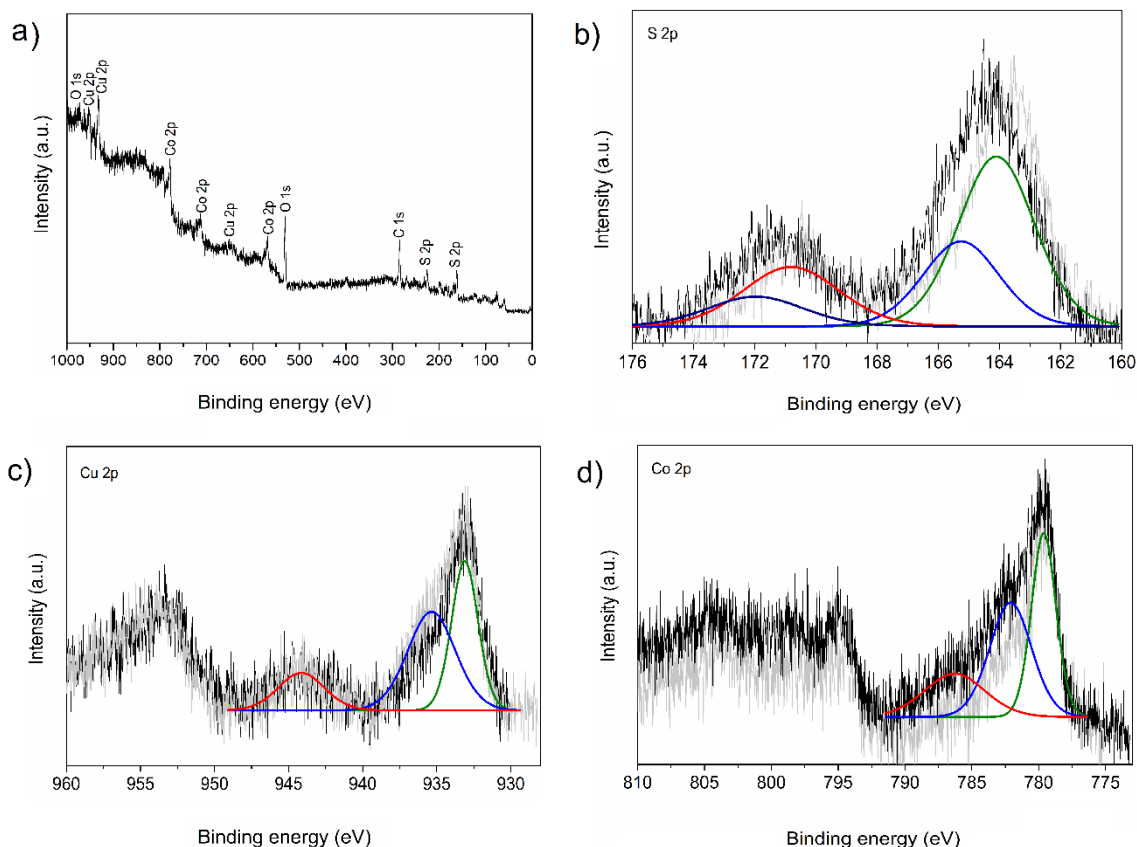
Figure 8.6. (a) XPS survey spectrum, and high-resolution XPS spectra of (b) S, (c) Cu, and (d) Co elements of the $CuCo_2S_4$ nanoparticles.

The $CuCo_2S_4$ nanoparticles will be applied to the electrocatalytic driven-water splitting. Reactions preliminary results showed an extraordinary enhanced electrocatalytic activity. Furthermore, the products are expected to be implemented in different fields, such as solar cell devices, amperometric gas sensors, Li-ion batteries, supercapacitors, and photocatalysis.

Chapter 9. Discussion

The field of synthesis of nanoparticles has become a fascinating branch of science, since their inception in the nineteenth century.[432-434] The synthesis of nanoparticles can be carried out by hydrothermal synthesis, chemical reduction, gas condensation, ion implantation, pyrolysis, thermal decomposition, and hot-injection method.[417-422,435] The morphology, size, and size distribution of the produced nanoparticles can be controlled by changing the method of synthesis, reducing agent, and stabilizing factors, besides other parameters such as pH, temperature, reaction time, concentration of the precursors and the solvent, and mechanical agitation.[27, 436]

Controlling the morphology, size and size distribution is an important requirements for the applications, which have been achieved through the careful selection of reducing agents. On the other hand, the occurrence of aggregation and agglomeration of the nanoparticles due to Ostwald ripening (Figure 9.1), their high surface energy, large surface area, and the continuous nucleation, can be controlled by using capping ligands such as polymer or surfactant to stabilize the nanoparticles sterically or electrostatically, respectively.[437-438]

The use of the capping ligands to stabilize the nanoparticles resulting in changing their surface properties and the accessibility to the surface of the nanoparticles, which lead to trying to find an alternative reaction media for synthesis and stabilize the nanoparticles.[27, 150]

Ionic liquids (ILs), which have been widely studied covering many fields, including organic synthesis, electrochemistry, mass spectroscopy, and electrophoresis because of their chemical tunability and their unusual physical and chemical properties, became a well-suited for the synthesis and stabilize the nanoparticles.

Of particular interest to the current study, metal-containing ionic liquids (MILs) and ionic liquid crystals (MILCs) have been extensively investigated, owing to their exciting and potentially physical and chemical properties with additional magnetic, optical, or catalytic properties depending on the type of the metal ion.[12, 231, 245-259] These MILs, where the metal is an integral part of the IL anion, act as metal source, morphology directing template, and stabilizer for the synthesis of metal chalcogenides (MCs), which present the most important class of nanoparticles.
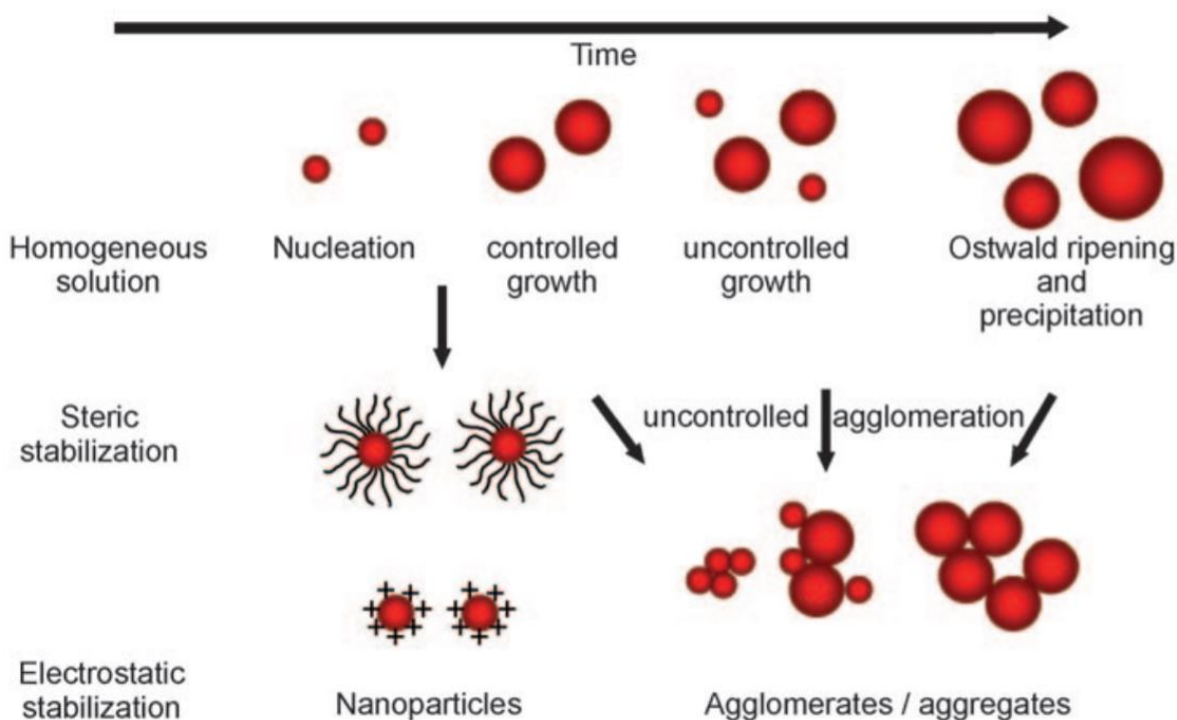
Figure 9.1. Growth and stabilization of nanoparticles.[439]

9.1. Metal-containing Ionic liquids (M-ILs): synthesis and crystal structures

A series of MILs based on alkyl pyridinium cations composed of various transition metal components have been synthesized, and their thermal behavior was found to depend on their crystal structures. *N*-butylpyridinium ILs $[C_4Py]_2[CuCl_4]$, $[C_4Py]_2[CoCl_4]$, $[C_4Py]_2[ZnCl_4]$, and $[C_4Py]_2[Cu_{0.39}Co_{0.61}Cl_4]$ were synthesized and their crystal structures were studied. They are isostructural and crystallize in the monoclinic space group $P2_1/n$. The asymmetric units contain four cations and two anions. The cations and anions are arranged in alternate layers where all the planar pyridinium rings are parallel to each other.

Furthermore, the IL, $[C_4Py]_2[Cu_2Cl_6]$, with a higher copper content was synthesized, and their crystal structure shows that it is isostructural with the family of *N*-butylpyridinium tetrachloridometllate. It crystallizes in the monoclinic space group $P2_1/n$ with two cations and half anion in the asymmetric units contains.

On the other hand, the crystal structures of *N*-dodecylpyridinium ILs $[C_{12}Py]_2[CoCl_4]$ and $[C_{12}Py]_2[ZnCl_4]$ are isostructural and crystallize in the triclinic space group $P\bar{1}$, consistent with the results reported in the literature of $[C_{12}Py]_2[PdCl_4]$.[264] The asymmetric units contains two cations and one anion.

Figure 9.2a shows the asymmetric unit of $[C_4Py]_2[CoCl_4]$, as an example of *N*-butylpyridinium ILs, and Figure 9.2b shows the asymmetric unit of $[C_{12}Py]_2[CoCl_4]$, as an example of *N*-dodecylpyridinium ILs. In the crystal structures of the short chain length ILs, the anions are located near the H^1 and H^5 of the ring, while with increasing the alkyl chain, the anions have been expelled from the head group of the cation. The alkyl chain of the cationic substituent became more twisted and screens the anions, consistent with the literature.[440]
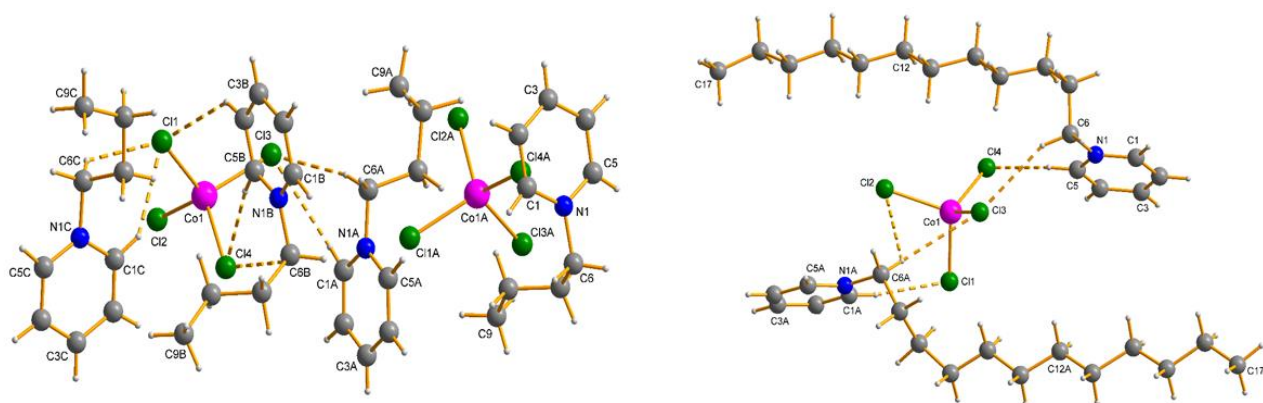
Figure 9.2. The asymmetric units of a) $[C_4Py]_2[CoCl_4]$, and b) $[C_{12}Py]_2[CoCl_4]$ with numbering scheme. Hydrogen bonds are shown as dashed lines.

Single crystal X-ray analysis showed that all compounds based on the same cation are isostructural. Powder X-ray diffraction (XRD) confirms the single-crystal X-ray analysis and shows that the alkyl chain length is the critical factor in controlling the crystal structure of these ILs. XRD indicates the purity of the powder samples, and they are identical to the single crystal samples.

Furthermore, the carbon atoms C7A to C9A in $[C_4Py]_2[CuCl_4]$ were disordered over two sites with occupation factors of 0.8/0.2 (Figure 9.3). This could be the reason that the single crystal of the long chain IL $[C_{12}Py]_2[CuCl_4]$ was hard to crystallize. However, yellow needles of $[C_{15}Py]_2[CuCl_4]$ with relatively poor crystal were formed by Neve et al.[263]
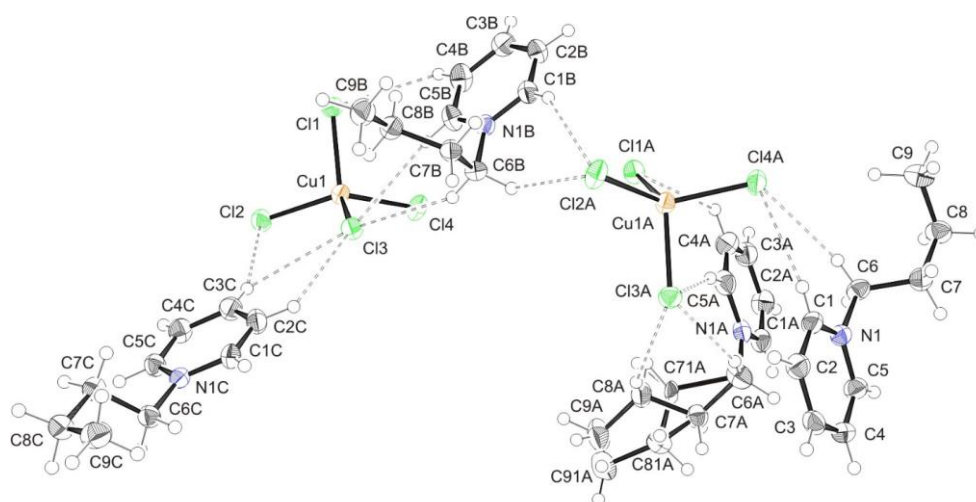
Figure 9.3. ORTEP plot of compound $[C_4Py]_2[CuCl_4]$. Hydrogen bonds as dashed lines.

The $[CuCl_4]^{2-}$ anion exhibits a high structural flexibility than the Co and the Zn analogs, which provides additional control over the phase behavior. The difference in the geometric flexibility indicates the subtle role of the metal ion on the stabilization of mesophases. The structural flexibility of the $[CuCl_4]^{2-}$ moieties was studied by EPR, as shown in Figure 9.4.

The variation of the g_{av} values, which correspond to the isotropic g_{iso} values, of both compounds $[C_4Py]_2[CuCl_4]$ and $[C_{12}Py]_2[CuCl_4]$ reveals their structural flexibility. For $[C_4Py]_2[CuCl_4]$, the g_{av} value is 2.155, while the g_{av} value of 2.201 in the case of $[C_{12}Py]_2[CuCl_4]$. The g_{av} values reflect a significant distortion of the expected tetrahedral coordination geometry of the $[CuCl_4]^{2-}$ dianion. On the other hand, the coordination environment of the Cu^{2+} ions of *N*-butylpyridinium hexadichloridocuprate (II) can be better described by a flattened tetrahedron rather than square-planar. The coordination geometries of copper (II) complexes depend on the Jahn-Teller distortions in the d^9 electronic system, crystal field stabilisation, ligand–ligand repulsion, ligand–lattice interactions, and crystal packing effects.[278, 282, 289]
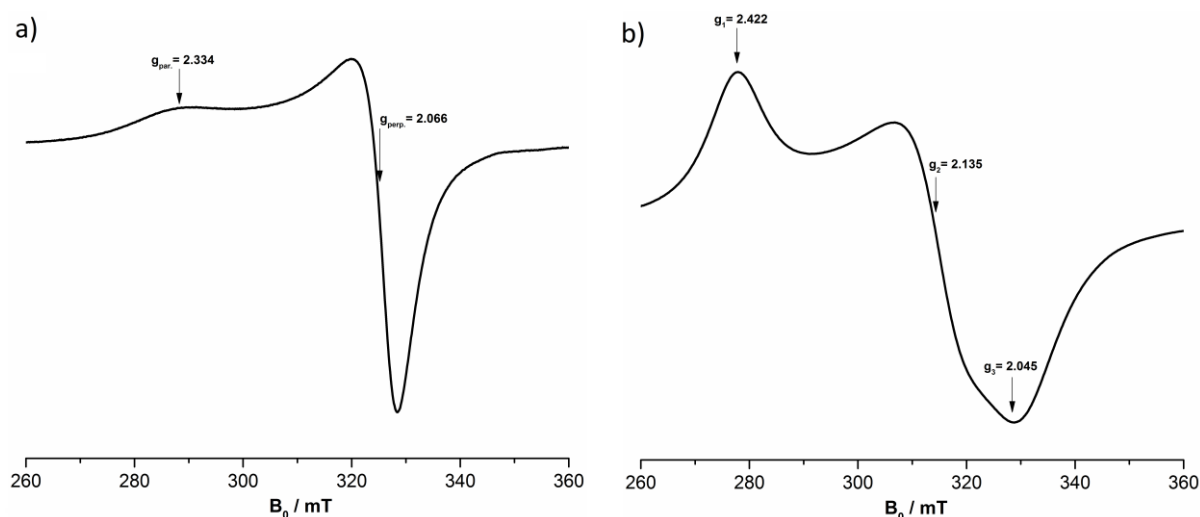
Figure 9.4. EPR spectrum of a pure sample of a) $[C_4Py]_2[CuCl_4]$, and b) $[C_{12}Py]_2[CuCl_4]$ measured at 150 K.

9.2. Thermal properties of ILs

The thermal stability of all ILs and the phase transition temperatures together with the transition enthalpy values were investigated by TGA, DSC, and POM. The glass transition temperature (T_g) of the IL $[C_{12}Py]_2[CuCl_4]$ (-43.9 °C) was slightly lower than their value of the shorter chain length $[C_4Py]_2[CuCl_4]$ (-40.4 °C) confirmed the influence of the alkyl chain length on the glass transition temperature. The alkyl chain elongation in the cation of the ILs results in lowering T_g due to the reduction of the lattice energies through disruption of the packing efficiencies as a result of the extension of the substituent attached to the nitrogen atom.[441]

In general, the evolution of T_g cannot be explained merely by the anion size, but the experiments show that T_g increases with increasing the anion size as T_g of $[C_4Py]_2[Cu_2Cl_6]$ (-34.0 °C) higher than T_g of $[C_4Py]_2[CuCoCl_4]$ (-37.6 °C) more than their value of $[C_4Py]_2[CuCl_4]$ (-40.4 °C). The T_g depends on the anion size due to the changing in the interaction strength between the anion and the cation. The current study does not agree with the suggestion by Binnemans et al.[442] They suggested that T_g increases with decreasing the anion size.

Consistent with the literature, the only derivatives with the longer chain (*N*-dodecylpyridinium ILs) exhibit liquid crystallinity due to the microphase segregation between the ionic parts and the long alkyl chains. The melting enthalpy changes for all compounds are relatively large (about 33 kJ·mol^{-1}) due to a significant structural change in the melting. In contrast, the enthalpy changes on clearing are small due to the weak van der Waals interaction between their alkyl chains. The existence of mesophases for *N*-dodecylpyridinium ILs is confirmed by POM, as shown in Figure 9.5. Their optical texture

appeared as well-developed focal conic fan texture characteristic of a lamellar phase (SmA phase) upon cooling from the isotropic liquid.
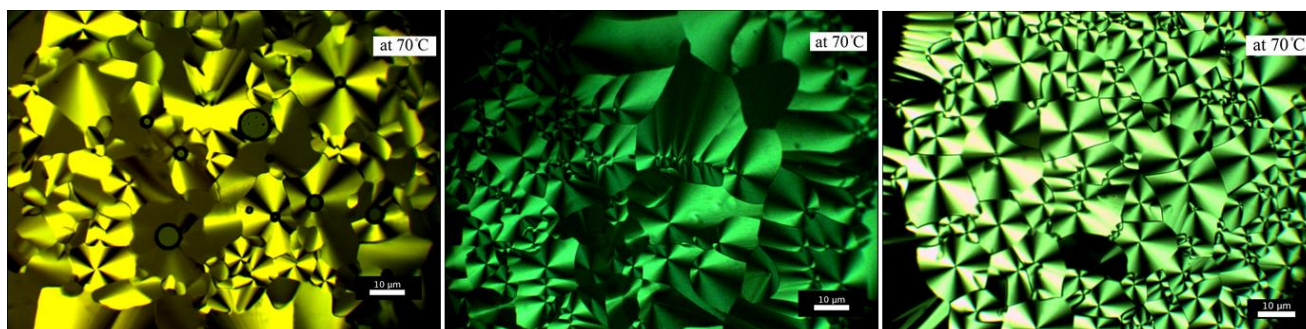
Figure 9.5. a) POM images of $[C_{12}Py]_2[CuCl_4]$ (left), $[C_{12}Py]_2[CoCl_4]$ (middle), and $[C_{12}Py]_2[ZnCl_4]$ (right) were taken at 70 °C.

The comparison of the melting temperatures (T_m) between the short and the long alkyl chain ILs cannot be done as the T_m is a result of a balance between the fusion enthalpy and fusion entropy. For short alkyl chain ILs, their fusion enthalpies are similar and their fusion entropies play the dominant role on the T_m. While for long alkyl chain ILs, their fusion enthalpies increases with increasing the alkyl chain length resulting rise in the T_m.[443]

The thermal stability of ILs increases with shorter chain length, $[C_4Py]_2[MCl_4] > [C_{12}Py]_2[MCl_4]$ (M = Cu, Co, Zn). The influence of the long chain length on the thermal stability could be interpreted that the long chain length increases the van der Waals forces resulting in decreasing the intermolecular electrostatic interaction, which leads to the lower thermal stability. However, the thermal stability caused by the different metal anions greater than the influence of the chain length. This is consistent with the literature, that the thermal stability of ILs is highly anion dependent. The impact of increasing coordinating nature, nucleophilicity, and hydrophilicity of the corresponding anion is to decrease the thermal stability of their ILs.[102, 110, 444-445]

Based on the crystal structures, the current study refines the suggestion by Bowlas et al.,[279] They suggested that the anions are positioned between the aromatic rings and the mesophase behavior resulted from the interdigitating of the alkyl chains (Figure 9.6a). The crystal packing, driven by coulombic interactions with non-classical hydrogen bonding, has pyridinium rings arranged in a parallel and the alkyl chains are arranged in an antiparallel to each other. In the ionic sublayer, $[MCl_4]^{2-}$ is located in the inversion center between two pyridinium rings. As a result, the layer structure is arranged with alternating polar and apolar

112

sublayer (Figure 9.6b). This study, consistent with a suggestion from Neve et al.,[264] proposes that the focal conic fan texture characteristic of a lamellar phase (SmA phase) is caused by the bilayer structure. However, these mesomorphic structures are different from that observed for $[C_{16}Py]_2[PdCl_4]$ salt, in which a fully interdigitated bilayer structure has been suggested.[262] The layer spacing of the interdigitated structures increases with increasing the alkyl chain length resulting in induced and stabilized the mesophase.
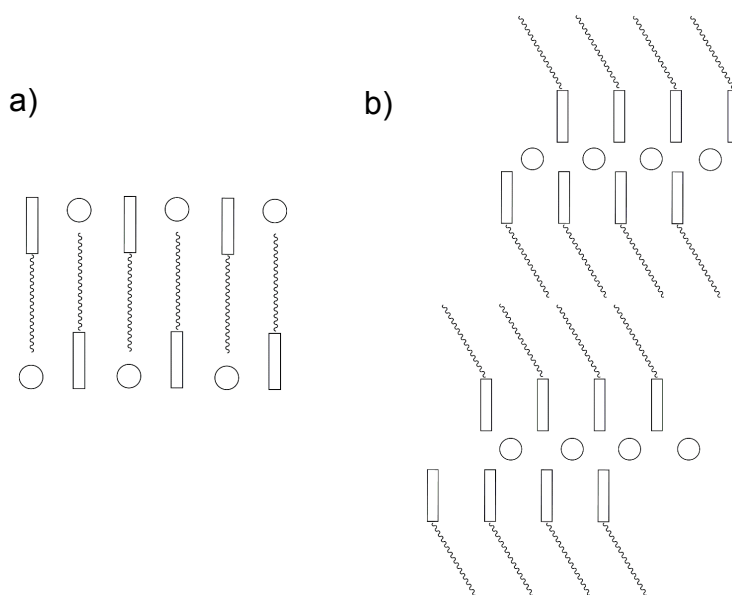
Figure 9.6. (a) Original structure model for the LC phase as suggested by Bowlas et al.,[279] and (b) the structure proposed based on the current data for the smectic phase of $[C_{12}Py]_2[MCl_4]$ (M= Cu, Co, and Zn). Rectangles: organic cation connected to the alkyl chain and circles: anions.

9.3. Nanomaterials: synthesis, morphology, and crystal phase

This study has been expanded on the fundamental aspects of the ionic liquid (crystal) precursor (ILCP). The general concept has been demonstrated to provide access to inorganic nanomaterials, which cannot be obtained via conventional methods such as the unique platelets morphology of $CuCl$ and the high fraction of Fe_3C, which increases their magnetic moment.[1, 50, 265, 446]

In the current study, a tailored and priori design of micro-/nano-materials, including CuS 3D-microstructures, and CuS hexagonal nanoplates were synthesized via a novel, facile, and highly controllable hot-injection synthesis method using the ILP where the metal is an integral part of the IL anion as the metal source. Furthermore, Carrolite ($CuCo_2S_4$) nanoparticles have been obtained by using ILP containing two metal as a single source precursor. The morphology of the resulting materials can be tuning with increasing the carbon chain length of the ILP, which exhibit liquid crystal phase behavior. The crystal phases have been adjusted with reaction conditions, which enables to understand the mechanism of the phase transformation (see also Sec. 9.5.1).

The XRD reflections of the CuS particles can be indexed to the hexagonal phase of the covellite (CuS) structure (*P6₃/mmc*, primitive hexagonal unit cell with $a = b = 3.7900$ and $c = 16.3400$ Å, JCPDS 98-002-6968), as shown in Figure 9.7a. The possible mechanism of forming such hexagonal CuS structure could be due to its anisotropic structure. The CuS crystal structure consists of Cu-S layers linked together by S-S covalent bonds. Every Cu-S layer comprising of a triangular CuS_3 layer which is sandwiched between two layers of tetrahedral CuS_4, as shown in Figure 9.7b. The interactions between the CuS_3 triangular layer and the CuS_4 tetrahedral layer are covalent bonds, while the interactions between the disulfide layers are Van der Waals interactions, the green bonds in Figure 9.7c. The intrinsic anisotropic crystal properties dominate the shape of the hexagonal CuS structure. The rate of crystal growth along the top-bottom crystalline planes much be more significant than along the *c-axis*.[281, 447]
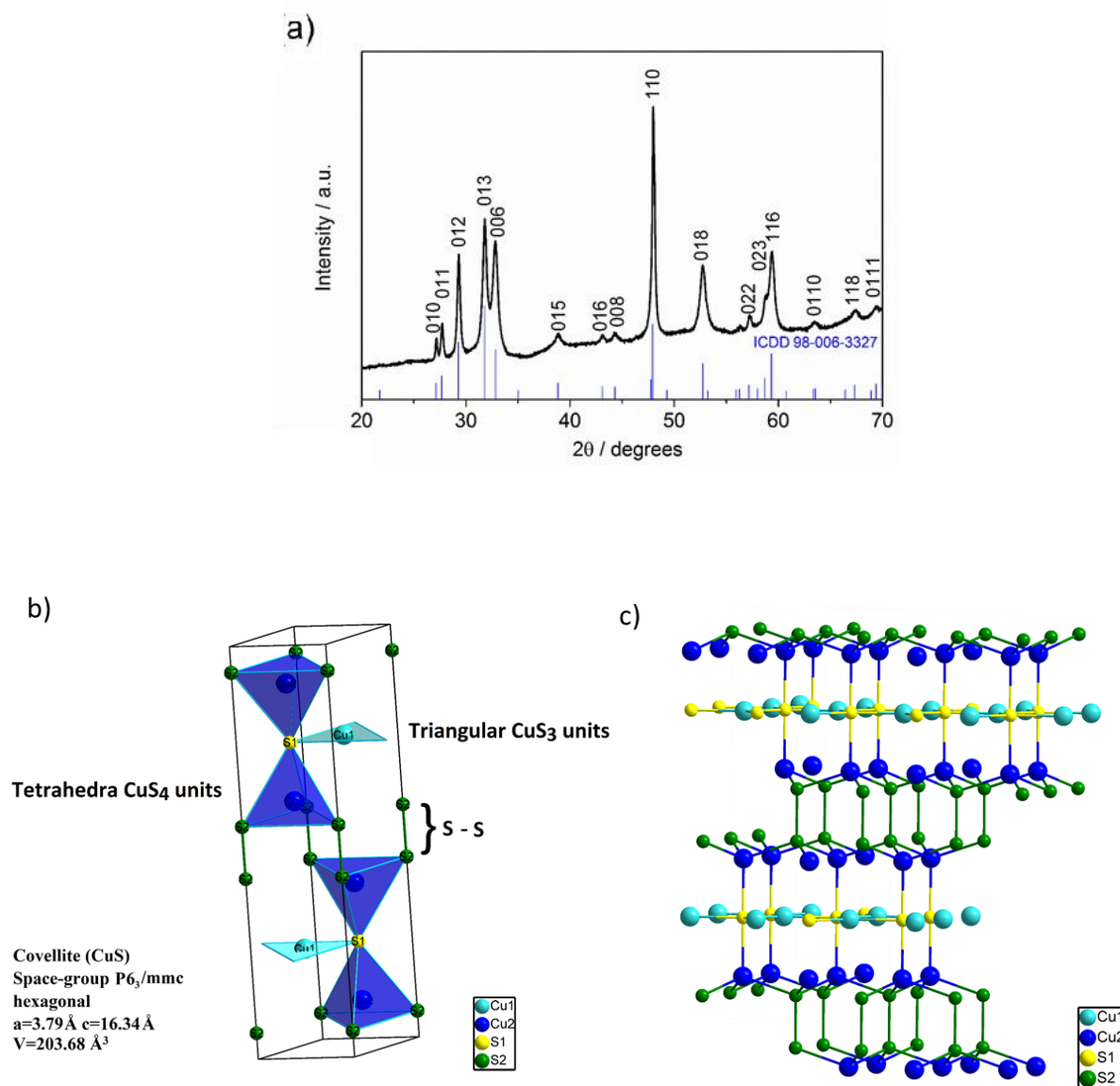
Figure 9.7. a) XRD pattern of CuS nanoparticles, b) Structure of covellite CuS. Adapted from Evans et al.,[332] and b) A schematic illustration of the crystal structure of CuS.

9.4.   Alkyl chain effects

To investigate the effect of the IL on the morphology of CuS, CuS samples were prepared by two different ILPs $[C_{12}Py]_2[CuCl_4]$ and $[C_4Py]_2[CuCl_4]$. The ILP $[C_{12}Py]_2[CuCl_4]$ tend to form thermotropic LC with increasing of the alkyl chain length, and the arrangement of the $[Cation]^+$ is more ordered along a preferred direction. Additionally, long chain ILs possess large steric effects to form a tighter coverage layer resulting the as-prepared nanoparticles grown in a lamellar liquid crystal will have a plate-like morphology (Figure 9.8a),

while the as-prepared nanoparticles grown in a disordered IL matrix will likely have a spherical morphology (Figure 9.8b).[279, 281] This is consistent with the literature, Zheng et al.,[281] investigated the effect of ILP on the morphology of CuS. The disordered plate-like structure is obtained when $CuCl_2.H_2O$ is used as Cu source, while the sphere-like structure assembled by nanosheets is obtained when $[Bmim]_2[Cu_2Cl_6]$ was used as a precursor. By increasing the carbon chains in $[Omim]_2[Cu_2Cl_6]$, the arrangement of the nanosheets is orderly with large intervals between them.
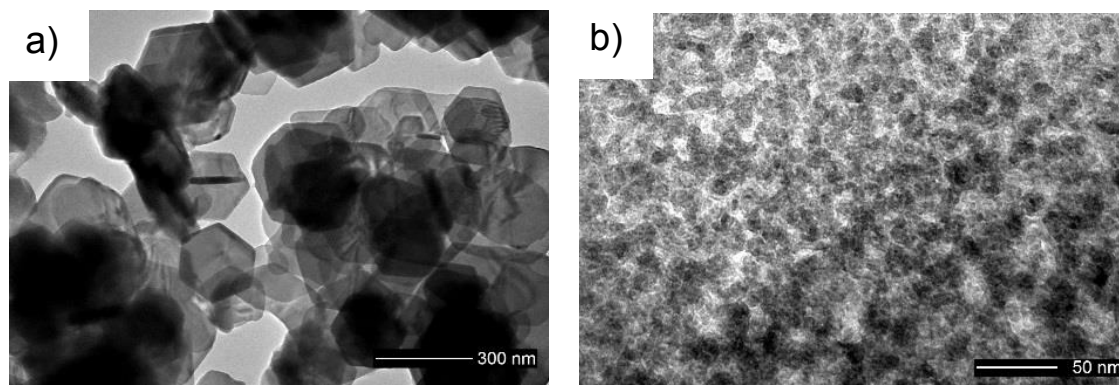
Figure 9.8. TEM images of CuS nanoparticles made from ILPs based on (a) the *N*-dodecylpyridinium, and (b) the *N*-butylpyridinium cation and the $[CuCl_4]^{2-}$ anion.

9.5. CuS microstructures synthesis

In chapter 6, copper sulfide microflowers were synthesized using the bis butylpyridinium tetrachoridocuprate (II) IL and their morphology, size, and the chemical composition are controlled by reaction time and temperature. The results show that the reaction temperature and growth time are crucial factors on the final morphology and size of the as-prepared CuS, beside the strong influence of the stirring on the particle formation process.

On increasing the reaction time, pure hexagonal with high crystallinity was synthesized at 160 °C at different reaction times. The crystallite size was calculated as 25 nm from XRD data using Scherrer's equation. SEM images show that the size of the individual building blocks (the flakes) remains roughly identical with increasing their aggregation. CuS nanoflakes are self-assembled to form ball-like microstructures (Figure 9.9B), and then form chrysanthemum-like microstructures (Figure 9.9C), to result in hierarchical flower-like microstructures (Figure 9.9D).
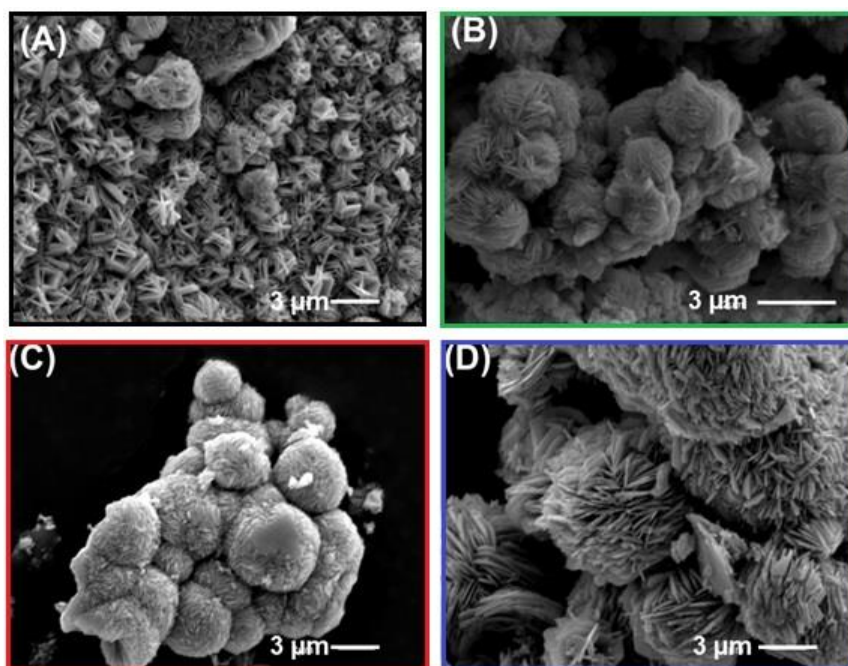
Figure 9.9. SEM images of CuS particles obtained at 160℃ after various reaction times; (A) 1 h, (B) 4 h,   (C) 6 h, and (D) 8 h.

On increasing the reaction temperature, the morphologies of the products evolve from irregular particles morphologies at 120 °C (Figure 9.10A), highly aggregated flakes with 2μm of the size of the flake at 140 °C (Figure 9.10B) to hierarchically structured flower-like microstructures composed of intersecting nanoflakes at 160 ℃ (Figure 9.10C). Higher reaction temperature of 170 °C produce particles with a rather diverse set of morphologies with a "stacks of pancakes" morphology (Figure 9.10D). Ball-like microstructures with a diameter around 3 μm are observed at 180 °C (Figure 9.10E). The "stacks of pancakes" morphology is observed again with much lower degree of morphological order at 200 °C (Figure 9.10F).
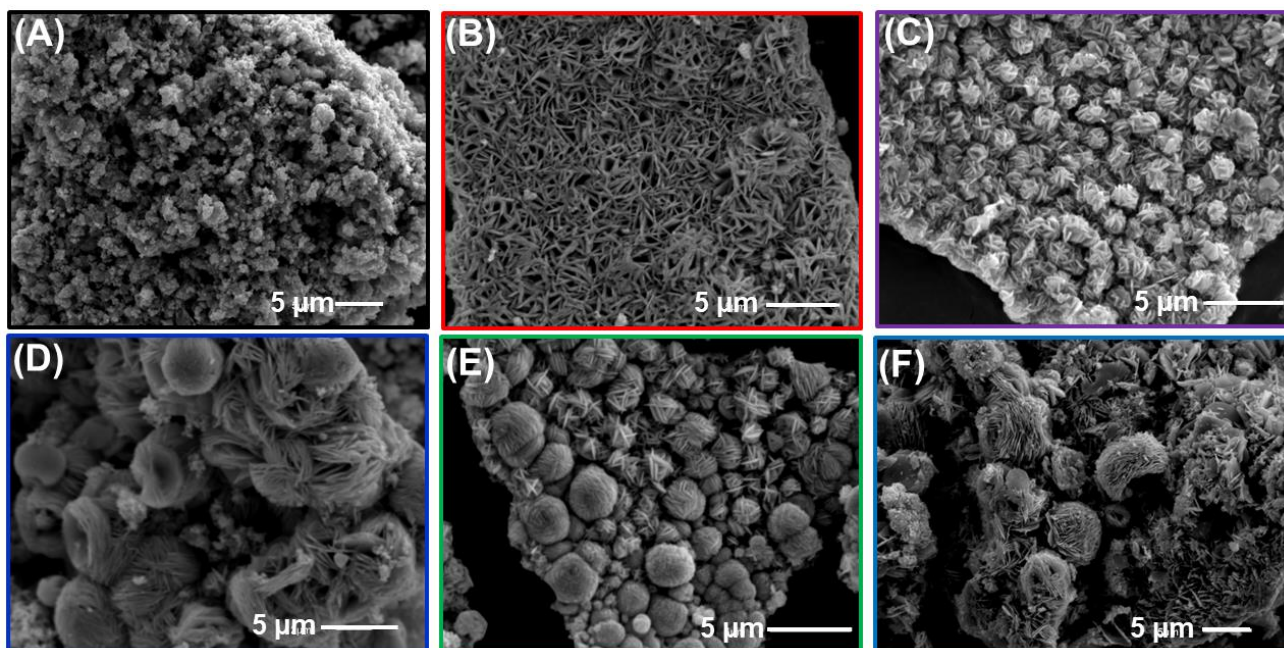
Figure 9.10. SEM images of CuS particles synthesized at different reaction temperatures. (A) 120 ℃,

(B) 140 ℃, (C) 160 ℃, (D) 170 ℃, (E) 180 ℃, and (F) 200 ℃ using a constant reaction time of 1 h.

The size and shape of the copper sulfides particles depend on different parameters, such as the rate of nucleation or primary particles, the reactants concentration, the reaction temperature, the growth time, and the time of precipitation.[448] These parameters will need to be understood with simulation studies before we are able to adjust or predict the size and shape of copper sulfides nanocrystals.

The formation of different morphologies of the as-prepared CuS is believed to be due to the fabrication and self-organization of the particles (oriented-attachment mechanism) with the low solubility of products of CuS (K_{sp} = *6.3* · *10^{-36} mol·dm^{-3}*).[448-451] The precipitation will occur when the reactants concentration exceeds the solubility of the precipitate. The nucleation centers firstly are formed homogenously in the solution. They then further grow into primary particles and aggregate to form larger particles. When the nucleation rate or formation of primary particles is fast, the time taken to complete the precipitation is consequently short leading to forming small particles due to the short time of aggregation. On the other hand, when the nucleation rate is short, the large particles are formed.[448]

Based on the results of the experiments, it can be concluded that the large size distribution and their aggregation could be due to adhesive mechanism of growth typical of high supersaturation conditions with the occurrence of continuous nucleation, which the

precursors are still formed as nucleation takes place. The nucleation and growth phases are not separated, which distinguished from the Finke - Watzky models from LaMer's nucleation and growth mechanism.[396, 452-454]

Furthermore, the reversible phase transformation between covellite (CuS) and digenite (Cu_9S_5) has been observed for the as-prepared copper sulfide particles which were synthesized by ILP $[C_4Py]_2[CuCl_4]$ at 160 °C ≤ T ≤ 180 °C, as shown in Figure 9.11a. The reduction reaction which exists during the experiments leading to changing $Cu(II)$ into $Cu(I)$. The reductive degree, which is affected by the reaction temperature, tend to increase the diffusion rate of ions. The diffusion rate of Cu^{+2} ions is faster than the diffusion rate of S^{-2} leading to forming the hollow sphere (Figure 9.11b). This phenomena can be explained by localized Ostwald ripening, which refers to the growth of larger particles from the smaller CuS primary particles which are present in the center. These primary particles have higher solubility than the larger one.[428, 455-456]
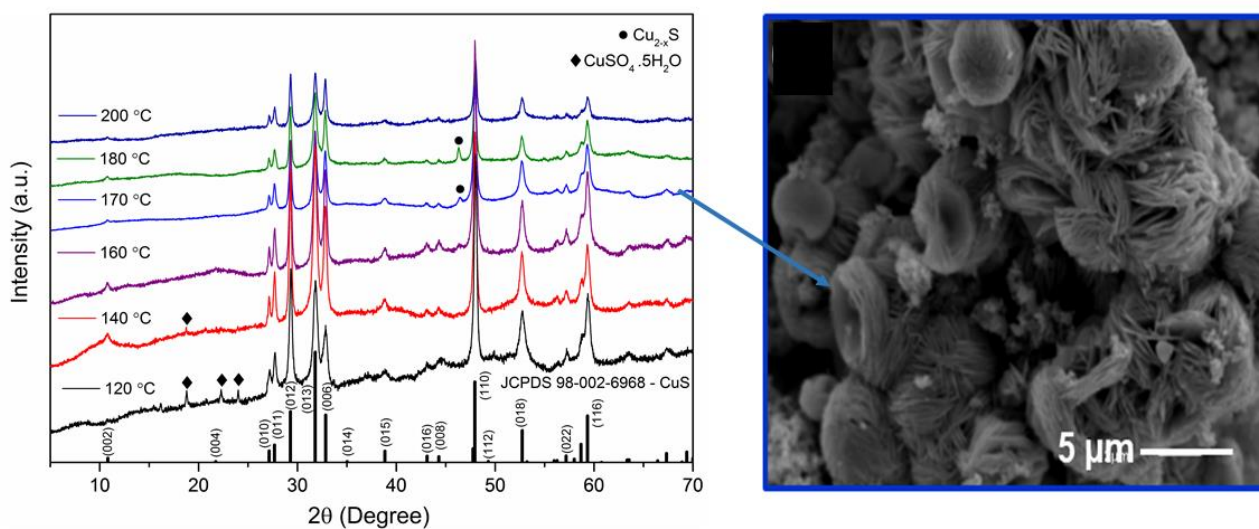
Figure 9.11. (a) XRD patterns of CuS particles prepared at different temperatures, and (b) SEM image of CuS particles synthesized at 170 ℃ for 1 h.

9.5.1. Phase transformation

For comparison, another ILP $[C_{12}Py]_2[CuCl_4]$, which serves as a copper source, has been used to drive the reversible phase transformation mechanism. Figure 9.12 shows the corresponding XRD patterns of the CuS particles, which were synthesized by ILP $[C_{12}Py]_2[CuCl_4]$. The products obtained at 1, 8, and 12 h exhibit reflections that can be indexed to the pure hexagonal phase of the covellite (CuS) structure (P6$_3$/mmc, a primitive hexagonal unit cell with a = b = 3.7900 and c = 16.3400 Å, JCPDS 98-002-6968). Furthermore, particles prepared at 6 and 8 h display the forward transformation from the hexagonal phase of the covellite (CuS) structure to the rhombohedral phase of the digenite (Cu$_9$S$_5$) structure (*R-3m*, rhombohedral unit cell with a = b = 3.930 Å, c = 48.140 Å, JCPDS Card no: 47-1748). Additionally, the reversible transformation was observed at 8 h.
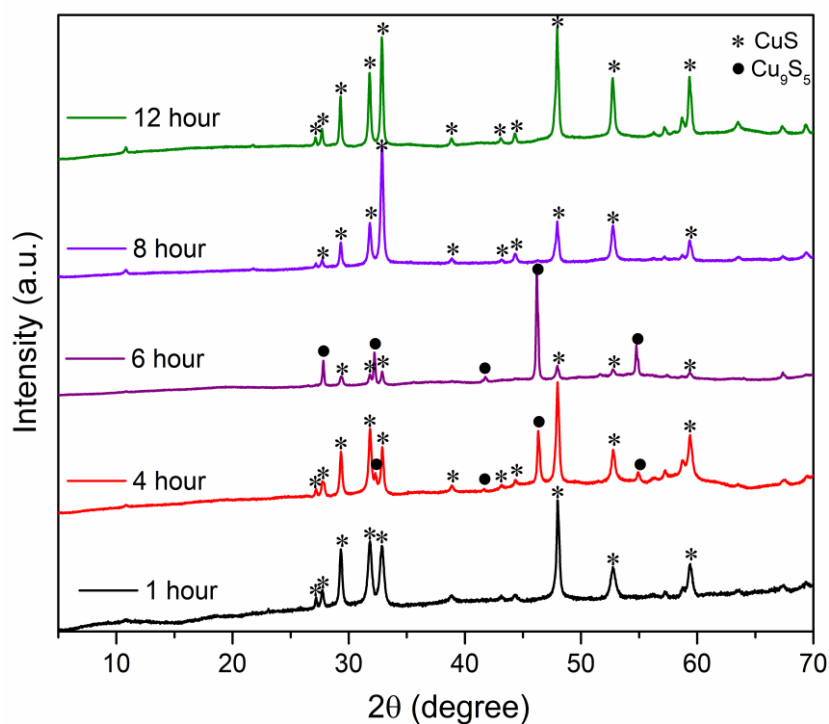
Figure 9.12. XRD patterns of CuS particles prepared by ILP $[C_{12}Py]_2[CuCl_4]$ at 180 ℃ for different reaction time.

9.5.2. Crystal structures

Firstly, Figures 9.13 and 9.14 show the crystal structures of the covellite (CuS) and the digenite (Cu_9S_5), respectively, to understand the phase transformation between both structures. Covalent (CuS) contains six Cu atoms and six S atoms, in which four Cu ions have tetrahedral coordination (CuS_4), and two Cu ions have triangular coordination (CuS_3), while two S atoms are present as sulfide ions and four S atoms form disulfide ions (Figure 9.13a). The disulfide ions are aligned with the *c*-axis and arranged perpendicular to the *c*-axis, as shown in Figure 9.13b.
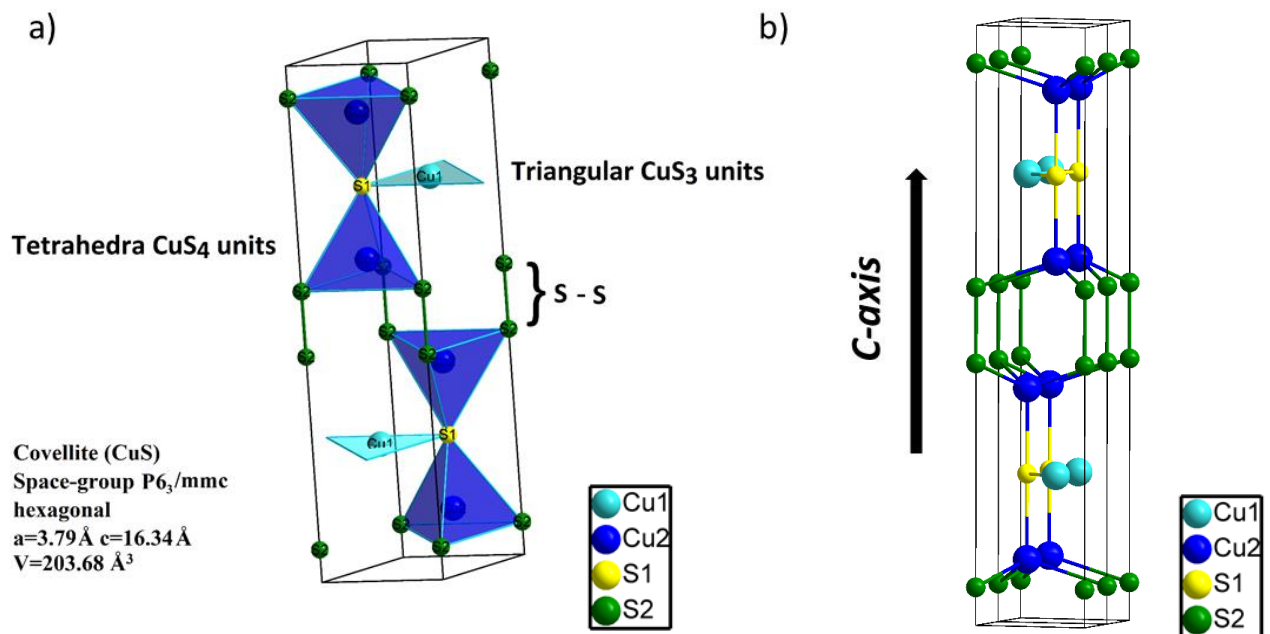
Figure 9.13. a) Crystal structure of covellite (CuS), and b) Cu and S atomic arrangements viewed along the *c*-axis direction of covellite (CuS).

On the other hand, the atoms of the digenite structure (Cu_9S_5) are arranged based on the *fcc* sub-lattice of S. The Cu atoms are located in three positions as $Cu1$ (octahedron CuS_6 units), $Cu2$ (tetrahedron CuS_4 units), and $Cu3$ (triangular plane CuS_3 units), as shown in Figure 9.14. The Cu atoms are occupied only 9/10 of their sites, leading to a robust p-type semiconductor.[457]
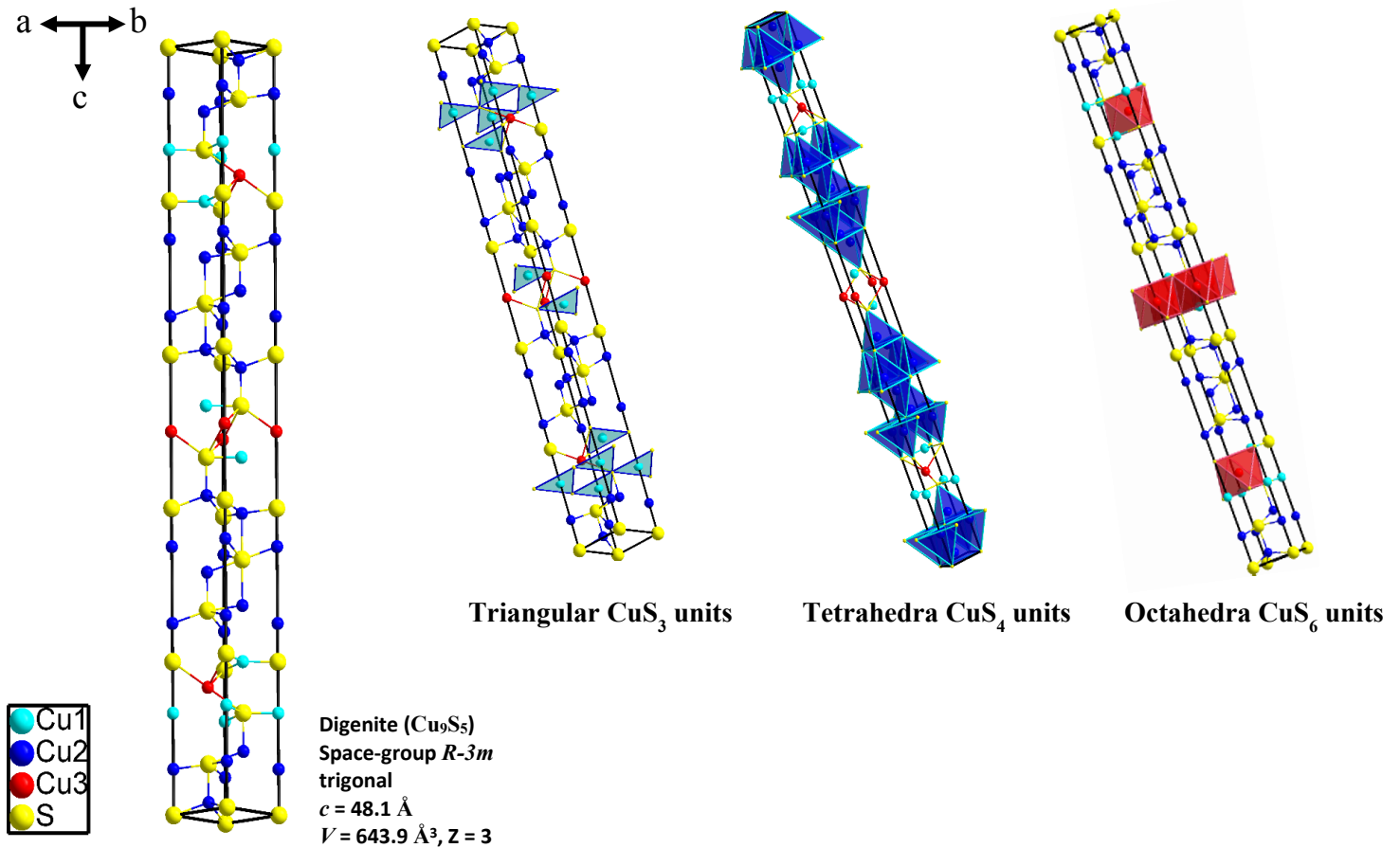
Figure 9.14. Crystal structure of digenite (Cu_9S_5).

9.5.3. Forward and reverse transformation

In the forward transformation from the covellite (CuS) structure to digenite (Cu_9S_5) structure, the ILP was used as a reducing agent to break the disulfide bonds. The breaking of the disulfide bonds was accompanied by the high activity of the excess of copper atoms, which fill the interstices in the S network resulting in increased the sulfur layers and expansion along the *c*-axis. The *c*-axis in covellite structure equal to 1.63 nm which expands to be 4.81 nm in digenite structure, as shown in Figure 9.15. With the presence of an excess of sulfur atoms in the system, the disulfide bonds will be retransformed, and the reverse transformation will occur which leading to shrinking of the crystal structure, as shown in Figure 9.15.
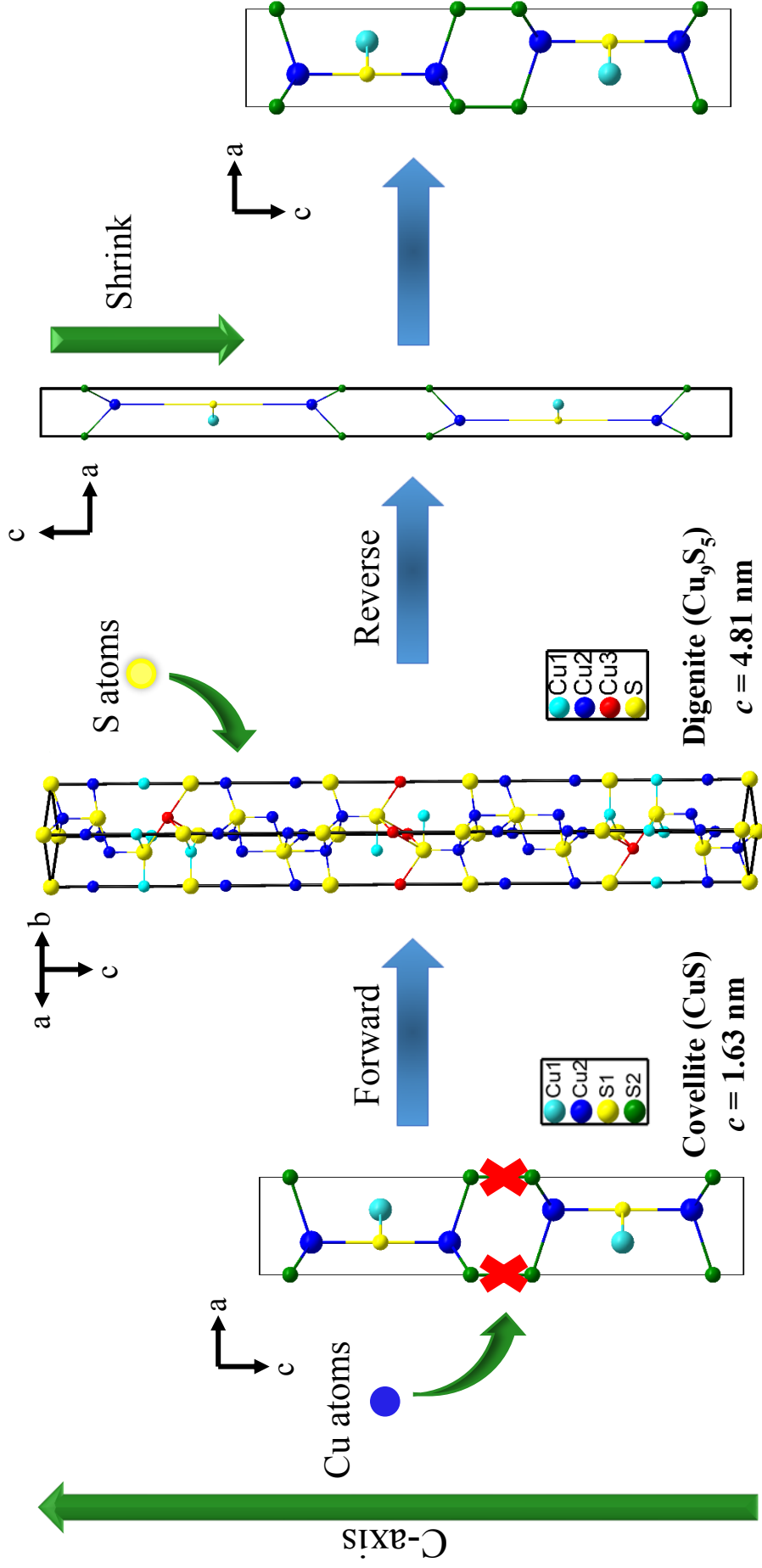
Figure 9.15. Schematic illustration of forwarding and reverse transformation between covellite (CuS) and digenite (Cu_9S_5) structures.

The primary peaks for covellite structure, corresponding to (100), (101), (102), (103), (006), (105), (106), (008), (110), (108), and (116) planes transformed to the corresponding peaks of digenite structure (111$\underline{5}$), (012$\underline{0}$), (101$\underline{7}$), (101$\underline{0}$), and (001$\underline{5}$) planes. The rapid reverse transformation, which occurred at 6 h, was observed by XRD. The XRD reflections revealed that the reverse transformed CuS have a similar covellite structure with different relative diffraction intensities.

The XRD reflections in Figure 9.16a and the crystal structures in Figure 9.16b shows that the (006) and (002) planes are critical points to understand the phase transformation from covellite structure to digenite structure. The (006) and (002) planes in covellite structure with a lattice spacing of 0.27 nm and 0.82 nm become to be 0.8 nm and 2.41 nm in digenite structure, respectively, which corresponds to breaking the disulfide bonds and the expansion in the *c-axis* during the forward transformation. This also can give an explanation of the rapid reverse transformation with different relative diffraction intensities. As it is mentioned before, the excess of S atoms will reform the disulfide bonds and increase the sulfur layers. This study provides new insights into the mechanism of the phase transformation of copper sulfides, and it also provides some explanation about their ability to form compounds with various stoichiometries.
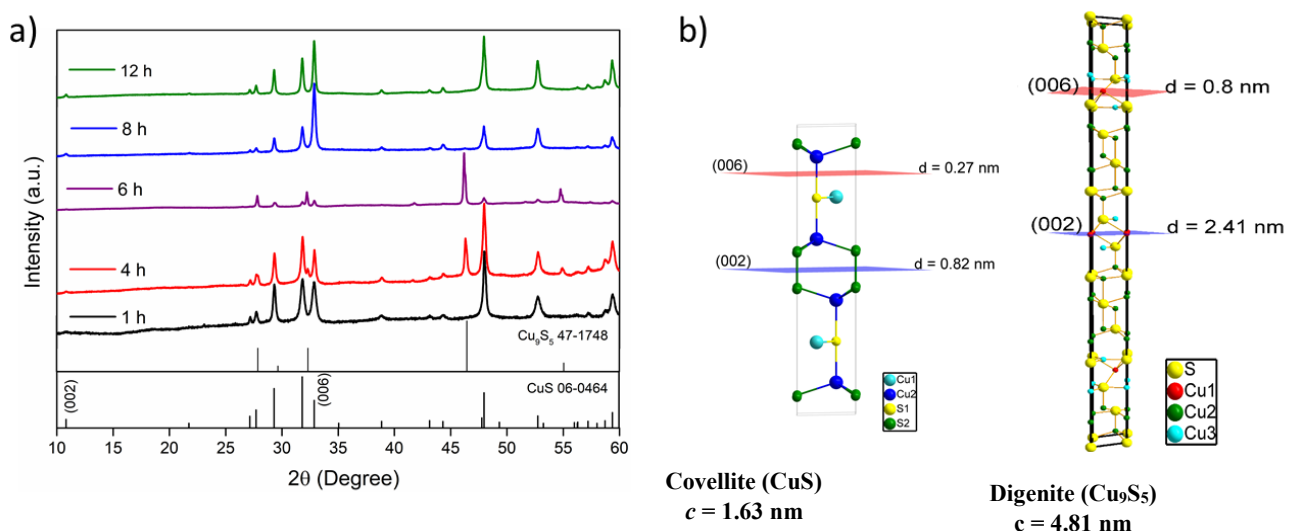
Figure 9.16. a) XRD patterns of CuS particles, and b) Crystal structures of covellite (CuS) and digenite (Cu_9S_5).

9.6. Electrochemical sensing of hydrogen peroxide

Furthermore, cyclic voltammograms (CVs) of glass-carbon electrodes modified with $CuS_{irregular}$, $CuS_{nanoflakes}$, and CuS_{flower} were recorded in neat PBS resulting in the redox couple transformation of the Cu_2S/CuS for all electrodes. By repeating the same process at different scans, CuS_{flower} exhibits fast electron transfer kinetics.

By adding $2mM$ of H_2O_2, the as-prepared CuS_{flower} exhibit higher electrocatalytic activity for H_2O_2, and higher electrochemically active surface area than non-assembled CuS nanoflakes, as shown in Figure 9.17. This substantial enhancement is attributed to the high number of the active surface sites and a facilitated charge transfer attributed to their unique morphology.
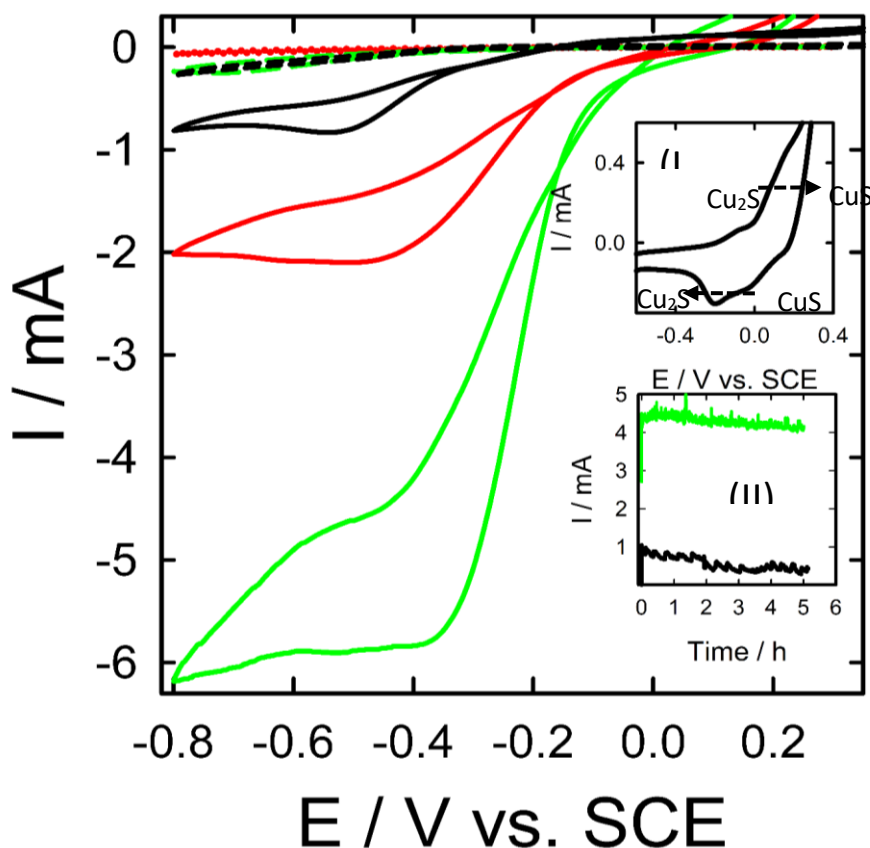
Figure 9.17. CVs measured at $CuS_{irregular}$ (black-lines), $CuS_{nanoflakes}$ (red-lines) and CuS_{flower} (green-lines) modified GC electrodes in 0.1 M PBS (*pH*~7.4) in the absence (dashed lines) and presence of 2 mM H_2O_2 with scan rate of 20 mV s^{-1}. Insets show (I) Zoom of the CuS_{flower} in the blank PBS (in the absence of H_2O_2) and (II) current transients (i-t, stability test) obtained at CuS_{flower} (green-line) and $CuS_{irregular}$ (black-line) modified GC electrodes in 0.1 M PBS containing 2 mM H_2O_2 at -0.3 V vs. SCE.

The inset II of Figure 9.17 shows that the high electrochemical stability of the as-prepared CuS flower-like microstructures, which their catalytic activity is only reduced by 2.5%, resulting in decreased the rate of in-situ oxygen bubble size 8 times and increased the oxygen bubble detachment rate 17 times compared to the $CuS_{irregular}$. This study demonstrates the significant role of the morphology on the catalytic performance.

Based on the results of the experiments, the improvement of the electrocatalytic activity of the CuS flower structures cannot only be attributed to their morphology and their electrochemically active surface area but also to the phase transformation between covellite and digenite with the diffution rate of ions on the surface.

Figure 9.18 shows that the decisive role of the morphology on the outstanding activity for H_2O_2 reduction. The CuS_{flower} materials exhibits a lower charge transfer resistance compared to non-assembled CuS. Furthermore, the high durability on the electrocatalytic activity of the CuS_{flower} materials for H_2O_2 electroreduction was investigated for 10 days from their CVs (Inset I of Figure 9.18) and their Nyquist plots (Inset II of Figure 9.18).
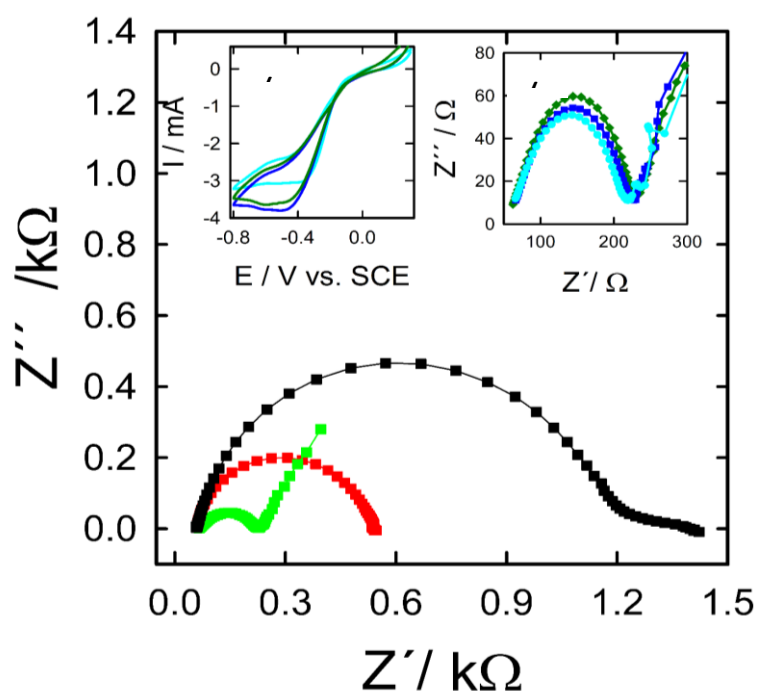
Figure 9.18. Nyquist plots obtained at $CuS_{irregular}$ (black-lines), $CuS_{nanoflakes}$ (red-lines) and CuS_{flower} (green-lines) modified GC electrodes in 0.1 M PBS (pH~7.4) containing 2 mM H_2O_2 at -0.2 V vs. SCE. Insets show (I) CVs and (II) their respective Nyquist plots obtained at CuS_{flower} modified GC electrode in the above-mentioned solution after 1 (cyan-lines), 7 (blue-lines) and 10 (green-lines) days

9.7. CuS nanoplates for organic photovoltaic cells

In chapter 7, hexagonal CuS nanoplates were synthesized using ILP $[C_{12}Py]_2[CuCl_4]$ and (TMS)$_2$S for the fabrication of OPV devices. The broad reflections in the XRD patterns and the Moiré patterns which are observed by TEM prove the high crystallinity of the nanoparticles.

Nevertheless, there have been challenges with the broad size distribution and the initially rather poor dispersibility. As the broad size distribution ranging from 30 to 680 nm, and some particles are standing vertical comparison to the other particles. Filtration has been used to remove the larger particles and aggregates. On the other hand, capping with Oleylamine (OAm) was used for the stabilization of the nanoparticles dispersion. The reduction of the particle size was confirmed by TEM.

After these modification processes, the optical properties of the NPs are improved – strong absorption below 450 nm, and the disappearance of the absorption above 450 nm in the UV-vis-NIR. The absorption above 450 nm can be assigned to large particles and their aggregation. The modified particles show larger bandgap (3.1 eV) than their bandgap before filtration (2.1 eV), which indicates the removal of the large particles. In consequences, the modified particles are interesting candidates for the active blend layer in OPV cells.

The surface morphology of the active P3HT:PCBM:CuS blend layer were evaluated via AFM. The embedded CuS NPs in the blend film has a slightly higher roughness than the blend film without the CuS NPS resulting that the P3HT:PCBM:CuS films are very homogenous without any protrusions, crazes, or other features.

Several devices with different architectures and compositions were made to investigate the role of the CuS NPs in both conventional and inverted device architectures. The high crystallinity of the P-type CuS NPs, which distributed in the BHJ active layer, provides increasing the carrier mobility by the additional interfacial area between the CuS NPs and the conjugated polymer resulting in increased the PCE from 0.14% to 0.35% in Device B (Figure 9.19a).

By improving the contact property between the Ag anode and the active layer upon embedding the CuS NPs in the active layer, V_{oc} improves from 0.39 to 0.56 V in Device D (Figure 9.19b). In addition, both V_{oc} and J_{sc} increase by adding an additional MoO$_3$ HCL between the active layer and the Ag anode in the control device (i.e., ITO/ZnO/P3HT:PCBM/MoO$_3$/Ag).

The experiments show that the contact property between the metal and the semiconductor in OPV cells are responsible for the improved V_{oc}. Additionally, the increased effective bandgap (the energy level difference between the acceptor LUMO and the donor HOMO) by embedded CuS NPs in P3HT:PCBM blend is also responsible for the increased V_{oc}.[458-461]
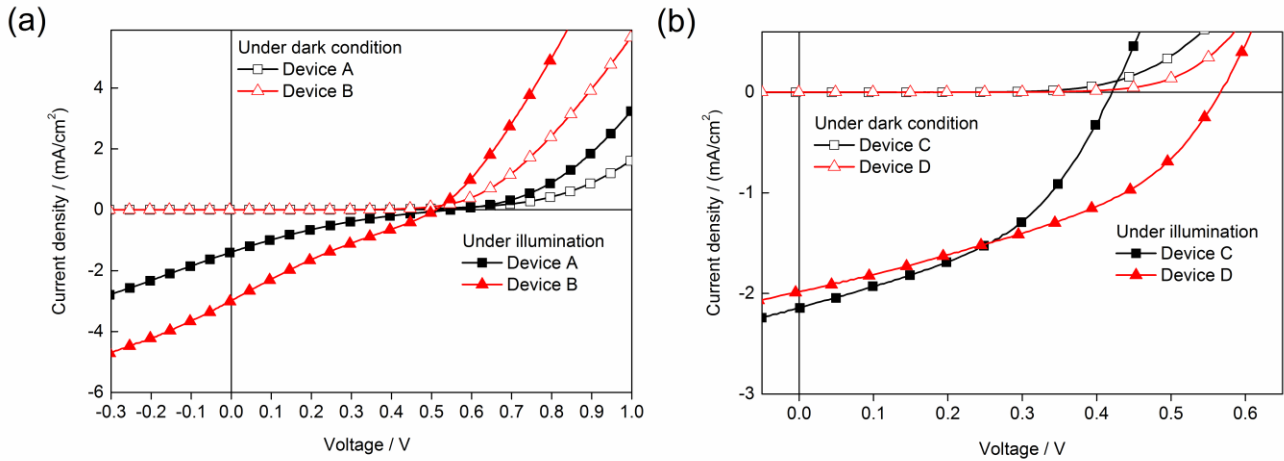
Figure 9.19. (a) J-V characteristics of conventional, and (b) inverted OPV cells.

The effect of the different CuS NPs concentrations on the device performance was investigated. Even though the FF of the devices decreases with increasing the CuS NPs concentrations due to the effect of the enhanced carrier recombination rate with the increased hole mobility or interface defects, the J_{sc} increases resulting in increased the PCE from 2.27% to 2.64% (i.e., by 16%). The changes of J_{sc} strongly depends on the CuS NPs concentrations. One more point, a higher concentration of the CuS NPs could be a leakage path in the BHJ due to the agglomeration.

Chapter 10. Conclusion

In this study, a facile hot-injection method was developed for synthesis binary and ternary metal chalcogenides (MCs), and their different crystal structures were carefully identified. CuS 3D-microstructures, CuS nanoplates, and $CuCo_2S_4$ nanoparticles were synthesized using the ILP where the metal is an integral part of the IL anion as the metal source. The ILP not only acts as a metal source but also as a morphology directing template and as a stabilizer for the resulting nanoparticles. Besides, their applications as non-enzymatic hydrogen peroxide sensor and as a hole conduction material into organic photovoltaic cells (OPV) are tested. This study provides new insights can be concluded as follows:

The results show that the subtle differences in the composition of the cations, especially the alkyl chain length, can have a large influence on the phase behavior and the structural organization of both the crystalline and the liquid crystalline phase. The stabilization of the mesomorphism of these ILs depends on the length of the alkyl chain and the structural flexibility of the anion moieties.

Furthermore, the morphology tuning of the copper sulfide revealed the structure directing effect of the ILP. Spherical NPs were grown in a disordered ILP, while hexagonal nanoplates were grown in a lamellar LC. Moreover, the particle morphology of the as-prepared CuS could be easily tuned by the reaction temperature and growth time. On increasing the reaction temperature, CuS nanoflakes self-assembled to form ball-like microstructures, and then form chrysanthemum-like microstructures, to result in hierarchical flower-like microstructures. It was concluded that the size of the flakes roughly will not change by the variation of the reaction parameters in contrast to their aggregation which is strongly affected by the reaction temperature.

A further investigation into the copper sulfide structures, the reversible phase transformation has been demonstrated between covellite (CuS) and digenite (Cu_9S_5). The forward transformation results in digenite (Cu_9S_5), induced by ILP reduction of the disulfide bonds in the covellite structure (CuS). This process results in increasing the growth along the *c-axis* of covellite CuS. The reversible transformation was induced by an excess of S atoms results in reforming the disulfide bonds and shrinking along with the *c-axis*, which leads to the transformation back to the covellite structure (CuS).

With the production of various CuS structures, the as-prepared CuS flower-like morphology exhibit excellent electrocatalytic activity toward H_2O_2 detection and excellent analytical performances with a 48 times higher sensitivity of 3.8 mM^{-1} cm^{-2}, and a lower detection limit (about 0.1 μM, 18 times lower) than non-assembled CuS nanoflakes. In addition, the as-prepared CuS microflowers showed a much better stability higher than non-assembled CuS nanoflakes. Their higher stability was believed to originate from the smaller oxygen bubbles formed and their faster detachment rates along with the lower rate of bubble accumulation on the flowerlike surface compared to non-assembled CuS nanoflakes.

Nevertheless, the hexagonal nanoplates CuS were successfully embedded in the active matrix of P3HT:PCBM using both conventional and inverted structures. The PCE of OPV cells fabricated with the nanoplates CuS shows an increase of 16% when compared to control devices made without the nanoplates.

The key finding of this work can be concluded in these points: (i) An efficient one-step (one-pot) procedure has been developed for the synthesis of ILs based on nitrogen-containing pyridinium cations and mono-, bi-, or di-metallic halide anions. (ii) These ILs have been transformed with high yields to binary and ternary MCs via low cost, environmental friendliness, and simple hot-injection method. (iii) The as-synthesized MCs are viable candidates for high performance non-enzymatic H_2O_2 amperometric detection and for the fabrication of OPV devices.

This study developed a facile approach for the crystal phase- and the shape-controlled synthesis of binary and ternary MCs, and provided an attractive single hole collection layer (HCL) in an organic solar cell and an electrocatalyst for H_2O_2 detection. The current research provides new insights for the design of semiconductor MCs nanostructures synthesis with special compositions for various applications, which includes photovoltaics, gas sensors, supercapacitors and water splitting.

Chapter 11. Appendix

Appendix A – Article I

Table 4.S1. Selected bond lengths [Å] of **1**.

C1 – N1	1.349(3)	C1 – C2	1.373(4)
C2 – C3	1.375(4)	C3 – C4	1.382(4)
C4 – C5	1.366(4)	C5 – N1	1.351(3)
C6 – N1	1.488(3)	C6 – C7	1.516(3)
C7 – C8	1.523(3)	C8 – C9	1.523(4)
C1A – N1A	1.343(3)	C1A – C2A	1.364(4)
C2A – C3A	1.376(4)	C3A – C4A	1.389(4)
C4A – C5A	1.362(4)	C5A – N1A	1.347(3)
C6A – N1A	1.491(3)	C6A – C7A	1.498(4)
C6A – C71A	1.816(13)	C7A – C8A	1.515(5)
C8A – C9A	1.525(6)	C71A – C81A	1.493(18)
C81A – C91A	1.529(19)	C1B – N1B	1.344(3)
C1B – C2B	1.368(4)	C2B – C3B	1.379(4)
C3B – C4B	1.378(4)	C4B – C5B	1.367(4)
C5B – N1B	1.346(3)	C6B – N1B	1.482(3)
C6B – C7B	1.517(3)	C7B – C8B	1.516(3)
C8B – C9B	1.513(4)	C1C – N1C	1.349(3)
C1C – C2C	1.365(4)	C2C – C3C	1.386(4)
C3C – C4C	1.383(4)	C4C – C5C	1.367(4)
C5C – N1C	1.352(3)	C6C – N1C	1.482(3)
C6C – C7C	1.521(3)	C7C – C8C	1.524(4)
C8C – C9C	1.519(4)	Cl1 – Cu1	2.2843(6)
Cl2 – Cu1	2.2319(6)	Cl3 – Cu1	2.2715(6)
Cl4 – Cu1	2.2325(6)	Cl1A – Cu1A	2.2759(6)
Cl2A – Cu1A	2.2284(6)	Cl3A – Cu1A	2.2782(6)
Cl4A – Cu1A	2.2369(6)		

Table 4.S2. Selected bond angles [°] of **1**.

N1 − C1 − C2	120.0(2)	C1 − C2 − C3	120.0(2)
C2 − C3 − C4	119.1(2)	C5 − C4 − C3	119.6(2)
N1 − C5 − C4	120.5(2)	N1 − C6 − C7	110.45(18)
C6 − C7 − C8	112.3(2)	C9 − C8 − C7	112.8(2)
N1A − C1A − C2A	120.6(2)	C1A − C2A − C3A	119.9(3)
C2A − C3A − C4A	118.8(3)	C5A − C4A − C3A	119.5(3)
N1A − C5A − C4A	120.6(2)	N1A − C6A − C7A	114.9(2)
N1A − C6A − C71A	92.8(5)	C6A − C7A − C8A	112.4(3)
C7A − C8A − C9A	112.7(3)	C81A − C71A − C6A	103.7(8)
C71A − C81A − C91A	113.2(11)	N1B − C1B − C2B	120.7(2)
C1B − C2B − C3B	119.6(2)	C2B − C3B − C4B	118.9(3)
C5B − C4B − C3B	119.8(2)	N1B − C5B − C4B	120.5(2)
N1B − C6B − C7B	111.55(19)	C8B − C7B − C6B	114.5(2)
C9B − C8B − C7B	113.0(2)	N1C − C1C − C2C	120.6(2)
C1C − C2C − C3C	119.7(2)	C4C − C3C − C2C	118.9(3)
C5C − C4C − C3C	119.7(2)	N1C − C5C − C4C	120.5(2)
N1C − C6C − C7C	111.30(19)	C6C − C7C − C8C	112.6(2)
C9C − C8C − C7C	112.9(2)	Cl2 − Cu1 − Cl4	133.86(3)
Cl2 − Cu1 − Cl3	102.58(2)	Cl4 − Cu1 − Cl3	100.49(2)
Cl2 − Cu1 − Cl1	101.58(2)	Cl4 − Cu1 − Cl1	101.48(3)
Cl3 − Cu1 − Cl1	118.64(2)	Cl2A − Cu1A − Cl4A	132.81(3)
Cl2A − Cu1A − Cl1A	101.19(2)	Cl4A − Cu1A − Cl1A	101.85(2)
Cl2A − Cu1A − Cl3A	103.44(3)	Cl4A − Cu1A − Cl3A	100.15(2)
Cl1A − Cu1A − Cl3A	119.36(2)	C1 − N1 − C5	120.7(2)
C1 − N1 − C6	119.89(19)	C5 − N1 − C6	119.3(2)
C1A − N1A − C5A	120.6(2)	C1A − N1A − C6A	118.6(2)
C5A − N1A − C6A	120.8(2)	C5B − N1B − C1B	120.4(2)
C5B − N1B − C6B	121.0(2)	C1B − N1B − C6B	118.61(19)
C1C − N1C − C5C	120.5(2)	C1C − N1C − C6C	120.21(19)
C5C − N1C − C6C	119.24(19)		

Table 4.S3. Selected torsion angles [°] of **1**.

N1 − C1 − C2 − C3	0.4(4)	C1 − C2 − C3 − C4	175.7(2)
C2 − C3 − C4 − C5	0.4(4)	C3 − C4 − C5 − N1	0.6(4)
N1 − C6 − C7 − C8	-176.3(2)	C6 − C7 − C8 − C9	70.3(3)
N1A − C1A − C2A − C3A	0.6(4)	C1A − C2A − C3A − C4A	0.1(4)
C2A − C3A − C4A − C5A	-0.4(4)	C3A − C4A − C5A − N1A	0.0(4)
N1A − C6A − C7A − C8A	-68.3(3)	C6A − C7A − C8A − C9A	-179.3(4)
N1A − C6A − C71A − C81A	175.2(8)	C6A − C71A − C81A − C91A	-175.6(10)
N1B − C1B − C2B − C3B	0.4(4)	C1B − C2B − C3B − C4B	-0.2(4)
C2B − C3B − C4B − C5B	-0.3(4)	C3B − C4B − C5B − N1B	0.4(4)
N1B − C6B − C7B − C8B	67.5(3)	C6B − C7B − C8B − C9B	173.9(2)
N1C − C1C − C2C − C3C	0.3(4)	C1C − C2C − C3C − C4C	-0.6(4)
C2C − C3C − C4C − C5C	0.3(4)	C3C − C4C − C5C − N1C	0.4(4)
N1C − C6C − C7C − C8C	-175.6(2)	C6C − C7C − C8C − C9C	67.1(3)
C2 − C1 − N1 − C5	0.5(3)	C2 − C1 − N1 − C6	-176.2(2)
C4 − C5 − N1 − C1	-1.0(3)	C4 − C5 − N1 − C6	175.7(2)
C7 − C6 − N1 − C1	104.7(2)	C7 − C6 − N1 − C5	-72.0(3)
C2A − C1A − N1A − C5A	-1.0(4)	C2A − C1A − N1A − C6A	179.1(2)
C4A − C5A − N1A − C1A	0.7(4)	C4A − C5A − N1A − C6A	-179.4(2)
C7A − C6A − N1A − C1A	-73.1(3)	C71A − C6A − N1A − C1A	-93.5(5)
C7A − C6A − N1A − C5A	106.9(3)	C71A − C6A − N1A − C5A	86.5(5)
C4B − C5B − N1B − C1B	-0.1(4)	C4B − C5B − N1B − C6B	179.9(2)
C2B − C1B − N1B − C5B	-0.3(3)	C2B − C1B − N1B − C6B	179.7(2)
C7B − C6B − N1B − C5B	-104.2(2)	C7B − C6B − N1B − C1B	75.7(3)
C2C − C1C − N1C − C5C	0.5(3)	C2C − C1C − N1C − C6C	-178.3(2)
C4C − C5C − N1C − C1C	-0.8(3)	C4C − C5C − N1C − C6C	178.0(2)
C7C − C6C − N1C − C1C	112.0(2)	C7C − C6C − N1C − C5C	-66.8(3)

Table 4.S4. Hydrogen bond geometry (Å, °) in **1**.

D–H…A	D–H	H…A	D…A	D-H…A
C2 – H2…Cl1A^{I}	0.95(3)	2.91(3)	3.560(3)	126(2)
C5 – H5…Cl1^{II}	0.92(3)	2.90(3)	3.728(3)	150(2)
C6 – H61…Cl4A	0.89(3)	2.77(3)	3.649(2)	169(2)
C6 – H62…Cl1^{II}	0.99(3)	2.77(3)	3.580(3)	139.7(19)
C2A – H2A…Cl1^{III}	0.92(3)	2.99(3)	3.586(3)	125(2)

C4A – H4A…Cl1A	0.95(3)	2.91(3)	3.612(3)	131(2)
C5A – H5A…Cl3A	0.94(3)	2.81(3)	3.719(3)	163(2)
C6A – H61A…Cl3A	0.98(3)	2.92(3)	3.806(3)	152(2)
C6A – H62A…Cl2^{II}	1.02(3)	2.70(3)	3.549(3)	141(2)
C71A – H74A…Cl2A^{IV}	0.99	2.88	3.806(12)	155.7
C2B – H2B…Cl3A^{V}	0.93(3)	2.89(3)	3.551(3)	130(2)
C4B – H4B…Cl1	0.93(3)	2.94(3)	3.647(3)	133(2)
C5B – H5B…Cl3	0.90(3)	2.87(3)	3.754(3)	168(2)
C6B – H61B…Cl2A	0.97(3)	2.79(3)	3.540(3)	134.0(19)
C6B – H62B…Cl3	0.96(3)	2.96(3)	3.839(3)	152(2)
C2C – H2C…Cl3	0.98(3)	2.84(3)	3.541(3)	129(2)
C4C – H4C…Cl3A^{VI}	0.86(3)	2.98(3)	3.608(3)	131(2)
C5C – H5C…Cl1A^{VI}	0.96(3)	2.88(3)	3.669(3)	141(2)
C6C – H61C…Cl4^{VI}	0.90(3)	2.85(3)	3.725(2)	164(2)
C6C – H62C…Cl1A^{VI}	0.95(3)	2.82(3)	3.601(3)	140(2)
C7C – H72C…Cl4A^{VII}	0.95(3)	2.97(3)	3.865(3)	158(2)

Symmetry codes: ^{I} -0.5+x, 1.5-y, -0.5+z; ^{II} -1+x, y, z; ^{III} -x, 1-y, 1-z; ^{IV} -0.5-x, -0.5+y, 0.5-z; ^{V} 0.5+x, 1.5-y, -0.5+z; ^{VI} -x, 1-y, -z; ^{VII} 0.5+x, 1.5-y, -0.5+z.

Table 4.S5. Selected bond lengths [Å] of **2**.

C1 – N1	1.342(3)	C1 − C2	1.363(3)
C2 – C3	1.372(3)	C3 – C4	1.374(3)
C4 – C5	1.369(3)	C5 – N1	1.338(2)
C6 – N1	1.485(2)	C6 – C7	1.519(3)
C7 – C8	1.509(3)	C8 – C9	1.513(3)
C1A – N1A	1.338(2)	C1A – C2A	1.370(3)
C2A – C3A	1.374(3)	C3A – C4A	1.380(3)
C4A – C5A	1.363(3)	C5A – N1A	1.350(2)
C6A – N1A	1.489(2)	C6A – C7A	1.532(3)
C7A – C8A	1.523(3)	C8A – C9A	1.487(3)
C1B – N1B	1.339(3)	C1B – C2B	1.364(3)
C2B – C3B	1.376(3)	C3B – C4B	1.375(3)
C4B – C5B	1.363(3)	C5B – N1B	1.344(3)
C6B – N1B	1.491(3)	C6B – C7B	1.506(3)
C7B – C8B	1.489(4)	C8B – C9B	1.538(3)

C1C – N1C	1.350(2)	C1C – C2C	1.364(3)
C2C – C3C	1.371(3)	C3C – C4C	1.376(3)
C4C – C5C	1.369(3)	C5C – N1C	1.339(2)
C6C – N1C	1.491(2)	C6C – C7C	1.514(3)
C7C – C8C	1.515(3)	C8C – C9C	1.520(3)
Cl1 – Co1	2.2880(5)	Cl2 – Co1	2.2657(5)
Cl3 – Co1	2.2682(5)	Cl4 – Co1	2.2891(5)
Cl1A – Co1A	2.2622(5)	Cl2A – Co1A	2.2856(5)
Cl3A – Co1A	2.2915(5)	Cl4A – Co1A	2.2721(5)

Table 4.S6. Selected bond angles [°] of **2**.

N1 – C1 – C2	120.4(2)	C1 – C2 – C3	119.9(2)
C2 – C3 – C4	119.0(2)	C5 – C4 – C3	119.5(2)
N1 – C5 – C4	120.5(2)	N1 – C6 – C7	112.04(16)
C8 – C7 – C6	114.77(18)	C7 – C8 – C9	113.0(2)
N1A – C1A – C2A	120.57(18)	C1A – C2A – C3A	119.39(19)
C2A – C3A – C4A	119.23(19)	C5A – C4A – C3A	119.84(19)
N1A – C5A – C4A	120.02(18)	N1A – C6A – C7A	109.50(15)
C8A – C7A – C6A	113.25(19)	C9A – C8A – C7A	113.4(2)
N1B – C1B – C2B	120.8(2)	C1B – C2B – C3B	119.5(2)
C2B – C3B – C4B	119.0(2)	C5B – C4B – C3B	119.8(2)
N1B – C5B – C4B	120.4(2)	N1B – C6B – C7B	113.67(18)
C8B – C7B – C6B	113.7(2)	C7B – C8B – C9B	112.2(2)
N1C – C1C – C2C	120.37(19)	C1C – C2C – C3C	119.9(2)
C2C – C3C – C4C	119.1(2)	C5C – C4C – C3C	119.6(2)
N1C – C5C – C4C	120.61(18)	N1C – C6C – C7C	110.94(15)
C6C – C7C – C8C	112.66(17)	C7C – C8C – C9C	113.48(18)
Cl2 – Co1 – Cl3	113.62(2)	Cl2 – Co1 – Cl1	107.25(2)
Cl3 – Co1 – Cl1	110.185(19)	Cl2 – Co1 – Cl4	111.56(2)
Cl3 – Co1 – Cl4	107.38(2)	Cl1 – Co1 – Cl4	106.640(19)
Cl1A – Co1A – Cl4A	114.96(2)	Cl1A – Co1A – Cl2A	108.02(2)
Cl4A – Co1A – Cl2A	109.487(19)	Cl1A – Co1A – Cl3A	109.08(2)
Cl4A – Co1A – Cl3A	108.32(2)	Cl2A – Co1A – Cl3A	106.653(19)
C5 – N1 – C1	120.60(17)	C5 – N1 – C6	118.29(16)
C1 – N1 – C6	121.12(16)	C1A – N1A – C5A	120.94(16)

C1A – N1A – C6A	119.94(15)	C5A – N1A – C6A	119.00(16)
C1B – N1B – C5B	120.58(18)	C1B – N1B – C6B	118.57(17)
C5B – N1B – C6B	120.84(17)	C5C – N1C – C1C	120.47(17)
C5C – N1C – C6C	120.22(16)	C1C – N1C – C6C	119.29(16)

Table 4.S7. Selected torsion angles [°] of **2**.

N1 − C1 − C2 − C3	-0.6(4)	C1 − C2 − C3 – C4	0.9(4)
C2 – C3 − C4 − C5	-0.7(4)	C3 – C4 − C5 − N1	0.1(3)
N1 – C6 – C7 – C8	-68.9(2)	C6 – C7 – C8 – C9	-175.80(18)
N1A – C1A – C2A – C3A	-0.1(3)	C1A – C2A – C3A – C4A	0.6(3)
C2A – C3A – C4A – C5A	-0.4(3)	C3A – C4A – C5A – N1A	-0.3(3)
N1A – C6A – C7A – C8A	174.19(18)	C6A – C7A – C8A – C9A	-72.7(3)
N1B – C1B – C2B – C3B	-0.3(3)	C1B – C2B – C3B – C4B	0.2(4)
C2B – C3B – C4B – C5B	0.1(4)	C3B – C4B – C5B – N1B	-0.2(4)
N1B – C6B – C7B – C8B	69.2(3)	C6B – C7B – C8B – C9B	177.8(2)
N1C – C1C – C2C – C3C	0.1(3)	C1C – C2C – C3C – C4C	0.2(3)
C2C – C3C – C4C – C5C	-0.3(3)	C3C – C4C – C5C – N1C	-0.1(3)
N1C – C6C – C7C – C8C	-171.52(16)	C6C – C7C – C8C – C9C	69.1(2)
C4 – C5 – N1 – C1	0.2(3)	C4 – C5 – N1 – C6	-179.36(19)
C2 – C1 – N1 – C5	0.0(3)	C2 – C1 – N1 – C6	179.6(2)
C7 – C6 – N1 – C5	-75.5(2)	C7 – C6 – N1 – C1	104.9(2)
C2A – C1A – N1A – C5A	-0.5(3)	C2A – C1A – N1A – C6A	175.54(18)
C4A – C5A – N1A – C1A	0.7(3)	C4A – C5A – N1A – C6A	-175.38(18)
C7A – C6A N1A – C1A	-104.4(2)	C7A – C6A – N1A – C5A	71.7(2)
C2B – C1B – N1B – C5B	0.2(3)	C2B – C1B – N1B – C6B	179.95(19)
C4B – C5B – N1B – C1B	0.0(3)	C4B – C5B – N1B – C6B	-179.7(2)
C7B – C6B – N1B – C1B	73.4(3)	C7B – C6B – N1B – C5B	-106.9(2)
C4C – C5C – N1C – C1C	0.5(3)	C4C – C5C – N1C – C6C	-177.72(18)
C2C – C1C – N1C – C5C	-0.5(3)	C2C – C1C – N1C – C6C	177.72(19)
C7C – C6C – N1C – C5C	112.1(2)	C7C – C6C – N1C – C1C	-66.1(2)

Table 4.S8. Hydrogen bond geometry (Å, °) in **2**.

D–H…A	D–H	H…A	D…A	D-H…A
C1 – H1…Cl2A^I	0.88(2)	2.82(2)	3.689(2)	169(2)
C2 – H2…Cl3A^I	0.91(3)	2.96(3)	3.642(3)	132.1(19)
C4 – H4…Cl4^{II}	0.90(2)	2.89(2)	3.561(2)	133.0(18)
C5 – H5…Cl2^{III}	0.90(2)	2.92(2)	3.781(2)	159.4(17)
C6 – H61…Cl2^{III}	0.94(2)	2.96(2)	3.610(2)	127.3(16)
C6 – H62…Cl2A^I	0.97(2)	2.96(2)	3.861(2)	155.5(17)
C1A – H1A…Cl3	0.92(2)	2.92(2)	3.751(2)	151.7(16)
C2A – H2A…Cl1^{IV}	0.91(2)	2.91(2)	3.556(2)	129.2(17)
C5A – H5A…Cl2A^I	0.93(2)	2.95(2)	3.579(2)	126.5(16)
C5A – H5A…Cl3A^I	0.93(2)	2.86(2)	3.705(2)	152.5(17)
C6A – H61A…Cl3A^I	0.98(2)	2.82(2)	3.619(2)	139.7(16)
C6A – H62A…Cl3	0.92(2)	2.78(2)	3.687(2)	167.0(17)
C1B – H1B…Cl4A^I	0.94(2)	2.85(2)	3.738(2)	158.0(17)
C4B – H4B…Cl1	0.91(3)	2.96(3)	3.644(2)	132.9(19)
C5B – H5B…Cl4	0.94(2)	2.76(2)	3.688(2)	168.8(19)
C6B – H61B…Cl4A^I	0.98(2)	2.91(2)	3.610(2)	129.2(16)
C6B – H62B…Cl4	1.00(2)	2.92(2)	3.849(2)	154.8(17)
C1C – H1C…Cl1	0.91(2)	2.82(2)	3.606(2)	145.2(18)
C1C – H1C…Cl4	0.91(2)	2.98(2)	3.576(2)	124.6(17)
C4C – H4C…Cl2A^V	0.94(2)	2.88(2)	3.567(2)	130.6(17)
C5C – H5C…Cl1A^{VI}	0.92(2)	2.94(2)	3.785(2)	153.3(17)
C6C – H61C…Cl1	0.98(2)	2.87(2)	3.629(2)	135.0(15)
C6C – H62C…Cl1A^{VI}	0.97(2)	2.79(2)	3.734(2)	165.0(17)
C7C – H72C…Cl3^{VI}	0.97(2)	2.87(2)	3.732(2)	149.6(16)

Symmetry codes: ^{I} 2.5-x, 0.5+y, 1.5-z; ^{II} 0.5+x, 0.5-y, -0.5+z; ^{III} 1+x, y, z; ^{IV} 0.5+x, 0.5-y, 0.5+z; ^{V} -0.5+x, 0.5-y, 0.5+z; ^{VI} 1.5-x, 0.5+y, 1.5-z.

Table 4.S9. Selected bond lengths [Å] of **3**.

C1 – N1	1.351(4)	C1 – C2	1.362(4)
C2 – C3	1.380(5)	C3 – C4	1.377(5)
C4 – C5	1.372(4)	C5 – N1	1.337(3)
C6 – N1	1.494(4)	C6 – C7	1.527(5)

C7 – C8	1.526(5)	C8 – C9	1.486(5)
C1A – N1A	1.341(4)	C1A – C2A	1.369(5)
C2A – C3A	1.379(5)	C3A – C4A	1.360(5)
C4A – C5A	1.373(5)	C5A – N1A	1.341(4)
C6A – N1A	1.480(4)	C6A – C7A	1.514(4)
C7A – C8A	1.507(4)	C8A – C9A	1.514(5)
C1B – N1B	1.341(4)	C1B – C2B	1.365(5)
C2B – C3B	1.378(5)	C3B – C4B	1.365(5)
C4B – C5B	1.367(5)	C5B – N1B	1.342(4)
C6B – N1B	1.484(4)	C6B – C7B	1.521(4)
C7B – C8B	1.517(4)	C7B – H71B	0.95(3)
C7B – H72B	0.87(3)	C8B – C9B	1.516(5)
C1C – N3C	1.348(4)	C1C – C2C	1.356(5)
C2C – C3C	1.367(5)	C3C – C4C	1.377(5)
C4C – C5C	1.361(5)	C5C – N3C	1.348(4)
C6C – N3C	1.488(4)	C6C – C7C	1.511(4)
C7C – C8C	1.478(5)	C8C – C9C	1.546(5)
Cl1A – Zn1A	2.2558(7)	Cl2A – Zn1A	2.2872(8)
Cl3A – Zn1A	2.2950(9)	Cl4A – Zn1A	2.2629(8)
Cl1 – Zn1	2.2577(8)	Cl2 – Zn1	2.2902(8)
Cl3 – Zn1	2.2628(7)	Cl4 – Zn1	2.2894(9)

Table 4.S10. Selected bond angles [°] of **3**.

N1 − C1 − C2	120.1(3)	C1 − C2 − C3	119.6(3)
C4 − C3 − C2	119.5(3)	C5 − C4 − C3	119.2(3)
N1 − C5 − C4	120.4(3)	N1 − C6 − C7	109.8(2)
C8 − C7 − C6	113.0(3)	C9 − C8 − C7	113.6(3)
N1A − C1A − C2A	120.4(3)	C1A − C2A − C3A	119.5(3)
C4A − C3A − C2A	119.2(3)	C3A − C4A − C5A	119.9(3)
N1A − C5A − C4A	120.4(3)	N1A − C6A − C7A	112.0(3)
C8A − C7A − C6A	115.1(3)	C7A − C8A − C9A	113.3(3)
N1B − C1B − C2B	120.6(3)	C1B − C2B − C3B	119.5(3)
C4B − C3B − C2B	119.0(3)	C3B − C4B − C5B	120.1(3)
N1B − C5B − C4B	120.2(3)	N1B − C6B − C7B	110.9(3)
C8B − C7B − C6B	112.8(3)	C9B − C8B − C7B	113.5(3)

N3C − C1C − C2C	120.5(3)	C1C − C2C − C3C	120.0(3)
C2C − C3C − C4C	119.2(4)	C5C − C4C − C3C	119.5(3)
N3C − C5C − C4C	120.6(3)	N3C − C6C − C7C	113.4(3)
C8C − C7C − C6C	114.3(3)	C7C − C8C − C9C	112.1(3)
Cl1 − Zn1 − Cl3	113.62(3)	Cl1 − Zn1 − Cl4	111.34(3)
Cl3 − Zn1 − Cl4	107.61(3)	Cl1 − Zn1 − Cl2	107.53(3)
Cl3 − Zn1 − Cl2	110.02(3)	Cl4 − Zn1 − Cl2	106.51(3)
Cl1A − Zn1A − Cl4A	114.85(3)	Cl1A − Zn1A − Cl2A	108.20(3)
Cl4A − Zn1A − Cl2A	109.58(3)	Cl1A − Zn1A − Cl3A	109.12(3)
Cl4A − Zn1A − Cl3A	108.37(3)	Cl2A − Zn1A − Cl3A	106.39(3)
C5 − N1 − C1	121.2(3)	C5 − N1 − C6	119.7(2)
C1 − N1 − C6	118.9(2)	C1A − N1A − C5A	120.5(3)
C1A − N1A − C6A	121.4(3)	C5A − N1A − C6A	118.1(3)
C5B − N1B − C1B	120.6(3)	C5B − N1B − C6B	120.0(2)
C1B − N1B − C6B	119.4(2)	C5C − N3C − C1C	120.2(3)
C5C − N3C − C6C	118.7(3)	C1C − N3C − C6C	121.1(3)

Table 4.S11. Selected torsion angles [°] of **3**.

N1 − C1 − C2 − C3	0.2(5)	C1 − C2 − C3 − C4	-0.9(5)
C2 − C3 − C4 − C5	0.9(5)	C3 − C4 − C5 − N1	-0.2(5)
N1 − C6 − C7 − C8	174.0(3)	C6 − C7 − C8 − C9	-72.7(4)
N1A − C1A − C2A − C3A	0.3(6)	C1A − C2A − C3A − C4A	-0.2(6)
C2A − C3A − C4A − C5A	0.2(5)	C3A − C4A − C5A − N1A	-0.4(5)
N1A − C6A − C7A − C8A	-68.8(4)	C6A − C7A − C8A − C9A	-175.8(3)
N1B − C1B − C2B − C3B	0.7(5)	C1B − C2B − C3B − C4B	-1.4(5)
C2B − C3B − C4B − C5B	1.5(5)	C3B − C4B − C5B − N1B	-0.9(5)
N1B − C6B − C7B − C8B	171.8(2)	C6B − C7B − C8B − C9B	-70.1(4)
N3C − C1C − C2C − C3C	-0.1(5)	C1C − C2C − C3C − C4C	0.3(6)
C2C − C3C − C4C − C5C	-0.4(5)	C3C − C4C − C5C − N3C	0.2(5)
N3C − C6C − C7C − C8C	68.6(4)	C6C − C7C − C8C − C9C	177.1(3)
C4 − C5 − N1 − C1	-0.5(4)	C4 − C5 − N1 − C6	175.3(3)
C2 − C1 − N1 − C5	0.5(4)	C2 − C1 − N1 − C6	-175.3(3)
C7 − C6 − N1 − C5	-104.5(3)	C7 − C6 − N1 − C1	71.4(3)
C2A − C1A − N1A − C5A	-0.6(5)	C2A − C1A − N1A − C6A	179.3(3)
C4A − C5A − N1A − C1A	0.6(4)	C4A − C5A − N1A − C6A	-179.3(3)

C7A − C6A − N1A − C1A	104.7(3)	C7A − C6A − N1A − C5A	-75.4(3)
C4B − C5B − N1B − C1B	0.1(4)	C4B − C5B − N1B − C6B	178.4(3)
C2B − C1B − N1B − C5B	0.0(5)	C2B − C1B − N1B − C6B	-178.4(3)
C7B − C6B − N1B − C5B	-111.4(3)	C7B − C6B − N1B − C1B	66.9(3)
C4C − C5C − N3C − C1C	0.0(5)	C4C − C5C − N3C − C6C	179.4(3)
C2C − C1C − N3C − C5C	-0.1(5)	C2C − C1C − N3C − C6C	-179.4(3)
C7C − C6C − N3C − C5C	73.9(3)	C7C − C6C − N3C − C1C	-106.8(3)

Table 4.S12. Hydrogen bond geometry (Å, °) in **3**.

D–H…A	D–H	H…A	D…A	D-H…A
C1 – H1…Cl2A[I]	0.95(3)	2.93(3)	3.576(3)	126(2)
C1 – H1…Cl3A[I]	0.95(3)	2.85(3)	3.703(3)	151(2)
C4 – H4…Cl2[II]	0.92(3)	2.87(3)	3.559(3)	133(3)
C5 – H5…Cl3	0.92(3)	2.91(3)	3.753(3)	152(3)
C6 – H61…Cl3A[I]	0.97(3)	2.83(3)	3.619(3)	139(2)
C6 – H62…Cl3	0.92(3)	2.78(3)	3.688(3)	171(3)
C1A – H1A…Cl2A	0.93(3)	2.76(4)	3.682(4)	169(3)
C2A – H2A…Cl3A	0.89(4)	2.99(4)	3.638(4)	131(3)
C4A – H4A…Cl4[III]	0.92(3)	2.89(3)	3.565(3)	131(3)
C5A – H5A…Cl1[IV]	0.93(3)	2.90(3)	3.782(4)	160(2)
C6A – H61A…Cl2A	0.95(3)	2.99(3)	3.862(3)	152(2)
C6A – H62A…Cl1[IV]	0.98(3)	2.95(3)	3.606(4)	126(2)
C1B – H1B…Cl2[V]	0.90(3)	2.80(3)	3.610(3)	151(3)
C4B – H4B…Cl2A	0.95(3)	2.89(3)	3.574(3)	130(3)
C5B – H5B…Cl1A[VI]	0.94(3)	2.93(3)	3.791(4)	153(3)
C6B – H61B…Cl2[V]	1.04(3)	2.83(3)	3.625(3)	133(2)
C6B – H62B…Cl1A[VI]	1.00(3)	2.77(3)	3.737(3)	162(2)
C7B – H71B…Cl3[VI]	0.95(3)	2.87(3)	3.729(3)	152(2)
C1C – H1C…Cl4[VII]	0.98(3)	2.73(3)	3.694(3)	168(3)
C5C – H5C…Cl4A	0.96(3)	2.83(3)	3.744(4)	161(3)
C6C – H61C…Cl4[VII]	0.97(3)	2.95(3)	3.855(3)	156(2)
C6C – H62C…Cl4A	1.03(3)	2.82(3)	3.608(4)	133(2)

Symmetry codes: [I] 0.5-x, 0.5+y, 0.5-z; [II] -0.5+x, 0.5-y, -0.5+z; [III] 1-x, -y, -z; [IV] 1.5-x, -0.5+y, 0.5-z; [V] -0.5+x, 0.5-y, 0.5+z; [VI] 1-x, -y, 1-z; [VII] 0.5-x, -0.5+y, 0.5-z.

Table 4.S13. Selected bond lengths [Å] of **5**.

C1 – N1	1.350(3)	C1 – C2	1.373(4)
C2 – C3	1.380(4)	C3 – C4	1.380(4)
C4 – C5	1.369(4)	C5 – N1	1.346(3)
C6 – N1	1.488(3)	C6 – C7	1.517(4)
C7 – C8	1.531(3)	C8 – C9	1.525(3)
C9 – C10	1.528(3)	C10 – C11	1.519(3)
C11 – C12	1.522(3)	C12 – C13	1.519(3)
C13 – C14	1.526(3)	C14 – C15	1.515(3)
C15 – C16	1.512(4)	C16 – C17	1.528(4)
C1A – N1A	1.344(3)	C1A – C2A	1.369(4)
C2A – C3A	1.389(4)	C3A – C4A	1.369(4)
C4A – C5A	1.369(4)	C5A – N1A	1.345(3)
C6A – C7A	1.470(4)	C6A – N1A	1.490(3)
C7A – C8A	1.435(5)	C8A – C9A	1.601(5)
C9A – C10A	1.449(5)	C10A – C11A	1.512(5)
C11A – C12A	1.494(5)	C12A – C13A	1.454(5)
C13A – C14A	1.564(5)	C14A – C15A	1.493(5)
C15A – C16A	1.497(5)	C16A – C17A	1.500(5)
Cl1 – Co1	2.2763(7)	Cl2 – Co1	2.2945(6)
Cl3 – Co1	2.2848(6)	Cl4 – Co1	2.2570(7)

Table 4.S14. Selected bond angles [°] of **5**.

N1 – C1 – C2	120.0(2)	C1 – C2 – C3	119.5(2)
C2 – C3 – C4	119.7(2)	C5 – C4 – C3	119.2(2)
N1 – C5 – C4	120.5(2)	N1 – C6 – C7	111.7(2)
C6 – C7 – C8	115.3(2)	C9 – C8 – C7	113.2(2)
C8 – C9 – C10	113.7(2)	C11 – C10 – C9	111.5(2)
C10 – C11 – C12	114.6(2)	C13 – C12 – C11	112.3(2)
C12 – C13 – C14	115.0(2)	C15 – C14 – C13	112.4(2)
C16 – C15 – C14	115.0(2)	C15 – C16 – C17	111.9(2)
N1A – C1A – C2A	120.3(2)	C1A – C2A – C3A	119.2(2)
C4A – C3A – C2A	119.3(2)	C3A – C4A – C5A	119.8(2)
N1A – C5A – C4A	120.1(2)	C7A – C6A – N1A	115.0(3)
C8A – C7A – C6A	115.3(3)	C7A – C8A – C9A	112.5(3)

C10A − C9A − C8A	113.0(3)	C9A − C10A − C11A	118.2(3)
C12A − C11A − C10A	115.1(3)	C13A − C12A − C11A	117.5(4)
C12A − C13A − C14A	114.6(3)	C15A − C14A − C13A	115.6(3)
C14A − C15A − C16A	116.0(3)	C15A − C16A − C17A	114.3(3)
Cl4 − Co1 − Cl1	109.71(3)	Cl4 − Co1 − Cl3	109.70(3)
Cl1 − Co1 − Cl3	109.90(3)	Cl4 − Co1 − Cl2	111.59(3)
Cl1 − Co1 − Cl2	107.20(3)	Cl3 − Co1 − Cl2	108.70(2)
C5 − N1 − C1	121.2(2)	C5 − N1 − C6	119.59(19)
C1 − N1 − C6	119.2(2)	C1A − N1A − C5A	121.1(2)
C1A − N1A − C6A	119.8(2)	C5A − N1A − C6A	119.1(2)

Table 4.S15. Selected torsion angles [°] of **5**.

N1 − C1 − C2 − C3	-0.3(4)	C1 − C2 − C3 − C4	0.0(4)
C2 − C3 − C4 − C5	0.4(4)	C3 − C4 − C5 − N1	-0.5(4)
N1 − C6 − C7 − C8	-69.8(3)	C6 − C7 − C8 − C9	-66.3(3)
C7 − C8 − C9 − C10	-176.8(2)	C8 − C9 − C10 − C11	-177.7(2)
C9 − C10 − C11 − C12	179.5(2)	C10 − C11 − C12 − C13	179.9(2)
C11 − C12 − C13 − C14	176.7(2)	C12 − C13 − C14 − C15	-177.1(2)
C13 − C14 − C15 − C16	179.0(2)	C14 − C15 − C16 − C17	-175.5(2)
N1A − C1A − C2A − C3A	-0.3(4)	C1A − C2A − C3A − C4A	0.0(4)
C2A − C3A − C4A − C5A	-0.1(4)	C3A − C4A − C5A − N1A	0.3(4)
N1A − C6A − C7A − C8A	-68.5(4)	C6A − C7A − C8A − C9A	-160.7(3)
C7A − C8A − C9A − C10A	73.4(4)	C8A − C9A − C10A − C11A	178.3(3)
C9A − C10A − C11A − C12A	-171.7(4)	C10A − C11A − C12A − C13A	-178.4(4)
C11A − C12A − C13A − C14A	-176.7(4)	C12A − C13A − C14A − C15A	-178.6(4)
C13A − C14A − C15A − C16A	174.2(4)	C14A − C15A − C16A − C17A	-179.2(4)
C4 − C5 − N1 − C1	0.1(4)	C4 − C5 − N1 − C6	-179.1(2)
C2 − C1 − N1 − C5	0.3(4)	C2 − C1 − N1 − C6	179.5(2)
C7 − C6 − N1 − C5	94.9(3)	C7 − C6 − N1 − C1	-84.3(3)
C2A − C1A − N1A − C5A	0.5(4)	C2A − C1A − N1A − C6A	178.7(2)
C4A − C5A − N1A − C1A	-0.6(4)	C4A − C5A − N1A − C6A	-178.7(2)
C7A − C6A − N1A − C1A	94.2(3)	C7A − C6A − N1A − C5A	-87.6(3)

Table 4.S16. Hydrogen bond geometry (Å, °) in **5**.

D–H…A	D–H	H…A	D…A	D-H…A
C1 – H1…Cl4^{I}	0.95	2.68	3.585(3)	158.5
C2 – H2…Cl1^{II}	0.95	2.96	3.862(3)	158.3
C4 – H4…Cl1^{III}	0.95	2.83	3.652(3)	145.8
C5 – H5…Cl4	0.95	2.58	3.426(2)	147.7
C6 – H6A…Cl3	0.99	2.91	3.833(3)	156.3
C6 – H6B…Cl1^{I}	0.99	2.98	3.858(3)	147.8
C6 – H6B…Cl2^{I}	0.99	2.97	3.699(2)	131.6
C1A – H1A…Cl1	0.95	2.65	3.593(3)	170.9
C2A – H2A…Cl3^{IV}	0.95	2.83	3.660(3)	147.2
C5A – H5A…Cl3^{V}	0.95	2.96	3.466(3)	114.6
C6A – H61A…Cl2^{V}	0.99	2.81	3.682(3)	147.1
C6A – H62A…Cl2	0.99	2.92	3.560(3)	123.4
C6A – H62A…Cl3	0.99	2.97	3.800(3)	142.3

Symmetry codes: ^{I}-1+x, y, z; ^{II} -1-x, 1-y, -z; ^{III} -x, 1-y, -z; ^{IV}1+x, y, z; ^{V}-x, -y, -z.

Table 4.S17. Selected bond lengths [Å] of **6**.

C1 N1	1.347(4)	C1 C2	1.373(5)
C2 C3	1.365(6)	C3 C4	1.385(6)
C4 C5	1.371(5)	C5 N1	1.342(5)
C6 N1	1.490(4)	C6 C7	1.525(5)
C7 C8	1.507(5)	C8 C9	1.510(6)
C9 C10	1.531(5)	C10 C11	1.506(6)
C11 C12	1.531(5)	C12 C13	1.487(6)
C13 C14	1.540(5)	C14 C15	1.491(6)
C15 C16	1.513(6)	C16 C17	1.509(7)
C1A N1A	1.348(4)	C1A C2A	1.362(6)
C2A C3A	1.376(6)	C3A C4A	1.367(6)
C4A C5A	1.363(6)	C5A N1A	1.341(5)
C6A N1A	1.481(5)	C6A C7A	1.600(9)
C7A C8A	1.343(10)	C8A C9A	1.497(10)
C9A C10A	1.506(13)	C10A C11A	1.421(14)
C11A C12A	1.538(15)	C12A C13A	1.267(14)

C13A C14A	1.633(13)	C14A C15A	1.384(10)
C15A C16A	1.503(9)	C16A C17A	1.421(10)
Cl1 Zn1	2.2744(11)	Cl2 Zn1	2.2881(10)
Cl3 Zn1	2.2785(9)	Cl4 Zn1	2.2493(11)

Table 4.S18. Selected bond angles [°] of **6**.

N1 − C1 − C2	119.8(4)	C1 − C2 − C3	119.6(4)
C4 − C3 − C2	120.1(4)	C3 − C4 − C5	118.7(4)
N1 − C5 − C4	120.4(3)	N1 − C6 − C7	111.2(3)
C8 − C7 − C6	115.7(3)	C7 − C8 − C9	114.2(3)
C8 − C9 − C10	115.0(3)	C11 − C10 − C9	111.8(3)
C10 − C11 − C12	114.4(3)	C13 − C12 − C11	112.9(3)
C12 − C13 − C14	115.5(3)	C15 − C14 − C13	114.1(3)
C14 − C15 − C16	115.4(4)	C17 − C16 − C15	112.6(4)
N1A − C1A − C2A	120.3(4)	C1A − C2A − C3A	119.5(4)
C4A − C3A − C2A	119.2(4)	C5A − C4A − C3A	120.0(4)
N1A − C5A − C4A	120.2(3)	N1A − C6A − C7A	108.9(4)
C8A − C7A − C6A	116.3(7)	C7A − C8A − C9A	112.3(11)
C8A − C9A − C10A	96.6(10)	C11A − C10A − C9A	115.8(12)
C10A − C11A − C12A	92.8(11)	C13A − C12A − C11A	108.4(13)
C12A − C13A − C14A	121.0(14)	C15A − C14A − C13A	117.1(9)
C14A − C15A − C16A	121.1(9)	C17A − C16A − C15A	115.8(8)
C5 − N1 − C1	121.4(3)	C5 − N1 − C6	119.5(3)
C1 − N1 − C6	119.1(3)	C5A − N1A − C1A	120.8(3)
C5A − N1A − C6A	119.9(3)	C1A − N1A − C6A	119.3(3)
Cl4 − Zn1 − Cl1	110.03(4)	Cl4 − Zn1 − Cl3	109.39(4)
Cl1 − Zn1 − Cl3	109.93(4)	Cl4 − Zn1 − Cl2	111.70(4)
Cl1 − Zn1 − Cl2	107.45(4)	Cl3 − Zn1 − Cl2	108.30(4)

Table 4.S19. Selected torsion angles [°] of **6**.

N1 − C1 − C2 − C3	-0.7(6)	C1 − C2 − C3 − C4	1.0(6)
C2 − C3 − C4 − C5	-0.5(6)	C3 − C4 − C5 − N1	-0.3(6)
N1 − C6 − C7 − C8	-69.8(4)	C6 − C7 − C8 − C9	-65.6(5)
C7 − C8 − C9 − C10	-176.7(3)	C8 − C9 − C10 − C11	-178.3(3)

C9 − C10 − C11 − C12	178.9(4)	C10 − C11 − C12 − C13	179.3(4)
C11 − C12 − C13 − C14	176.5(4)	C12 − C13 − C14 − C15	-179.1(4)
C13 − C14 − C15 − C16	179.1(4)	C14 − C15 − C16 − C17	-176.6(4)
N1A − C1A − C2A − C3A	-0.6(6)	C1A − C2A − C3A − C4A	-0.2(6)
C2A − C3A − C4A − C5A	0.9(6)	C3A − C4A − C5A − N1A	-0.9(6)
N1A − C6A − C7A − C8A	-170.5(7)	C6A − C7A − C8A − C9A	175.1(6)
C7A − C8A − C9A − C10A	-172.1(9)	C8A − C9A − C10A − C11A	-167.6(12)
C9A − C10A − C11A − C12A	-163.0(12)	C10A − C11A − C12A − C13A	-153.1(18)
C11A − C12A − C13A − C14A	-175.2(12)	C12A − C13A − C14A − C15A	164.2(18)
C13A − C14A − C15A − C16A	170.4(10)	C14A − C15A − C16A − C17A	177.6(11)
C4 − C5 − N1 − C1	0.6(5)	C4 − C5 − N1 − C6	179.6(3)
C2 − C1 − N1 − C5	-0.1(5)	C2 − C1 − N1 − C6	-179.1(3)
C7 − C6 − N1 − C5	-84.0(4)	C7 − C6 − N1 − C1	95.1(4)
C4A − C5A − N1A − C1A	0.2(6)	C4A − C5A − N1A − C6A	179.0(4)
C2A − C1A − N1A − C5A	0.6(6)	C2A − C1A − N1A − C6A	-178.2(4)
C7A − C6A − N1A − C5A	-102.3(5)	C7A − C6A − N1A − C1A	76.5(5)

Table 4.S20. Hydrogen bond geometry (Å, °) in **6**.

D–H…A	D–H	H…A	D…A	D-H…A
C1 – H1…Cl4	0.94	2.6	3.432(4)	147.2
C2 – H2…Cl1[I]	0.94	2.84	3.665(4)	146.6
C4 – H4…Cl1[II]	0.94	2.97	3.851(4)	157.5
C5 – H5…Cl4[III]	0.94	2.7	3.594(4)	159.4
C6 – H6A…Cl3	0.98	2.9	3.817(4)	156.9
C1A – H1A…Cl1	0.94	2.66	3.583(4)	168.8
C2A – H2A…Cl3[IV]	0.94	2.81	3.643(4)	148.8
C6A – H61A…Cl2	0.98	2.93	3.651(5)	131.1
C6A – H62A…Cl2[V]	0.98	2.78	3.751(5)	170

Symmetry codes: [I] 2-x, 1-y, -z; [II] 1-x, 1-y, -z; [III] -1+x, y, z; [IV] 1+x, y, z; [V] 2-x, 1-y, -z.

Table 4.S21. Experimental and calculated of selected bond lengths (Å) for **5**.

Selected bond lengths (Å)	Experimental	Calculated
C1-N1	1.3506	1.3503
C2-C3	1.3925	1.3804
C4-C5	1.3827	1.3694
C6-N1	1.4716	1.4883

C7-C8	1.5231	1.5313
C9-C10	1.5204	1.5283
C11-C12	1.5204	1.5223
C13-C14	1.5207	1.5263
C15-C16	1.5207	1.5124
C1A-N1A	1.3502	1.3443
C2A-C3A	1.3872	1.3894
C4A-C5A	1.3776	1.3694
C6A-C7A	1.5187	1.4704
C7A-C8A	1.5243	1.4355
C9A-C10A	1.5231	1.4495
C11A-C12A	1.5217	1.4945
C13A-C14A	1.5212	1.5645
C15A-C16A	1.5212	1.4975
Cl1-Co1	2.2371	2.27637
Cl3-Co1	2.2367	2.28486
C1-C2	1.3817	1.3734
C3-C4	1.3900	1.3804
C5-N1	1.3473	1.3463
C6-C7	1.5218	1.5174
C8-C9	1.5218	1.5253
C10-C11	1.5198	1.5193
C12-C13	1.5208	1.5193
C14-C15	1.5205	1.5153
C16-C17	1.5198	1.5284
C1A-C2A	1.3858	1.3694
C3A-C4A	1.3960	1.3694
C5A-N1A	1.3511	1.3453
C6A-N1A	1.4732	1.4903
C8A-C9A	1.5287	1.6015
C10A-C11A	1.5198	1.5125
C12A-C13A	1.5203	1.4545
C14A-C15A	1.5205	1.4935
C16A-C17A	1.5199	1.5005
Cl2-Co1	2.2285	2.29456
Cl4-Co1	2.2220	2.25707

Table 4.S22. Experimental and calculated of selected bond angles (°) for **5**.

Selected bond angles (°)	Experimental	Calculated
N1-C1-C2	119.823	120.02
C2-C3-C4	119.275	119.72
N1-C5-C4	120.374	120.52
C6-C7-C8	114.807	115.32
C8-C9-C10	113.779	113.72
C10-C11-C12	114.157	114.62
C12-C13-C14	114.275	115.02
C16-C15-C14	114.217	115.02
N1A-C1A-C2A	120.023	120.32
C4A-C3A-C2A	119.325	119.32
N1A-C5A-C4A	120.853	120.12
C8A-C7A-C6A	115.293	115.33
C10A-C9A-C8A	111.991	113.03
C12A-C11A-C10A	112.838	115.13
C12A-C13A-C14A	113.608	114.63
C14A-C15A-C16A	113.764	116.03
Cl4-Co1-Cl1	105.318	109.713
Cl1-Co1-Cl3	110.917	109.903
Cl1-Co1-Cl2	107.944	107.203
C5-N1-C1	121.669	121.22
C1-N1-C6	118.730	119.22
C1A-N1A-C6A	119.164	119.82
C1-C2-C3	119.654	119.52
C5-C4-C3	119.204	119.22
N1-C6-C7	111.277	111.72
C9-C8-C7	113.751	113.22
C11-C10-C9	112.510	111.52
C13-C12-C11	112.741	112.32
C15-C14-C13	113.318	112.42
C15-C16-C17	112.850	111.92
C1A-C2A-C3A	119.637	119.22
C3A-C4A-C5A	118.984	119.82
C7A-C6A-N1A	113.824	115.03

C7A-C8A-C9A	111.557	112.53
C9A-C10A-C11A	114.610	118.23
C13A-C12A-C11A	114.055	117.54
C15A-C14A-C13A	113.470	115.63
C15A-C16A-C17A	112.983	114.33
Cl4-Co1-Cl3	113.957	109.703
Cl4-Co1-Cl2	112.139	111.593
Cl3-Co1-Cl2	106.484	108.702
C5-N1-C6	119.561	119.5919
C1A-N1A-C5A	121.163	121.12
C5A-N1A-C6A	119.638	119.12

Table 4.S23. Experimental and calculated of selected torsion angles (°) for **5**.

Selected torsion angles (°)	Experimental	Calculated
N1-C1-C2-C3	-0.187	-0.34
C2-C3-C4-C5	0.226	0.44
N1-C6-C7-C8	-69.454	-69.83
C7-C8-C9-C10	-178.462	-176.82
C9-C10-C11-C12	177.543	179.52
C11-C12-C13-C14	178.066	176.72
C13-C14-C15-C16	179.739	179.02
N1A-C1A-C2A-C3A	-1.068	-0.34
C2A-C3A-C4A-C5A	-0.920	-0.14
N1A-C6A-C7A-C8A	-58.243	-68.54
C7A-C8A-C9A-C10A	81.055	73.44
C9A-C10A-C11A-C12A	-174.313	-171.74
C11A-C12A-C13A-C14A	-177.343	-176.74
C13A-C14A-C15A-C16A	179.860	174.24
C4-C5-N1-C1	0.192	0.14
C2-C1-N1-C5	0.075	0.34
C7-C6-N1-C5	97.728	94.93
C2A-C1A-N1A-C5A	-0.127	0.54
C4A-C5A-N1A-C1A	-0.417	-0.64
C7A-C6A-N1A-C1A	93.618	94.23
C1-C2-C3-C4	0.034	0.04

|		
C3-C4-C5-N1	-0.341	-0.54
C6-C7-C8-C9	-68.027	-66.33
C8-C9-C10-C11	-178.556	-177.72
C10-C11-C12-C13	178.975	179.92
C12-C13-C14-C15	-178.494	-177.12
C14-C15-C16-C17	-178.484	-175.52
C1A-C2A-C3A-C4A	-1.454	0.04
C3A-C4A-C5A-N1A	0.012	0.34
C6A-C7A-C8A-C9A	-157.038	-160.73
C8A-C9A-C10A-C11A	170.565	178.33
C10A-C11A-C12A-C13A	-176.529	-178.44
C12A-C13A-C14A-C15A	-178.675	-178.64
C14A-C15A-C16A-C17A	-177.872	-179.24
C4-C5-N1-C6	-177.468	-179.12
C2-C1-N1-C6	177.754	179.52
C7-C6-N1-C1	-80.001	-84.33
C2A-C1A-N1A-C6A	177.966	178.72
C4A-C5A-N1A-C6A	-177.411	-178.72
C7A-C6A-N1A-C5A	-88.510	-87.63
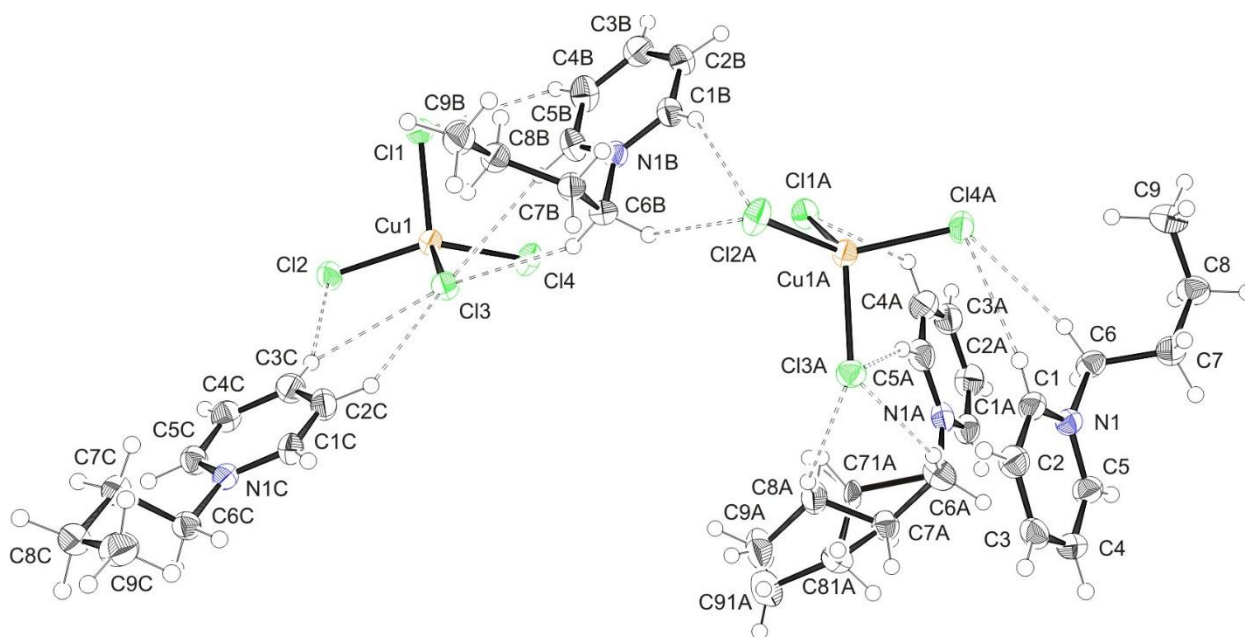
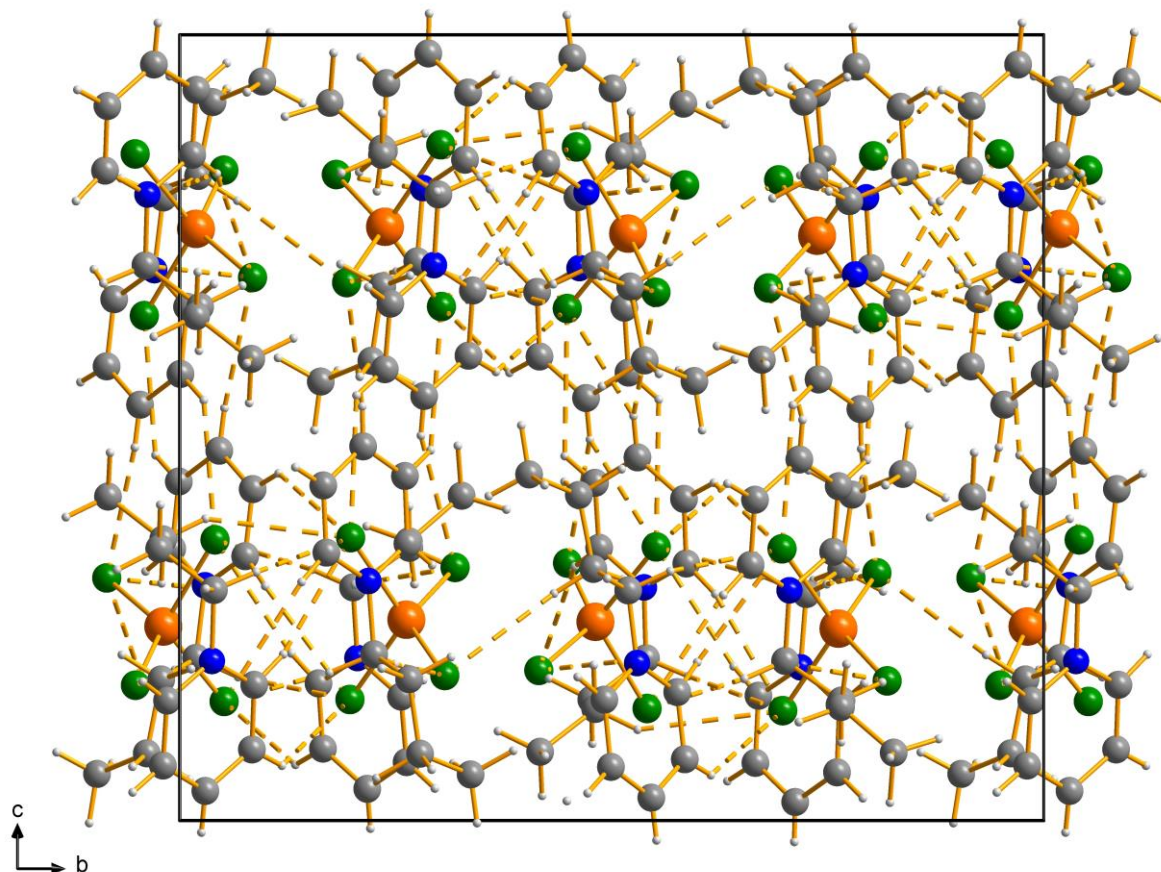**Figure.4.S1.** ORTEP plot of compound **1**. Hydrogen bonds as dashed lines.

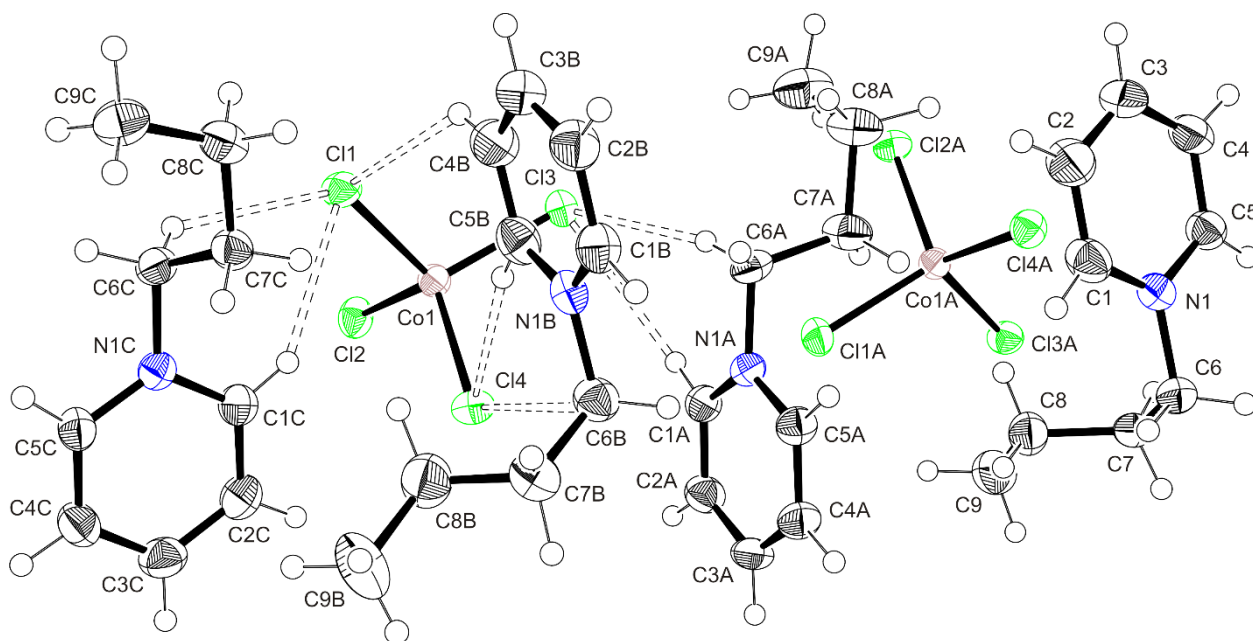**Figure.4.S2.** Packing diagram of compound **1**. View along the crystallographic *a* axis. Hydrogen bonds as dashed lines.

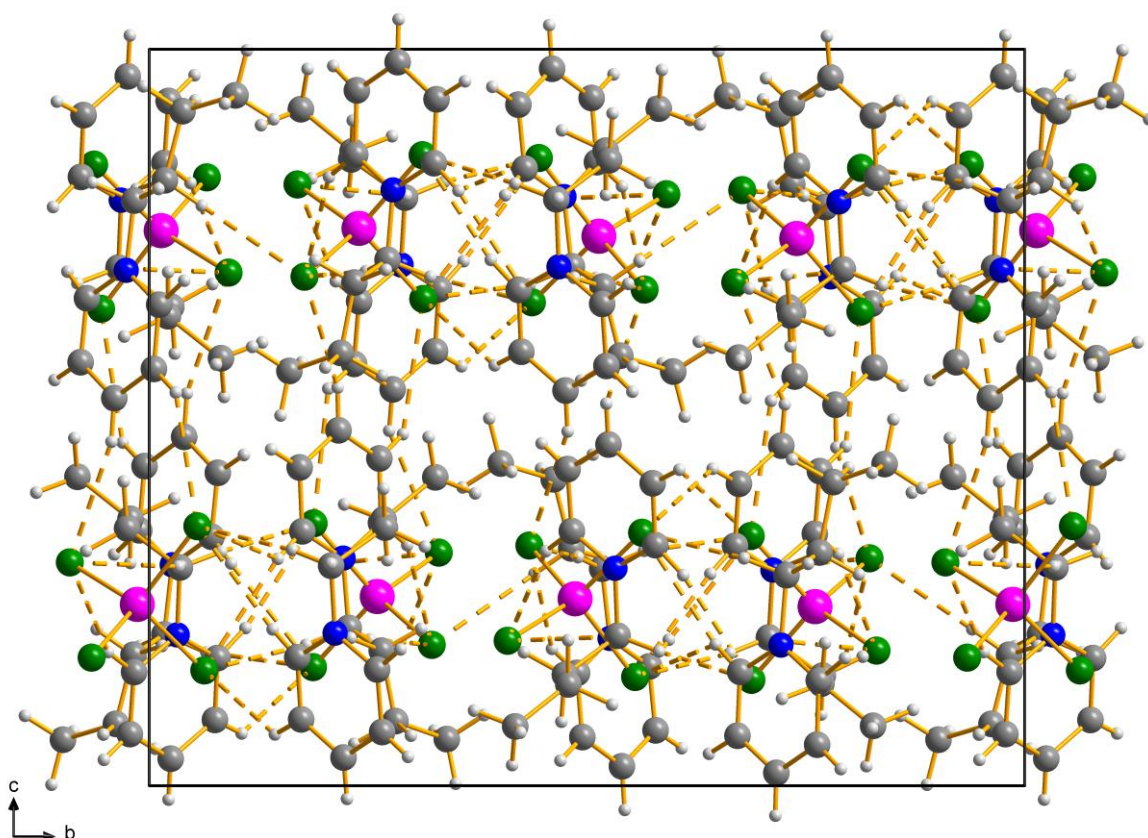**Figure.4.S3.** ORTEP plot of compound **2**. Hydrogen bonds as dashed lines.

Figure.4.S4. Packing diagram of compound **2**. View along the crystallographic *a* axis. Hydrogen bonds as dashed lines.

Figure.4.S5. ORTEP plot of compound **3**. Hydrogen bonds as dashed lines.

Figure.4.S6. Packing diagram of compound **3**. View along the crystallographic *a* axis. Hydrogen bonds as dashed lines.
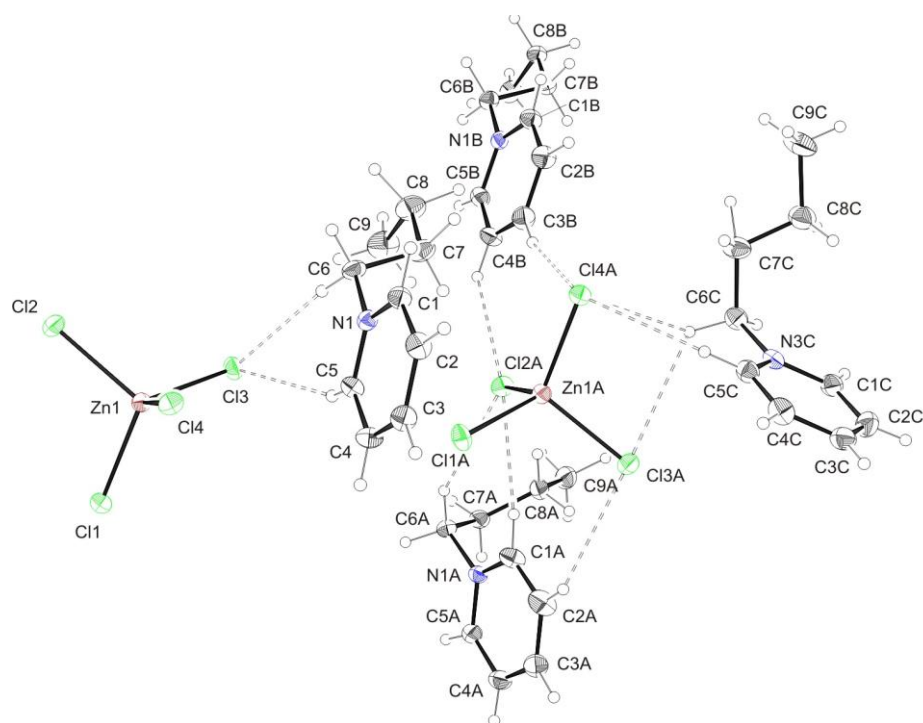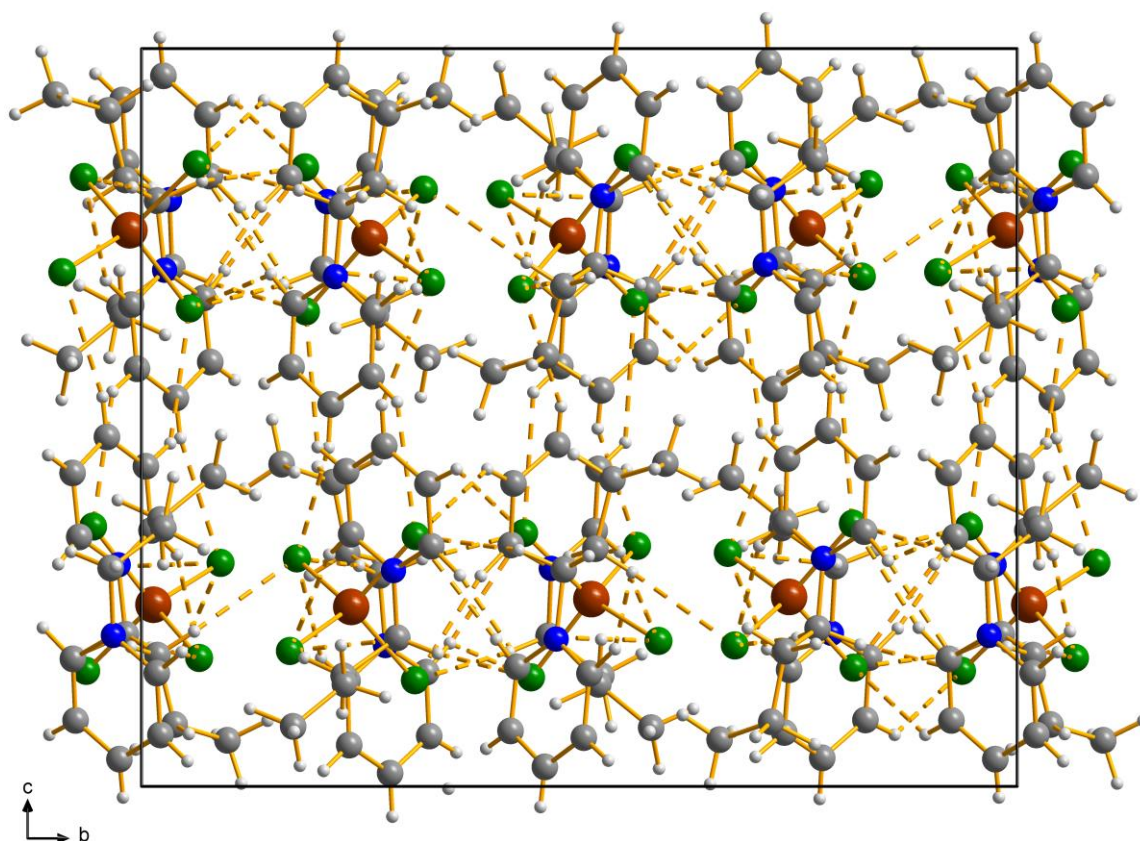
Figure.4.S7. ORTEP plot of compound **5**. Hydrogen bonds as dashed lines.

Figure.4.S8. Packing diagram of compound **5**. View along the crystallographic *a* axis. Hydrogen bonds as dashed lines.

153
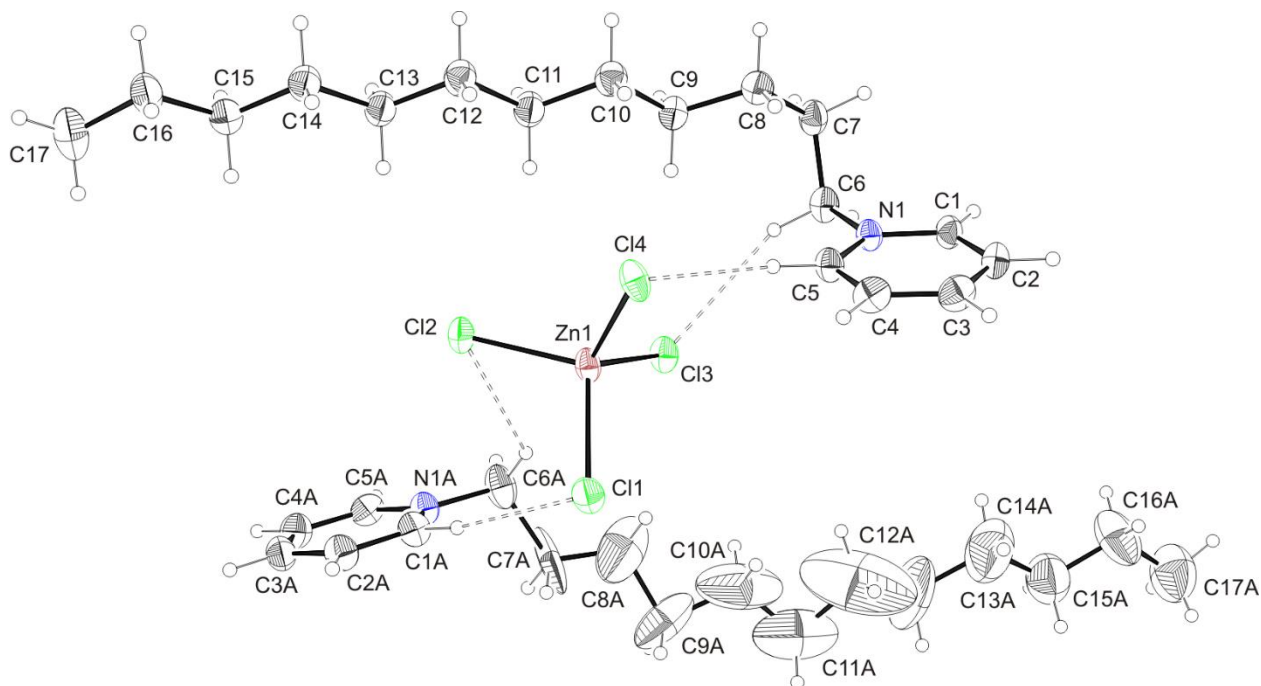
Figure.4.S9. ORTEP plot of compound **6**. Hydrogen bonds as dashed lines.
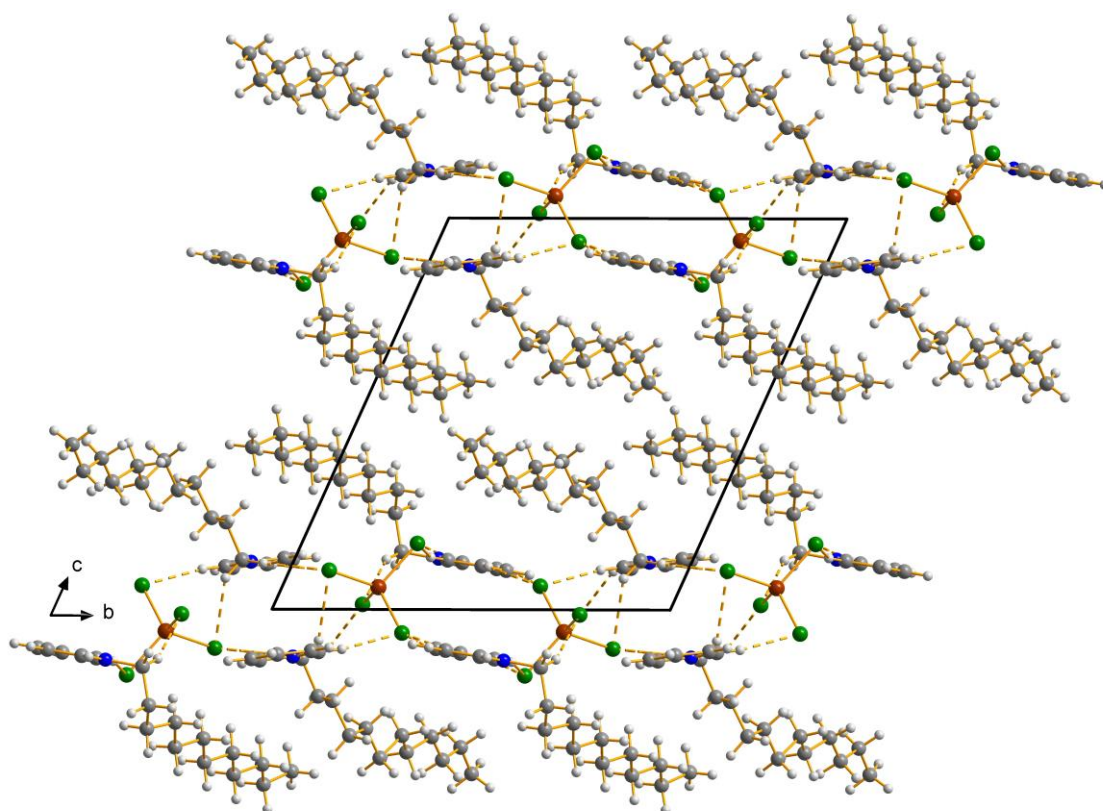
Figure.4.S10. Packing diagram of compound **6**. View along the crystallographic *a* axis. Hydrogen bonds as dashed lines.
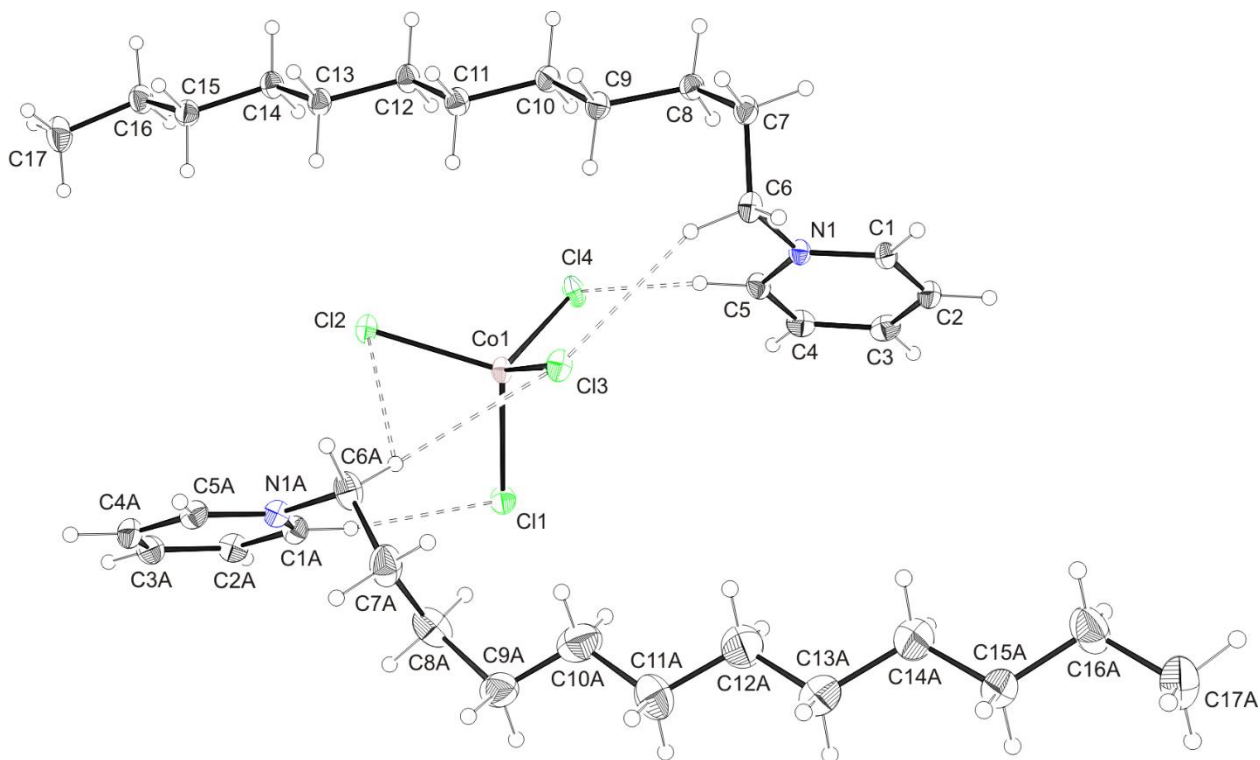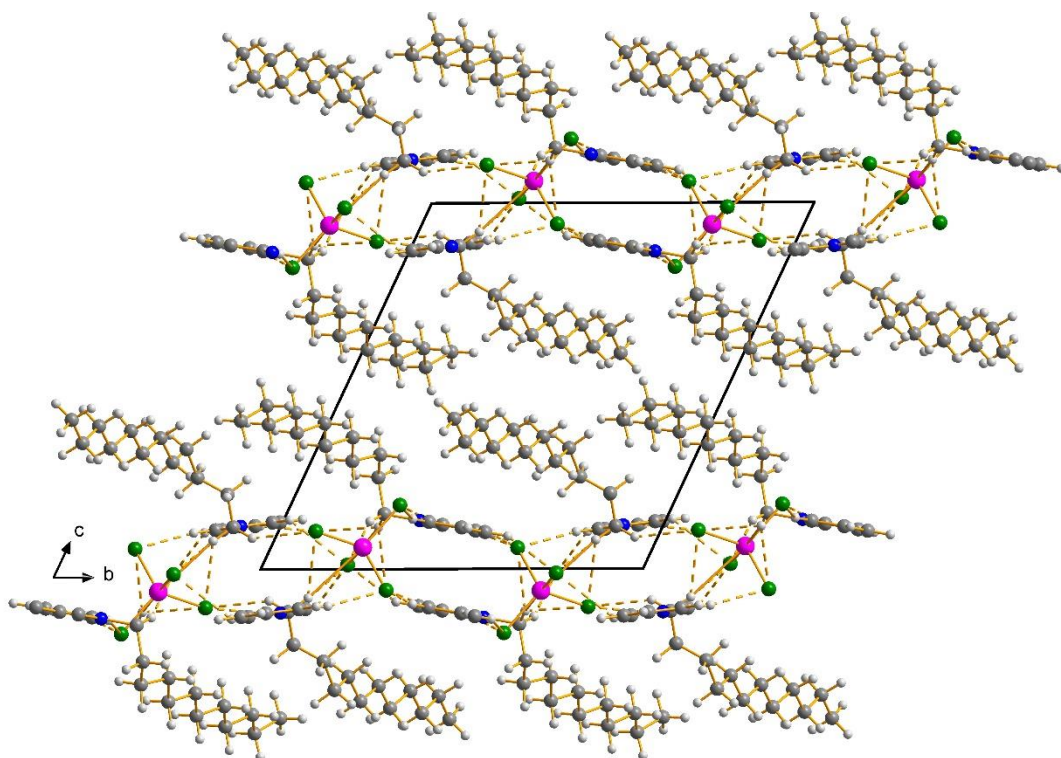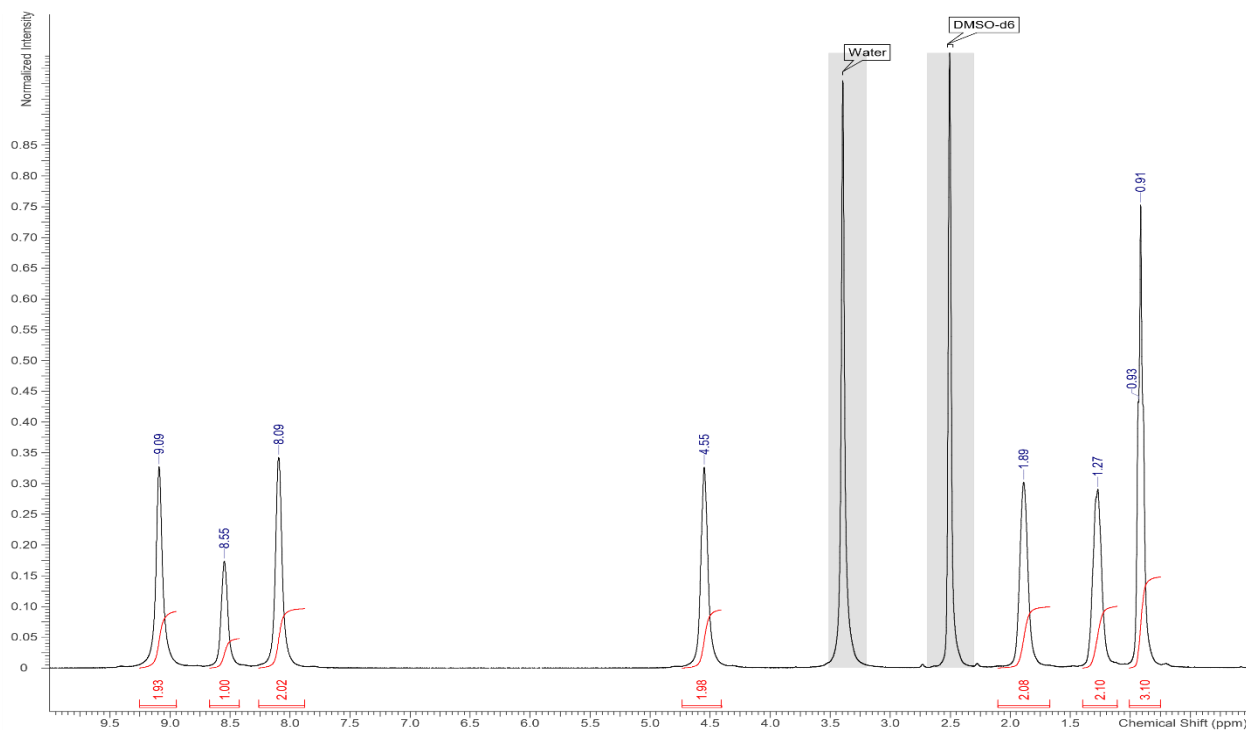
Figure.4.S11. ^{1}H NMR spectrum of compound **2**.
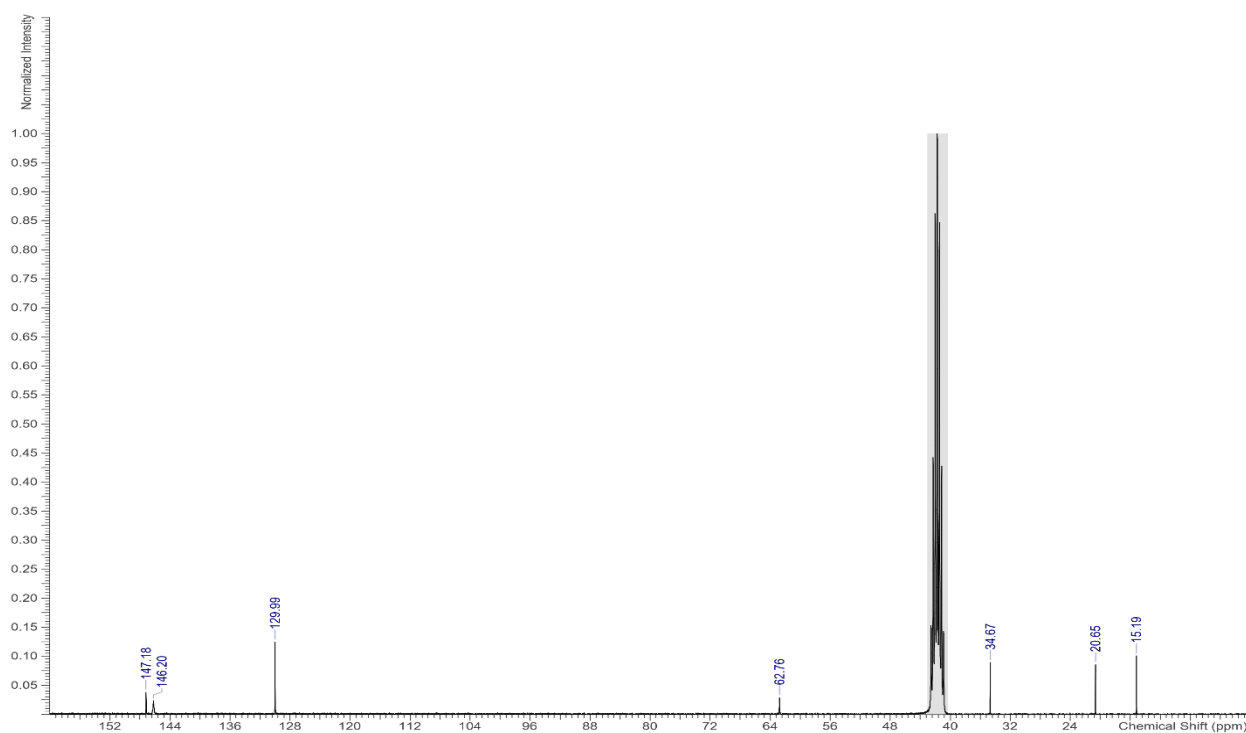
Figure.4.S12. ^{13}C NMR spectrum of compound **2**.
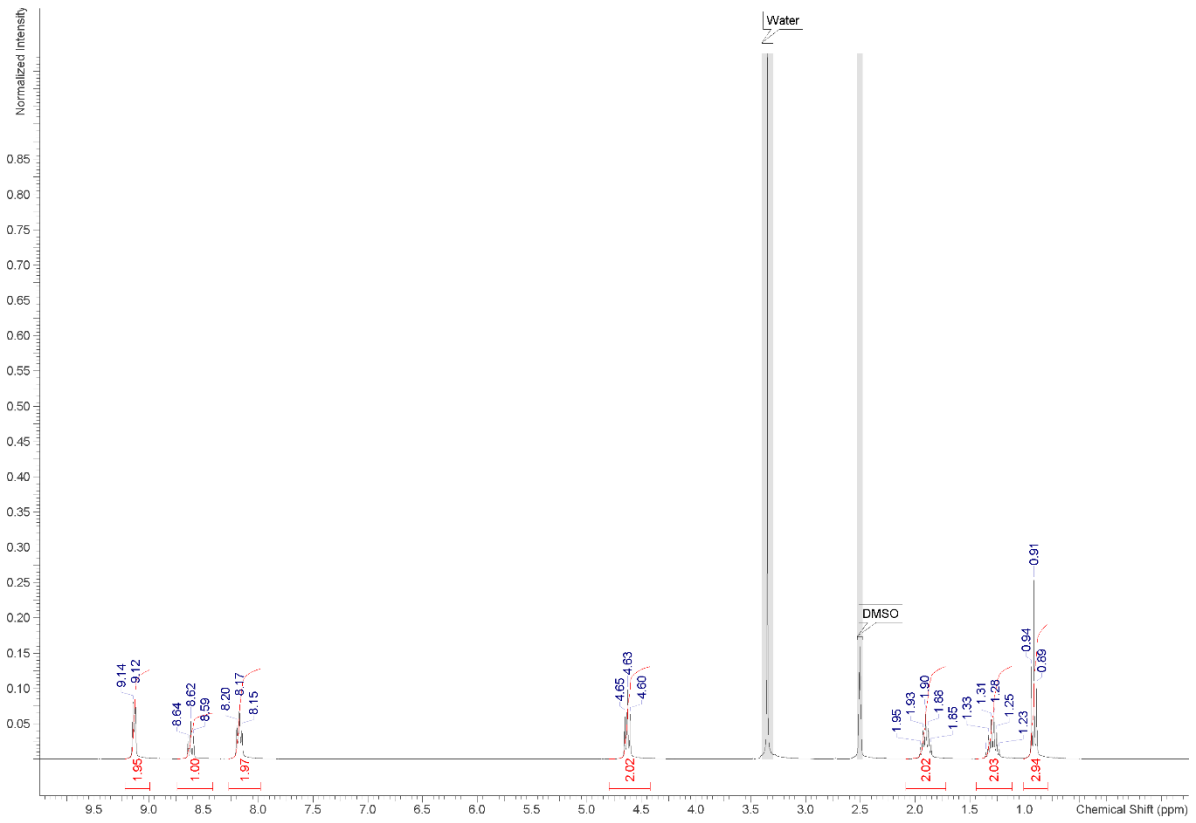
Figure.4.S13. ^{1}H NMR spectrum of compound **3**.
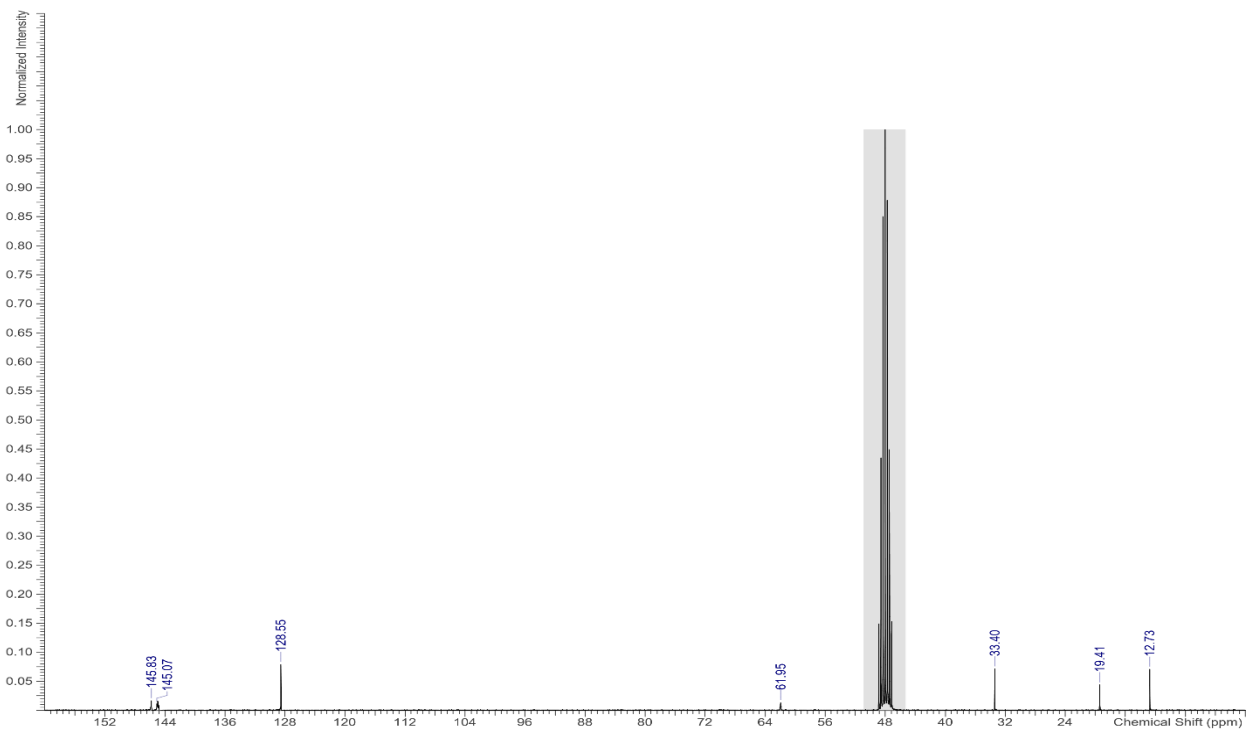
Figure.4.S14. ^{13}C NMR spectrum of compound **3**.
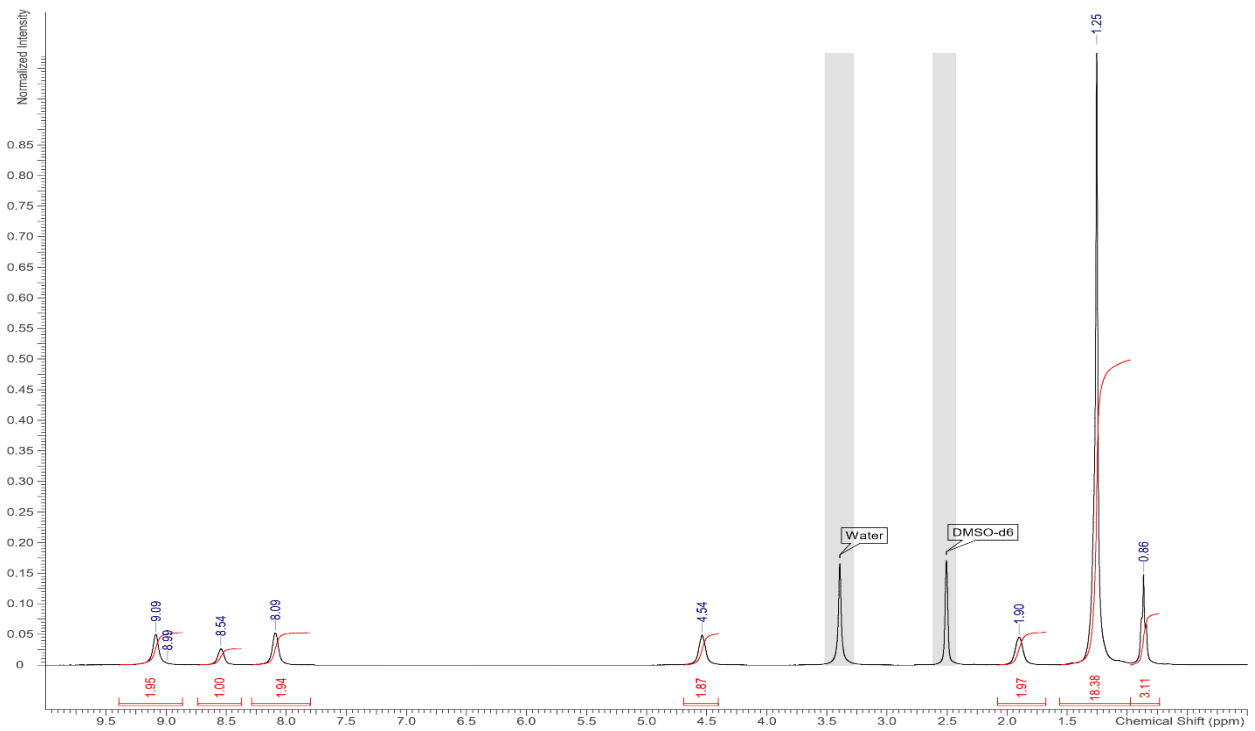
Figure.4.S15. ^{1}H NMR spectrum of compound **5**.
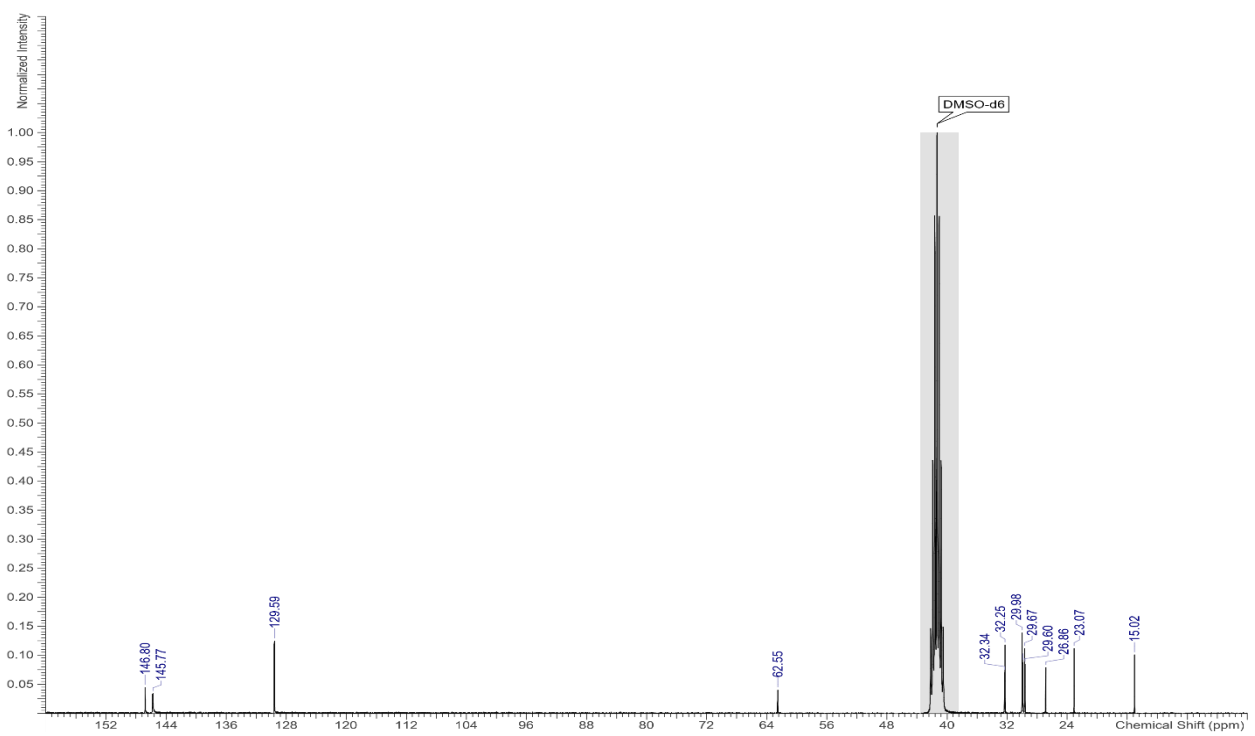
Figure.4.S16. ^{13}C NMR spectrum of compound **5**.
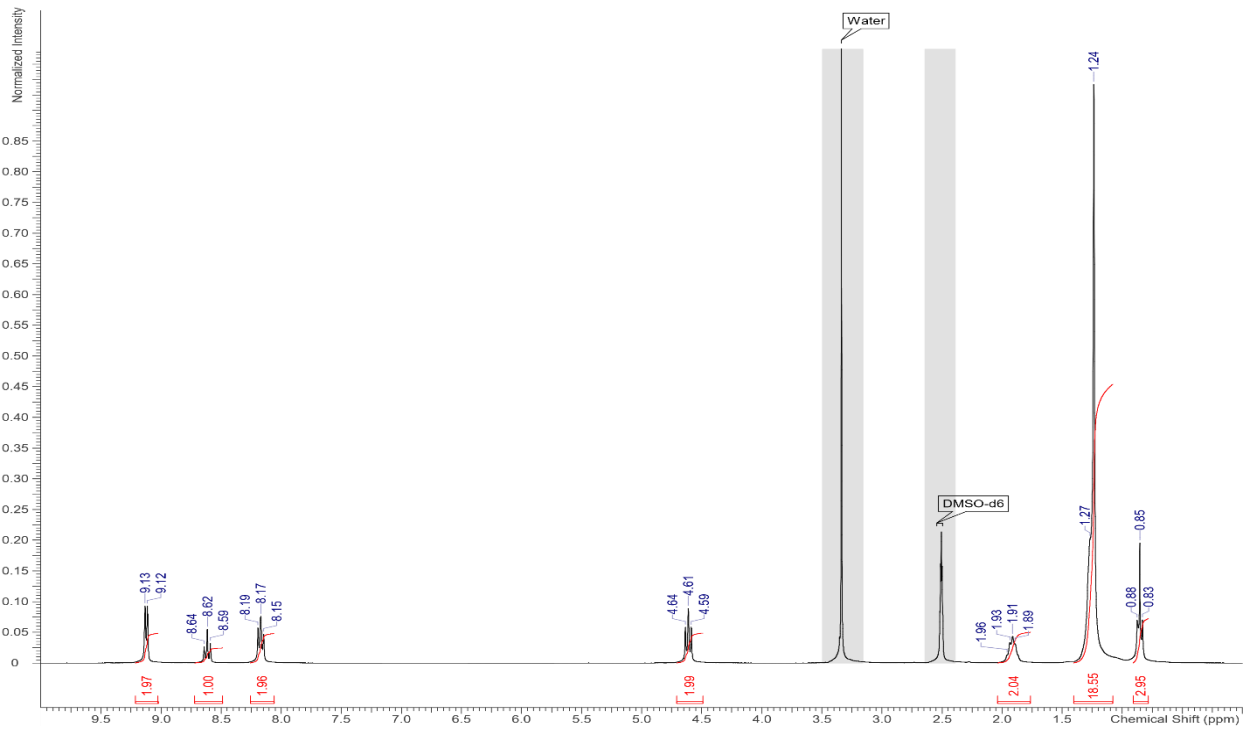
Figure.4.S17. ^{1}H NMR spectrum of compound **6**.
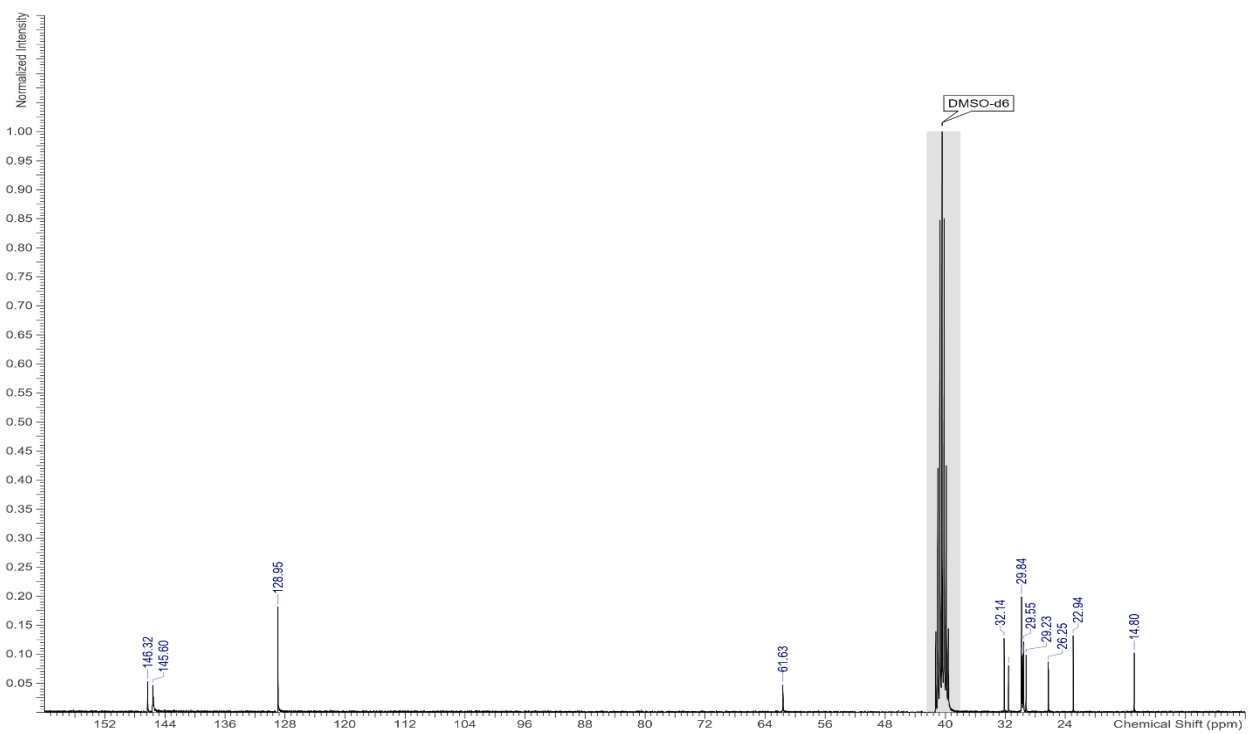
Figure.4.S18. ^{13}C NMR spectrum of compound **6**.

Appendix B – Article IV

CuS OAm

w/ 0.45 μm

w/ 0.2 μm
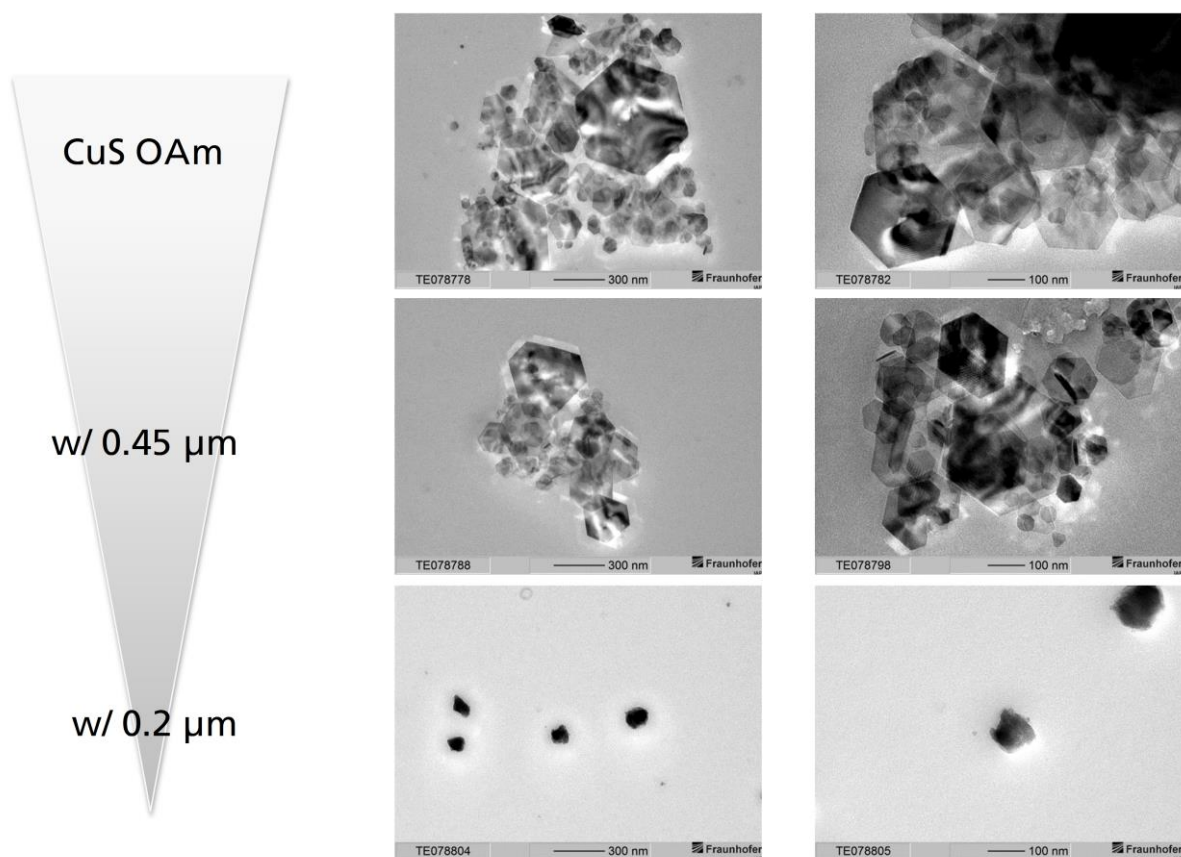
Figure 7.S1. TEM images of CNPs filtration.

Table 7.S1. Device performance for different device layer structures. The average and standard deviation were calculated from three different pixels.

Device	Active layer	V_{OC} (V)	I_{SC} (mA/cm^2)	FF (%)	PCE (%)
A	P3HT:PCBM	0.53 ± 0.03	1.26 ± 0.17	17.78 ± 1.47	0.14 ± 0.03
B	P3HT:PCBM:CuS	0.49 ± 0.04	2.68 ± 0.45	22.60 ± 1.30	0.35 ± 0.10
C	P3HT:PCBM	0.39 ± 0.03	2.07 ± 0.06	42.58 ± 0.38	0.39 ± 0.04
D	P3HT:PCBM:CuS	0.56 ± 0.01	1.91 ± 0.05	40.67 ± 0.33	0.49 ± 0.02

Table 7.S2. Overview of device architectures and compositions.

Device	ITO (Ω/sq)	Composition	Active blends (P3HT:PCBM or P3HT:PCBM:CuS)	Conventional (C) / Inverted (I)
S1	50-70	ITO/PEDOT:PSS/P3HT:PCBM/Ca/Ag	1 : 0.8	C
S2	10-15	ITO/PEDOT:PSS/P3HT:PCBM/Ca/Ag	1 : 0.8	C
S3	50-70	ITO/ZnO/P3HT:PCBM/Ag	1 : 1	I
S4	50-70	ITO /P3HT:PCBM/Ca/Ag	1 : 1	C
S5	50-70	ITO/CuS_5μm filter/P3HT:PCBM/Ca/Ag	1 : 1	C
S6	50-70	ITO/ CuS_1μm filter/P3HT:PCBM /Ca/Ag	1 : 1	C
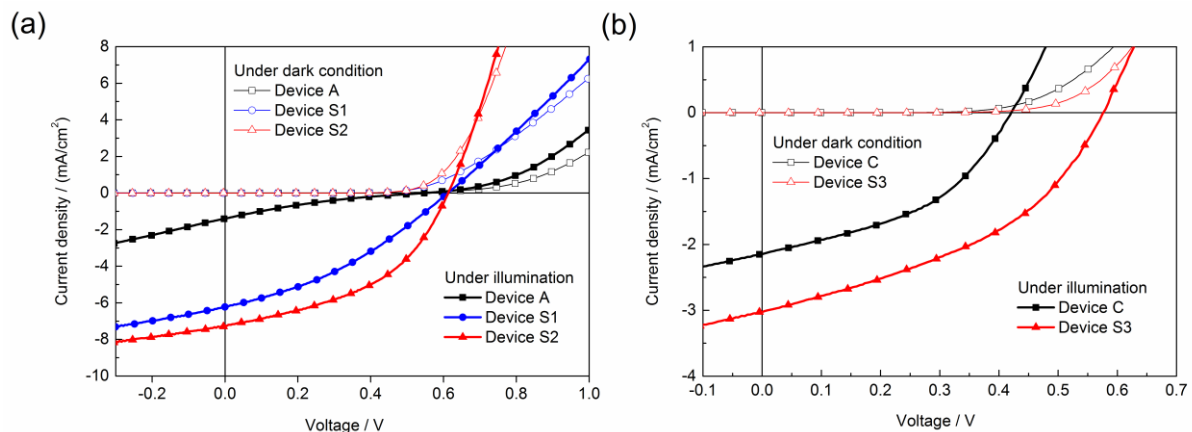
Figure 7.S2. J-V characteristics of (a) conventional OPV cells with different active blending ratio and sheet resistance of ITO (device A: P3HT:PCBM (1:1), 50-70 Ω/sq, showing an S-shape; device S1: P3HT:PCBM (1:0.8), 50-70 Ω/sq; device S2: P3HT:PCBM (1:0.8), 10-15 Ω/sq) and (b) inverted OPV cells (device C: without MoO$_3$, device S3: ITO/ZnO/P3HT:PCBM/MoO$_3$/Ag, which is fabricated with an additional 5 nm of a MoO$_3$ HCL deposited by thermal evaporation).

Table 7.S3. Device performance for different device layer structures as shown in Figure.7.S2. The average and standard deviation were calculated from three different pixels.

Device	Conditions	V_{OC} (V)	I_{SC} (mA/cm^2)	FF (%)	PCE (%)
A	P3HT:PCBM (1:1), 50-70 Ω/sq	0.53 ± 0.03	1.26 ± 0.17	17.78 ± 1.47	0.14 ± 0.03
S1	P3HT:PCBM (1:0.8), 50-70 Ω/sq	0.61 ± 0.01	6.24 ± 0.06	34.75 ± 0.20	1.48 ± 0.01
S2	P3HT:PCBM (1:0.8), 10-15 Ω/sq	0.61 ± 0.01	7.01 ± 0.02	46.41 ± 0.15	2.28 ± 0.01
C	w/o MoO$_3$	0.39 ± 0.03	2.07 ± 0.06	42.58 ± 0.38	0.39 ± 0.04
S3	w/ MoO$_3$	0.58 ± 0.01	2.98 ± 0.04	41.10 ± 0.24	0.79 ± 0.02

Table 7.S4. Surface roughness of the active layer with different blending ratio of P3HT:PCBM:CuS.

Device	P3HT:PCBM:CuS	R_q (nm)	R_{pv} (nm)	J_{dc} @ -0.4 V (mA/cm^2)
E	1:0.8:0	1.22	9.19	1×10^{-3}
F	1:0.8:0.1	1.25	10.06	22×10^{-3}
G	1:0.8:0.2	1.13	8.96	5×10^{-3}
H	1:0.8:0.3	1.14	9.90	10×10^{-3}
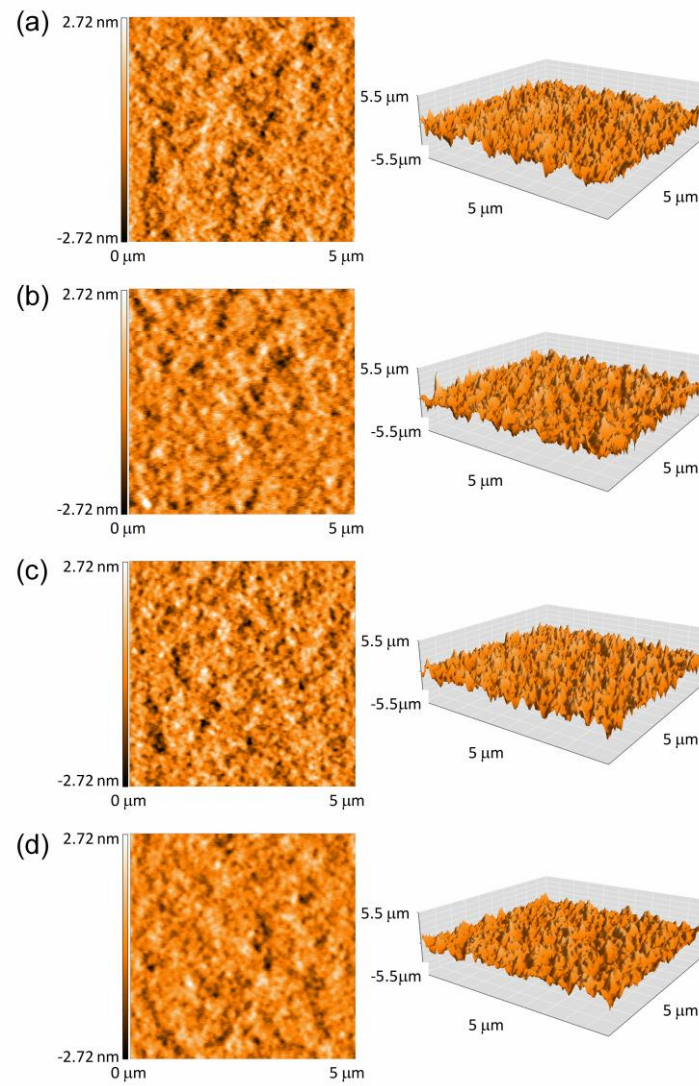
Figure 7.S3. AFM images obtained from the layers based on P3HT:PCBM:CuS with different CNP concentration. (a) 1:0.8:0.0, (b) 1:0.8:0.1, (c) 1:0.8:0.2 and (d) 1:0.8:0.3.

Table 7.S5. Reproducibility of the OPV cell performance with different pixel areas from devices E, F, G, and H. All devices were made with the same blend ratio. The averages and standard deviations were calculated from 2 different pixels.

| Device	P3HT:PCBM:CuS (weight ratio)	Pixel area (mm^2)	V_{oc} (V)	J_{sc} (mA/cm^2)	FF (%)	PCE (%)
E'	1:0.8:0.0	16	0.59 ± 0.01	6.77 ± 0.26	43.39 ± 0.70	1.98 ± 0.11
		100	0.59 ± 0.01	6.66 ± 0.13	42.80 ± 0.25	1.91 ± 0.04
F'	1:0.8:0.1	16	0.59 ± 0.01	7.07 ± 0.26	43.85 ± 1.56	2.08 ± 0.17
		100	0.59 ± 0.01	6.78 ± 0.02	44.18 ± 0.02	2.04 ± 0.01
G'	1:0.8:0.2	16	0.61 ± 0.01	7.30 ± 0.35	45.60 ± 0.10	2.32 ± 0.12
		100	0.61 ± 0.01	6.96 ± 0.10	44.53 ± 0.28	2.15 ± 0.04
H'	1:0.8:0.3	16	0.61 ± 0.01	6.80 ± 0.31	44.97 ± 0.39	2.14 ± 0.10
		100	0.61 ± 0.01	6.64 ± 0.15	44.03 ± 0.11	2.04 ± 0.06

To evaluate the hole contact properties of CNPs in a single layer application on OPV cells (i.e. ITO/CuS/P3HT:PCBM/Ca/Ag), the NPs were dispersed in butanol with a concentration of 10 mg/mL, filtered through a hydrophilic membrane filter (1 µm pore size), spin-coated at 1000 rpm for 30 sec, and then dried at 150 °C for 15 min under nitrogen atmosphere. Then the P3HT:PCBM (i.e. 1:1 blending ratio) and Ca/Ag layer were deposited. Figure 7.S4 and Table 7.S6 show the corresponding device performances. A control device S4 made without CuS layer exhibits an S-shaped J-V curve. Application of a CNP layer strongly influences the performance. CNP filtered through a 5 µm pore size (device S5) leads to high leakage currents in the dark J-V measurements as shown in Figure 7.S4. In contrast, devices prepared with CNPs filtered through a 1 µm pore size (device S6) show no leakage currents. This behavior is due to the different film roughness caused by the different CuS particle sizes. The 5 µm filter removes large aggregates but is not sufficient to remove smaller aggregates, as a result, the layers are not smooth and still have an $R_{pv} \sim 450$ nm. Application of a 1 µm filter reduces produces particle sizes that reduce the leakage current and produce smooth surfaces with an R_{pv} less than 25 nm. As a result, the CNPs work as HCL and enhance V_{oc} from 0.28 to 0.42 V and the PCE from 0.03 % to 0.04% (Table.7.S6).
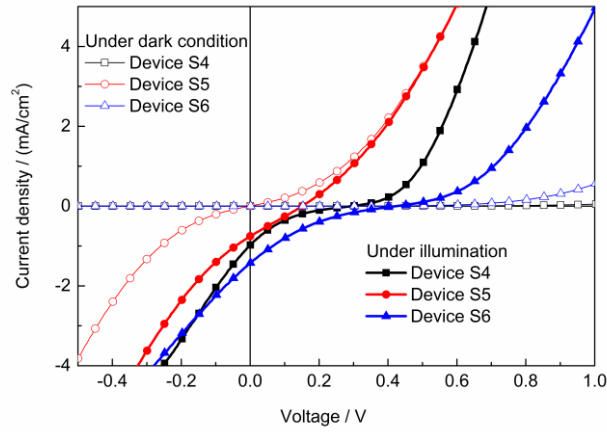
Figure 7.S4. J-V curves of conventional OPV cell fabricated with CNPs as a single HCL.

Table 7.S6. Device performance for different device layer structures. The average and standard deviation were calculated from three different pixels.

Device	HCL		V_{OC} (V)	I_{SC} (mA/cm^2)	FF (%)	PCE (%)
S4	w/o CuS	best	0.30	0.98	12.30	0.04
		mean ± SD	0.28 ± 0.02	0.77 ± 0.13	13.23 ± 0.72	0.03 ± 0.01
S5	CuS_5μm filter	best	0.16	0.78	24.64	0.04
		mean ± SD	0.15 ± 0.01	0.74 ± 0.07	25.09 ± 0.47	0.03 ± 0.01
S6	CuS_1μm filter	best	0.42	1.46	14.73	0.11
		mean ± SD	0.40 ± 0.02	0.57 ± 0.55	13.10 ± 0.89	0.04 ± 0.04
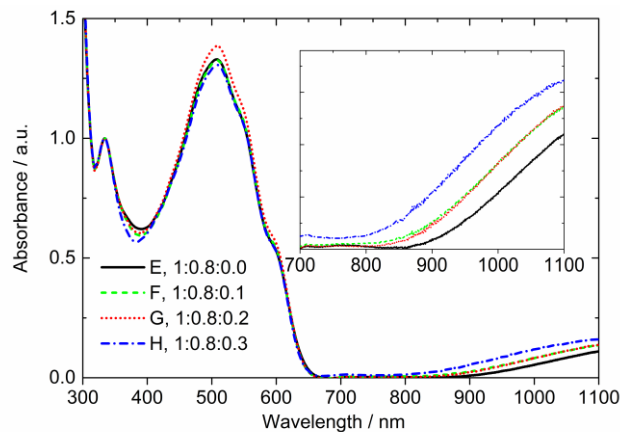
Figure 7.S5. Absorption spectra of P3HT:PCBM:CuS films with different CNP concentrations. The inset is a magnified view of the region between 700 and 1000 nm. The spectra were normalized to the isotropic PCBM peak at around 330 nm.

Chapter 12. Bibliography

1. Taubert, A., Inorganic nanomaterials synthesis using ionic liquids. *Encyclopedia of Inorganic and Bioinorganic Chemistry* **2008**.

2. Wasserscheid, P.; Welton, T., *Ionic liquids in synthesis*. John Wiley & Sons: 2008.

3. Scott, M. P.; Brazel, C. S.; Benton, M. G.; Mays, J. W.; Holbrey, J. D.; Rogers, R. D., Application of ionic liquids as plasticizers for poly (methyl methacrylate). *Chemical Communications* **2002,** (13), 1370-1371.

4. Armand, M.; Endres, F.; MacFarlane, D. R.; Ohno, H.; Scrosati, B., Ionic-liquid materials for the electrochemical challenges of the future. *Nature materials* **2009,** *8* (8), 621.

5. Welton, T., Ionic liquids in catalysis. *Coordination chemistry reviews* **2004,** *248* (21-24), 2459-2477.

6. Huddleston, J. G.; Willauer, H. D.; Swatloski, R. P.; Visser, A. E.; Rogers, R. D., Room temperature ionic liquids as novel media for 'clean'liquid–liquid extraction. *Chemical Communications* **1998,** (16), 1765-1766.

7. Vidal, L.; Riekkola, M.-L.; Canals, A., Ionic liquid-modified materials for solid-phase extraction and separation: a review. *Analytica chimica acta* **2012,** *715*, 19-41.

8. Seddon, K. R., Ionic liquids for clean technology. *Journal of Chemical Technology and Biotechnology* **1997,** *68* (4), 351-356.

9. Francis, C., What Mad Pursuit: A Personal View of Scientific Discovery. *United State of America* **1988**.

10. Freemantle, M., *An introduction to ionic liquids*. Royal Society of chemistry: 2010.

11. Hayes, R.; Warr, G. G.; Atkin, R., Structure and nanostructure in ionic liquids. *Chemical reviews* **2015,** *115* (13), 6357-6426.

12. Welton, T., Room-temperature ionic liquids. Solvents for synthesis and catalysis. *Chemical reviews* **1999,** *99* (8), 2071-2084.

13. Ueki, T.; Watanabe, M., Macromolecules in ionic liquids: progress, challenges, and opportunities. *Macromolecules* **2008,** *41* (11), 3739-3749.

14. Weingärtner, H., Understanding ionic liquids at the molecular level: facts, problems, and controversies. *Angewandte Chemie International Edition* **2008,** *47* (4), 654-670.

15. Smiglak, M.; Metlen, A.; Rogers, R. D., The Second Evolution of Ionic Liquids: From Solvents and Separations to Advanced Materials · Energetic Examples from the Ionic Liquid Cookbook. *Accounts of Chemical Research* **2007,** *40* (11), 1182-1192.

16. Greaves, T. L.; Kennedy, D. F.; Mudie, S. T.; Drummond, C. J., Diversity observed in the nanostructure of protic ionic liquids. *The Journal of Physical Chemistry B* **2010,** *114* (31), 10022-10031.

17. Han, X.; Armstrong, D. W., Ionic liquids in separations. *Accounts of Chemical Research* **2007,** *40* (11), 1079-1086.

18. Visser, A. E.; Swatloski, R. P.; Reichert, W. M.; Mayton, R.; Sheff, S.; Wierzbicki, A.; Davis Jr, J. H.; Rogers, R. D., Task-specific ionic liquids for the extraction of metal ions from aqueous solutions. *Chemical Communications* **2001,** (1), 135-136.

19. Dietz, M. L., Ionic liquids as extraction solvents: Where do we stand? *Separation Science and Technology* **2006,** *41* (10), 2047-2063.

20. Buzzeo, M. C.; Evans, R. G.; Compton, R. G., Non-haloaluminate room-temperature ionic liquids in electrochemistry—A review. *ChemPhysChem* **2004,** *5* (8), 1106-1120.

21. De Souza, R. F.; Padilha, J. C.; Gonçalves, R. S.; Dupont, J., Room temperature dialkylimidazolium ionic liquid-based fuel cells. *Electrochemistry Communications* **2003,** *5* (8), 728-731.

22. Zakeeruddin, S. M.; Graetzel, M., Solvent-Free Ionic Liquid Electrolytes for Mesoscopic Dye-Sensitized Solar Cells. *Advanced Functional Materials* **2009,** *19* (14), 2187-2202.

23. Palacio, M.; Bhushan, B., A review of ionic liquids for green molecular lubrication in nanotechnology. *Tribology Letters* **2010,** *40* (2), 247-268.

24. Hough, W. L.; Smiglak, M.; Rodríguez, H.; Swatloski, R. P.; Spear, S. K.; Daly, D. T.; Pernak, J.; Grisel, J. E.; Carliss, R. D.; Soutullo, M. D., The third evolution of ionic liquids: active pharmaceutical ingredients. *New Journal of Chemistry* **2007,** *31* (8), 1429-1436.

25. Axenov, K. V.; Laschat, S., Thermotropic ionic liquid crystals. *Materials* **2011,** *4* (1), 206-259.

26. Mehrkesh, A.; Karunanithi, A., Predicting Melting point and Viscosity of Ionic Liquids Using New Quantum Chemistry Descriptors. *arXiv preprint arXiv:1612.00879* **2016.**

27. Wegner, S.; Janiak, C., Metal nanoparticles in ionic liquids. *Topics in Current Chemistry* **2017,** *375* (4), 65.

28. He, Z.; Alexandridis, P., Nanoparticles in ionic liquids: interactions and organization. *Physical Chemistry Chemical Physics* **2015,** *17* (28), 18238-18261.

29. Walden, P., Molecular weights and electrical conductivity of several fused salts. *Bull. Acad. Imper. Sci.(St. Petersburg)* **1914,** *1800.*

30. Graenacher, C., Cellulose solution. Google Patents: 1934.

31. Knight, G.; Shaw, B., 121. Long-chain alkylpyridines and their derivatives. New examples of liquid crystals. *Journal of the Chemical Society (Resumed)* **1938,** 682-683.

32. Barrer, R., The viscosity of pure liquids. II. Polymerised ionic melts. *Transactions of the Faraday Society* **1943,** *39,* 59-67.

33. Wier, T. P., Jr.; Hurley, F. H. Electrodeposition of aluminum. US2446349, 1948.

34. Hurley, F. H.; Wier, T. P., Electrodeposition of metals from fused quaternary ammonium salts. *Journal of The Electrochemical Society* **1951,** *98* (5), 203-206.

35. Bloom, H., Eleventh Spiers Memorial Lecture. Structural models for molten salts and their mixtures. *Discussions of the Faraday Society* **1961,** *32,* 7-13.

36. Yoke III, J. T.; Weiss, J. F.; Tollin, G., Reactions of triethylamine with copper (I) and copper (II) halides. *Inorganic Chemistry* **1963,** *2* (6), 1210-1216.

37. King, L.; Brown Jr, A.; Frayer, F. *High-energy density electrochemical cells.[Aluminium anodes for use in molten salt electrolytes]*; Air Force Academy, CO (USA): 1968.

38. Parshall, G. W., Catalysis in molten salt media. *Journal of the American Chemical Society* **1972,** *94* (25), 8716-8719.

39. Chum, H. L.; Koch, V.; Miller, L.; Osteryoung, R., Electrochemical scrutiny of organometallic iron complexes and hexamethylbenzene in a room temperature molten salt. *Journal of the American Chemical Society* **1975,** *97* (11), 3264-3265.

40. Koch, V.; Miller, L.; Osteryoung, R., Electroinitiated Friedel-Crafts transalkylations in a room-temperature molten-salt medium. *Journal of the American Chemical Society* **1976,** *98* (17), 5277-5284.

41. Gale, R.; Gilbert, B.; Osteryoung, R., Raman spectra of molten aluminum chloride: 1-butylpyridinium chloride systems at ambient temperatures. *Inorganic Chemistry* **1978,** *17* (10), 2728-2729.

42. Knifton, J. F., Ethylene glycol from synthesis gas via ruthenium melt catalysis. *J. Am. Chem. Soc.* **1981,** *103* (13), 3959-61.

43. Wilkes, J. S.; Levisky, J. A.; Wilson, R. A.; Hussey, C. L., Dialkylimidazolium chloroaluminate melts: a new class of room-temperature ionic liquids for electrochemistry, spectroscopy and synthesis. *Inorganic Chemistry* **1982,** *21* (3), 1263-1264.

44. Pacholec, F.; Butler, H. T.; Poole, C. F., Molten organic salt phase for gas-liquid chromatography. *Analytical Chemistry* **1982,** *54* (12), 1938-1941.

45. Magnuson, D. K.; Bodley, J. W.; Evans, D. F., The activity and stability of alkaline phosphatase in solutions of water and the fused salt ethylammonium nitrate. *Journal of solution chemistry* **1984,** *13* (8), 583-587.

46. Chauvin, Y.; Gilbert, B.; Guibard, I., Catalytic dimerization of alkenes by nickel complexes in organochloroaluminate molten salts. *Journal of the Chemical Society, Chemical Communications* **1990,** (23), 1715-1716.

47. Wilkes, J. S.; Zaworotko, M. J., Air and water stable 1-ethyl-3-methylimidazolium based ionic liquids. *Journal of the Chemical Society, Chemical Communications* **1992,** (13), 965-967.

48. Taubert, A.; Steiner, P.; Mantion, A., Ionic liquid crystal precursors for inorganic particles: Phase diagram and thermal properties of a CuCl nanoplatelet precursor. *The Journal of Physical Chemistry B* **2005,** *109* (32), 15542-15547.

49. Taubert, A.; Palivan, C.; Casse, O.; Gozzo, F.; Schmitt, B., Ionic liquid-crystal precursors (ILCPs) for CuCl platelets: The origin of the exothermic peak in the DSC curves. *The Journal of Physical Chemistry C* **2007,** *111* (11), 4077-4082.

50. Taubert, A., CuCl Nanoplatelets from an Ionic Liquid-Crystal Precursor. *Angewandte Chemie* **2004,** *116* (40), 5494-5496.

51. Angell, C. A.; Ansari, Y.; Zhao, Z., Ionic liquids: past, present and future. *Faraday discussions* **2012,** *154*, 9-27.

52. Ohno, H., *Electrochemical aspects of ionic liquids*. John Wiley & Sons: 2005.

53. Zhong, C.; Deng, Y.; Hu, W.; Sun, D.; Han, X.; Qiao, J.; Zhang, J., *Electrolytes for electrochemical supercapacitors*. CRC Press: 2016.

54. Greaves, T. L.; Drummond, C. J., Protic ionic liquids: properties and applications. *Chemical reviews* **2008,** *108* (1), 206-237.

55. MSS Esperança, J.; Canongia Lopes, J. N.; Tariq, M.; Santos, L. s. M.; Magee, J. W.; Rebelo, L. s. P. N., Volatility of Aprotic Ionic Liquids・A Review. *Journal of Chemical & Engineering Data* **2009,** *55* (1), 3-12.

56. Belieres, J.-P.; Angell, C. A., Protic ionic liquids: preparation, characterization, and proton free energy level representation. *The Journal of Physical Chemistry B* **2007,** *111* (18), 4926-4937.

57. Plechkova, N. V.; Seddon, K. R., Applications of ionic liquids in the chemical industry. *Chemical Society Reviews* **2008,** *37* (1), 123-150.

58. De Los Rios, A. P.; Fernandez, F. J. H., *Ionic Liquids in Separation Technology*. Elsevier: **2014**.

59. Hardacre, C.; Parvulescu, V., *Catalysis in Ionic Liquirds: From Catalyst Synthesis to Application*. Royal society of chemistry: **2014**; Vol. 15.

60. Mun, J.; Sim, H., *Handbook of Ionic Liquids: Properties, applications, and hazards*. Nova Science Publishers: **2012**.

61. Rogers, R.; Plechkova, N.; Seddon, K. In *Ionic liquids: From knowledge to application*, ACS Symposium Series, **2009**; pp 123-150.

62. Chen, R.; Zhang, H.; Wu, F., Applications of ionic liquids in batteries. *Prog. Chem* **2011,** *23*, 366-373.

63. Patel, D. D.; Lee, J.-M., Applications of ionic liquids. *The Chemical Record* **2012,** *12* (3), 329-355.

64. Lee, H.-J.; Lee, J.-S.; Kim, H.-S., Applications of ionic liquids: the state of arts. *Applied Chemistry for Engineering* **2010,** *21* (2), 129-136.

65. Li, X.; Zhao, D.; Fei, Z.; Wang, L., Applications of functionalized ionic liquids. *Science in China Series B: Chemistry* **2006,** *49* (5), 385-401.

66. Ohno, H.; Washiro, S.; Yoshizawa, M., Novel solid polymer electrolytes composed of zwitterionic liquids and polymerized ionic liquids. ACS Publications: 2005.

67. Zazybin, A. G.; Rafikova, K.; Yu, V.; Zolotareva, D.; Dembitsky, V. M.; Sasaki, T., Metal-containing ionic liquids: current paradigm and applications. *Russian Chemical Reviews* **2017,** *86* (12), 1254.

68. Abbott, A. P.; Bell, T. J.; Handa, S.; Stoddart, B., O-Acetylation of cellulose and monosaccharides using a zinc based ionic liquid. *Green Chemistry* **2005,** *7* (10), 705-707.

69. Taubert, A.; Li, Z., Inorganic materials from ionic liquids. *Dalton Transactions* **2007,** (7), 723-727.

70. Duan, X.; Ma, J.; Lian, J.; Zheng, W., The art of using ionic liquids in the synthesis of inorganic nanomaterials. *CrystEngComm* **2014,** *16* (13), 2550-2559.

71. Saeva, D. F., *Liquid Crystals: Fourth State of Matter*. Marcel Dekker: 1979.

72. Laidlaw, D. H.; Weickert, J., *Visualization and Processing of Tensor Fields: Advances and Perspectives*. Springer Science & Business Media: 2009.

73. barrett-group.mcgill.ca/tutorials/liquid_crystal/LC02.htm

74. http://www.imp.tu-darmstadt.de/forschung_imp/mwt_imp/liquid_crystals_imp/index.de.jsp

75. Goossens, K.; Lava, K.; Bielawski, C. W.; Binnemans, K., Ionic liquid crystals: versatile materials. *Chemical reviews* **2016,** *116* (8), 4643-4807.

76. Alvarez Fernandez, A.; Kouwer, P. H., Key Developments in Ionic Liquid Crystals. *International journal of molecular sciences* **2016,** *17* (5), 731.

77. Averill, B.; Eldredge, P., *General Chemistry: Principles, Patterns, and Applications*. The Saylor Foundation: 2011.

78. Koide, N., *The liquid crystal display story: 50 years of liquid crystal R&D that lead the way to the future*. Springer: 2014.

79. Goodby, J.; Görtz, V.; Cowling, S.; Mackenzie, G.; Martin, P.; Plusquellec, D.; Benvegnu, T.; Boullanger, P.; Lafont, D.; Queneau, Y., Thermotropic liquid crystalline glycolipids. *Chemical Society Reviews* **2007,** *36* (12), 1971-2032.

80. Reinitzer, F., Beiträge zur kenntniss des cholesterins. *Monatshefte für Chemie/Chemical Monthly* **1888,** *9* (1), 421-441.

81. Lehmann, O., Über fliessende krystalle. *Zeitschrift für physikalische Chemie* **1889,** *4* (1), 462-472.

82. Gattermann, L.; Ritschke, A., Ueber azoxyphenoläther. *European Journal of Inorganic Chemistry* **1890,** *23* (1), 1738-1750.

83. Demus, D., 100 Years liquid crystal chemistry. *Molecular crystals and liquid crystals* **1988,** *165* (1), 45-84.

84. Vorländer, D., *Kristallinisch-flüssige substanzen*. Enke: 1908.

85. Friedel, G. In *The mesomorphic states of matter*, Annales de Physique, 1922; p 5.

86. de Broglie, M.; Friedel, E., The diffraction of X-rays by "smectic" substances. *Compt. rend.* **1923,** *176*, 738-40.

87. Tsvetkov, V., Uber die Molekülanordnung in der anisotrop-flüssigen Phase. *Acta Physicochimica URSS* **1942,** *15*, 132-147.

88. Heilmeier, G. H.; Zanoni, L. A.; Barton, L. A., Dynamic scattering: A new electrooptic effect in certain classes of nematic liquid crystals. *Proceedings of the IEEE* **1968,** *56* (7), 1162-1171.

89. SCHADT, M., and HELFRICH, W., 1971, Appl. Phys. Lett., 18, 127. 1970, Swiss Patent 532261 (4 December).

90. FERGASON, J. 1971, U.S. Patent 3918796 (9 February).

91. Cîrcu, V., Ionic liquid crystals based on pyridinium salts. In *Progress and Developments in Ionic Liquids*, InTech: 2017.

92. Butschies, M.; Frey, W.; Laschat, S., Designer ionic liquid crystals based on congruently shaped guanidinium sulfonates. *Chemistry-A European Journal* **2012,** *18* (10), 3014-3022.

93. Casella, G.; Causin, V.; Rastrelli, F.; Saielli, G., Viologen-based ionic liquid crystals: induction of a smectic A phase by dimerisation. *Physical Chemistry Chemical Physics* **2014,** *16* (11), 5048-5051.

94. Mathevet, F.; Masson, P.; Nicoud, J. F.; Skoulios, A., Smectic liquid crystals from supramolecular guanidinium alkylbenzenesulfonates. *Chemistry-A European Journal* **2002,** *8* (10), 2248-2254.

95. Kato, T.; Yasuda, T.; Kamikawa, Y.; Yoshio, M., Self-assembly of functional columnar liquid crystals. *Chemical Communications* **2009,** (7), 729-739.

96. Kumar, S.; Pal, S. K., Synthesis and characterization of novel imidazolium-based ionic discotic liquid crystals with a triphenylene moiety. *Tetrahedron letters* **2005,** *46* (15), 2607-2610.

97. Tanabe, K.; Suzui, Y.; Hasegawa, M.; Kato, T., Full-color tunable photoluminescent ionic liquid crystals based on tripodal pyridinium, pyrimidinium, and quinolinium salts. *Journal of the American Chemical Society* **2012,** *134* (12), 5652-5661.

98. Abouserie, A.; Zehbe, K.; Metzner, P.; Kelling, A.; Günter, C.; Schilde, U.; Strauch, P.; Körzdörfer, T.; Taubert, A., Alkylpyridinium Tetrahalidometallate Ionic Liquids and Ionic Liquid Crystals: Insights into the Origin of Their Phase Behavior. *European Journal of Inorganic Chemistry*.

99. Men, S.; Mitchell, D. S.; Lovelock, K. R.; Licence, P., X-ray Photoelectron Spectroscopy of Pyridinium-Based Ionic Liquids: Comparison to Imidazolium-and Pyrrolidinium-Based Analogues. *ChemPhysChem* **2015,** *16* (10), 2211-2218.

100. Vilas, M.; Rocha, M. A.; Fernandes, A. M.; Tojo, E.; Santos, L. M., Novel 2-alkyl-1-ethylpyridinium ionic liquids: synthesis, dissociation energies and volatility. *Physical Chemistry Chemical Physics* **2015,** *17* (4), 2560-2572.

101. Sanchez, L. G.; Espel, J. R.; Onink, F.; Meindersma, G. W.; Haan, A. B. d., Density, viscosity, and surface tension of synthesis grade imidazolium, pyridinium, and pyrrolidinium based room temperature ionic liquids. *Journal of Chemical & Engineering Data* **2009,** *54* (10), 2803-2812.

102. Crosthwaite, J. M.; Muldoon, M. J.; Dixon, J. K.; Anderson, J. L.; Brennecke, J. F., Phase transition and decomposition temperatures, heat capacities and viscosities of pyridinium ionic liquids. *The Journal of Chemical Thermodynamics* **2005,** *37* (6), 559-568.

103. Deyko, A.; Lovelock, K. R.; Corfield, J.-A.; Taylor, A. W.; Gooden, P. N.; Villar-Garcia, I. J.; Licence, P.; Jones, R. G.; Krasovskiy, V. G.; Chernikova, E. A., Measuring and predicting Δ vap H 298 values of ionic liquids. *Physical Chemistry Chemical Physics* **2009,** *11* (38), 8544-8555.

104. Yunus, N. M.; Mutalib, M. A.; Man, Z.; Bustam, M. A.; Murugesan, T., Thermophysical properties of 1-alkylpyridinum bis (trifluoromethylsulfonyl) imide ionic liquids. *The Journal of Chemical Thermodynamics* **2010,** *42* (4), 491-495.

105. Cadena, C.; Zhao, Q.; Snurr, R. Q.; Maginn, E. J., Molecular modeling and experimental studies of the thermodynamic and transport properties of pyridinium-based ionic liquids. *The Journal of Physical Chemistry B* **2006,** *110* (6), 2821-2832.

106. Papaiconomou, N.; Yakelis, N.; Salminen, J.; Bergman, R.; Prausnitz, J. M., Properties of some ionic liquids based on 1-methyl-3-octylimidazolium and 4-methyl-N-butylpyridinium cations. *Lawrence Berkeley National Laboratory* **2005**.

107. Mohamed, N. F.; Mutalib, A.; Ibrahim, M.; Bustam, M. A.; Leveque, J. M.; El-Harabawi, M. In *Ecotoxicity of Pyridinium Based Ionic Liquids: A Review*, Applied Mechanics and Materials, Trans Tech Publ: 2014; pp 152-155.

108. Docherty, K. M.; Dixon, J. K.; Kulpa Jr, C. F., Biodegradability of imidazolium and pyridinium ionic liquids by an activated sludge microbial community. *Biodegradation* **2007,** *18* (4), 481-493.

109. Haiß, A.; Jordan, A.; Westphal, J.; Logunova, E.; Gathergood, N.; Kümmerer, K., On the way to greener ionic liquids: identification of a fully mineralizable phenylalanine-based ionic liquid. *Green Chemistry* **2016,** *18* (16), 4361-4373.

110. Cao, Y.; Mu, T., Comprehensive investigation on the thermal stability of 66 ionic liquids by thermogravimetric analysis. *Industrial & engineering chemistry research* **2014,** *53* (20), 8651-8664.

111. Karmakar, R.; Samanta, A., Intramolecular excimer formation kinetics in room temperature ionic liquids. *Chemical physics letters* **2003,** *376* (5), 638-645.

112. Oliveira, M. B.; Llovell, F.; Coutinho, J. A.; Vega, L. F., Modeling the [NTf2] pyridinium ionic liquids family and their mixtures with the soft statistical associating fluid theory equation of state. *The Journal of Physical Chemistry B* **2012,** *116* (30), 9089-9100.

113. Chaban, V. V.; Prezhdo, O. V., Polarization versus temperature in pyridinium ionic liquids. *The Journal of Physical Chemistry B* **2014,** *118* (48), 13940-13945.

114. Knight, G. A.; Shaw, B. D., Long-chain alkylpyridines and their derivatives. New examples of liquid crystals. *J. Chem. Soc.* **1938**, 682-3.

115.	Garti, N., *Thermal behavior of dispersed systems*. CRC Press: 2000.

116.	Sudholter, E. J.; Engberts, J. B.; De Jeu, W. H., Thermotropic liquid-crystalline behavior of some single-and double-chained pyridinium amphiphiles. *The Journal of Physical Chemistry* **1982,** *86* (10), 1908-1913.

117.	Somashekar, R., Mesomorphic behaviour of n-4-hexadecylpyridinium chloride. *Molecular Crystals and Liquid Crystals* **1987,** *146* (1), 225-233.

118.	Fürst, H.; Dietz, H., Langkettige Pyridinderivate und ihre tertiären Imoniumsalze. *Advanced Synthesis & Catalysis* **1956,** *4* (3), 147-160.

119.	Nusselder, J. J. H.; Engberts, J. B.; Van Doren, H. A., Liquid-crystalline and thermochromic behaviour of 4-substituted 1-methylpyridinium iodide surfactants. *Liquid Crystals* **1993,** *13* (2), 213-225.

120.	Papaiconomou, N.; Salminen, J.; Lee, J.-M.; Prausnitz, J. M., Physicochemical properties of hydrophobic ionic liquids containing 1-octylpyridinium, 1-octyl-2-methylpyridinium, or 1-octyl-4-methylpyridinium cations. *Journal of Chemical & Engineering Data* **2007,** *52* (3), 833-840.

121.	Rebeiro, G. L.; Khadilkar, B. M., Chloroaluminate ionic liquid for Fischer indole synthesis. *Synthesis* **2001,** *2001* (03), 0370-0372.

122.	Yunus, N. M.; Mutalib, M. A.; Man, Z.; Bustam, M. A.; Murugesan, T., Solubility of CO 2 in pyridinium based ionic liquids. *Chemical engineering journal* **2012,** *189*, 94-100.

123.	Wasserscheid, P.; Waffenschmidt, H., Ionic liquids in regioselective platinum-catalysed hydroformylation. *Journal of Molecular Catalysis A: Chemical* **2000,** *164* (1), 61-67.

124.	Arnautov, S., Electrochemical synthesis of polyphenylene in a new ionic liquid. *Synthetic metals* **1997,** *84* (1), 295-296.

125.	Zhao, S.; Zhao, E.; Shen, P.; Zhao, M.; Sun, J., An atom-efficient and practical synthesis of new pyridinium ionic liquids and application in Morita–Baylis–Hillman reaction. *Ultrasonics sonochemistry* **2008,** *15* (6), 955-959.

126.	Malhotra, S. V.; Xiao, Y., Diels-alder and friedel-crafts reactions in pyridinium-based ionic liquids. ACS Publications: 2007.

127.	Ford, L.; Atefi, F.; Singer, R. D.; Scammells, P. J., Grignard reactions in pyridinium and phosphonium ionic liquids. *European Journal of Organic Chemistry* **2011,** *2011* (5), 942-950.

128.	Wu, X. Y., Facile and green synthesis of 1, 4-dihydropyridine derivatives in n-butyl pyridinium tetrafluoroborate. *Synthetic Communications* **2012,** *42* (3), 454-459.

129.	Ghandi, K., A review of ionic liquids, their limits and applications. *Green and sustainable chemistry* **2014,** *4* (01), 44.

130.	Hajipour, A. R.; Seddighi, M., Pyridinium-based brønsted acidic ionic liquid as a highly efficient catalyst for one-pot synthesis of dihydropyrimidinones. *Synthetic Communications* **2012,** *42* (2), 227-235.

131.	Pajuste, K.; Plotniece, A.; Kore, K.; Intenberga, L.; Cekavicus, B.; Kaldre, D.; Duburs, G.; Sobolev, A., Use of pyridinium ionic liquids as catalysts for the synthesis of 3, 5-bis (dodecyloxycarbonyl)-1, 4-dihydropyridine derivative. *Open Chemistry* **2011,** *9* (1), 143-148.

132.	Duan, Z.; Gu, Y.; Zhang, J.; Zhu, L.; Deng, Y., Protic pyridinium ionic liquids: Synthesis, acidity determination and their performances for acid catalysis. *Journal of Molecular Catalysis A: Chemical* **2006,** *250* (1), 163-168.

133.	Dinnebier, R. E.; Billinge, S. J., *Powder diffraction: theory and practice*. Royal Society of Chemistry: 2008.

134.	Zhao, X.; Gu, Y.; Li, J.; Ding, H.; Shan, Y., An environment-friendly method for synthesis of 1, 4-dibromo-naphthalene in aqueous solution of ionic liquids. *Catalysis Communications* **2008,** *9* (13), 2179-2182.

135.	Li, K.-X.; Chen, L.; Yan, Z.-C.; Wang, H.-L., Application of pyridinium ionic liquid as a recyclable catalyst for acid-catalyzed transesterification of Jatropha oil. *Catalysis letters* **2010,** *139* (3-4), 151-156.

136.   Neve, F., Transition metal-based ionic mesogens. *Adv. Mater. (Weinheim, Ger.)* **1996**, *8* (4), 277-89.

137.   Goossens, K.; Lava, K.; Bielawski, C. W.; Binnemans, K., Ionic Liquid Crystals: Versatile Materials. *Chem. Rev. (Washington, DC, U. S.)* **2016**, *116* (8), 4643-4807.

138.   Ma, Z.; Yu, J.; Dai, S., Preparation of inorganic materials using ionic liquids. *Advanced materials* **2010**, *22* (2), 261-285.

139.   Dupont, J.; Fonseca, G. S.; Umpierre, A. P.; Fichtner, P. F.; Teixeira, S. R., Transition-metal nanoparticles in imidazolium ionic liquids: recyclable catalysts for biphasic hydrogenation reactions. *Journal of the American Chemical Society* **2002**, *124* (16), 4228-4229.

140.   Nakashima, T.; Kimizuka, N., Interfacial synthesis of hollow TiO2 microspheres in ionic liquids. *Journal of the American Chemical Society* **2003**, *125* (21), 6386-6387.

141.   Zhou, Y.; Antonietti, M., Synthesis of very small TiO2 nanocrystals in a room-temperature ionic liquid and their self-assembly toward mesoporous spherical aggregates. *Journal of the American Chemical Society* **2003**, *125* (49), 14960-14961.

142.   Hamill, N. A.; Hardacre, C.; McMath, S. J., In situ XAFS investigation of palladium species present during the Heck reaction in room temperature ionic liquids. *Green Chemistry* **2002**, *4* (2), 139-142.

143.   Cooper, E. R.; Andrews, C. D.; Wheatley, P. S.; Webb, P. B.; Wormald, P.; Morris, R. E., Ionic liquids and eutectic mixtures as solvent and template in synthesis of zeolite analogues. *Nature* **2004**, *430* (7003), 1012-1016.

144.   Migowski, P.; Dupont, J., Catalytic applications of metal nanoparticles in imidazolium ionic liquids. *Chemistry-A European Journal* **2007**, *13* (1), 32-39.

145.   Itoh, H.; Naka, K.; Chujo, Y., Synthesis of gold nanoparticles modified with ionic liquid based on the imidazolium cation. *Journal of the American Chemical Society* **2004**, *126* (10), 3026-3027.

146.   Taubert, A.; Arbell, I.; Mecke, A.; Graf, P., Photoreduction of a crystalline Au (III) complex: A solidstate approach to metallic nanostructures. *Gold Bulletin* **2006**, *39* (4), 205-211.

147.   Taubert, A., Cubes and Hollow Rods From Ionic Liquid Emulsions. *Acta Chim. Slov* **2005**, *52*, 168-170.

148.   Li, Z.; Khimyak, Y. Z.; Taubert, A., Lessons from a "Failed" experiment: Zinc silicates with complex morphology by reaction of Zinc acetate, the ionic liquid precursor (ILP) tetrabutylammonium hydroxide (TBAH), and glass. *Materials* **2008**, *1* (1), 3-24.

149.   Ayi, A. A.; Khare, V.; Strauch, P.; Girard, J.; Fromm, K. M.; Taubert, A., On the chemical synthesis of titanium nanoparticles from ionic liquids. *Monatshefte für Chemie-Chemical Monthly* **2010**, *141* (12), 1273-1278.

150.   Vollmer, C.; Janiak, C., Naked metal nanoparticles from metal carbonyls in ionic liquids: Easy synthesis and stabilization. *Coordination Chemistry Reviews* **2011**, *255* (17-18), 2039-2057.

151.   Ninham, B., On progress in forces since the DLVO theory. *Advances in colloid and interface science* **1999**, *83* (1), 1-17.

152.   Obliosca, J. M.; Arellano, I. H. J.; Huang, M. H.; Arco, S. D., Double layer micellar stabilization of gold nanocrystals by greener ionic liquid 1-butyl-3-methylimidazolium lauryl sulfate. *Materials Letters* **2010**, *64* (9), 1109-1112.

153.   He, Z.; Alexandridis, P., Ionic liquid and nanoparticle hybrid systems: Emerging applications. *Advances in colloid and interface science* **2016**.

154.   Qurashi, A., *Metal chalcogenide nanostructures for renewable energy applications*. John Wiley & Sons: 2014.

155.   Parkinson, B., Electrochemistry of Metal Chalcogenides. ACS Publications: 2010.

156.   Somiya, S., *Handbook of advanced ceramics: materials, applications, processing, and properties*. Academic Press: 2013.

157.   Jiang, Y.; Zhu, Y.-J., Microwave-assisted synthesis of nanocrystalline metal sulfides using an ionic liquid. *Chemistry letters* **2004**, *33* (10), 1390-1391.

158.   Jiang, Y.; Zhu, Y.-J., Microwave-assisted synthesis of sulfide M2S3 (M= Bi, Sb) nanorods using an ionic liquid. *The Journal of Physical Chemistry B* **2005,** *109* (10), 4361-4364.

159.   Biswas, K.; Rao, C. e. N. e. R., Use of ionic liquids in the synthesis of nanocrystals and nanorods of semiconducting metal chalcogenides. *Chemistry-A European Journal* **2007,** *13* (21), 6123-6129.

160.   Li, H.; Li, W.; Ma, L.; Chen, W.; Wang, J., Electrochemical lithiation/delithiation performances of 3D flowerlike MoS 2 powders prepared by ionic liquid assisted hydrothermal route. *Journal of Alloys and Compounds* **2009,** *471* (1), 442-447.

161.   Jie-Hui, Y.; Ji-Qing, X.; Yu-Jiang, S.; Hai-Ying, B.; Jing, L.; Tie-Gang, W., Syntheses and Characterization of Several Copper-halo Clusters. *Chinese Journal of Chemistry* **2005,** *23* (8), 1030-1036.

162.   Wu, Y.; Hao, X.; Yang, J.; Tian, F.; Jiang, M., Ultrasound-assisted synthesis of nanocrystalline ZnS in the ionic liquid [BMIM]· BF 4. *Materials Letters* **2006,** *60* (21), 2764-2766.

163.   Xu, C.; Wang, L.; Zou, D.; Ying, T., Ionic liquid-assisted synthesis of hierarchical CuS nanostructures at room temperature. *Materials Letters* **2008,** *62* (17), 3181-3184.

164.   Wu, Y.; Wadia, C.; Ma, W.; Sadtler, B.; Alivisatos, A. P., Synthesis and photovoltaic application of copper (I) sulfide nanocrystals. *Nano letters* **2008,** *8* (8), 2551-2555.

165.   Wang, F.; Dong, H.; Pan, J.; Li, J.; Li, Q.; Xu, D., One-step electrochemical deposition of hierarchical CuS nanostructures on conductive substrates as robust, high-performance counter electrodes for quantum-dot-sensitized solar cells. *The Journal of Physical Chemistry C* **2014,** *118* (34), 19589-19598.

166.   Lai, C.-H.; Huang, K.-W.; Cheng, J.-H.; Lee, C.-Y.; Hwang, B.-J.; Chen, L.-J., Direct growth of high-rate capability and high capacity copper sulfide nanowire array cathodes for lithium-ion batteries. *Journal of Materials Chemistry* **2010,** *20* (32), 6638-6645.

167.   Kundu, J.; Pradhan, D., Controlled synthesis and catalytic activity of copper sulfide nanostructured assemblies with different morphologies. *ACS applied materials & interfaces* **2014,** *6* (3), 1823-1834.

168.   Yu, X. L.; Cao, C. B.; Zhu, H. S.; Li, Q. S.; Liu, C. L.; Gong, Q. H., Nanometer-Sized Copper Sulfide Hollow Spheres with Strong Optical-Limiting Properties. *Advanced Functional Materials* **2007,** *17* (8), 1397-1401.

169.   Bai, J.; Jiang, X., A facile one-pot synthesis of copper sulfide-decorated reduced graphene oxide composites for enhanced detecting of H2O2 in biological environments. *Analytical chemistry* **2013,** *85* (17), 8095-8101.

170.   Wang, J., Electrochemical biosensors: towards point-of-care cancer diagnostics. *Biosensors and Bioelectronics* **2006,** *21* (10), 1887-1892.

171.   Grozdanov, I.; Najdoski, M., Optical and electrical properties of copper sulfide films of variable composition. *Journal of Solid State Chemistry* **1995,** *114* (2), 469-475.

172.   Zhao, Y.; Pan, H.; Lou, Y.; Qiu, X.; Zhu, J.; Burda, C., Plasmonic Cu2− x S nanocrystals: optical and structural properties of copper-deficient copper (I) sulfides. *Journal of the American Chemical Society* **2009,** *131* (12), 4253-4261.

173.   W.R. Cook, "The Copper Sulfur Phase Diagram", Ph.D. Thesis, Case Western Reserve Univ. (1971).

174.   Chakrabarti, D.; Laughlin, D., The Cu-S (copper-sulfur) system. *Journal of Phase Equilibria* **1983,** *4* (3), 254-271.

175.   Wang, Y.; Hu, Y.; Zhang, Q.; Ge, J.; Lu, Z.; Hou, Y.; Yin, Y., One-pot synthesis and optical property of copper (I) sulfide nanodisks. *Inorganic chemistry* **2010,** *49* (14), 6601-6608.

176.   Huang, S.; Liu, J.; He, Q.; Chen, H.; Cui, J.; Xu, S.; Zhao, Y.; Chen, C.; Wang, L., Smart Cu1. 75S nanocapsules with high and stable photothermal efficiency for NIR photo-triggered drug release. *Nano Res* **2015,** *8* (12), 4038-4047.

177. Tian, Q.; Jiang, F.; Zou, R.; Liu, Q.; Chen, Z.; Zhu, M.; Yang, S.; Wang, J.; Wang, J.; Hu, J., Hydrophilic Cu9S5 nanocrystals: A photothermal agent with a 25.7% heat conversion efficiency for photothermal ablation of cancer cells in vivo. *ACS nano* **2011,** *5* (12), 9761-9771.

178. Farhadyar, N.; Sadjadi, M.; Farhadyar, F.; Farhadyar, A. In *Wet Chemistry Synthesis of Semiconductor Gold/Cu1. 96S Nanorod and Study of its Photoluminescence Properties*, Journal of Nano Research, Trans Tech Publ: 2013; pp 51-56.

179. Lukashev, P. Crystal and Electronic Structure of Copper Sulfides. Case Western Reserve University, 2007.

180. Hirahara, E., The physical properties of cuprous sulfides-semiconductors. *Journal of the Physical Society of Japan* **1951,** *6* (6), 422-427.

181. Sun, S.; Li, P.; Liang, S.; Yang, Z., Diversified copper sulfide (Cu 2− x S) micro-/nanostructures: a comprehensive review on synthesis, modifications and applications. *Nanoscale* **2017,** *9* (32), 11357-11404.

182. W.R. Cook, "The Copper Sulfur Phase Diagram", Ph.D. Thesis, Case Western Reserve Univ. (1971).

183. Xu, Q.; Huang, B.; Zhao, Y.; Yan, Y.; Noufi, R.; Wei, S.-H., Crystal and electronic structures of Cu x S solar cell absorbers. *Applied Physics Letters* **2012,** *100* (6), 061906.

184. Morales-García, A.; Soares Jr, A. L.; Dos Santos, E. C.; de Abreu, H. A.; Duarte, H. l. A., First-principles calculations and electron density topological analysis of covellite (CuS). *The Journal of Physical Chemistry A* **2014,** *118* (31), 5823-5831.

185. Sakamoto, T.; Sunamura, H.; Kawaura, H.; Hasegawa, T.; Nakayama, T.; Aono, M., Nanometer-scale switches using copper sulfide. *Applied physics letters* **2003,** *82* (18), 3032-3034.

186. Sagade, A. A.; Sharma, R.; Sulaniya, I., Enhancement in sensitivity of copper sulfide thin film ammonia gas sensor: Effect of swift heavy ion irradiation. *Journal of Applied Physics* **2009,** *105* (4), 043701.

187. Zhao, Y.; Burda, C., Development of plasmonic semiconductor nanomaterials with copper chalcogenides for a future with sustainable energy materials. *Energy & Environmental Science* **2012,** *5* (2), 5564-5576.

188. Xie, Y.; Bertoni, G.; Riedinger, A.; Sathya, A.; Prato, M.; Marras, S.; Tu, R.; Pellegrino, T.; Manna, L., Nanoscale transformations in covellite (CuS) nanocrystals in the presence of divalent metal cations in a mild reducing environment. *Chemistry of Materials* **2015,** *27* (21), 7531-7537.

189. Roy, P.; Srivastava, S. K., Nanostructured copper sulfides: synthesis, properties and applications. *CrystEngComm* **2015,** *17* (41), 7801-7815.

190. Ghosh, A.; Mondal, A., A simple electrochemical route to deposit Cu7S4 thin films and their photocatalytic properties. *Applied Surface Science* **2015,** *328*, 63-70.

191. Goel, S.; Chen, F.; Cai, W., Synthesis and biomedical applications of copper sulfide nanoparticles: from sensors to theranostics. *Small* **2014,** *10* (4), 631-645.

192. Ramasamy, K.; Malik, M. A.; Revaprasadu, N.; O'Brien, P., Routes to nanostructured inorganic materials with potential for solar energy applications. *Chemistry of Materials* **2013,** *25* (18), 3551-3569.

193. Roy, P.; Srivastava, S. K., Nanostructured anode materials for lithium ion batteries. *Journal of Materials Chemistry A* **2015,** *3* (6), 2454-2484.

194. Yogeswaran, U.; Chen, S.-M., A review on the electrochemical sensors and biosensors composed of nanowires as sensing material. *Sensors* **2008,** *8* (1), 290-313.

195. Zhu, C.; Yang, G.; Li, H.; Du, D.; Lin, Y., Electrochemical sensors and biosensors based on nanomaterials and nanostructures. *Analytical chemistry* **2014,** *87* (1), 230-249.

196. Lee, K. J.; Elgrishi, N.; Kandemir, B.; Dempsey, J. L., Electrochemical and spectroscopic methods for evaluating molecular electrocatalysts. *Nature Reviews Chemistry* **2017,** *1*, 0039.

197. Wolfgang, G.; Jones, T.; Kleitz, M.; Seiyama, T., *Sensors, Chemical and Biochemical Sensors*. John Wiley & Sons: 2008; Vol. 2.

198.   Lam, B. Nanostructured Electrochemical Biosensors: Towards Point of Care Diagnostics. 2013.

199.   Rackus, D. G.; Shamsi, M. H.; Wheeler, A. R., Electrochemistry, biosensors and microfluidics: a convergence of fields. *Chemical Society Reviews* **2015**, *44* (15), 5320-5340.

200.   Luque, A.; Hegedus, S., *Handbook of photovoltaic science and engineering*. John Wiley & Sons: 2011.

201.   Abou-Ras, D.; Kirchartz, T.; Rau, U., *Advanced characterization techniques for thin film solar cells*. Wiley Online Library: 2011.

202.   Scheer, R.; Schock, H.-W., *Chalcogenide photovoltaics: physics, technologies, and thin film devices*. John Wiley & Sons: 2011.

203.   www2.pv.unsw.edu.au/nsitefiles/pdfs/UNSW_Understanding_the_p-n_Junction.pdf

204.   www.physics-and-radio-electronics.com

205.   www.physics-and-radio-electronics.com

206.   Abdulrazzaq, O. A.; Saini, V.; Bourdo, S.; Dervishi, E.; Biris, A. S., Organic solar cells: a review of materials, limitations, and possibilities for improvement. *Particulate science and technology* **2013**, *31* (5), 427-442.

207.   Tilley, R. J., *Crystals and crystal structures*. John Wiley & Sons: 2006.

208.
    https://chem.libretexts.org/Textbook_Maps/General_Chemistry_Textbook_Maps/Map%3A_Che mPRIME_(Moore_et_al.)/10Solids%2C_Liquids_and_Solutions/10.03%3A_Crystal_Systems

209.   Fava, R. A.; Editor, *Methods of Experimental Physics, Vol. 16: Polymers, Pt. B: Crystal Structure and Morphology*. Academic Press: 1980; p 421 pp.

210.   Suryanarayana, C.; Norton, M. G., *X-ray diffraction: a practical approach*. Springer Science & Business Media: 2013.

211.   Demus, D.; Goodby, J. W.; Gray, G. W.; Spiess, H. W.; Vill, V., *Handbook of liquid crystals, low molecular weight liquid crystals I: calamitic liquid crystals*. John Wiley & Sons: 2011.

212.   Borfecchia, E.; Gianolio, D.; Agostini, G.; Bordiga, S.; Lamberti, C., *Characterization of MOFs. 2. Long and local range order structural determination of MOFs by combining EXAFS and diffraction techniques*. The Royal Society of Chemistry: Cambridge: 2013.

213.   Sardela, M., *Practical Materials Characterization*. Springer: 2014.

214.   Clearfield, A.; Reibenspies, J. H.; Bhuvanesh, N., *Principles and applications of powder diffraction*. John Wiley and Sons, Ltd.: 2008.

215.   Waeselmann, N., Structural transformations in complex perovskite-type relaxor and relaxor-based ferroelectrics at high pressures and temperatures. **2012**.

216.   Bennett, D. W., *Understanding single-crystal x-ray crystallography*. John Wiley & Sons: 2010.

217.   Yan, Y. Exploring and Analysing the Structural Diversity of Organic Co-crystals. Cardiff University, 2014.

218.   Scharf, T., *Polarized light in liquid crystals and polymers*. John Wiley & Sons: 2007.

219.   Bunzli, J.-C. G.; Pecharsky, V. K.; Editors, *Handbook on physics and chemistry of rare earths: Including actinides: Volume 43*. Elsevier: 2013; p 601 pp.

220.   Atwood, J. L.; Steed, J. W., *Encyclopedia of supramolecular chemistry*. CRC Press: 2004; Vol. 1.

221.   https://www.olympus-lifescience.com/de/microscope-resource/primer/lightandcolor/birefringence/

222.   Hayat, M. A., *Principles and techniques of electron microscopy. Biological applications*. Edward Arnold.: 1981.

223.   Goldstein, J. I.; Newbury, D. E.; Michael, J. R.; Ritchie, N. W.; Scott, J. H. J.; Joy, D. C., *Scanning electron microscopy and X-ray microanalysis*. Springer: 2017.

224.   Michler, G. H., Electron microscopy. In *Polypropylene*, Springer: 1999; pp 186-197.

225.   Williams, D. B.; Carter, C. B., The transmission electron microscope. In *Transmission electron microscopy*, Springer: 1996; pp 3-17.

226.   Castner Jr, E. W.; Wishart, J. F., Spotlight on ionic liquids. *The Journal of chemical physics* **2010,** *132* (12), 120901.

227.   Hallett, J. P.; Welton, T., Room-temperature ionic liquids: solvents for synthesis and catalysis. 2. *Chemical Reviews* **2011,** *111* (5), 3508-3576.

228.   Wasserscheid, P.; Keim, W., Ionic liquids—new "solutions" for transition metal catalysis. *Angewandte Chemie International Edition* **2000,** *39* (21), 3772-3789.

229.   Wishart, J. F.; Castner, E. W., The physical chemistry of ionic liquids. *The Journal of Physical Chemistry B* **2007,** *111* (18), 4639-4640.

230.   Endres, F.; Höfft, O.; Borisenko, N.; Gasparotto, L. H.; Prowald, A.; Al-Salman, R.; Carstens, T.; Atkin, R.; Bund, A.; El Abedin, S. Z., Do solvation layers of ionic liquids influence electrochemical reactions? *Physical Chemistry Chemical Physics* **2010,** *12* (8), 1724-1732.

231.   Holbrey, J.; Seddon, K., Ionic liquids. *Clean Products and Processes* **1999,** *1* (4), 223-236.

232.   Noguera, G.; Mostany, J.; Agrifoglio, G.; Dorta, R., Room Temperature Liquid Salts of Cr and Mo as Self-Supported Oxidants. *Advanced Synthesis & Catalysis* **2005,** *347* (2-3), 231-234.

233.   Del Sesto, R. E.; McCleskey, T. M.; Burrell, A. K.; Baker, G. A.; Thompson, J. D.; Scott, B. L.; Wilkes, J. S.; Williams, P., Structure and magnetic behavior of transition metal based ionic liquids. *Chemical Communications* **2008,** (4), 447-449.

234.   Wang, C.; Luo, X.; Luo, H.; Jiang, D. e.; Li, H.; Dai, S., Tuning the basicity of ionic liquids for equimolar CO2 capture. *Angewandte Chemie International Edition* **2011,** *50* (21), 4918-4922.

235.   Wang, C.; Luo, H.; Jiang, D. e.; Li, H.; Dai, S., Carbon Dioxide Capture by Superbase-Derived Protic Ionic Liquids. *Angewandte Chemie* **2010,** *122* (34), 6114-6117.

236.   Mondal, S. S.; Müller, H.; Junginger, M.; Kelling, A.; Schilde, U.; Strehmel, V.; Holdt, H. J., Imidazolium 2-Substituted 4, 5-Dicyanoimidazolate Ionic Liquids: Synthesis, Crystal Structures and Structure–Thermal Property Relationships. *Chemistry–A European Journal* **2014,** *20* (26), 8170-8181.

237.   Zhang, P.; Gong, Y.; Lv, Y.; Guo, Y.; Wang, Y.; Wang, C.; Li, H., Ionic liquids with metal chelate anions. *Chemical Communications* **2012,** *48* (17), 2334-2336.

238.   Wasserscheid, P.; Welton, T., *Ionic liquids in synthesis*. Wiley Online Library: **2008**; Vol. 1.

239.   Ohno, H., *Electrochemical aspects of ionic liquids*. John Wiley & Sons: **2011**.

240.   Gray, G. W.; Winsor, P. A., *Liquid crystals & plastic crystals*. Ellis Horwood: **1974**.

241.   Binnemans, K., Ionic liquid crystals. *Chemical Reviews* **2005,** *105* (11), 4148-4204.

242.   Hitchcock, P. B.; Seddon, K. R.; Welton, T., Hydrogen-bond acceptor abilities of tetrachlorometalate (II) complexes in ionic liquids. *Journal of the Chemical Society, Dalton Transactions* **1993,** (17), 2639-2643.

243.   Douce, L.; Suisse, J.-M.; Guillon, D.; Taubert, A., Imidazolium-based liquid crystals: a modular platform for versatile new materials with finely tuneable properties and behaviour. *Liquid Crystals* **2011,** *38* (11-12), 1653-1661.

244.   Yoshio, M.; Mukai, T.; Ohno, H.; Kato, T., One-dimensional ion transport in self-organized columnar ionic liquids. *Journal of the American Chemical Society* **2004,** *126* (4), 994-995.

245.   Dolling, B.; Gillon, A. L.; Orpen, A. G.; Starbuck, J.; Wang, X.-M., Homologous families of chloride-rich 4, 4′-bipyridinium salt structures. *Chemical Communications* **2001,** (6), 567-568.

246.   Angeloni, A.; Orpen, A. G., Control of hydrogen bond network dimensionality in tetrachloroplatinate salts. *Chemical Communications* **2001,** (4), 343-344.

247.   Gillon, A. L.; Orpen, A. G.; Starbuck, J.; Wang, X.-M.; Rodríguez-Martín, Y.; Ruiz-Pérez, C., Cation-controlled formation of [{MCl 4} n] 2n‑chains in [4, 4′-H 2 bipy][MCl 4](M= Mn, Cd): an alternative to the A 2 MCl 4< 100> layer perovskite structure†. *Chemical Communications* **1999,** (22), 2287-2288.

248.   Lewis, G. R., A metal-containing synthon for crystal engineering: synthesis of the hydrogen bond ribbon polymer [4, 4′ -H 2 bipy][MCl 4](M= Pd, Pt). *Chemical Communications* **1998,** (17), 1873-1874.

249.   Rivas, J. M.; Brammer, L., Self-assembly of lD chains of different topologies using the hydrogen-bonded inorganic supramolecular synthons NH-Cl2M or NH-Cl3M. *Inorganic Chemistry* **1998,** *37* (19), 4756-4757.

250.   Freemantle, M., Designer solvents: ionic liquids may boost clean technology development. *Chemical & engineering news* **1998,** *76* (13), 32-37.

251.   Jin, C.-M.; Twamley, B.; Shreeve, J. n. M., Low-melting dialkyl-and bis (polyfluoroalkyl)-substituted 1, 1'-methylenebis (imidazolium) and 1, 1'-methylenebis (1, 2, 4-triazolium) bis (trifluoromethanesulfonyl) amides: Ionic liquids leading to bis (N-heterocyclic carbene) complexes of palladium. *Organometallics* **2005,** *24* (12), 3020-3023.

252.   Zhuang, R.; Jian, F.; Wang, K., A new binuclear Cd (II)-containing ionic liquid: Preparation and electrocatalytic activities. *Journal of Organometallic Chemistry* **2009,** *694* (22), 3614-3618.

253.   Rampon, D. S.; Rodembusch, F. S.; Schneider, J. M.; Bechtold, I. H.; Gonçalves, P. F.; Merlo, A. A.; Schneider, P. H., Novel selenoesters fluorescent liquid crystalline exhibiting a rich phase polymorphism. *Journal of Materials Chemistry* **2010,** *20* (4), 715-722.

254.   Lee, C. K.; Hsu, K.-M.; Tsai, C.-H.; Lai, C. K.; Lin, I. J., Liquid crystals of silver complexes derived from simple 1-alkylimidazoles. *Dalton transactions* **2004,** (8), 1120-1126.

255.   Wang, H. M.; Lin, I. J., Facile synthesis of silver (I)-carbene complexes. Useful carbene transfer agents. *Organometallics* **1998,** *17* (5), 972-975.

256.   Lee, C. K.; Ling, M. J.; Lin, I. J., Organic–inorganic hybrids of imidazole complexes of palladium (II), copper (II) and zinc (II). Crystals and liquid crystals. *Dalton Transactions* **2003,** (24), 4731-4737.

257.   Lee, C. K.; Peng, H. H.; Lin, I. J., Liquid crystals of N, N'-dialkylimidazolium salts comprising palladium (II) and copper (II) ions. *Chemistry of materials* **2004,** *16* (3), 530-536.

258.   Hardacre, C.; Holbrey, J. D.; McCormac, P. B.; McMath, S. J.; Nieuwenhuyzen, M.; Seddon, K. R., Crystal and liquid crystalline polymorphism in 1-alkyl-3-methylimidazolium tetrachloropalladate (II) salts. *Journal of Materials Chemistry* **2001,** *11* (2), 346-350.

259.   Lin, I. J.; Vasam, C. S., Metal-containing ionic liquids and ionic liquid crystals based on imidazolium moiety. *Journal of organometallic chemistry* **2005,** *690* (15), 3498-3512.

260.   Fannin Jr, A. A.; Floreani, D. A.; King, L. A.; Landers, J. S.; Piersma, B. J.; Stech, D. J.; Vaughn, R. L.; Wilkes, J. S.; Williams, J. L., Properties of 1, 3-dialkylimidazolium chloride-aluminum chloride ionic liquids. 2. Phase transitions, densities, electrical conductivities, and viscosities. *The Journal of Physical Chemistry* **1984,** *88* (12), 2614-2621.

261.   Bica, K.; Gaertner, P., An iron-containing ionic liquid as recyclable catalyst for aryl Grignard cross-coupling of alkyl halides. *Organic letters* **2006,** *8* (4), 733-735.

262.   Neve, F.; Francescangeli, O.; Crispini, A., Crystal architecture and mesophase structure of long-chain N-alkylpyridinium tetrachlorometallates. *Inorganica Chimica Acta* **2002,** *338*, 51-58.

263.   Neve, F.; Francescangeli, O.; Crispini, A.; Charmant, J., A2 [MX4] copper (II) pyridinium salts. From ionic liquids to layered solids to liquid crystals. *Chemistry of materials* **2001,** *13* (6), 2032-2041.

264.   Neve, F.; Crispini, A.; Armentano, S.; Francescangeli, O., Synthesis, structure, and thermotropic mesomorphism of layered N-alkylpyridinium tetrahalopalladate (II) salts. *Chemistry of materials* **1998,** *10* (7), 1904-1913.

265.   Taubert, A., Inorganic materials synthesis-a bright future for ionic liquids? *Acta Chimica Slovenica* **2005,** *52* (3), 183.

266.   Antonietti, M.; Kuang, D.; Smarsly, B.; Zhou, Y., Ionic liquids for the convenient synthesis of functional nanoparticles and other inorganic nanostructures. *Angew. Chem. Int. Ed.* **2004,** *43* (38), 4988-4992.

267.	Taubert, A., Cubes and Hollow Rods From Ionic Liquid Emulsions. *Acta Chimica Slovenica* **2005,** *52*, 168-170.

268.	Thiel, K.; Klamroth, T.; Strauch, P.; Taubert, A., On the interaction of ascorbic acid and the tetrachlorocuprate ion [CuCl 4] 2− in CuCl nanoplatelet formation from an ionic liquid precursor (ILP). *Physical Chemistry Chemical Physics* **2011,** *13* (30), 13537-13543.

269.	X-Area (Stoe 2015).

270.	Sheldrick, G. M., SHELXS-2013/1, Program for the Crystal Structure Solution, University of Göttingen, Germany, **2013**.

271.	Sheldrick, G. M., SHELXL-2014/7, Program for the Crystal Solution Refinement, University of Göttingen, Germany, **2014**.

272.	Diamond, V. Crystal Impact **2016**: 4.2.1.

273.	Farrugia, L. J., ORTEP-3 for WINDOWS - version of ORTEP-III with a graphical user interface, Journal of Applied Crystallography **1997**, 30 (5), 565.

274.	Perdew, J. P.; Ruzsinszky, A.; Csonka, G. I.; Vydrov, O. A.; Scuseria, G. E.; Constantin, L. A.; Zhou, X.; Burke, K., Restoring the density-gradient expansion for exchange in solids and surfaces. *Physical Review Letters* **2008,** *100* (13), 136406.

275.	Blum, V.; Gehrke, R.; Hanke, F.; Havu, P.; Havu, V.; Ren, X.; Reuter, K.; Scheffler, M., Ab initio molecular simulations with numeric atom-centered orbitals. *Computer Physics Communications* **2009,** *180* (11), 2175-2196.

276.	Vongbupnimit, K.; Noguchi, K.; Okuyama, K., 1-Dodecylpyridinium chloride monohydrate. *Acta Crystallographica Section C: Crystal Structure Communications* **1995,** *51* (9), 1940-1941.

277.	Bondi, A., van der Waals volumes and radii. *The Journal of physical chemistry* **1964,** *68* (3), 441-451.

278.	Winter, A.; Thiel, K.; Zabel, A.; Klamroth, T.; Pöppl, A.; Kelling, A.; Schilde, U.; Taubert, A.; Strauch, P., Tetrahalidocuprates (II)–structure and EPR spectroscopy. Part 2: tetrachloridocuprates (II). *New journal of chemistry* **2014,** *38* (3), 1019-1030.

279.	Bowlas, C. J.; Bruce, D. W.; Seddon, K. R., Liquid-crystalline ionic liquids. *Chemical Communications* **1996,** (14), 1625-1626.

280.	El-Nagar, G. A.; Sarhan, R. M.; Abouserie, A.; Maticiuc, N.; Bargheer, M.; Lauermann, I.; Roth, C., Efficient 3D-Silver Flower-like Microstructures for Non-Enzymatic Hydrogen Peroxide (H 2 O 2) Amperometric Detection. *Scientific reports* **2017,** *7* (1), 12181.

281.	Zhang, J.; Feng, H.; Yang, J.; Qin, Q.; Fan, H.; Wei, C.; Zheng, W., Solvothermal synthesis of three-dimensional hierarchical CuS microspheres from a Cu-based ionic liquid precursor for high-performance asymmetric supercapacitors. *ACS applied materials & interfaces* **2015,** *7* (39), 21735-21744.

282.	Bhattacharya, R.; Ray, M. S.; Dey, R.; Righi, L.; Bocelli, G.; Ghosh, A., Synthesis, crystal structure and thermochromism of benzimidazolium tetrachlorocuprate:(C 7 H 7 N 2) 2 [CuCl 4]. *Polyhedron* **2002,** *21* (25), 2561-2565.

283.	Losee, D. B.; Hatfield, W. E., Megnetization measurements on diethylenetriammonium chlorocuprate (II): Anisotropy and exchange fields in a two-dimensional Heisenberg ferromagnet. *Physical Review B* **1974,** *10* (3), 1122.

284.	Rubtsova, T.; Kireeva, O.; Bulychev, B.; Streltsova, N.; Belsky, V.; Tarasov, B., Complex formation of metal salts with macrocyclic polyethers in aprotic organic solvents: crystal structures of the molecular complex [MeCN· Mg· 15C5 (µ 2-Cl) CuCl 3] and the ionic complexes [(MeCN) 2· Mg· 15C5][Cu 2 Cl 6], {[(MeCN) 2· Mg· 15C5][Cu 3 Cl 8]} n,[(H 2 O) 2· Mg· 15C5][CuCl 4]· H 2 O and {[(H 2 O) 2· Cu 3 Cl 8][Mg·(H 2 O) 6]·[2 (15C5)]· H 2 On. *Polyhedron* **1992,** *11* (15), 1929-1938.

285.	Natarajan, M.; Prakash, B., Phase transitions in ABX3 type halides. *physica status solidi (a)* **1971,** *4* (3).

286.   Bloomquist, D. R.; Willett, R. D.; Dodgen, H. W., Thermochromism in copper (II) halide salts. 2. Bis (isopropylammonium) tetrachlorocuprate (II). *Journal of the American Chemical Society* **1981,** *103* (10), 2610-2615.

287.   Willett, R.; Haugen, J.; Lebsack, J.; Morrey, J., Thermochromism in copper (II) chlorides. Coordination geometry changes in tetrachlorocuprate (2-) anions. *Inorganic Chemistry* **1974,** *13* (10), 2510-2513.

288.   Lei, Z.; Chen, B.; Koo, Y.-M.; MacFarlane, D. R., Introduction: ionic liquids. ACS Publications: 2017.

289.   Farra, R.; Thiel, K.; Winter, A.; Klamroth, T.; Pöppl, A.; Kelling, A.; Schilde, U.; Taubert, A.; Strauch, P., Tetrahalidocuprates (II)—structure and EPR spectroscopy. Part 1: Tetrabromidocuprates (II). *New Journal of Chemistry* **2011,** *35* (12), 2793-2803.

290.   Pârvulescu, V. I.; Hardacre, C., Catalysis in ionic liquids. *Chemical Reviews* **2007,** *107* (6), 2615-2665.

291.   Abai, M.; Atkins, M. P.; Hassan, A.; Holbrey, J. D.; Kuah, Y.; Nockemann, P.; Oliferenko, A. A.; Plechkova, N. V.; Rafeen, S.; Rahman, A. A., An ionic liquid process for mercury removal from natural gas. *Dalton Transactions* **2015,** *44* (18), 8617-8624.

292.   Kim, Y.; Heyne, B.; Abouserie, A.; Pries, C.; Ippen, C.; Günter, C.; Taubert, A.; Wedel, A., CuS nanoplates from ionic liquid precursors—Application in organic photovoltaic cells. *The Journal of Chemical Physics* **2018,** *148* (19), 193818.

293.   Dobbs, W.; Suisse, J. M.; Douce, L.; Welter, R., Electrodeposition of Silver Particles and Gold Nanoparticles from Ionic Liquid-Crystal Precursors. *Angew. Chem.* **2006,** *118* (25), 4285-4288.

294.   Li, R.; Du, J.; Luan, Y.; Xue, Y.; Zou, H.; Zhuang, G.; Li, Z., Ionic liquid precursor-based synthesis of CuO nanoplates for gas sensing and amperometric sensing applications. *Sensors and Actuators B: Chemical* **2012,** *168*, 156-164.

295.   Tran Qui, D.; Daoud, A.; Mhiri, T., Structure of tetraphenylphosphonium trichlorocuprate. *Acta Crystallographica Section C: Crystal Structure Communications* **1989,** *45* (1), 33-35.

296.   Daoud, A.; Salah, A. B.; Chappert, C.; Renard, J.; Cheikhrouhou, A.; Duc, T.; Verdaguer, M., Crystal structure and magnetic properties of piperazinium hexadichlorocuprate: A new S=(1/2) antiferromagnetic chain with alternating exchange. *Physical Review B* **1986,** *33* (9), 6253.

297.   Guan, J.; Peng, J.; Jin, X., Synthesis of copper sulfide nanorods as peroxidase mimics for the colorimetric detection of hydrogen peroxide. *Analytical Methods* **2015,** *7* (13), 5454-5461.

298.   Liu, C.-Y.; Hu, J.-M., Hydrogen peroxide biosensor based on the direct electrochemistry of myoglobin immobilized on silver nanoparticles doped carbon nanotubes film. *Biosensors and Bioelectronics* **2009,** *24* (7), 2149-2154.

299.   Halliwell, B., Oxidants and human disease: some new concepts. *The FASEB Journal* **1987,** *1* (5), 358-364.

300.   Reth, M., Hydrogen peroxide as second messenger in lymphocyte activation. *Nature immunology* **2002,** *3* (12), 1129-1134.

301.   Foreman, J.; Demidchik, V.; Bothwell, J. H. F.; Mylona, P.; Miedema, H.; Torres, M. A.; Linstead, P.; Costa, S.; Brownlee, C.; Jones, J. D. G.; Davies, J. M.; Dolan, L., Reactive oxygen species produced by NADPH oxidase regulate plant cell growth. *Nature* **2003,** *422* (6930), 442-446.

302.   Liu, Z.; Zhao, B.; Shi, Y.; Guo, C.; Yang, H.; Li, Z., Novel nonenzymatic hydrogen peroxide sensor based on iron oxide–silver hybrid submicrospheres. *Talanta* **2010,** *81* (4), 1650-1654.

303.   Shoji, E.; Freund, M. S., Potentiometric Sensors Based on the Inductive Effect on the pKa of Poly(aniline): A Nonenzymatic Glucose Sensor. *Journal of the American Chemical Society* **2001,** *123* (14), 3383-3384.

304.   Xiao, F.; Zhao, F.; Zhang, Y.; Guo, G.; Zeng, B., Ultrasonic electrodeposition of gold−platinum alloy nanoparticles on ionic liquid− chitosan composite film and their application in fabricating nonenzyme hydrogen peroxide sensors. *The Journal of Physical Chemistry C* **2008,** *113* (3), 849-855.

305.   Wang, J., Electrochemical biosensing based on noble metal nanoparticles. *Microchimica Acta* **2012,** *177* (3-4), 245-270.

306.   Pingarrón, J. M.; Yáñez-Sedeño, P.; González-Cortés, A., Gold nanoparticle-based electrochemical biosensors. *Electrochimica Acta* **2008,** *53* (19), 5848-5866.

307.   Chen, S.; Yuan, R.; Chai, Y.; Hu, F., Electrochemical sensing of hydrogen peroxide using metal nanoparticles: a review. *Microchimica Acta* **2013,** *180* (1-2), 15-32.

308.   Rad, A. S.; Mirabi, A.; Binaian, E.; Tayebi, H., A review on glucose and hydrogen peroxide biosensor based on modified electrode included silver nanoparticles. *Int J Electrochem Sci* **2011,** *6* (8), 3671-3683.

309.   Huang, J.; Wang, D.; Hou, H.; You, T., Electrospun Palladium Nanoparticle-Loaded Carbon Nanofibers and Their Electrocatalytic Activities towards Hydrogen Peroxide and NADH. *Advanced Functional Materials* **2008,** *18* (3), 441-448.

310.   Sun, X.; Guo, S.; Liu, Y.; Sun, S., Dumbbell-like PtPd–Fe3O4 Nanoparticles for Enhanced Electrochemical Detection of H2O2. *Nano Letters* **2012,** *12* (9), 4859-4863.

311.   He, S.; Zhang, B.; Liu, M.; Chen, W., Non-enzymatic hydrogen peroxide electrochemical sensor based on a three-dimensional MnO 2 nanosheets/carbon foam composite. *RSC Advances* **2014,** *4* (90), 49315-49323.

312.   Batchelor-McAuley, C.; Du, Y.; Wildgoose, G. G.; Compton, R. G., The use of copper (II) oxide nanorod bundles for the non-enzymatic voltammetric sensing of carbohydrates and hydrogen peroxide. *Sensors and Actuators B: Chemical* **2008,** *135* (1), 230-235.

313.   Ping, J.; Ru, S.; Fan, K.; Wu, J.; Ying, Y., Copper oxide nanoparticles and ionic liquid modified carbon electrode for the non-enzymatic electrochemical sensing of hydrogen peroxide. *Microchimica Acta* **2010,** *171* (1-2), 117-123.

314.   Šljukić, B.; Banks, C. E.; Compton, R. G., Iron oxide particles are the active sites for hydrogen peroxide sensing at multiwalled carbon nanotube modified electrodes. *Nano letters* **2006,** *6* (7), 1556-1558.

315.   Yan, Q.; Wang, Z.; Zhang, J.; Peng, H.; Chen, X.; Hou, H.; Liu, C., Nickel hydroxide modified silicon nanowires electrode for hydrogen peroxide sensor applications. *Electrochimica Acta* **2012,** *61*, 148-153.

316.   He, W.; Jia, H.; Li, X.; Lei, Y.; Li, J.; Zhao, H.; Mi, L.; Zhang, L.; Zheng, Z., Understanding the formation of CuS concave superstructures with peroxidase-like activity. *Nanoscale* **2012,** *4* (11), 3501-3506.

317.   Cheng, X.-L.; Jiang, J.-S.; Jiang, D.-M.; Zhao, Z.-J., Synthesis of rhombic dodecahedral Fe3O4 nanocrystals with exposed high-energy {110} facets and their peroxidase-like activity and lithium storage properties. *The Journal of Physical Chemistry C* **2014,** *118* (24), 12588-12598.

318.   Gao, L.; Zhuang, J.; Nie, L.; Zhang, J.; Zhang, Y.; Gu, N.; Wang, T.; Feng, J.; Yang, D.; Perrett, S., Intrinsic peroxidase-like activity of ferromagnetic nanoparticles. *Nature nanotechnology* **2007,** *2* (9), 577-583.

319.   Naşcu, C.; Pop, I.; Ionescu, V.; Indrea, E.; Bratu, I., Spray pyrolysis deposition of CuS thin films. *Materials letters* **1997,** *32* (2-3), 73-77.

320.   Gorai, S.; Ganguli, D.; Chaudhuri, S., Synthesis of copper sulfides of varying morphologies and stoichiometries controlled by chelating and nonchelating solvents in a solvothermal process. *Crystal growth & design* **2005,** *5* (3), 875-877.

321.   Wang, H.; Zhang, J.-R.; Zhao, X.-N.; Xu, S.; Zhu, J.-J., Preparation of copper monosulfide and nickel monosulfide nanoparticles by sonochemical method. *Materials Letters* **2002,** *55* (4), 253-258.

322.   Qiao, Z.; Xie, Y.; Xu, J.; Zhu, Y.; Qian, Y., γ-radiation synthesis of the nanocrystalline semiconductors PbS and CuS. *Journal of colloid and interface science* **1999,** *214* (2), 459-461.

323.   Min, Y.; Akbulut, M.; Kristiansen, K.; Golan, Y.; Israelachvili, J., The role of interparticle and external forces in nanoparticle assembly. *Nature materials* **2008,** *7* (7), 527-538.

324.   Hotze, E. M.; Phenrat, T.; Lowry, G. V., Nanoparticle aggregation: challenges to understanding transport and reactivity in the environment. *Journal of environmental quality* **2010,** *39* (6), 1909-1924.

325.   Liu, J.; Hu, X.; Hou, S.; Wen, T.; Liu, W.; Zhu, X.; Wu, X., Screening of inhibitors for oxidase mimics of Au@ Pt nanorods by catalytic oxidation of OPD. *Chemical Communications* **2011,** *47* (39), 10981-10983.

326.   Liu, R.; Duay, J.; Lee, S. B., Heterogeneous nanostructured electrode materials for electrochemical energy storage. *Chemical Communications* **2011,** *47* (5), 1384-1404.

327.   Scherrer, P., Bestimmung der inneren Struktur und der Größe von Kolloidteilchen mittels Röntgenstrahlen. In *Kolloidchemie Ein Lehrbuch*, Springer: 1912; pp 387-409.

328.   Birks, L.; Friedman, H., Particle size determination from X-ray line broadening. *Journal of Applied Physics* **1946,** *17* (8), 687-692.

329.   Taubert, A.; Palms, D.; Weiss, Ö.; Piccini, M.-T.; Batchelder, D. N., Polymer-assisted control of particle morphology and particle size of zinc oxide precipitated from aqueous solution. *Chemistry of materials* **2002,** *14* (6), 2594-2601.

330.   Liu, Y.; Liu, M.; Swihart, M. T., Reversible Crystal Phase Interconversion Between Covellite CuS and High Chalcocite Cu2S Nanocrystals. *Chemistry of Materials* **2017**.

331.   Roberts, W.; Buchanan, A., The effects of temperature, pressure, and oxygen on copper and iron sulphides synthesised in aqueous solution. *Mineralium Deposita* **1971,** *6* (1), 23-33.

332.   Evans, H.; Konnert, J., Crystal structure refinement of covellite. *Am. Mineral* **1976,** *61* (9-10), 996-1000.

333.   Niu, X.; Pan, J.; Qiu, F.; Li, X.; Yan, Y.; Shi, L.; Zhao, H.; Lan, M., Anneal-shrinked Cu 2 O dendrites grown on porous Cu foam as a robust interface for high-performance nonenzymatic glucose sensing. *Talanta* **2016,** *161*, 615-622.

334.   Liu, M.; Liu, R.; Chen, W., Graphene wrapped Cu 2 O nanocubes: non-enzymatic electrochemical sensors for the detection of glucose and hydrogen peroxide with enhanced stability. *Biosensors and Bioelectronics* **2013,** *45*, 206-212.

335.   Dutta, A. K.; Das, S.; Samanta, P. K.; Roy, S.; Adhikary, B.; Biswas, P., Non–enzymatic amperometric sensing of hydrogen peroxide at a CuS modified electrode for the determination of urine H 2 O 2. *Electrochimica Acta* **2014,** *144*, 282-287.

336.   Dutta, A. K.; Maji, S. K.; Srivastava, D. N.; Mondal, A.; Biswas, P.; Paul, P.; Adhikary, B., Synthesis of FeS and FeSe nanoparticles from a single source precursor: a study of their photocatalytic activity, peroxidase-like behavior, and electrochemical sensing of H2O2. *ACS applied materials & interfaces* **2012,** *4* (4), 1919-1927.

337.   ElKaoutit, M.; Naranjo-Rodriguez, I.; Domínguez, M.; Hernández-Artiga, M. P.; Bellido-Milla, D.; de Cisneros, J. L. H.-H., A third-generation hydrogen peroxide biosensor based on Horseradish Peroxidase (HRP) enzyme immobilized in a Nafion–Sonogel–Carbon composite. *Electrochimica Acta* **2008,** *53* (24), 7131-7137.

338.   Bangal, M.; Ashtaputre, S.; Marathe, S.; Ethiraj, A.; Hebalkar, N.; Gosavi, S.; Urban, J.; Kulkarni, S., Semiconductor nanoparticles. *Hyperfine interactions* **2005,** *160* (1), 81-94.

339.   Bera, D.; Qian, L.; Tseng, T.-K.; Holloway, P. H., Quantum dots and their multimodal applications: a review. *Materials* **2010,** *3* (4), 2260-2345.

340.   Mall, M.; Kumar, P.; Chand, S.; Kumar, L., Influence of ZnS quantum dots on optical and photovoltaic properties of poly (3-hexylthiophene). *Chemical Physics Letters* **2010,** *495* (4), 236-240.

341.   Wang, M.; Batabyal, S. K.; Li, Z.; Li, D.; Mhaisalkar, S. G.; Lam, Y. M., Nanocrystalline copper indium selenide (CuInSe 2) particles for solar energy harvesting. *RSC Advances* **2013,** *3* (25), 9829-9834.

342.   Lefrançois, A.; Luszczynska, B.; Pepin-Donat, B.; Lombard, C.; Bouthinon, B.; Verilhac, J.-M.; Gromova, M.; Faure-Vincent, J.; Pouget, S.; Chandezon, F., Enhanced charge separation in ternary P3HT/PCBM/CuInS2 nanocrystals hybrid solar cells. *Scientific reports* **2015,** *5*.

343.	Mousavi, S.; Müller, T.; de Oliveira, P., Synthesis of colloidal nanoscaled copper–indium–gallium–selenide (CIGS) particles for photovoltaic applications. *Journal of colloid and interface science* **2012,** *382* (1), 48-52.

344.	Guo, Q.; Ford, G. M.; Hillhouse, H. W.; Agrawal, R. In *Selenization of copper indium gallium disulfide nanocrystal films for thin film solar cells*, Photovoltaic Specialists Conference (PVSC), 2009 34th IEEE, IEEE: 2009; pp 002126-002129.

345.	Rao, S.; Morankar, A.; Verma, H.; Goswami, P., Emerging Photovoltaics: Organic, Copper Zinc Tin Sulphide, and Perovskite-Based Solar Cells. *Journal of Applied Chemistry* **2016,** *2016.*

346.	Ramasamy, K.; Malik, M. A.; O'Brien, P., Routes to copper zinc tin sulfide Cu 2 ZnSnS 4 a potential material for solar cells. *Chemical Communications* **2012,** *48* (46), 5703-5714.

347.	Isac, L.; Popovici, I.; Enesca, A.; Duta, A., Copper sulfide () thin films as possible p-type absorbers in 3D solar cells. *Energy Procedia* **2010,** *2* (1), 71-78.

348.	Ameta, S. C.; Ameta, R., *Solar Energy Conversion and Storage: Photochemical Modes*. CRC Press: 2015; Vol. 10.

349.	Kumar, A.; Sista, S.; Yang, Y., Dipole induced anomalous S-shape I-V curves in polymer solar cells. *Journal of Applied Physics* **2009,** *105* (9), 094512.

350.	Chang, J.-Y.; Su, L.-F.; Li, C.-H.; Chang, C.-C.; Lin, J.-M., Efficient "green" quantum dot-sensitized solar cells based on Cu 2 S–CuInS 2–ZnSe architecture. *Chemical Communications* **2012,** *48* (40), 4848-4850.

351.	Tang, A.; Teng, F.; Wang, Y.; Hou, Y.; Han, W.; Yi, L.; Gao, M., Investigation on Photovoltaic Performance based on Matchstick-Like Cu2S–In2S3Heterostructure Nanocrystals and Polymer. *Nanoscale research letters* **2008,** *3* (12), 502.

352.	Borchert, H., *Solar cells based on colloidal nanocrystals*. Springer Science & Business Media: 2014; Vol. 196.

353.	Panigrahi, S.; Basak, D., Solution-processed novel core–shell n–p heterojunction and its ultrafast UV photodetection properties. *RSC Advances* **2012,** *2* (31), 11963-11968.

354.	Nemade, K.; Waghuley, S., Band gap engineering of CuS nanoparticles for artificial photosynthesis. *Materials Science in Semiconductor Processing* **2015,** *39,* 781-785.

355.	Lei, H.; Qin, P.; Ke, W.; Guo, Y.; Dai, X.; Chen, Z.; Wang, H.; Li, B.; Zheng, Q.; Fang, G., Performance enhancement of polymer solar cells with high work function CuS modified ITO as anodes. *Organic Electronics* **2015,** *22,* 173-179.

356.	Rao, H.; Sun, W.; Ye, S.; Yan, W.; Li, Y.; Peng, H.; Liu, Z.; Bian, Z.; Huang, C., Solution-processed CuS NPs as an inorganic hole-selective contact material for inverted planar perovskite solar cells. *ACS applied materials & interfaces* **2016,** *8* (12), 7800-7805.

357.	Li, J.; Jiu, T.; Tao, G.-H.; Wang, G.; Sun, C.; Li, P.; Fang, J.; He, L., Manipulating surface ligands of Copper Sulfide nanocrystals: Synthesis, characterization, and application to organic solar cells. *Journal of Colloid and interface Science* **2014,** *419,* 142-147.

358.	Gao, M.-R.; Xu, Y.-F.; Jiang, J.; Yu, S.-H., Nanostructured metal chalcogenides: synthesis, modification, and applications in energy conversion and storage devices. *Chemical Society Reviews* **2013,** *42* (7), 2986-3017.

359.	Malik, M. A., Nanomaterials for solar energy. *Nanoscience: Nanostructures through Chemistry* **2013,** *2,* 23.

360.	Gollu, S. R.; Sharma, R.; Srinivas, G.; Kundu, S.; Gupta, D., Effects of incorporation of copper sulfide nanocrystals on the performance of P3HT: PCBM based inverted solar cells. *Organic Electronics* **2014,** *15* (10), 2518-2525.

361.	Liao, H.-C.; Tsao, C.-S.; Lin, T.-H.; Jao, M.-H.; Chuang, C.-M.; Chang, S.-Y.; Huang, Y.-C.; Shao, Y.-T.; Chen, C.-Y.; Su, C.-J., Nanoparticle-tuned self-organization of a bulk heterojunction hybrid solar cell with enhanced performance. *Acs Nano* **2012,** *6* (2), 1657-1666.

362.   Mashford, B. S.; Stevenson, M.; Popovic, Z.; Hamilton, C.; Zhou, Z.; Breen, C.; Steckel, J.; Bulovic, V.; Bawendi, M.; Coe-Sullivan, S., High-efficiency quantum-dot light-emitting devices with enhanced charge injection. *Nature photonics* **2013,** *7* (5), 407.

363.   Wood, A.; Giersig, M.; Hilgendorff, M.; Vilas-Campos, A.; Liz-Marzán, L. M.; Mulvaney, P., Size effects in ZnO: the cluster to quantum dot transition. *Australian journal of chemistry* **2003,** *56* (10), 1051-1057.

364.   Singh, A.; Manivannan, R.; Victoria, S. N., Simple one-pot sonochemical synthesis of copper sulphide nanoparticles for solar cell applications. *Arabian Journal of Chemistry* **2015**.

365.   Brown, P. D., Transmission Electron Microscopy-A Textbook for Materials Science, by David B. Williams and C. Barry Carter. *Microscopy and Microanalysis* **1999,** *5* (6), 452-453.

366.   Haram, S. K.; Mahadeshwar, A. R.; Dixit, S. G., Synthesis and characterization of copper sulfide nanoparticles in Triton-X 100 water-in-oil microemulsions. *The Journal of Physical Chemistry* **1996,** *100* (14), 5868-5873.

367.   Du, Y.; Yin, Z.; Zhu, J.; Huang, X.; Wu, X.-J.; Zeng, Z.; Yan, Q.; Zhang, H., A general method for the large-scale synthesis of uniform ultrathin metal sulphide nanocrystals. *Nature communications* **2012,** *3*, 1177.

368.   Luther, J. M.; Jain, P. K.; Ewers, T.; Alivisatos, A. P., Localized surface plasmon resonances arising from free carriers in doped quantum dots. *Nature materials* **2011,** *10* (5), 361.

369.   Wei, T.; Liu, Y.; Dong, W.; Zhang, Y.; Huang, C.; Sun, Y.; Chen, X.; Dai, N., Surface-dependent localized surface plasmon resonances in CuS nanodisks. *ACS applied materials & interfaces* **2013,** *5* (21), 10473-10477.

370.   Mukherjee, N.; Sinha, A.; Khan, G. G.; Chandra, D.; Bhaumik, A.; Mondal, A., A study on the structural and mechanical properties of nanocrystalline CuS thin films grown by chemical bath deposition technique. *Materials Research Bulletin* **2011,** *46* (1), 6-11.

371.   Abbas, S. J.; Rani, M.; Tripathi, S., Preparation and characterization of nanocomposite between poly (aniline-co-m-chloroaniline)–copper sulfide nanoparticles. *Physica B: Condensed Matter* **2014,** *443*, 107-113.

372.   Li, B.; Xie, Y.; Xue, Y., Controllable synthesis of CuS nanostructures from self-assembled precursors with biomolecule assistance. *The Journal of Physical Chemistry C* **2007,** *111* (33), 12181-12187.

373.   Wu, H.; Chen, W., Synthesis and reaction temperature-tailored self-assembly of copper sulfide nanoplates. *Nanoscale* **2011,** *3* (12), 5096-5102.

374.   Güneri, E.; Kariper, A., Optical properties of amorphous CuS thin films deposited chemically at different pH values. *Journal of Alloys and Compounds* **2012,** *516*, 20-26.

375.   Gautam, U. K.; Mukherjee, B., A simple synthesis and characterization of CuS nanocrystals. *Bulletin of Materials Science* **2006,** *29* (1), 1-5.

376.   Meyer, J.; Kahn, A. L., Electronic structure of molybdenum-oxide films and associated charge injection mechanisms in organic devices. *Journal of Photonics for Energy* **2011,** *1* (1), 011109.

377.   Tress, W., Device physics of organic solar cells. **2011**.

378.   Sandberg, O. J.; Nyman, M.; Österbacka, R., Effect of contacts in organic bulk heterojunction solar cells. *Physical Review Applied* **2014,** *1* (2), 024003.

379.   Wagenpfahl, A.; Rauh, D.; Binder, M.; Deibel, C.; Dyakonov, V., S-shaped current-voltage characteristics of organic solar devices. *Physical Review B* **2010,** *82* (11), 115306.

380.   Zhang, H.; Stubhan, T.; Li, N.; Turbiez, M.; Matt, G. J.; Ameri, T.; Brabec, C. J., A solution-processed barium hydroxide modified aluminum doped zinc oxide layer for highly efficient inverted organic solar cells. *Journal of Materials Chemistry A* **2014,** *2* (44), 18917-18923.

381.   Servaites, J. D.; Ratner, M. A.; Marks, T. J., Organic solar cells: A new look at traditional models. *Energy & Environmental Science* **2011,** *4* (11), 4410-4422.

382.   Bica, K.; Gaertner, P., Metal-Containing Ionic Liquids as Efficient Catalysts for Hydroxymethylation in Water. *European Journal of Organic Chemistry* **2008,** *2008* (20), 3453-3456.

383.   Abo-Hamad, A.; Hayyan, M.; AlSaadi, M. A.; Hashim, M. A., Potential applications of deep eutectic solvents in nanotechnology. *Chemical Engineering Journal* **2015,** *273*, 551-567.

384.   Endres, F.; Abbott, A.; MacFarlane, D. R., *Electrodeposition from ionic liquids*. John Wiley & Sons: 2017.

385.   Wang, C.; Guo, Y.; Zhu, X.; Cui, G.; Li, H.; Dai, S., Highly efficient CO_2 capture by tunable alkanolamine-based ionic liquids with multidentate cation coordination. *Chemical Communications* **2012,** *48* (52), 6526-6528.

386.   Luo, J.; Cai, M.; Gu, T., Pretreatment of lignocellulosic biomass using green ionic liquids. In *Green biomass pretreatment for biofuels production*, Springer: 2013; pp 127-153.

387.   Pendleton, J. N.; Gilmore, B. F., The antimicrobial potential of ionic liquids: a source of chemical diversity for infection and biofilm control. *International journal of antimicrobial agents* **2015,** *46* (2), 131-139.

388.   Li, Z.; Geßner, A.; Richters, J. P.; Kalden, J.; Voss, T.; Kübel, C.; Taubert, A., Hollow zinc oxide mesocrystals from an ionic liquid precursor (ILP). *Advanced Materials* **2008,** *20* (7), 1279-1285.

389.   Paraknowitsch, J. P.; Zhang, J.; Su, D.; Thomas, A.; Antonietti, M., Ionic Liquids as Precursors for Nitrogen-Doped Graphitic Carbon. *Advanced Materials* **2010,** *22* (1), 87-92.

390.   Paraknowitsch, J. P.; Thomas, A.; Antonietti, M., A detailed view on the polycondensation of ionic liquid monomers towards nitrogen doped carbon materials. *Journal of Materials Chemistry* **2010,** *20* (32), 6746-6758.

391.   Zhao, L.; Hu, Y. S.; Li, H.; Wang, Z.; Chen, L., Porous Li4Ti5O12 Coated with N-Doped Carbon from Ionic Liquids for Li-Ion Batteries. *Advanced Materials* **2011,** *23* (11), 1385-1388.

392.   Migowski, P.; Machado, G.; Texeira, S. R.; Alves, M. C.; Morais, J.; Traverse, A.; Dupont, J., Synthesis and characterization of nickel nanoparticles dispersed in imidazolium ionic liquids. *Physical Chemistry Chemical Physics* **2007,** *9* (34), 4814-4821.

393.   Jacob, D. S.; Genish, I.; Klein, L.; Gedanken, A., Carbon-coated core shell structured copper and nickel nanoparticles synthesized in an ionic liquid. *The Journal of Physical Chemistry B* **2006,** *110* (36), 17711-17714.

394.   Alammar, T.; Shekhah, O.; Wohlgemuth, J.; Mudring, A.-V., Ultrasound-assisted synthesis of mesoporous β-Ni (OH) 2 and NiO nano-sheets using ionic liquids. *Journal of Materials Chemistry* **2012,** *22* (35), 18252-18260.

395.   Khare, V.; Kraupner, A.; Mantion, A.; Jelicic, A.; Thunemann, A. F.; Giordano, C.; Taubert, A., Stable iron carbide nanoparticle dispersions in [Emim][SCN] and [Emim][N (CN) 2] ionic liquids. *Langmuir* **2010,** *26* (13), 10600-10605.

396.   Wang, F.; Richards, V. N.; Shields, S. P.; Buhro, W. E., Kinetics and mechanisms of aggregative nanocrystal growth. *Chemistry of Materials* **2013,** *26* (1), 5-21.

397.   Li, R.; Luan, Y.; Zou, H.; Du, J.; Mu, T.; Li, Z., Synthesis and gas-sensing properties of ZnO particles from an ionic liquid precursor. *RSC advances* **2012,** *2* (7), 3049-3056.

398.   Li, Z.; Yu, Q.; Luan, Y.; Zhuang, G.; Fan, R.; Li, R.; Wang, C., Morphology-controlled ZnO particles from an ionic liquid precursor. *CrystEngComm* **2009,** *11* (12), 2683-2687.

399.   Pereiro, A. B.; Llovell, F.; Araújo, J. M.; Santos, A. S.; Rebelo, L. P. N.; Piñeiro, M. M.; Vega, L. F., Thermophysical Characterization of Ionic Liquids Based on the Perfluorobutanesulfonate Anion: Experimental and Soft-SAFT Modeling Results. *ChemPhysChem* **2017,** *18* (15), 2012-2023.

400.   Pereiro, A. B.; Araújo, J. o. M.; Martinho, S.; Alves, F.; Nunes, S.; Matias, A.; Duarte, C. M.; Rebelo, L. P. N.; Marrucho, I. M., Fluorinated ionic liquids: properties and applications. *ACS Sustainable Chemistry & Engineering* **2013,** *1* (4), 427-439.

401.   Vanhoutte, G.; Hojniak, S. D.; Bardé, F.; Binnemans, K.; Fransaer, J., Fluorine-functionalized ionic liquids with high oxygen solubility. *RSC Advances* **2018,** *8* (9), 4525-4530.

402.   Rauber, D.; Heib, F.; Dier, T.; Volmer, D. A.; Hempelmann, R.; Schmitt, M., On the physicochemical and surface properties of 1-alkyl 3-methylimidazolium bis (nonafluorobutylsulfonyl) imide ionic liquids. *Colloids and Surfaces A: Physicochemical and Engineering Aspects* **2017,** *529,* 169-177.

403.   Zhang, T.; Doert, T.; Ruck, M., Synthesis of Metal Sulfides from a Deep Eutectic Solvent Precursor (DESP). *Zeitschrift für anorganische und allgemeine Chemie* **2017,** *643* (23), 1913-1919.

404.   Wagle, D. V.; Zhao, H.; Baker, G. A., Deep eutectic solvents: sustainable media for nanoscale and functional materials. *Accounts of chemical research* **2014,** *47* (8), 2299-2308.

405.   Liao, H. G.; Jiang, Y. X.; Zhou, Z. Y.; Chen, S. P.; Sun, S. G., Shape-controlled synthesis of gold nanoparticles in deep eutectic solvents for studies of structure–functionality relationships in electrocatalysis. *Angewandte Chemie* **2008,** *120* (47), 9240-9243.

406.   Heine, T., Transition metal chalcogenides: ultrathin inorganic materials with tunable electronic properties. *Accounts of chemical research* **2014,** *48* (1), 65-72.

407.   Shao, Y.; Shi, X.; Pan, H., Electronic, Magnetic, and Catalytic Properties of Thermodynamically Stable Two-Dimensional Transition-Metal Phosphides. *Chemistry of Materials* **2017,** *29* (20), 8892-8900.

408.   Hou, W.; Xiao, Y.; Han, G., Interconnected ternary MIn2S4 (M= Fe, Co, Ni) thiospinels nanosheets array: a type of efficient Pt-free counter electrodes for the dye-sensitized solar cells. *Angewandte Chemie* **2017.**

409.   Liu, W.; Niu, H.; Yang, J.; Cheng, K.; Ye, K.; Zhu, K.; Wang, G.; Cao, D.; Yan, J., Ternary transition metal sulfides embedded in graphene nanosheets as both anode and cathode for high-performance asymmetric supercapacitors. *Chemistry of Materials* **2018.**

410.   Yang, Z.; Zhang, S.; Fu, Y.; Zheng, X.; Zheng, J., Shape-controlled synthesis of CuCo2S4 as highly-efficient electrocatalyst for nonenzymatic detection of H2O2. *Electrochimica Acta* **2017,** *255,* 23-30.

411.   Feng, C.; Zhang, L.; Wang, Z.; Song, X.; Sun, K.; Wu, F.; Liu, G., Synthesis of copper sulfide nanowire bundles in a mixed solvent as a cathode material for lithium-ion batteries. *Journal of Power Sources* **2014,** *269,* 550-555.

412.   Su, Q.; Xie, J.; Zhang, J.; Zhong, Y.; Du, G.; Xu, B., In situ transmission electron microscopy observation of electrochemical behavior of CoS2 in lithium-ion battery. *ACS applied materials & interfaces* **2014,** *6* (4), 3016-3022.

413.   Vaughan, D. J.; Burns, R. G.; Burns, V. M., Geochemistry and bonding of thiospinel minerals. *Geochimica et Cosmochimica Acta* **1971,** *35* (4), 365-381.

414.   Jacobs, J.-P.; Maltha, A.; Reintjes, J. G.; Drimal, J.; Ponec, V.; Brongersma, H. H., The surface of catalytically active spinels. *Journal of Catalysis* **1994,** *147* (1), 294-300.

415.   Liu, Y.; Xiao, C.; Lyu, M.; Lin, Y.; Cai, W.; Huang, P.; Tong, W.; Zou, Y.; Xie, Y., Ultrathin Co3S4 nanosheets that synergistically engineer spin states and exposed polyhedra that promote water oxidation under neutral conditions. *Angewandte Chemie* **2015,** *127* (38), 11383-11387.

416.   Chauhan, M.; Reddy, K. P.; Gopinath, C. S.; Deka, S., Copper Cobalt Sulfide Nanosheets Realizing a Promising Electrocatalytic Oxygen Evolution Reaction. *ACS Catalysis* **2017,** *7* (9), 5871-5879.

417.   Hodes, G.; Cahen, D., Electrodeposition of CuInSe2 and CuInS2 films. *solar Cells* **1986,** *16,* 245-254.

418.   Yin, L.; Ye, C., Review of quantum dot deposition for extremely thin absorber solar cells. *Science of advanced materials* **2011,** *3* (1), 41-58.

419.   Möller, J.; Fischer, C.-H.; Muffler, H.-J.; Könenkamp, R.; Kaiser, I.; Kelch, C.; Lux-Steiner, M. C., A novel deposition technique for compound semiconductors on highly porous substrates: ILGAR. *Thin Solid Films* **2000,** *361,* 113-117.

420.   Cayzac, R.; Boulc'h, F.; Bendahan, M.; Pasquinelli, M.; Knauth, P., Preparation and optical absorption of electrodeposited or sputtered, dense or porous nanocrystalline CuInS2 thin films. *Comptes Rendus Chimie* **2008,** *11* (9), 1016-1022.

421.   Mousavi-Kamazani, M.; Salavati-Niasari, M., A simple microwave approach for synthesis and characterization of Ag2S–AgInS2 nanocomposites. *Composites Part B: Engineering* **2014,** *56*, 490-496.

422.   Vahidshad, Y.; Ghasemzadeh, R.; Irajizad, A.; Mirkazemi, S., Synthesis and characterization of copper indium sulfide chalcopyrite structure with hot injection method. *Journal of Nanostructures* **2013,** *3* (2), 145-154.

423.   De Jong, W.; Hoog, A., Carrollit (Sychnodymit). *Zeitschrift für Kristallographie* **1928,** *66*, 168-171.

424.   Mahmoudkhani, A. H.; Langer, V.; Casari, B. M., Two-dimensional network of C–H··· Cl–Co hydrogen bonds in the structure of 1, 1, 4, 4-tetraisopropylpiperazinium tetrachlorocobaltate (II). *Acta Crystallographica Section E: Structure Reports Online* **2001,** *57* (9), m393-m395.

425.   Macdonald, A. L.; Trotter, J., Crystal Structure of Bis [hexakis (dimethylamino) cyclotriphosphonitrilium] Tetrachlorocobaltate (II). *Canadian Journal of Chemistry* **1974,** *52* (5), 734-737.

426.   Yu, J.; Hai, Y.; Cheng, B., Enhanced photocatalytic H2-production activity of TiO2 by Ni (OH) 2 cluster modification. *The Journal of Physical Chemistry C* **2011,** *115* (11), 4953-4958.

427.   Zhang, J.; Yu, J.; Zhang, Y.; Li, Q.; Gong, J. R., Visible light photocatalytic H2-production activity of CuS/ZnS porous nanosheets based on photoinduced interfacial charge transfer. *Nano Letters* **2011,** *11* (11), 4774-4779.

428.   Yu, J.; Zhang, J.; Liu, S., Ion-exchange synthesis and enhanced visible-light photoactivity of CuS/ZnS nanocomposite hollow spheres. *The Journal of Physical Chemistry C* **2010,** *114* (32), 13642-13649.

429.   Hou, L.; Hua, H.; Bao, R.; Chen, Z.; Yang, C.; Zhu, S.; Pang, G.; Tong, L.; Yuan, C.; Zhang, X., Anion-Exchange Formation of Hollow NiCo2S4 Nanoboxes from Mesocrystalline Nickel Cobalt Carbonate Nanocubes towards Enhanced Pseudocapacitive Properties. *ChemPlusChem* **2016,** *81* (6), 557-563.

430.   Nie, L.; Wang, H.; Liu, S.; Yuan, R., SOLVOTHERMAL SYNTHESIS OF CuCo2S4 NANOPARTICLES FOR RECHARGEABLE LITHIUM-ION BATTERY ANODES. *Chalcogenide Letters* **2016,** *13* (12), 555-562.

431.   Pattrick, R. A.; Coker, V. S.; Pearce, C. I.; Telling, N. D.; van der Laan, G., The oxidation state of copper and cobalt in carrollite, CuCo2S4. *The Canadian Mineralogist* **2008,** *46* (5), 1317-1322.

432.   Aiken III, J. D.; Finke, R. G., A review of modern transition-metal nanoclusters: their synthesis, characterization, and applications in catalysis. *Journal of Molecular Catalysis A: Chemical* **1999,** *145* (1-2), 1-44.

433.   Turkevich, J.; Stevenson, P. C.; Hillier, J., A study of the nucleation and growth processes in the synthesis of colloidal gold. *Discussions of the Faraday Society* **1951,** *11*, 55-75.

434.   Brust, M.; Walker, M.; Bethell, D.; Schiffrin, D. J.; Whyman, R., Synthesis of thiol-derivatised gold nanoparticles in a two-phase liquid–liquid system. *Journal of the Chemical Society, Chemical Communications* **1994,** (7), 801-802.

435.   Li, M.; Su, J.; Guo, L., Preparation and characterization of ZnIn2S4 thin films deposited by spray pyrolysis for hydrogen production. *International Journal of Hydrogen Energy* **2008,** *33* (12), 2891-2896.

436.   Qin, Y.; Ji, X.; Jing, J.; Liu, H.; Wu, H.; Yang, W., Size control over spherical silver nanoparticles by ascorbic acid reduction. *Colloids and Surfaces A: Physicochemical and Engineering Aspects* **2010,** *372* (1-3), 172-176.

437.   Janiak, C., Ionic liquids for the synthesis and stabilization of metal nanoparticles. *Zeitschrift für Naturforschung B* **2013,** *68* (10), 1059-1089.

438.   Liu, Y.; Kathan, K.; Saad, W.; Prud'homme, R. K., Ostwald ripening of β-carotene nanoparticles. *Physical Review Letters* **2007,** *98* (3), 036102.

439.   Goesmann, H.; Feldmann, C., Nanoparticulate functional materials. *Angewandte Chemie International Edition* **2010,** *49* (8), 1362-1395.

440.   Sashina, E.; Kashirskii, D.; Martynova, E., Features of the molecular structure of pyridinium salts and their dissolving power with respect to cellulose. *Russian Journal of General Chemistry* **2012,** *82* (4), 729-735.

441.   Niemczak, M.; Chrzanowski, Ł.; Praczyk, T.; Pernak, J., Biodegradable herbicidal ionic liquids based on synthetic auxins and analogues of betaine. *New Journal of Chemistry* **2017,** *41* (16), 8066-8077.

442.   Leys, J.; Rajesh, R. N.; Menon, P. C.; Glorieux, C.; Longuemart, S.; Nockemann, P.; Pellens, M.; Binnemans, K., Influence of the anion on the electrical conductivity and glass formation of 1-butyl-3-methylimidazolium ionic liquids. *The Journal of chemical physics* **2010,** *133* (3), 034503.

443.   Zhang, Y.; Maginn, E. J., Molecular dynamics study of the effect of alkyl chain length on melting points of [C n MIM][PF 6] ionic liquids. *Physical Chemistry Chemical Physics* **2014,** *16* (26), 13489-13499.

444.   Ngo, H. L.; LeCompte, K.; Hargens, L.; McEwen, A. B., Thermal properties of imidazolium ionic liquids. *Thermochimica Acta* **2000,** *357*, 97-102.

445.   Huddleston, J. G.; Visser, A. E.; Reichert, W. M.; Willauer, H. D.; Broker, G. A.; Rogers, R. D., Characterization and comparison of hydrophilic and hydrophobic room temperature ionic liquids incorporating the imidazolium cation. *Green chemistry* **2001,** *3* (4), 156-164.

446.   Göbel, R.; Xie, Z.-L.; Neumann, M.; Günter, C.; Löbbicke, R.; Kubo, S.; Titirici, M.-M.; Giordano, C.; Taubert, A., Synthesis of mesoporous carbon/iron carbide hybrids with unusually high surface areas from the ionic liquid precursor [Bmim][FeCl 4]. *CrystEngComm* **2012,** *14* (15), 4946-4951.

447.   Lu, W.; Ding, Y.; Chen, Y.; Wang, Z. L.; Fang, J., Bismuth telluride hexagonal nanoplatelets and their two-step epitaxial growth. *Journal of the American Chemical Society* **2005,** *127* (28), 10112-10116.

448.   Wang, M.; Xie, F.; Li, W.; Chen, M.; Zhao, Y., Preparation of various kinds of copper sulfides in a facile way and the enhanced catalytic activity by visible light. *Journal of Materials Chemistry A* **2013,** *1* (30), 8616-8621.

449.   Ryan, L.; Norris, R., *Cambridge International AS and A Level Chemistry Coursebook with CD-ROM*. Cambridge University Press: 2014.

450.   Lou, W.; Chen, M.; Wang, X.; Liu, W., Size control of monodisperse copper sulfide faceted nanocrystals and triangular nanoplates. *The Journal of Physical Chemistry C* **2007,** *111* (27), 9658-9663.

451.   Yang, H. G.; Zeng, H. C., Self-Construction of Hollow SnO2 Octahedra Based on Two-Dimensional Aggregation of Nanocrystallites. *Angewandte Chemie* **2004,** *116* (44), 6056-6059.

452.   Mer, V. K. L., Nucleation in phase transitions. *Industrial & Engineering Chemistry* **1952,** *44* (6), 1270-1277.

453.   Watzky, M. A.; Finke, R. G., Transition metal nanocluster formation kinetic and mechanistic studies. A new mechanism when hydrogen is the reductant: slow, continuous nucleation and fast autocatalytic surface growth. *Journal of the American Chemical Society* **1997,** *119* (43), 10382-10400.

454.   Watzky, M. A.; Finke, R. G., Nanocluster size-control and "Magic Number" investigations. experimental tests of the "Living-metal polymer" concept and of mechanism-based size-control predictions leading to the syntheses of iridium (0) nanoclusters centering about four sequential magic numbers. *Chemistry of materials* **1997,** *9* (12), 3083-3095.

455.   Yu, J. G.; Guo, H.; Davis, S. A.; Mann, S., Fabrication of Hollow Inorganic Microspheres by Chemically Induced Self-Transformation. *Advanced Functional Materials* **2006,** *16* (15), 2035-2041.

456.	Yu, H.; Yu, J.; Liu, S.; Mann, S., Template-free hydrothermal synthesis of CuO/Cu2O composite hollow microspheres. *Chemistry of materials* **2007,** *19* (17), 4327-4334.

457.	Peng, Z.; Li, S.; Weng, M.; Zhang, M.; Xin, C.; Du, Z.; Zheng, J.; Pan, F., First-Principles Study of Cu9S5: A Novel p-Type Conductive Semiconductor. *The Journal of Physical Chemistry C* **2017,** *121* (42), 23317-23323.

458.	Hancox, I. Utilising High Work Function Metal Oxides as Hole Extracting Layers for Organic Photovoltaic Cells. University of Warwick, 2013.

459.	Chambon, S.; Derue, L.; Lahaye, M.; Pavageau, B.; Hirsch, L.; Wantz, G., MoO3 thickness, thermal annealing and solvent annealing effects on inverted and direct polymer photovoltaic solar cells. *Materials* **2012,** *5* (12), 2521-2536.

460.	Hancox, I.; Chauhan, K.; Sullivan, P.; Hatton, R.; Moshar, A.; Mulcahy, C.; Jones, T., Increased efficiency of small molecule photovoltaic cells by insertion of a MoO 3 hole-extracting layer. *Energy & Environmental Science* **2010,** *3* (1), 107-110.

461.	Elumalai, N. K.; Uddin, A., Open circuit voltage of organic solar cells: an in-depth review. *Energy & Environmental Science* **2016,** *9* (2), 391-410.

A. List of Publications

- ***Abouserie, A.**, Zehbe, K., Metzner, P., Kelling, A., Günter, C., Schilde, U., Strauch, P., Körzdörfer, T., and Taubert, A., New alkylpyridinium tetrahalidometallate ionic liquids and ionic liquid crystals-insights into the origin of their phase behavior. European Journal of Inorganic Chemistry,* **2017**(48), 5640.

- *El-Nagar, G.A., Sarhan, R.M., **Abouserie, A.**, Maticiuc, N., Bargheer, M., Lauermann, I., and Roth, C., 2017. Efficient 3D-Silver Flower-like Microstructures for Non-Enzymatic Hydrogen Peroxide (H_2O_2) Amperometric Detection. Scientific Reports,* **7**(1), 12181.

- *Kim, Y., Heyne, B., **Abouserie, A.**, Pries, C., Ippen, C., Günter, C., Taubert, A., and Wedel, A., CuS Nanoplates from Ionic Liquid Precursors - application in Organic Photovoltaic Cells. The Journal of Chemical Physics,* **148**(19), 193818.

- *Abouserie, A., El-Nagar, G. A., Heyne, B., Sarhan, R. M., Kim, Y., Pries, C., Ribacki, E., Günter, C., Roth, C., Wedel, A., and Taubert, A., Hierarchically structured Copper Sulfide Microflowers with Excellent Amperometric Hydrogen Peroxide Detection Performance. Journal of Materials Chemistry A (**Submitted**)*

- ***Abouserie, A.**, Schilde, U., and Taubert, A.,* Crystal structure of N-butylpyridinium bis(μ$_2$-dichlorido)-tetrachlorido-di-copper(II), $C_{18}H_{28}N_2Cu_2Cl_6$. *Zeitschrift für Kristallographie - New Crystal Structures (**Submitted**)*

- ***Abouserie, A.**, El-Nagar, G. A., Heyne, B., Kelling, A., Günter, C., Schilde, U., Wedel, A., Roth, C., and Taubert, A., The ionic liquid $[C_4Py]_2[Cu_{0.39}Co_{0.61}Cl_4]$ is a single source ionic liquid precursor (ILP) for carrolite $CuCo_2S_4$ nanomaterials and its exploitation for water splitting. (**Planned submission in May 2018**)*

B. Acknowledgment

C. Eigenständigkeitserklärung

Hiermit versichere ich, dass ich die vorliegende Arbeit selbstständig und nur unter Zuhilfenahme der angegebenen Quellen und Hilfsmittel angefertigt habe. Ich versichere auch, dass diese Arbeit noch an keiner anderen Hochschule eingereicht wurde.

Potsdam, den 28. März 2018

Ahed Abouserie